technische universität
dortmund

Dissertation zur Erlangung des akademischen Grades
Doctor rerum naturalium

Traces of Gravity: Bridging Scales from Cosmological Observables to Neutrino Oscillations

Sara Krieg
geboren in Ibbenbüren

2025

Lehrstuhl für Theoretische Physik III - Arbeitsgruppe Päs
Fakultät Physik
Technische Universität Dortmund

Erstgutachter:	Prof. Dr. Heinrich Päs
Zweitgutachter:	Prof. Dr. Gudrun Hiller
Vorsitzender der Prüfungskomission:	Prof. Dr. Carsten Westphal
Mitglied der Prüfungskomission:	Prof. Dr. Igor Schapiro
Abgabedatum:	11. November 2025
Datum der mündlichen Prüfung:	20. Januar 2026

Veröffentlichte und genehmigte Dissertation an der Fakultät Physik der Technischen Universität Dortmund.

List of Publications

The research presented in this thesis is primarily based on the following publications:

[1] Patrick Adolf, Martin Hirsch, Sara Krieg, Heinrich Päs, and Mustafa Tabet. "Fitting the DESI BAO data with dark energy driven by the Cohen-Kaplan-Nelson bound". In: *JCAP* 08 (2024), p. 048. DOI: 10.1088/1475-7516/2024/08/048. arXiv: 2406.09964 [astro-ph.CO]

[2] Patrick Adolf, Martin Hirsch, Sara Krieg, Heinrich Päs, and Mustafa Tabet. "Addendum: Fitting the DESI BAO Data with Dark Energy Driven by the Cohen-Kaplan-Nelson Bound". In: *JCAP* (Apr. 2025). arXiv: 2504.15332 [astro-ph.CO]

[3] Dominik Hellmann, Sara Krieg, Heinrich Päs, and Mustafa Tabet. "Neutrino oscillations as a gravitational wave detector?" In: *JCAP* 05 (2025), p. 075. DOI: 10.1088/1475-7516/2025/05/075. arXiv: 2405.05000 [hep-ph]

[4] Alba Domi, Thomas Eberl, Dominik Hellmann, Sara Krieg, and Heinrich Päs. "Potential of neutrino telescopes to detect quantum gravity-induced decoherence in the presence of dark fermions". In: *JCAP* 01 (2025), p. 063. DOI: 10.1088/1475-7516/2025/01/063. arXiv: 2409.12633 [hep-ph]

Parts of the work presented in Chapters 3, 4, and 5 have not yet been published at the time of this thesis.

Abstract

The guiding idea of this thesis is to investigate how subtle traces of gravity manifest themselves across different scales. First, we examine whether the Cohen, Kaplan and Nelson (CKN) bound can form the basis of a consistent cosmological model and whether such a model is favored by observational data, in particular the recent baryonic acoustic oscillation measurements from the Dark Energy Spectroscopic Instrument. Taking into account additional late-universe measurements, there is a mild preference for the (ν)CKN model over the standard ΛCDM scenario with cold dark matter and a cosmological constant. However, once weak lensing and cosmological microwave background data are included and the early-time dynamics are accounted for, the resulting bounds on the model parameter ν restrict the (ν)CKN model to a regime in which the (ν)CKN framework is observationally indistinguishable from ΛCDM. Second, we develop an internal wave packet formalism for neutrino oscillations in weakly curved spacetimes. Gravitational corrections appear as phase modifications, but these effects lie far beyond current experimental sensitivity. Importantly, if deviations from expected oscillation patterns are observed, classical gravity can be ruled out as their source, thereby pointing to new physics beyond the Standard Model, such as quantum gravity. Finally, we employ the open quantum system framework to model Quantum Gravity (QG)-induced decoherence of high-energy neutrinos and perform a sensitivity analysis using IceCube data. Using current experimental data we also derive bounds on the damping parameter γ_0 for different energy scalings and obtain the first constraints for scenarios involving additional dark fermions.

Zusammenfassung

Die zentrale Idee dieser Arbeit ist es, zu untersuchen, wie sich die subtilen Spuren der Gravitation auf verschiedenen Skalen bemerkbar machen. Zunächst prüfen wir, ob die durch Gravitation motivierte Cohen, Kaplan und Nelson (CKN)-Grenze ein Fundament für ein konsistentes kosmologisches Modell bilden kann und ob dieses gegenüber ΛCDM durch Beobachtungsdaten bevorzugt wird, insbesondere durch die aktuellen Messungen der baryonischen akustischen Oszillationen des Dark Energy Spectroscopic Instrument. Unter Einbeziehung zusätzlicher Messungen des späten Universums ergibt sich eine leichte Präferenz für das (ν)CKN-Modell gegenüber ΛCDM. Werden jedoch Daten aus schwacher Gravitationslinsenwirkung und vom kosmischen Mikrowellenhintergrund berücksichtigt und die Dynamik zur frühen Zeit einbezogen, so wird das Modell so stark beschränkt, dass es nicht mehr von ΛCDM unterscheidbar ist. Im zweiten Teil entwickeln wir einen internen Wellenpaket-Formalismus für Neutrinooszillationen in schwach gekrümmten Raumzeiten. Gravitative Korrekturen treten als Phasenmodifikationen auf, liegen jedoch weit außerhalb aktueller experimenteller Sensitivität. Sollten Abweichungen vom erwarteten Oszillationsmuster beobachtet werden, können klassische Gravitationseffekte als Ursache mit hoher Sicherheit ausgeschlossen werden. Die Erklärung müsste dann in neuer Physik wie der Quantengravitation liegen. Abschließend nutzen wir den Formalismus offener Quantensysteme, um quantengravitativ induzierte Dekohärenz hochenergetischer Neutrinos zu modellieren, und führen eine Sensitivitätsanalyse mit IceCube-Daten durch. Dabei leiten wir Schranken für den Dämpfungsparameter γ_0 in verschiedenen Energieskalierungen ab und gewinnen erstmals

auch Einschränkungen für Szenarien mit zusätzlichen dunklen Fermionen.

Acknowledgements

Although I am the sole author of this dissertation, I owe a profound debt of gratitude to many people in my life.
First and foremost, I would like to thank my supervisor, Prof. Päs, for his continuous support. Our weekly meetings always gave me a sense of security and helped steer me in the right direction. I am also grateful to Prof. Hiller, who kindly agreed to serve as second examiner of my thesis, and who was always a wonderful conversational partner—whether about running or about designing the website.
I am deeply thankful for the amazing group of colleagues at our institute, ranging from former members such as Nico Adolph, Lara Nollen, Tim Höhne, and Tim Brune to current colleagues Daniel Wendler, Kai Sieja, Dominik Suelmann, Patrick Adolf, Max Uetrecht, Jordi, Moritz Bosse, and Tom Steudtner. I have so many fond memories of parties with all of you and of countless conversations that lifted me up during difficult times. I also wish to thank Manos for the many fun conversations and for giving the best lectures I have ever had the pleasure to attend.
A very special thanks goes to Dominik Hellmann, with whom I had the privilege of sharing an office for most of the past three years, and with whom I also share many "arXiv-children." I am deeply grateful for your guidance, your constant motivation, and your perfectionism—especially whenever I felt like giving up. You played a huge role in keeping me sane throughout this journey. Honestly, thank you, brudi!
I also want to thank my wonderful circle of physics friends. The core of this group formed already in the very first semesters of our studies, and all of you have accompanied me through both my academic path and many personal phases of my life. Marek, Jan Leo, Alina, Cyrus, Tristan, Nils—you have been by my side through so much, and I am incredibly proud that we never lost each other along the way and that we can now celebrate this achievement together. I truly don't know if I would have made it this far without you.
Within this group, I owe a very special thanks to Tristan, through whom Steffi has also become such an important part of my life. Thank you, Steffi, for being honest with me when I was completely losing perspective, for being there through every high and every low, and for our "Trash TV Tuesday" with Alina, which kept me grounded and laughing.
Looking even further back, I am grateful to my friends from Ibbenbüren, who accompanied me through school years and shaped me more than almost anyone else: Carmen, Maire, Greta, and Carly. Thank you for always being so understanding when I disappeared into my formula sheets for… anywhere between one day and three months.
There are so many more friends I would like to thank—such as Natalie and Marc, who always encouraged and supported me. But I cannot possibly forget one person: the famous Dr. Musti. Not only did you teach me more, both personally and academically, than almost anyone else, you also became one of my closest friends. You lifted me up whenever I felt uncertain about my work, ranted with me, or simply stayed by my side through mental breakdowns. I am deeply thankful that you are always there for me. Truly—thank you.
Before turning to my own family, I would also like to thank the family of my partner:

Simone, Detlef, Linus, and Gisela. You never made me feel like just an “add-on,” but welcomed me as part of your family from the very beginning. You might believe that I completed this dissertation with ease, but in truth, there were many difficult times—and knowing that I could always count on you made all the difference. Thank you for letting me be part of your family.
Now, to my own family: First of all, my deepest gratitude goes to my parents. None of this would have been possible without you—not only because you made my studies feasible in the first place, but also because you always encouraged me to believe in myself and my abilities. From you I learned what my mind can accomplish.
To my siblings, I owe heartfelt thanks, especially to my sister Lena. I have always admired your strength. You are one of the few people who love me unconditionally, and for that I thank you. I am also grateful to my brothers Daniel and Thomas, as well as my half-brother Helge and his family, Anni, Janna, and Paula. You have not been part of my life for very long yet, but you have quickly become incredibly important to me.
Finally, I want to thank the most important person of all: my partner, Jannis. My life shines in so many more colors when you are by my side, and nothing calms me as much as your embrace. Without you, I could never have made it this far—at least not like this. I love you with all my heart, and I am grateful every day for the certainty that you love me just as much. Here’s to forever!

Contents

List of Acronyms

AIC Akaike Information Criterion

BAO Baryonic Acoustic Oscillations

BBN Big Bang Nucleosynthesis

BSM Beyond the Standard Model

CKM Cabibbo–Kobayashi–Maskawa

CKN Cohen, Kaplan and Nelson

CL Confidence Level

CMB Cosmic Microwave Background

DESI Dark Energy Spectroscopic Instrument

DM Dark Matter

DOF Degree of Freedom

EFT Effective Field Theory

EMRI Extreme Mass Ratio Inspiral

FLRW Friedmann–Lemaître–Robertson–Walker

GR General Relativity

GW Gravitational Wave

IR Infrared

LSS Large Scale Structure

MC Monte Carlo

MCMC Markov Chain Monte Carlo

MSW Mikheyev–Smirnov–Wolfenstein

PMNS Pontecorvo–Maki–Nakagawa–Sakata

QCD Quantum Chromodynamics

QFT Quantum Field Theory

QG Quantum Gravity

RNC Riemann Normal Coordinate System

SGWB Stochastic Gravitational Wave Background

SM Standard Model

SMBHB Supermassive Black Hole Binaries

SVT Scalar–Vector–Tensor

UV Ultraviolet

VED Vacuum Energy Density

VEV Vacuum Expectation Value

WIMPs Weakly Interacting Massive Particles

List of Tables

List of Figures

Chapter 1

Introduction

Subtle patterns through the universe,
Threads that in their silence rhyme,
Echoes carried through space and time,
Are the silent traces of gravity's chime.

These lines capture the spirit of this thesis. They speak of patterns and threads, of echoes and traces. Gravity often acts in such a subtle way, yet it is the binding force of the cosmos. While gravity is ever-present in our lives, its influence often reveals itself through consequences both grand and subtle: in the orbits of planets, in the bending of light, in the expansion of space, in the faint ripples of Gravitational Waves (GW), and in the growth of cosmic structures. Gravity is the background music of the universe, a subtle chime that fades in the microscopic realm, yet shapes the stage of physics itself. Like faint footprints in the sand, the presence and influence of gravity must often be inferred from the marks it imprints upon matter, radiation, and the very geometry of spacetime. Physicists become readers of these traces, interpreting the patterns rather than observing gravity directly. To follow such traces is to follow the story of the cosmos itself.

This thesis also searches for such traces. On different levels, we will encounter gravity: implicitly, as a regulator of cosmological dynamics; explicitly, as a classical spacetime background underlying a Quantum Field Theory (QFT); and finally as a quantum imprint, leaving its mark in phenomena accessible to today's observations. Each chapter is, in a sense, a step along this path of deciphering gravity's handwriting across the universe. We attempt to read and interpret its subtle script, one trace at a time.

Human curiosity has always been driven not only by practical benefit, but by the desire to uncover the underlying principles of nature. Since ancient times, people have sought to understand what holds the world together at its core. Today, such questions are pursued systematically in the framework of fundamental research. Although often criticized for its lack of immediate application, basic science continuously expands our worldview. Discoveries that once seemed purposeless, such as quantum mechanics, now form the foundation of modern technology. Beyond its practical impact, fundamental research is also part of our culture, an expression of humanity's creativity and imagination. As a society, we must therefore allow ourselves the pursuit of pure knowledge. History itself shows how fruitful this quest can be, and gravity provides a telling example.

Even though early cultures lacked a fomulated theory of gravity, its observable effects, such as the motion of celestial bodies, were already interpreted and woven into religious views, while also laying the foundation for the first astronomical theories. In the 17th century, Newton formulated the law of universal gravitation, unifying the description of

celestial and terrestrial motion. In 1915, Einstein revolutionized this picture by showing that gravity is not a force but the manifestation of curved spacetime itself.
Einstein's general relativity has by now been tested with remarkable precision on astrophysical and cosmological scales: From the deflection of light to the detection of GWs. Yet it remains a classical theory, as it does not provide a quantum description of gravity. A consistent theory of Quantum Gravity (QG) is still missing. While various approaches have been proposed, none has gained experimental confirmation. Even without a complete theory, however, one can search for phenomenological imprints of QG.
The history of the universe is meanwhile successfully described within the standard model of cosmology, i.e., the ΛCDM model, which yields a well-tested framework for understanding the universe's evolution. This framework accounts for a wealth of cosmological observations, yet it relies on two components that remain unexplained at a fundamental level: Dark Matter (DM) and dark energy. In particular, the origin and nature of dark energy, which drives the accelerated expansion of the universe, is still a profound mystery. Addressing this question motivates the first part of this thesis, where gravity enters implicitly as a regulator of cosmological dynamics.
At the same time, neutrinos provide a complementary window into gravity that is rather independent of the cosmological perspective. Unlike most other particles, they can traverse the universe almost unhindered, carrying information from otherwise inaccessible regions. Their oscillations already demonstrate physics beyond the standard model, and their weak interaction makes them sensitive probes of both spacetime structure and potential QG effects. This motivates the second part of the thesis, where gravity enters explicitly.
By addressing both cosmological and particle physics perspectives, this thesis aims to shed light on different manifestations of gravity and the subtle traces it leaves across the universe. Therefore, it is structured as follows: Chapter 2 introduces the theoretical foundations, covering the Standard Model (SM), General Relativity (GR), cosmology, and neutrino oscillations, thereby setting the stage for the subsequent chapters.
In chapter 3, gravity appears implicitly, as a regulator of cosmological dynamics. We investigate a model in which the time evolution of dark energy is constrained by the Cohen, Kaplan and Nelson (CKN) bound. This bound, motivated by gravitational arguments, imposes interdependent Ultraviolet (UV) and Infrared (IR) cutoffs on a QFT. The cosmological constant acquires a contribution from the vacuum energy of the underlying QFT, while phenomenological considerations, in particular, identifying the IR cutoff with the size of the observable universe, lead to an effective time dependence of the dark energy. Such a dynamical behavior is further motivated by recent experimental indications, in particular from the Dark Energy Spectroscopic Instrument (DESI) [5]. The resulting model is first confronted with late-universe data and subsequently tested in a global analysis that incorporates additional early-universe observations.
Chapter 4 moves to an explicit, classical manifestation of gravity. Here, we study how spacetime curvature affects neutrino oscillations and assess whether such effects could in principle be observable. Building on this, we turn to dynamical scenarios, considering both GWs and the Stochastic Gravitational Wave Background (SGWB), and analyze their potential impact on neutrino flavor evolution.
Once the effect of classical gravity is understood, we explore the quantum imprint of gravity in chapter 5. We search for QG effects through decoherence in neutrino oscillations. For this purpose, we employ the framework of open quantum systems, which provides a model independent parametrization of possible QG effects. This allows us to

derive explicit bounds on QG parameters using data of the IceCube neutrino observatory. Finally, chapter 6 summarizes the results and offers an outlook on future directions. Taken together, these stages form a coherent arc: each reveals a different manifestation of the *traces of gravity*, ranging from its implicit role in cosmology to its explicit quantum imprints.

The question of the nature of gravity does not concern specialists alone; it forms the foundation of our understanding of space and time, and thus of nothing less than our reality. These are therefore not merely physical questions, but part of humanity's cultural heritage. This thesis seeks to contribute a small yet concrete step towards answering them, by following the silent traces that gravity has inscribed across the universe.

Chapter 2

Theoretical Foundations

In this chapter we introduce the essential theoretical concepts required for the discussions in this work. Since our current understanding of particle physics is fundamentally based on the well-established Standard Model (SM) of particle physics, we begin by briefly introducing it in section 2.1. While the SM has been remarkably successful, it still leaves many questions unanswered. We therefore close this section with a discussion of the most pertinent unresolved issues. Following this, we turn to neutrino oscillations in section 2.2, an observed phenomenon that requires the existence of Beyond the Standard Model (BSM) physics. We examine the various theoretical approaches used to determine oscillation probabilities. Given the profound implications for particle physics and cosmology, neutrino oscillations serve as a key example of how theoretical and experimental insights drive our understanding beyond established paradigms. We proceed by providing an introduction to the fundamental principles of General Relativity (GR) in section 2.3. Finally, we discuss in section 2.4 the standard cosmological model, its key predictions, and the observational evidence supporting it. Additionally, we present alternative models that have been proposed in the literature to address the open questions in cosmology.

2.1 The Standard Model of Particle Physics

The SM is a widely accepted and well-established theory, providing the fundamental framework of particle physics. It describes all known interactions—except gravity—and groups all known elementary particles within the framework of a renormalizable Quantum Field Theory (QFT). Its broad acceptance is based on extensive experimental evidence, which has consistently confirmed its predictions [6–12]. Despite its success, there are certain observations suggesting and some even requiring BSM physics [13–15]. For a comprehensive introduction to the SM see reference [16]. According to the SM, all known elementary particles are either of fermionic or bosonic nature. Fermions possess half-integer spin, whereas bosons have integer spin. The group of fermions is further divided into leptons and quarks, both of which constitute the building blocks of all known matter. There are six leptons, classified according to their electric charge Q, three of them falling into the group of the electrically neutral neutrinos, and the other three fall into the group of the charged leptons. Each charged lepton together with a corresponding neutrino defines a so-called lepton family with lepton family number L_f, where $f = e,\ \mu,\ \tau$ corresponds to the electron, muon and tau, respectively.
Similarly, the six flavors of quarks belong to the group of up-type quarks with charge $Q = 2/3$ (up, charm, top) or down-type quarks with charge $Q = -1/3$ (down, strange,

bottom). These also organize into three generations each one consisting of an up- and down-type quark pair. Unlike the leptons, however, quarks usually do not exist freely but form bound states known as hadrons due to a phenomenon called *confinement*, a consequence of the color charge they carry, which is the charge associated with the strong interaction [17]. The hadrons are mainly categorized into baryons (three quarks) and mesons (quark–antiquark pairs). Each of these fermions has a corresponding antiparticle with opposite charges and same mass.
Vector bosons (spin 1) are the mediators of fundamental interactions, responsible for transmitting the corresponding forces. The photon γ mediates the electromagnetic force and couples to all particles with an electric charge. The weak interaction is mediated by the two $W^{\pm}$ bosons and the Z boson. The former couple only to left-handed fermions and right-handed antifermions due to the chiral nature of the charged current [18]. Additionally, the eight gluons g mediate the strong interaction by coupling to color charge. Since gluons themselves carry color charge, they can interact with both quarks and other gluons.
Lastly, the Higgs boson H, as the only scalar boson (spin 0), plays a unique role in the SM. Its field is responsible for the electroweak symmetry breaking, where through the non-zero Vacuum Expectation Value (VEV), the SM masses of all particles are generated.

2.1.1 Symmetry Structure of the SM

As a QFT the SM is formulated in terms of quantum fields, where each field is associated with a corresponding particle species. The interactions of the SM arise from the requirement of local gauge invariance of the SM action S_{SM} under the symmetry group

$$G = \mathrm{SU}(3)_{\mathrm{C}} \times \mathrm{SU}(2)_{\mathrm{L}} \times \mathrm{U}(1)_{\mathrm{Y}}\,, \tag{2.1}$$

where (S)U(n) denotes the (special) unitary group of degree n. Here, each gauge group is associated with either the strong, weak or electromagnetic interaction. The subscripts C stands for color, L for left-handedness, and Y for hypercharge. The strong interaction is described by the Quantum Chromodynamics (QCD) sector which is governed by $\mathrm{SU}(3)_{\mathrm{C}}$ [19, 20] and mediated by the eight gluons G^a_μ ($a = 1, \dots, 8$). The electroweak interaction is described by $\mathrm{SU}(2)_{\mathrm{L}} \times \mathrm{U}(1)_{\mathrm{Y}}$ before electroweak symmetry breaking [21, 22] mediated by the three weak bosons W^a_μ ($a = 1, \dots, 3$) and the hypercharge boson B_μ. While the gauge bosons transform under the adjoint representation, as it turns out, the fermions of the SM transform under the fundamental representation of the symmetry groups they are charged under. This means, that quarks transform as triplets under $\mathrm{SU}(3)_{\mathrm{C}}$, while leptons are singlets under this group. Left-handed fermions, both quarks and leptons, form doublets under $\mathrm{SU}(2)_{\mathrm{L}}$, whereas right-handed fermions are singlets. Additionally, all fermions are assigned specific hypercharges under $\mathrm{U}(1)_{\mathrm{Y}}$, determining their interactions with the hypercharge gauge boson B. Ultimately, it is the invariance of the interaction terms under these transformations that dictates their structure in the SM. For clarity, these fields and their corresponding transformation properties are gathered in table 2.1.
The dynamics of all quantum fields in the SM can be described using the principle of least action $\delta S_{\mathrm{SM}} = 0$, with the action of the SM S_{SM} given by

$$S_{\mathrm{SM}} = \int \mathrm{d}^4x\, \mathcal{L}_{\mathrm{SM}}\left(\Phi_i(x), \partial\Phi_i(x)\right)\,, \tag{2.2}$$

Table 2.1: Field content of the SM and transformation properties under the SM gauge group. The subscript i indicates the different generations for the left- and right-handed quarks. The superscript $a = 1, \dots, 8$ labels the gluons, and $b = 1, \dots, 3$ labels the weak bosons.

Field	$U(1)_Y$	$SU(2)_L$	$SU(3)_C$
G^a_μ	0	1	8
W^b_μ	0	3	1
B_μ	0	1	1
$Q_L = (u_{Li}, d_{Li})^T$	1/6	2	3
$L_L = (\nu_{eL}, e_L)^T, (\nu_{\mu L}, \mu_L)^T, (\nu_{\tau L}, \tau_L)^T$	1/2	2	1
u_{Ri}	2/3	1	3
d_{Ri}	−1/3	1	3
$l_R = e_R, \mu_R, \tau_R$	−1	1	1
$H = (\varphi^+, \varphi^0)^T$	1/2	2	1

where Φ_i denote all quantum fields, c.f. table 2.1. Here, the SM Lagragian $\mathcal{L}_{SM}$ is given by

$$\mathcal{L}_{SM} = \mathcal{L}_{gauge} + \mathcal{L}_{matter} + \mathcal{L}_{Higgs} + \mathcal{L}_{Yukawa}\,. \tag{2.3}$$

To fully understand this Lagrangian, we discuss each of its components in the following. We begin with $\mathcal{L}_{gauge}$ containing those contributions that describe the dynamics of the gauge fields, in case of a a non-abelian group structure this includes self-interactions, as it is the case for $SU(3)_C$ and $SU(2)_L$. The term $\mathcal{L}_{gauge}$ is given by

$$\mathcal{L}_{gauge} = -\frac{1}{4}B_{\mu\nu}B^{\mu\nu} - \frac{1}{4}W^a_{\mu\nu}W^{a\mu\nu} - \frac{1}{4}G^a_{\mu\nu}G^{a\mu\nu}\,, \tag{2.4}$$

with the field strength tensor of the gauge bosons

$$F^a_{\mu\nu} = \partial_\mu A^a_\nu - \partial_\nu A^a_\mu + g f^{abc} A^b_\mu A^c_\nu\,, \tag{2.5}$$

where F stands for any gauge boson field strength with A^a_μ being the corresponding gauge field, g the associated coupling constant, and f^{abc} the structure constants of the gauge group.
The term $\mathcal{L}_{matter}$ governs the dynamics of the fermions and their interaction with the gauge fields of the SM. It is given by

$$\mathcal{L}_{matter} = i\bar{\psi}\gamma^\mu D_\mu \psi\,, \tag{2.6}$$

where γ^μ are the Dirac matrices, satisfying the Clifford algebra $\{\gamma^\mu, \gamma^\nu\} = 2\eta^{\mu\nu}\mathbb{1}$. Note, that we use the mostly minus convention, i.e., $\eta_{\mu\nu} = \mathrm{diag}(1, -1, -1, -1)$ in Cartesian coordinates. The field ψ represents all matter particles in the SM, while $\bar{\psi}$ denotes the corresponding conjugate field $\bar{\psi} = \psi^\dagger\gamma^0$. The interactions with the gauge bosons are introduced through the gauge covariant derivative D_μ, defined as

$$D_\mu = \partial_\mu - i g_3 G^a_\mu \frac{\lambda^a}{2} - i g_2 W^i_\mu \frac{\tau^i}{2} - i g_1 B_\mu Y\,, \tag{2.7}$$

which arises naturally from the afore-mentioned imposed invariance of the SM Lagragian under the symmetry group G. Again, G^a_μ are the gauge fields of the strong interaction, associated with the strong coupling constant g_3 and Gellmann matrices λ^a only acting on the color triplets, while W^i_μ correspond to the weak interaction, with coupling g_2 and the Pauli matrices τ^i acting on the SU(2) doublets. The field B_μ represents the gauge boson coupled via g_1 to particles with hypercharge Y.
Next, we discuss the Lagrangian $\mathcal{L}_{\text{Higgs}}$. It describes the dynamics of the Higgs field H and, in particular, its potential $V(H)$, which induces the spontaneous breakdown of the electroweak symmetry:

$$\mathcal{L}_{\text{Higgs}} = (D^\mu H)^\dagger (D_\mu H) - V(H)\,. \tag{2.8}$$

Here, H is the SU(2) Higgs doublet with hypercharge $Y = 1/2$, which interacts with the gauge fields via the gauge covariant derivative D_μ given in equation (2.7). The Higgs potential $V(H)$ is given by [22, 23]

$$V(H) = \mu^2 H^\dagger H + \lambda (H^\dagger H)^2\,, \tag{2.9}$$

where a value of the quartic coupling $\lambda > 0$ bounds the potential from below and a mass parameter $\mu^2 < 0$ leads to the spontaneous symmetry breaking. This results in a vacuum structure with an infinite number of degenerate minima differing by a complex phase and satisfying

$$|\langle H \rangle|^2 = \frac{\mu^2}{2\lambda} =: \frac{v^2}{2}\,, \tag{2.10}$$

where $v/\sqrt{2}$ is the VEV of H. Consequently, the Higgs field acquires a non-zero value in the vacuum. In the unitary gauge, one Degree of Freedom (DOF) of the Higgs remains a physical mode, while the other three are absorbed into the longitudinal components of the massive gauge bosons. The Higgs field can then be expanded around the VEV $v/\sqrt{2}$ as

$$H(x) = \frac{1}{\sqrt{2}} \begin{pmatrix} 0 \\ v + h(x) \end{pmatrix}. \tag{2.11}$$

Substituting this expansion into the kinetic terms of $\mathcal{L}_{\text{Higgs}}$ generates the mass terms for the electroweak gauge bosons. After diagonalizing these mass terms, one can read off the masses

$$\mathcal{L}_{\text{Higgs}} \supset m_W^2 W^+_\mu W^{-\mu} + \frac{m_Z^2}{2} Z_\mu Z^\mu\,, \tag{2.12}$$

with the weak bosons now in the mass basis given by

$$Z^\mu = \cos(\Theta_W) W^\mu_3 - \sin(\Theta_W) B^\mu\,, \qquad W^{\pm\mu} = \frac{W^\mu_1 \pm i W^\mu_2}{\sqrt{2}}\,, \tag{2.13}$$

$$A^\mu = \cos(\Theta_W) B^\mu + \sin(\Theta_W) W^\mu_3\,, \tag{2.14}$$

the weak mixing angle Θ_W, and the masses of the $W^\pm$ and Z boson, m_W and m_Z, respectively

$$m_W = \frac{v g_2}{2}\,, \qquad m_Z = \frac{m_W}{\cos(\Theta_W)}\,, \qquad \cos(\Theta_W) = \frac{g_2}{\sqrt{g_2^2 + g_1^2}}\,. \tag{2.15}$$

The Higgs boson itself acquires a mass by substituting the expansion in equation (2.11) into the Higgs potential $V(H)$ in equation (2.9) yielding

$$m_h = \sqrt{2\lambda}v\,. \tag{2.16}$$

Here, the electroweak symmetry is broken down to

$$\mathrm{SU(2)_L \times U(1)_Y \to U(1)_{EM}}\,. \tag{2.17}$$

After this spontaneous symmetry breaking, the generator $Q = T^3 + Y$ remains unbroken and is identified with the electromagnetic charge, while the gauge boson corresponding to the unbroken subgroup, i.e., the photon A^μ, remains massless.
Finally, the term $\mathcal{L}_{\text{Yukawa}}$ describes the coupling of the Higgs field to the fermions and is responsible for generating the masses of quarks and charged leptons:

$$\mathcal{L}_{\text{Yukawa}} = -y_\mathrm{u}\bar{Q}_\mathrm{L}H^c u_\mathrm{R} - y_\mathrm{d}\bar{Q}_\mathrm{L}Hd_\mathrm{R} - y_\mathrm{e}\bar{L}_\mathrm{L}Hl_\mathrm{R} + \text{h.c.} \tag{2.18}$$

Here, y_u, y_d and y_e are the Yukawa coupling matrices, Q_L represents the left-handed quark doublets, L_L the left-handed lepton doublets, while u_R, d_R and l_R are the corresponding right-handed fermion singlets. The field $H^c = i\sigma^2 H^*$ is the charged-conjugated Higgs doublet. Again, by inserting the Higgs expansion from equation (2.11) into $\mathcal{L}_{\text{Yukawa}}$, mass terms for the fermions emerge:

$$\mathcal{L}_{\text{Yukawa}} \supset \mathcal{L}^{\text{mass}}_{\text{Yukawa}} = -\bar{u}_\mathrm{L}M_\mathrm{u}u_\mathrm{R} - \bar{d}_\mathrm{L}M_\mathrm{d}d_\mathrm{R} + \text{h.c.}\,, \tag{2.19}$$

with the mass matrices

$$M_\mathrm{u} = \frac{v}{\sqrt{2}}y_\mathrm{u}\,, \qquad\qquad M_\mathrm{d} = \frac{v}{\sqrt{2}}y_\mathrm{d}\,. \tag{2.20}$$

However, the Yukawa matrices are not necessarily diagonal, meaning the flavor basis, where the weak interaction terms are diagonal, does not coincide with the mass basis, where the mass terms in equation (2.19) are diagonal. To obtain the mass eigenstates, the mass matrices must be diagonalized via unitary transformations

$$M_\mathrm{u}^{\text{diag}} = V_\mathrm{u}^\dagger M_\mathrm{u} U_\mathrm{u}\,, \qquad\qquad M_\mathrm{d}^{\text{diag}} = V_\mathrm{d}^\dagger M_\mathrm{d} U_\mathrm{d}\,. \tag{2.21}$$

Here, U_u and U_d are unitary matrices describing the transformations of right-handed quarks, while V_u and V_d correspond to the transformations of the left-handed quark sector, i.e., $u_\mathrm{L} \to V_\mathrm{u}u_\mathrm{L}$, etc. The relation corresponding to equation (2.20) in the mass basis shows that fermion masses are always proportional to their respective Yukawa couplings. Since the Yukawa couplings are free parameters in the SM, they must be determined experimentally. Their values vary over many orders of magnitude, from the heavy top quark at the electroweak scale to the tiny electron mass. Since only left-handed quarks participate in $W^\pm$ interactions, the transformations leave behind a residual mixing factor in the charged current interactions

$$V_{\text{CKM}} = V_\mathrm{u}^\dagger V_\mathrm{d}\,. \tag{2.22}$$

This is the Cabibbo–Kobayashi–Maskawa (CKM) matrix, which governs quark transitions in weak interactions [24, 25]. It is responsible for the existence of flavor changing charged currents at tree level in the SM. The CKM matrix contains three mixing angles

and a complex phase [26], which leads to CP violation—a fundamental asymmetry between matter and antimatter arising from the combined violation of charge conjugation (C) and parity (P) symmetry, manifesting in processes such as kaon and B-meson decays.
In BSM physics a similar mixing structure exists in the lepton sector, where the neutrino mass eigenstates differ from the flavor eigenstates. Analogous to the role of the CKM matrix here, this mixing is described by the Pontecorvo–Maki–Nakagawa–Sakata (PMNS) matrix [27–29]. Unlike the former case, where mixing is relatively small, neutrino mixing angles are large, which is crucial for the observed neutrino oscillations. We discuss this phenomenon in more detail in section 2.2.

2.1.2 Open Questions of the Standard Model

Despite the wide acceptance of the SM as the central framework of particle physics, we know with certainty that it cannot be the complete description of nature. In this subsection, we discuss some of the open questions and shortcomings of the SM that are particularly relevant to this work.
One major limitation of the SM is that it predicts neutrinos to be massless, as the usual Higgs mechanism does not provide a neutrino mass term. However, neutrino oscillation experiments have conclusively shown that at least two neutrinos must have non-zero masses [13, 30]. The observed oscillation can be understood analogously to quark mixing as a mismatch between the flavor and mass eigenstates. We will explore neutrino oscillations in detail in section 2.2. As the origin of neutrino masses cannot be explained within the SM, new interactions beyond the SM are required, such as for example the seesaw mechanism [31]. A key open question in this context is whether neutrinos are Dirac or Majorana particles [32], which will be discussed in more depth in subsection 2.2.3.
Another unresolved issue is the nature of Dark Matter (DM). Observations like galactic rotation curves [14] and gravitational lensing [33, 34] indicate that approximately 27 % of the universe's matter consists of non-electromagnetically charged particles [35], for which the SM offers no suitable candidate. Various BSM models predict a plethora of different DM particles, including Weakly Interacting Massive Particles (WIMPs) [36], axions [37] and sterile neutrinos [38].
Additionally, the universe exhibits a striking matter–antimatter asymmetry [15, 39, 40]. Any successful theory addressing this problem must satisfy the Sakharov conditions [15], which require violation of baryon number, violation of C and CP symmetry, and departure from thermal equilibrium. The SM alone cannot explain this discrepancy, as its sources of CP violation are too small to account for the observed asymmetry. Many proposed solutions rely on leptogenesis [41], where an initial asymmetry in the lepton sector translates into a baryon asymmetry through electroweak processes.
Moreover, the SM does not include gravity—a fundamental force that remains outside the framework of QFT. While GR successfully describes gravitational interactions on macroscopic scales, a complete theory of Quantum Gravity (QG) remains elusive.
Finally, observations of the accelerated expansion of the universe strongly suggest the existence of dark energy, an unknown component that drives cosmic acceleration [42, 43]. The simplest explanation within the framework of GR is a cosmological constant Λ. A common interpretation of Λ as the vacuum energy [44] leads to severe theoretical issues, as naive QFT predictions exceed the observed value by many orders of magnitude [45, 46]. Alternatively, the QFT contribution can be interpreted as an additional term to the

classical cosmological constant Λ. However, even in this case one is left with a severe finetuning problem. Alternative explanations include dynamical dark energy models such as quintessence, where a slowly evolving scalar field drives the expansion [47, 48]. Despite various theoretical proposals, the true nature of dark energy remains one of the biggest mysteries in modern physics.
Although there are additional unresolved questions in the SM, we focus on the ones mentioned above, as they are directly or indirectly relevant to this work. Some of this topics will be briefly touched upon, while others will be examined in more depth.

2.2 Neutrino Oscillations

Another key aspect of this work is the physics of neutrinos, particularly the phenomenon of neutrino oscillations, which we explore in more detail in this section.
The neutrino was first postulated in 1930 by Wolfgang Pauli to account for the continuous energy spectrum of the emitted electrons in beta decays without violating energy and momentum conservation [49]. The electron antineutrino $\bar{\nu}_e$ was experimentally discovered in 1956 by Clyde Cowan and Frederick Reines using a large nuclear reactor as the source [50]. The other neutrino flavors were subsequently discovered: the muon neutrino ν_μ in 1962 by Leon Lederman, Melvin Schwartz and Jack Steinberger [51], and the tau neutrino ν_τ in 2000 by the DONUT experiment [52].
As early as 1957, Bruno Pontecorvo proposed the idea of neutrino–antineutrino oscillations [27], inspired by the K^0–$\bar{K}^0$ mixing observed in neutral kaon systems [28]. After the discovery of the muon neutrino in 1962, this concept was extended to flavor oscillations, assuming non-zero neutrino masses [53]. In the late 1960s, the Homestake experiment, led by Raymond Davis Jr., measured the flux of solar electron neutrinos [54]. Their measurement revealed only about one third of the expected neutrino flux, providing the first experimental indication that electron neutrinos may transform into other flavors on their way to Earth. In 1998, the Super-Kamiokande experiment observed a zenith-angle-dependent deficit in atmospheric muon neutrinos, thereby providing compelling evidence for flavor oscillations [55]. The results demonstrated the path-length dependence of the oscillations probability and the oscillation pattern itself. This picture was further confirmed by the Sudbury Neutrino Observatory in 2001, which provided additional evidence for flavor transitions of solar neutrinos by distinguishing between charged-current and neutal-current interactions [13].
Apart from exotic scenarios [56], neutrino oscillations are only possible if at least two of the three neutrino mass eigenstates have non-zero masses. Consequently, the observation of neutrino oscillations implies physics beyond the SM and necessitates a thorough derivation of oscillation probabilities from first principles within the framework of QFT.
To fully understand the phenomenon of neutrino oscillations, it is essential to distinguish between the mass eigenstates (ν_1, ν_2, ν_3) and the flavor eigenstates $(\nu_e, \nu_\mu, \nu_\tau)$ of neutrinos. While neutrinos are produced and detected in flavor eigenstates via weak interactions, their propagation is governed by the mass eigenstates. Each flavor state is thus a coherent superposition of mass eigenstates, and the transformation between these bases is described by the PMNS matrix [57, 58]:

$$|\nu_\alpha\rangle = \sum_i U^*_{\alpha i} |\nu_i\rangle \ , \tag{2.23}$$

Table 2.2: Current best-fit values of the mixing angles Θ_{ij}, CP-violating phase δ and squared mass differences Δm^2_{ij} for neutrino oscillations [59] for normal mass ordering.

Parameter	Best-fit value
$\sin^2\Theta_{12}$	0.307 ± 0.013
$\sin^2\Theta_{23}$	$0.558^{+0.015}_{-0.021}$
$\sin^2\Theta_{13}$	$(2.19 \pm 0.07)10^{-2}$
Δm^2_{21}	$(7.53 \pm 0.18)10^{-5}\text{eV}^2$
Δm^2_{32}	$(2.455 \pm 0.028)10^{-3}\text{eV}^2$
δ	$(1.19 \pm 0.22)\,\pi$

where $U_{\alpha i}$ are the elements of the PMNS matrix. Note, that greek letters denote the flavor states and latin letters the mass eigenstates. For three neutrino flavors, the PMNS matrix can be parametrized as:

$$U = \begin{pmatrix} c_{12}c_{13} & s_{12}c_{13} & s_{13}e^{-i\delta} \\ -s_{12}c_{23} - c_{12}s_{23}s_{13}e^{i\delta} & c_{12}c_{23} - s_{12}s_{23}s_{13}e^{i\delta} & s_{23}c_{13} \\ s_{12}s_{23} - c_{12}c_{23}s_{13}e^{i\delta} & -c_{12}s_{23} - s_{12}c_{23}s_{12}e^{i\delta} & c_{23}c_{13} \end{pmatrix} \begin{pmatrix} e^{i\frac{\alpha_1}{2}} & 0 & 0 \\ 0 & e^{i\frac{\alpha_2}{2}} & 0 \\ 0 & 0 & 1 \end{pmatrix}, \tag{2.24}$$

where $c_{ij} = \cos\Theta_{ij}$, $s_{ij} = \sin\Theta_{ij}$, and δ is the Dirac CP-violating phase. The phases α_1 and α_2 are only physical if neutrinos are Majorana particles, meaning they are their own antiparticles. Thus, the PMNS matrix contains three mixing angles, one Dirac CP phase, and two additional Majorana phases. The currently measured values of these parameters are summarized in table 2.2 [59]. The PMNS matrix plays a role analogous to the CKM matrix in the quark sector, which describes quark mixing under the weak interaction. When neutrinos propagate through space, each mass eigenstate travels with a slightly different phase velocity due to its distinct mass. This leads to a time-dependent quantum superposition of mass eigenstates, and thus, to a different resulting flavor eigenstate at the point of detection. This interference effect is the physical origin of neutrino oscillations.

The simplest theoretical description of neutrino oscillations is given in the plane wave formalism [58, 60]. In this approximation, the time evolution of a mass eigenstate $|\nu_j\rangle$ is governed by

$$|\nu_j(t)\rangle = e^{-i(E_j t - \vec{p}_j\vec{x})}\,|\nu_j(0)\rangle\,, \tag{2.25}$$

where E_j and $\vec{p}_j$ denote the energy and momentum of the eigenstate j respectively, t is the time since emission, and $\vec{x}$ the position relative to the source. For most realistic scenarios, neutrinos are ultra-relativistic, i.e., $E \gg m_j$ where E denotes the average energy of the neutrino detected. With this, we can expand the energy as

$$E_j = \sqrt{\vec{p}_j^{\,2} + m_j^2} \approx \left|\vec{p}_j\right| + \frac{m_j^2}{2\left|\vec{p}_j\right|} \approx E + \frac{m_j^2}{2E}\,. \tag{2.26}$$

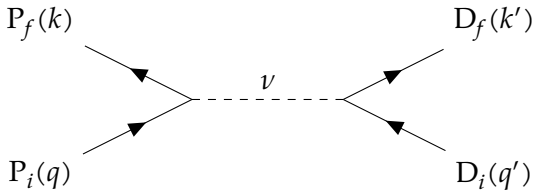

Figure 2.1: Schematic representation of the external wave packet approach. A neutrino is produced via a localized process involving the initial and final states P_i and P_f, and is subsequently detected via another localized process with states D_i and D_f. The neutrino ν propagates as an internal virtual particle between the two interaction vertices.

Additionally, assuming $t \approx L$, where L is the propagation distance, we obtain the transition probability:

$$P_{\alpha\beta} = \left|\langle \nu_\beta | \nu_\alpha(L) \rangle\right|^2 = \left| \sum_j U^*_{\alpha j} U_{\beta j} e^{-i \frac{m_j^2 L}{2E}} \right|^2 . \tag{2.27}$$

Despite the idealizations involved in this derivation, this formula reproduces many neutrino oscillation phenomena with remarkable accuracy. However, it comes with several limitations [61].
First, neutrinos are produced and detected in localized interactions and should therefore be described as wave packets rather than plane waves. This localization implies a finite spatial and temporal coherence, and the slight difference in group velocities between the mass eigenstates leads to the spatial separation of the wave packets. When this separation exceeds the coherence length, oscillations are no longer observable—a phenomenon known as wave packet decoherence and not included in the plane wave formalism. Second, plane waves are unphysical in the sense that they are not normalizable, which is inconsistent with the localized nature of realistic scattering processes. Finally, the substitution $t \approx L$ is heuristic and lacks rigorous justification. A more consistent treatment of the transition amplitude requires going beyond the plane wave approximation to include effects such as coherence length, energy resolution and the finite extent of production and detection processes.

2.2.1 Wave Packet Treatments of Neutrino Oscillations

The plane wave formalism suffers from several conceptual and physical shortcomings [58]. In this subsection, we introduce two alternative theoretical frameworks that provide a more realistic description of neutrino oscillations: the external wave packet approach and the internal wave packet approach. We conclude with a comparative analysis of all three formalisms.
We begin with the **external wave packet approach**, in which neutrinos are produced via localized processes, for instance $\pi^+ \to \mu^+ + \nu_\mu$, and are subsequently detected through another localized interaction such as for instance $\nu_e + n \to e^- + p$ [62]. A schematic representation of this process is shown in figure 2.1. In this framework, all external particles, i.e., those involved in the production and detection processes, are modeled as localized wave packets. The neutrino itself is not described as an asymptotic state but rather appears as a virtual particle mediating the two localized interactions. The initial

and final quantum states of the system can thus be written in terms of the wave packets as follows [63]:

$$|\mathrm{P}_i\rangle = \int \mathrm{d}q f_{\mathrm{P}_i}(\vec{q},\vec{Q})\,|\mathrm{P}_i,\vec{q}\rangle\ , \qquad |\mathrm{P}_f\rangle = \int \mathrm{d}k f_{\mathrm{P}_f}(\vec{k},\vec{K})\,|\mathrm{P}_f,\vec{k}\rangle\ , \tag{2.28}$$

$$|\mathrm{D}_i\rangle = \int \mathrm{d}q' f_{\mathrm{D}_i}(\vec{q}',\vec{Q}')\,|\mathrm{D}_i,\vec{q}'\rangle\ , \qquad |\mathrm{D}_f\rangle = \int \mathrm{d}k' f_{\mathrm{D}_f}(\vec{k}',\vec{K}')\,|\mathrm{D}_f,\vec{k}'\rangle\ , \tag{2.29}$$

where the momentum integrals are defined as

$$\mathrm{d}q = \frac{\mathrm{d}^3 q}{(2\pi)^3\sqrt{2E_i(\vec{q})}}\,. \tag{2.30}$$

All other momentum integrals are defined analogously and $f_{\mathrm{P}_i}, f_{\mathrm{P}_f}$ and $f_{\mathrm{D}_i}, f_{\mathrm{D}_f}$ are the momentum-space wave packet envelopes for the production and detection at the initial and the final point, respectively. These are usually assumed to be Gaussian wave packets [64]. In this case, the initial wave packet produced takes the form

$$f_{\mathrm{P}_i}(\vec{q},\vec{Q}) = \left(\frac{1}{2\pi\sigma_p^2}\right)^{\frac{3}{4}} \exp\left(-\frac{\left(\vec{q}-\vec{Q}\right)^2}{4\sigma^2_{p\mathrm{P}_i}}\right), \tag{2.31}$$

where $\sigma_{p\mathrm{P}_i}$ denotes the momentum uncertainty of the produced state [58] and $\vec{Q}$ its central momentum. The transition amplitude for the entire process is given by

$$iA_{\alpha\beta} = \langle \mathrm{P}_f\mathrm{D}_f|\hat{T}\exp\left(-i\int \mathrm{d}^4x\, H_{\mathrm{I}}(x)\right) - \mathbb{1}|\mathrm{P}_i\mathrm{D}_i\rangle\ , \tag{2.32}$$

where $\hat{T}$ denotes the time-ordering operator and H_{I} is the charged-current weak interaction Hamiltonian. Inserting equation (2.28) and (2.29) into the amplitude in equation (2.32), we find

$$\begin{aligned} iA_{\alpha\beta} = \sum_j U^*_{\alpha j}U_{\beta j} \int \mathrm{d}q f_{\mathrm{P}_i}(\vec{q},\vec{Q}) \int \mathrm{d}k f^*_{\mathrm{P}_f}(\vec{k},\vec{K}) \int \mathrm{d}q' f_{\mathrm{D}_i}(\vec{q}',\vec{Q}') \\ \times \int \mathrm{d}k' f^*_{\mathrm{D}_f}(\vec{k}',\vec{K}') iA_j(q,k;q',k')\,, \end{aligned} \tag{2.33}$$

with the amplitude A_j in terms of the plane wave amplitudes $\tilde{M}_{\mathrm{P}}$ and $\tilde{M}_{\mathrm{D}}$ with the j-th neutrino mass eigenstate:

$$\begin{aligned} iA_j(q,k;q',k') = \int \mathrm{d}^4x_1 \int \mathrm{d}^4x_2\, \tilde{M}_{\mathrm{D}}(q',k')e^{-i(q'-k')(x_2-x_{\mathrm{D}})} \\ \times i\int \frac{\mathrm{d}^4\mathrm{p}}{(2\pi)^4}\frac{\not{p}+m_j}{p^2-m_j^2+i\varepsilon}e^{-ip(x_2-x_1)}\tilde{M}_{\mathrm{P}}(q,k)e^{-i(q-k)(x_1-x_{\mathrm{P}})}\,. \end{aligned} \tag{2.34}$$

Here, x_1 and x_2 are the production and detection coordinates centered around x_{P} and x_{D}, respectively. The full amplitude can then be expressed as

$$iA_{\alpha\beta} = i\sum_j U^*_{\alpha j}U_{\beta j}\int \frac{\mathrm{d}^4p}{(2\pi)^4}\Phi_{j\mathrm{P}}(p^0,\vec{p})\Phi_{j\mathrm{D}}(p^0,\vec{p})\frac{2p_0e^{-ip^0T+i\vec{p}\vec{L}}}{p^2-m_j^2+i\varepsilon}\,, \tag{2.35}$$

where $\Phi_{j\mathrm{P}}$ and $\Phi_{j\mathrm{D}}$ are the Fourier-transformed overlap functions of the external wave packets [65]:

$$\Phi_{j\mathrm{P}}(p^0,\vec{p}) = \int \mathrm{d}^4x_1'\, e^{ipx_1'} \int \mathrm{d}q \int \mathrm{d}k f_{\mathrm{P}_i}(\vec{q},\vec{Q}) f^*_{\mathrm{P}_f}(\vec{k},\vec{K}) \times e^{-i(q-k)x_1'} M_{j\mathrm{P}}(q,k)\,, \tag{2.36}$$

$$\Phi_{j\mathrm{D}}(p^0,\vec{p}) = \int \mathrm{d}^4x_2'\, e^{-ipx_2'} \int \mathrm{d}q' \int \mathrm{d}k' f_{\mathrm{D}_i}(\vec{q}',\vec{Q}') f^*_{\mathrm{D}_f}(\vec{k}',\vec{K}') \times e^{-i(q'-k')x_2'} M_{j\mathrm{D}}(q',k')\,, \tag{2.37}$$

with

$$M_{j\mathrm{P}}(q,k) = \frac{\bar{u}_{jL}(p)}{\sqrt{2p_0}} \tilde{M}_{\mathrm{P}}(q,k)\,, \qquad M_{j\mathrm{D}}(q',k') = \tilde{M}_{\mathrm{D}}(q',k') \frac{u_{jL}(p)}{\sqrt{2p_0}}\,, \tag{2.38}$$

and $x_1 = x_{\mathrm{P}} + x_1'$ and $x_2 = x_{\mathrm{D}} + x_2'$. Further, we introduce the neutrino spinors $u_{jL}(p)$ by making use of the completeness relation for the neutrino momenta. With all of this, we finally arrive at the form [61]

$$iA_{\alpha\beta} = \Theta(T) \sum_j U^*_{\alpha j} U_{\beta j} \int \frac{\mathrm{d}^3p}{(2\pi)^3} \Phi_{j\mathrm{P}}(E_j(\vec{p}),\vec{p}) \Phi_{j\mathrm{D}}(E_j(\vec{p}),\vec{p}) e^{-iE_j(\vec{p})T + i\vec{p}\vec{L}}\,, \tag{2.39}$$

where $\Theta(x)$ is a Heaviside step function enforcing causality. Note that obtaining the final flavor oscillation probability in the external wave packet approach requires detailed knowledge of the neutrino production and detection processes. This results in a rather involved derivation, especially since those microscopic details are often unknown or poorly constrained. However, if the considered process is approximately independent of those microscopic details of neutrino production and detection, an alternative and conceptually simpler framework is given by the **internal wave packet approach** [60]. In this framework, the neutrino itself is modeled as a localized wave packet which can also be rigorously derived from the external wave packet formalism [63]:

$$A_{\alpha\beta} = \Theta\left(T_{\mathrm{D}} - T_{\mathrm{P}}\right) \sum_j U^*_{\alpha j} U_{\beta j} \int \mathrm{d}^3\vec{p} \int \mathrm{d}^3\,\vec{p}\,' \Psi^{\mathrm{D}*}_j(\vec{p}) \Psi^{\mathrm{P}}_j(\vec{p}\,') \left\langle \nu_j,\vec{p};\mathrm{D}|\nu_j,\vec{p}\,';\mathrm{P}\right\rangle\,, \tag{2.40}$$

where $\Psi^{\mathrm{D}}_j(\vec{p})$ and $\Psi^{\mathrm{P}}_j(\vec{p}\,')$ are the neutrino wave packets at the detection and production, respectively, which we assume to be Gaussian:

$$\Psi^{\mathrm{D}}_j(\vec{p}) = \left(\frac{1}{2\pi\sigma^2_{\mathrm{D}j}}\right)^{\frac{3}{4}} \exp\left(-\frac{\left(\vec{p}-\vec{Q}_j\right)^2}{4\sigma^2_{\mathrm{D}j}}\right), \tag{2.41}$$

$$\Psi^{\mathrm{P}}_j(\vec{p}) = \left(\frac{1}{2\pi\sigma^2_{\mathrm{P}j}}\right)^{\frac{3}{4}} \exp\left(-\frac{\left(\vec{p}-\vec{P}_j\right)^2}{4\sigma^2_{\mathrm{P}j}}\right), \tag{2.42}$$

where $\vec{Q}$ and $\vec{P}$ now denote the difference between the external outgoing and incoming mean momenta, respectively, with the wave packets widths $\sigma_{\mathrm{D}j}$ and $\sigma_{\mathrm{P}j}$. To obtain and interpret the resulting amplitude, we insert the Gaussian wave packets into equation (2.40), yielding

$$\begin{aligned} A_{\alpha\beta} =& \Theta(T_{\mathrm{D}} - T_{\mathrm{P}}) \sum_j U^*_{\alpha j} U_{\beta j} (2\pi\sigma_{\mathrm{P}j}\sigma_{\mathrm{D}j})^{-\frac{3}{2}} \\ & \times \int \mathrm{d}^3\vec{p}\, \exp\left(-\frac{\left(\vec{p}-\vec{Q}_j\right)^2}{4\sigma_{\mathrm{D}j}} - \frac{\left(\vec{p}-\vec{P}_j\right)^2}{4\sigma^2_{\mathrm{P}j}} - i\left(E_p\Delta T - \vec{p}\vec{L}\right)\right), \end{aligned} \tag{2.43}$$

where $\Delta T = T_\mathrm{D} - T_\mathrm{P}$ and E_p is the energy corresponding to the momentum p. We then expand the exponent around the dominant mean momentum $\bar{\vec{p}}_j$

$$\bar{\vec{p}}_j = \frac{\sigma_{\mathrm{D}j}^2 \vec{P}_j + \sigma_{\mathrm{P}j}^2 \vec{Q}_j}{\sigma_{\mathrm{P}j}^2 + \sigma_{\mathrm{D}j}^2}\,, \tag{2.44}$$

and perform all momentum integrals. This leads to the following expression for the amplitude:

$$\begin{aligned} A_{\alpha\beta} = \sum_j U_{\alpha j}^* U_{\beta j} \left(\sigma_{\mathrm{D}j}^3 \sigma_{\mathrm{P}j}^3 \det \Sigma_j\right)^{-\frac{1}{2}} \exp\left(-i\left(\bar{E}_j T - \bar{\vec{p}}_j \vec{L}\right)\right) \\ \times \exp\left(-\frac{1}{4}\frac{\left(\vec{P}_j - \vec{Q}_j\right)^2}{\sigma_{\mathrm{P}j}^2 + \sigma_{\mathrm{D}j}^2} - \frac{1}{2}\left(\bar{\vec{v}}_j \Delta T - \vec{L}\right)^T \Sigma_j^{-1} \left(\bar{\vec{v}}_j \Delta T - \vec{L}\right)\right), \end{aligned} \tag{2.45}$$

with the mean neutrino energy $\bar{E}_j = \sqrt{|\vec{p}_j|^2 + m_j^2}$, the group velocity $\bar{\vec{v}}_j = \bar{\vec{p}}_j / \bar{E}_j$ and the position space covariance matrix

$$\Sigma_j = \frac{1}{2}\left(\frac{1}{\sigma_{\mathrm{P}j}^2} + \frac{1}{\sigma_{\mathrm{D}j}^2}\right) + i\frac{\Delta T}{E_j}\left(1 - \bar{\vec{v}}_j \otimes \bar{\vec{v}}_j\right)\,, \tag{2.46}$$

which defines the overlap between the produced and detected wave packet. The first term in the exponent is already familiar from the plane wave formalism and gives rise to the characteristic oscillation pattern. The second term describes the damping of these oscillations due to the wave packet nature of the neutrino: only production and detection configurations with approximately matching mean momenta contribute significantly. The third term quantifies how well the spacetime coordinates of detection match the expected classical trajectory of a neutrino with mass m_j. Only those configurations for which this agreement is sufficiently good contribute appreciably. This also allows for the definition of a spacetime volume

$$V_x = 1/\sqrt{\det\left(\mathrm{Re}(\Sigma_j^{-1})\right)}\,, \tag{2.47}$$

within which the amplitude is non-vanishing. As a consequence, a natural relation between the propagation length L and the time T emerges.
To make the discussion more transparent, we now diagonalize the position space covariance matrix Σ_j into eigenvectors and eigenvalues

$$\Sigma_j = \sigma_{j\parallel}^2 \left(\vec{s}_\parallel^{\,j} \otimes \vec{s}_\parallel^{\,j}\right) + \sum_{a=1}^{2} \sigma_{\perp j}^2 \left(\vec{s}_{\perp,a}^{\,j} \otimes \vec{s}_{\perp,a}^{\,j}\right)\,. \tag{2.48}$$

Here, $\vec{s}_\parallel^{\,j}$ is aligned with the mean neutrino momentum, and the remaining $\vec{s}_{\perp,1}^{\,j}$ and $\vec{s}_{\perp,2}^{\,j}$ are orthonormal perpendicular to it. To simplify the discussion, we neglect wave packet

spreading at this stage, which leads to the following position uncertainties:

$$\sigma_{\parallel j}^2 = \frac{1}{2}\left(\frac{1}{\sigma_{\mathrm{P}j}^2} + \frac{1}{\sigma_{\mathrm{D}j}^2}\right) + \underbrace{i\frac{\Delta T}{\bar{E}_j}\left(1 - |\vec{\bar{v}}_j|\right)^2}_{\text{Wave Packet Spreading}\approx 0}, \tag{2.49}$$

$$\sigma_{\perp j}^2 = \underbrace{\frac{1}{2}\left(\frac{1}{\sigma_{\mathrm{P}j}^2} + \frac{1}{\sigma_{\mathrm{D}j}^2}\right)}_{=\Theta_j^2} + i\frac{\widetilde{\Delta T}}{\bar{E}_j}\,. \tag{2.50}$$

With these quantities, the exponent can be rewritten, yielding the amplitude:

$$A_{\alpha\beta} = \Theta(T_{\mathrm{D}} - T_{\mathrm{P}}) \sum_j U_{\alpha j}^* U_{\beta j} \left(\Theta_j^2 \sigma_{\mathrm{D}j}\sigma_{\mathrm{P}j}\right)^{-\frac{3}{2}} \exp\left(-i\left(\bar{E}_j T - |\vec{\bar{p}}_j| L\right)\right) \tag{2.51}$$

$$\times \exp\left(-\frac{1}{4}\frac{\left(|\vec{P}_j| - |\vec{Q}_j|\right)^2}{\sigma_{\mathrm{P}j}^2 + \sigma_{\mathrm{D}j}^2} - \frac{1}{2}\frac{\left(|\vec{\bar{v}}_j|\Delta T - L\right)^2}{2\Theta_j^2}\right). \tag{2.52}$$

Here, we assume that the propagation length $L = |\vec{L}|$ is much larger than the spatial width of the wave packet, i.e., $L \gg \Theta_j$. To obtain a probability, this amplitude must be squared and integrated over the propagation time interval ΔT:

$$P_{\alpha\beta} = \frac{\int_{-\infty}^{\infty} \mathrm{d}\Delta T\, |A_{\alpha\beta}|^2}{\int_{-\infty}^{\infty} \mathrm{d}\Delta T\, \sum_j |A_{\alpha j}|^2}\,. \tag{2.53}$$

Carrying out this integral explicitly, we finally arrive at:

$$\begin{aligned} P_{\alpha\beta}(L,p) =& \frac{1}{N}\sum_{j,k} U_{\alpha j}^* U_{\beta j} U_{\alpha k} U_{\beta k}^* \left(\Theta_j^2 \sigma_{\mathrm{P}j}\sigma_{\mathrm{D}j}\Theta_k^2\sigma_{\mathrm{P}k}\sigma_{\mathrm{D}k}\right)^{-\frac{3}{2}} \left(\frac{2\pi}{\sigma_{Ejk}^2}\right) \\ &\times \exp\left(i\Delta\bar{p}_{jk}L - i\frac{\Delta\bar{E}_{jk}}{|\vec{\bar{v}}_{jk}|}L - \left(\frac{L}{L_{jk}^{\mathrm{coh}}}\right)^2 - \frac{1}{2}\left(\frac{\Delta\bar{E}_{jk}}{\sigma_{Ejk}}\right)^2\right) \\ &\times \exp\left(-\frac{\left(|\vec{P}_j| - |\vec{Q}_j|\right)^2}{2\tilde{\sigma}_{Pj}^2} - \frac{\left(|\vec{P}_k| - |\vec{Q}_k|\right)^2}{2\tilde{\sigma}_{Pk}^2}\right), \end{aligned} \tag{2.54}$$

with the coherence length given by

$$L_{jk}^{\mathrm{coh}} = \sqrt{2}\frac{\sqrt{\Theta_j^2\vec{\bar{v}}_k^2 + \Theta_k^2\vec{\bar{v}}_j^2}}{|\vec{\bar{v}}_j - \vec{\bar{v}}_k|}\,, \tag{2.55}$$

and the effective momentum and energy resolution

$$\tilde{\sigma}_{Pj}^2 = 2\left(\sigma_{\mathrm{P}j}^2 + \sigma_{\mathrm{D}j}^2\right), \qquad \sigma_{Ejk}^2 = \left(\frac{\vec{\bar{v}}_j^2}{\Theta_j^2} + \frac{\vec{\bar{v}}_k^2}{\Theta_k^2}\right). \tag{2.56}$$

We also define the momentum and energy differences as

$$\Delta\bar{E}_{jk} = \bar{E}_j - \bar{E}_k\,, \qquad \Delta\bar{p}_{jk} = |\vec{\bar{p}}_j| - |\vec{\bar{p}}_k|\,, \qquad \bar{v}_{jk} = \frac{\Theta_j^2\bar{\vec{v}}_k^2 + \Theta_k^2\bar{\vec{v}}_j^2}{\Theta_j^2|\vec{\bar{v}}_k| + \Theta_k^2|\vec{\bar{v}}_j|}\,. \tag{2.57}$$

The resulting expression is rather general and valid in a wide range of scenarios. However, it is useful to consider certain approximations that simplify the interpretation—especially in comparison to standard neutrino oscillations in vacuum. First, we assume that the mean momentum $|\vec{P}_j|$ and $|\vec{Q}_j|$ differ only slightly among the mass eigenstates. Second, the neutrino masses are taken to be close to each other compared to the typical energy scale of the process. Additionally, we assume that all wave packets have similar shapes, such that $\sigma_{\mathrm{P}j} = \sigma_{\mathrm{P}}$ and $\sigma_{\mathrm{D}j} = \sigma_{\mathrm{D}}$ for all j. It is thus reasonable to expand all relevant quantifies to first order around a representative neutrino mass $\bar{m}^2$, set $|\vec{P}_j| = P = Q = |\vec{Q}_j|$, and to choose the energy as $E = \sqrt{P^2 + \bar{m}^2}$. In the limit where $m_j^2 - \bar{m}^2 \ll P^2$ and $|\vec{P}_j| - P \ll P$, we obtain:

$$\begin{aligned} P_{\alpha\beta}(L,E) = \sum_{j,k} U_{\alpha j}^* U_{\alpha k} U_{\beta j} U_{\beta k}^* \exp\left(-i\frac{\Delta m_{jk}^2}{2E}L\right) \\ \times \exp\left(-\left(\frac{L}{L^{\mathrm{coh}_{jk}}}\right)^2 - \frac{1}{2}\left(\frac{\Delta E_{jk}}{\sigma_E}\right)^2\right), \end{aligned} \tag{2.58}$$

with the corresponding energy given by

$$\Delta E_{jk} \approx \frac{\Delta m_{jk}^2}{2E} + v\Delta p_{jk}\,, \qquad \text{with} \qquad v = \frac{P}{E}\,, \tag{2.59}$$

and the coherence length

$$L_{jk}^{\mathrm{coh}} \approx \Theta\left|\frac{\Delta m_{jk}^2}{4E^2} + \frac{\bar{m}^2}{2E^2}\frac{\Delta p_{jk}}{P}\right|^{-1}, \qquad \text{with} \qquad \sigma_E^2 = \frac{2v^2}{\Theta^2}\,. \tag{2.60}$$

Several key features can be read off from this formula, especially in comparison to the vacuum oscillation probability: The first term in the exponent shows that for $L \ll L_{jk}^{\mathrm{coh}}$, i.e., if the propagation length L is much smaller than the coherence length L_{jk}^{coh}, the wave packets of the different mass eigenstates overlap sufficiently during propagation such that no decoherence due to wave packet separation occurs. The second term in the exponent involves the ratio $\Delta E_{jk}/\sigma_E$, which becomes large, and thus, supresses the oscillation when $|\Delta E_{jk}| \gg \sigma_E$. This implies that if the energy splitting between the different mass eigenstates becomes large enough to be experimentally resolved, the interference between the components is lost and the oscillation is damped accordingly. These neutrino pictures resolve therefore many of the criticisms directed at the plane wave approach, but they are also significantly more complex in both derivation and interpretation. An overview of the different frameworks can be found in table 2.3. Which of these neutrino oscillations frameworks is ultimately chosen depends entirely on the specific application and the particular aspect or phenomenon of interest. Each has its own valid justification and will play a role in this work.

Table 2.3: Overview of different theoretical frameworks for neutrino oscillations, compared by their treatment of localization, coherence effects, computational approach and physical fidelity.

Aspect	Plane-wave	External wave packet	Internal wave packet
Neutrino picture	Mass eigenstate as a plane wave	Intermediate state between localized source/detector	Localized neutrino wave packet
Localization	None	Source and detector localized	All particles localized
Coherence	Imposed externally	Depends on overlap of external WPs	Emerges from localization
Computational method	Simple analytic expressions	Full QFT treatment	Full QFT treatment
Physical fidelity	Limited (no spatial extent, no decoherence)	Very high (no approximations needed)	High (approximations applied)

2.2.2 Matter effects

So far, we have considered neutrino oscillations in vacuum, where the behavior is well understood. However, in the presence of matter, the effective oscillation pattern can change significantly. Matter effects can lead to a resonant enhancement of oscillations—known as the Mikheyev–Smirnov–Wolfenstein (MSW) effect—or suppress certain modes, both of which have observable consequences [66–69]. These effects are particularly relevant when neutrinos propagate through dense media, such as the Sun, the Earth or a supernova. Since neutrinos from many astrophysical and terrestial sources traverse such environments before reaching detectors, it is essential to account for matter effects when analyzing data from neutrino oscillation experiments.
The characteristic form of matter effects follows from the fact that all neutrino flavours undergo flavour-independent neutral-current interactions in matter, whereas electron neutrinos additionally interact via charged-current processes with electrons. Only this charged-current contribution introduces a flavour-dependent potential for the electron neutrino ν_e, since the phase evolution of the electron neutrino is modified relative to the muon and tau neutrino. This effective potential is given by [70, 71]

$$V_{\mathrm{CC}} = \sqrt{2} G_{\mathrm{F}} N_e \,, \tag{2.61}$$

where G_{F} is the Fermi constant and N_e is the electron number density in the medium. Note, that this is not a classical force field, like an electric potential, but rather arises from the coherent forward scattering amplitude averaged over the background of matter.

For low-energy scattering, the matter effects can be effectively described by introducing an additional term into the Hamiltonian [58]:

$$H = \frac{1}{2E} U \begin{pmatrix} 0 & 0 & 0 \\ 0 & \Delta m^2_{21} & 0 \\ 0 & 0 & \Delta m^2_{31} \end{pmatrix} U^\dagger + \begin{pmatrix} V_{\mathrm{CC}} & 0 & 0 \\ 0 & 0 & 0 \\ 0 & 0 & 0 \end{pmatrix}. \tag{2.62}$$

This modification exclusively affects electron neutrinos and leads to effective parameters in matter, such as an effective mixing angle Θ_{M} and an effective mass-squared difference Δm^2_{M}. As the mixing angle is modified, oscillations become maximal when $\Theta_{\mathrm{M}} \approx 45°$, a condition known as the MSW resonance. One can derive the corresponding resonance condition [66, 68] by requiring that the matter-induced potential exactly cancels the vacuum term in the Hamiltonian:

$$\Delta m^2_{21} \cos(2\theta) = 2\sqrt{2} E G_{\mathrm{F}} N_e \,, \tag{2.63}$$

where $\Delta m^2_{21} = m^2_2 - m^2_1$ and θ is the vacuum mixing angle. This condition marks the energy at which the effective mixing becomes maximal due to the interplay of vacuum and matter effects. Note, that for antineutrinos, the situation is reversed: the potential V_{CC} changes sign, which alters the resonance condition accordingly. It is important to note that this resonance involves the solar mass-squared difference Δm^2_{21}, whereas in long-baseline experiments the difference Δm^2_{31} is used to determine the neutrino mass ordering [72]. One speaks of normal ordering when $\Delta m^2_{31} > 0$, and of inverted ordering when $\Delta m^2_{31} < 0$. In the case of antineutrinos, the resonance condition might not be satisfied for a normal mass ordering—just as it may fail for neutrinos in the inverted scenario. Thus, experiments seek to infer the mass ordering by identifying the presence or absence of such resonances.
When the matter density is not constant, for instance, during propagation through the Earth, analytical solutions that account for matter effects become infeasible. Instead, one must numerically solve the corresponding equations of motion. This is where `NuSQUIDS` comes in: a numerical tool for solving the neutrino density matrix evolution, capable of handling a wide variety of physical scenarios [73]. In this work, `NuSQUIDS` is empolyed to incorporate matter effects into the analysis in chapter 5.

2.2.3 Research Frontiers in Neutrino Physics

As mentioned earlier, neutrino oscillations constitute one of the first confirmed evidence of BSM physics [30]. While the phenomenon of oscillations is well understood, there remain several fundamental properties of neutrinos that are still unknown, and thus, subject of ongoing research. To further highlight the importance of this reaseach frontier, we briefly discuss various fields of neutrino physics in this subsection.
One major open question concerns the absolute neutrino masses as we have seen. Oscillation experiments are only sensitive to the difference in mass-squared values, not the individual masses themselves. However, the absolute mass scale is crucial for cosmology. In the early universe, neutrino behaved as relativistic, free-streaming particles. The larger the sum of their masses $\sum_j m_j$, the more they suppress the growth of cosmic structures due to reduced gravitational clustering. This effect can be observed in the position and amplitude of the acoustic peaks in the Cosmic Microwave Background

(CMB) spectrum [74].
Another unresolved issue is the neutrino mass ordering—whether it follows a normal or inverted hierarchy. As discussed in subsection 2.2.2, this ordering influences how neutrinos interact in matter and can thus be probed experimentally, for example in upcoming experiments such as JUNO [75] and DUNE [76].
Furthermore, it is still unknown whether neutrinos are Dirac or Majorana particles. In the Majorana case, neutrinos are their own antiparticle and have only two DOFs ν_L, ν_L^C, compared to four for Dirac neutrinos ν_L, $\bar{\nu}_L$, ν_R, $\bar{\nu}_R$, which has profound implications for the symmetries of the theory. Majorana mass terms violate lepton number conservation by two units, while Dirac mass terms preserve it. Because of this natural lepton number violation, Majorana neutrinos are often featured in theoretical models that attempt to explain the baryon asymmetry of the universe. One prominent class of such models is leptogenesis [41], in which an initial asymmetry in the lepton sector, enabled by Majorana neutrino decays, gets converted into a baryon asymmetry via electroweak sphaleron processes.
A promising experimental approach to testing the Majorana nature of neutrinos is the search for neutrinoless double beta decay [77, 78]. In the process

$$(Z, A) \rightarrow (Z + 2, A) + 2e^- , \tag{2.64}$$

no neutrinos are emitted, meaning the lepton number would be violated by $\Delta L = 2$. Internally, the mechanism works as follows: One neutron in the nucleus undergoes a standard beta decay, emitting an electron and an antineutrino

$$n \rightarrow p + e^- + \bar{\nu}_e . \tag{2.65}$$

However, this antineutrino is not emitted, but rather absorbed by a second neutron undergoing an inverse beta decay

$$\bar{\nu}_e + n \rightarrow p + e^- . \tag{2.66}$$

The result is two protons and two electrons, but no neutrinos. This process can only occur if neutrinos are Majorana particles, otherwise, the intermediate neutrino would not be able to be reabsorbed as an antineutrino. Thus, an experimental detection of neutrinoless double beta decay would constitute direct evidence for the Majorana nature of neutrinos.
Another key question is the origin of neutrino masses, which cannot be explained within the SM framework, cf. section 2.1.2. This calls for new mechanisms, such as the seesaw mechanism [79, 80], which introduces heavy right-handed neutrinos that generate small neutrino masses via mixing.
Of course, many experiments are currently investigating these open questions. Since a full overview would exceed the scope of this thesis, a summary is instead presented in table 2.4, which lists the most relevant past, ongoing, and planned neutrino experiments for this work [59]. Each of these experiments naturally has additional objectives and applications; the table is meant only as a general overview and makes no claim to completeness.

Table 2.4: Selected past, ongoing and planned neutrino experiments [59].

Type	Experiment	Focus
Short-baseline	MiniBooNE, MicroBooNE	Sterile neutrinos, anomalies
Long-baseline	T2K, DUNE	CP-violation, mass ordering
Reactor	KamLAND, JUNO	Mass ordering, supernova signals
Atmospheric, solar	Kamiokande, Super-Kamiokande, Hyper-Kamiokande	Majorana, neutrinoless double beta
Cosmic	IceCube, ANTARES, KM3NeT	BSM signals, high energy ν
Cosmology	Planck, Euclid	Absolute mass, number of neutrino types

2.3 General Relativity

Alongside the SM of particle physics, GR forms a second cornerstone of modern theoretical physics. It is Einstein's theory of space, time, and gravity. While most fundamental forces of nature are mediated by fields defined on a spacetime manifold, gravity is an inherent property of spacetime itself, inseparably intertwined with it. Spacetime is typically described as a four-dimensional continuum consisting of three spatial dimensions and one time dimension. In the framework of GR, spacetime can be curved or deformed by mass and energy, and ultimately this curvature leads to the phenomenon we refer to as gravity.
The central principle of GR is the strong equivalence principle. Already, Galileo Galilei recognized that objects fall at the same rate, regardless of their mass. This has been incorporated by Newton as an equivalence of inertial and gravitational mass into his formulation of the classical laws of motion and gravity. Einstein was the first to realize that this property must be a fundamental principle of gravity, and from this, he deduced the strong equivalence principle [81, 82]. It states that gravity and acceleration are locally indistinguishable. In a locally free-falling reference frame, all physical laws take the same form as in a gravity-free space in an inertial reference frame, where the laws of special relativity apply.
The structure of spacetime in special relativity is described by the Minkowski metric [83] $\eta_{\mu\nu} = \mathrm{diag}(1, -1, -1, -1)$, which defines spacetime intervals between events via the equation

$$\mathrm{d}s^2 = \eta_{\mu\nu}\mathrm{d}x^\mu \mathrm{d}x^\nu = \mathrm{d}t^2 - \mathrm{d}x^2 - \mathrm{d}y^2 - \mathrm{d}z^2\,, \tag{2.67}$$

with the spacetime coordinates $x^\mu = (t, x, y, z)$.
While the isometries in Euclidean space, i.e., transformations that leave the standard scalar product invariant, are rotations and translations, this concept generalizes to

Minkowski space where the invariance of the spacetime interval ds^2 now defines the Lorentz transformations:

$$\eta_{\rho\sigma} = \Lambda^{\mu}{}_{\rho}\Lambda^{\nu}{}_{\sigma}\eta_{\mu\nu}\,. \tag{2.68}$$

Since in special relativity one assumes that the interval ds^2 remains invariant between any inertial frames, the transformation from one inertial reference frame S to S' is thus given as:

$$x'^{\mu} = \Lambda^{\mu}{}_{\nu}x^{\nu}\,. \tag{2.69}$$

In the presence of a gravitational field, the curvature of spacetime prevents the existence of a global inertial frame. As a result, the Minkowski description of spacetime is no longer sufficient to capture its geometric properties. Instead, spacetime is modeled as a manifold, i.e., a space that locally resembles Euclidean space but may be curved on larger scales. More precisely, in the context of GR, we are interested in manifolds, that locally resemble Minkowski space. These are known as pseudo-Riemannian manifolds, which are equipped with a metric tensor $g_{\mu\nu}$ that defines the geometric structure. Again, those metric tensors allow us to compute the spacetime interval between two points

$$ds^2 = g_{\mu\nu}dx^{\mu}dx^{\nu}\,. \tag{2.70}$$

In such a curved spacetime, the concept of "straight lines" is generalized to geodesics, which connect two events along the shortest path. Geodesics are thus also the natural trajectory of a free particle and are described by the geodesic equation

$$\frac{d^2x^{\mu}}{d\tau^2} + \Gamma^{\mu}_{\alpha\beta}\frac{dx^{\alpha}}{d\tau}\frac{dx^{\beta}}{d\tau} = 0\,, \tag{2.71}$$

where τ is the proper time, and $\Gamma^{\mu}_{\alpha\beta}$ represents the Christoffel symbols, which describe how much vector components change under parallel transport along a curve:

$$\Gamma^{\mu}_{\alpha\beta} = \frac{1}{2}g^{\mu\lambda}\left(\frac{\partial g_{\lambda\beta}}{\partial x^{\alpha}} + \frac{\partial g_{\lambda\alpha}}{\partial x^{\beta}} - \frac{\partial g_{\alpha\beta}}{\partial x^{\lambda}}\right). \tag{2.72}$$

In other words, the parallel transport decribes the moving of a vector along a curve in such a way that it stays parallel to itself according to the underlying connection, which is established by the covariant derivative ∇ with its components in local coordinates corresponding to the Christoffel symbols. The curvature itself is described by the Riemann tensor and is given in local coordinates as

$$R^{\rho}{}_{\sigma\mu\nu} = \frac{\partial\Gamma^{\rho}_{\sigma\nu}}{\partial x^{\mu}} - \frac{\partial\Gamma^{\rho}_{\sigma\mu}}{\partial x^{\nu}} + \Gamma^{\rho}_{\lambda\mu}\Gamma^{\lambda}_{\sigma\nu} - \Gamma^{\rho}_{\lambda\nu}\Gamma^{\lambda}_{\sigma\mu}\,. \tag{2.73}$$

Intuitively, it measures the difference of vectors from their original direction after parallel transport around an infinitesimal closed loop, thereby characterizing the intrinsic curvature of spacetime. In space without gravity, all components of the Riemann tensor should therefore be zero. The interplay between spacetime curvature and matter is described by the Einstein field equations [84]

$$R_{\mu\nu} - \frac{1}{2}Rg_{\mu\nu} = 8\pi G T_{\mu\nu}\,. \tag{2.74}$$

Here, $T_{\mu\nu}$ is the energy–momentum tensor, which encodes the matter content of the universe, $R_{\mu\nu} = R^{\lambda}{}_{\mu\lambda\nu}$ is the Ricci tensor, $R = g^{\mu\nu}R_{\mu\nu}$ is the Ricci scalar and G is the

Newtonian constant. These equations thus link the structure of spacetime to the distribution of matter in the universe.
This concludes the central equations of GR: the geodesic equation (2.71) and the Einstein field equations (2.74). They form the basis for numerous predictions of astrophysical phenomena. A Gravitational Wave (GW), for example, is described by ripples in spacetime generated by the acceleration of massive objects. They are described as a perturbation $h_{\mu\nu}$ to the flat spacetime metric $\eta_{\mu\nu}$:

$$g_{\mu\nu} = \eta_{\mu\nu} + h_{\mu\nu} \,. \tag{2.75}$$

In a historic breakthrough, GWs were first detected in 2015 through the highly sensitive measurements of LIGO [85].
Another observable phenomenon is gravitational lensing, which occurs when the light from a distant object is bent by a massive intervening object. Experimental observations of this effect are used to gain insights into the distribution of DM [86].
The Einstein equations also describe black holes, which are regions of spacetime so dense that not even light can escape. A well-known example is the Schwarzschild solution, which characterizes a non-rotating, electrically neutral black hole [87].
While GR explains gravity, it also serves as the foundation for modern cosmology, describing the evolution and large-scale structure of the universe.

2.4 Cosmology

Cosmology is the science of the structure, history and future of the universe. It builds upon the framework of GR to investigate the dynamics of the cosmos. The origins of cosmological thought reach far back into antiquity: Early cultures developed mythological cosmologies to explain the structure of the heavens and the motions of celestial bodies. From the 6th century BCE onward, natural philosophers in ancient Greece began to formulate more systematic models, culminating in the geocentric worldview developed by Aristotle in the 4th century BCE and formalized later in the 2nd century CE by Ptolemy [88].
This foundational picture remained dominant for centuries until it was fundamentally challenged in the 16th century by the revolutionary work of Copernicus, Kepler, and Galilei [89]. Their insights laid the foundation for the modern view of the universe and marked the transition from a natural philosophical worldview towards an empirical, scientific cosmology—one that seeks to understand the physical laws governing the evolution of the cosmos and to use them to make predictive statements about its development.
At the heart of modern cosmology lies the cosmological principle, which asserts that the universe is spatially homogeneous and isotropic on sufficiently large scales [90, 91]. Homogeneity means that, statistically, every point in the universe looks the same, i.e., it is invariant under translation, while isotropy implies that the universe appears the same in all directions, i.e., invariant under rotations. The only non-trivial spacetime metric compatible with these symmetry assumptions is the Friedmann–Lemaître–Robertson–Walker (FLRW) metric [88, 90]:

$$\mathrm{d}s^2 = \mathrm{d}t^2 - a^2(t)\left[\frac{\mathrm{d}r^2}{1-kr^2} + r^2\mathrm{d}\Omega^2\right] . \tag{2.76}$$

Here, $a(t)$ is the scale factor, describing how physical distances between comoving points in the universe evolve with time. The parameter k denotes the spatial curvature of the universe: it takes the values $k = -1$, 0 or 1, corresponding to an open, flat or closed universe, respectively. Current cosmological observations indicate that the universe is spatially flat to a very good approximation [74]. In the previous section, we have introduced the Einstein field equations in equation (2.74), which describe the gravitational dynamics of spacetime. So far, we have focused on small-scale phenomena, for which the standard form of the equations is sufficient. However, when applying GR to largest scales, additional considerations become relevant, as one must account for the global dynamics of spacetime whether the universe is expanding, contracting, or static. For this reason Einstein introduced in the early 20th century the cosmological constant Λ in an attempt to model a static universe, which at the time was the widely accepted view [92, 93]. He modified his field equations accordingly:

$$R_{\mu\nu} - \frac{1}{2} g_{\mu\nu} R + \Lambda g_{\mu\nu} = 8\pi G T_{\mu\nu} \,. \tag{2.77}$$

At that time Λ was introduced as an additional geometric contribution. However, after the discovery of the expansion of the universe, Einstein later referred to this addition as his "greatest blunder". Decades later, the discovery of the *accelerated* expansion of the universe in the late 20th century [42, 94] resurrected the cosmological constant Λ as a viable explanation for this surprising phenomenon which is now interpreted as a constant form of energy density associated with dark energy.
The matter content of the universe contributing to $T_{\mu\nu}$ can be described as a fluid characterized by a pressure p and an energy density ρ, measured in the rest frame of the fluid. We refer to this fluid as a perfect fluid if it satisfies the corresponding form of the energy–momentum tensor, required by the homogeneity and isotropy assumed by the cosmological principle:

$$T_{\mu\nu} = (\rho + p) U_\mu U_\nu + p g_{\mu\nu} \,. \tag{2.78}$$

Here, U^μ denotes the four-velocity of a comoving observer. One can additionally relate the density ρ and pressure p by the equation of state

$$p = \omega \rho \,. \tag{2.79}$$

Inserting the parametrization (2.78) of a perfect fluid together with the FLRW metric into the Einstein field equation from equation (2.77), one obtains two independent equations governing the dynamics of the scale factor. The first follows from the 00-component and reads:

$$\left(\frac{\dot{a}}{a}\right)^2 = \frac{8\pi G}{3}\rho + \frac{\Lambda}{3} - \frac{k}{a^2} \,. \tag{2.80}$$

Here, $H := \dot{a}/a$ defines the Hubble parameter, which describes the rate of expansion of the universe. The second equation, which follows from the spatial components of the Einstein equations, describes the acceleration of the expansion:

$$\frac{\ddot{a}}{a} = -\frac{4\pi G}{3}(\rho + 3p) + \frac{\Lambda}{3} \,. \tag{2.81}$$

These two equations, called the Friedmann equations, govern the temporal evolution of the universe [90, 91]. From the conservation of the energy–momentum tensor

$$\nabla_\mu T^{\mu\nu} = \partial_\mu T^{\mu\nu} + \Gamma^\mu_{\mu\lambda} T^{\lambda\nu} + \Gamma^\nu_{\mu\lambda} T^{\mu\lambda} = 0 \,, \tag{2.82}$$

one obtains the continuity equation from the $\nu = 0$ component:

$$\dot{\rho} + 3\frac{\dot{a}}{a}(\rho + p) = 0\,. \tag{2.83}$$

This equation describes how the energy density of the universe evolves with its expansion. The expansion of the universe can be observed through the Hubble law, which relates the recessional velocity v of galaxies to their comoving distance d:

$$v = H(t)d \tag{2.84}$$

for vanishing peculiar velocities. To connect the expansion with the causal structure of the universe, one introduces the concept of the particle horizon. It defines the maximum comoving distance that a light signal could have traveled since the Big Bang:

$$d_{\mathrm{H}}(t) = \int_0^t \frac{\mathrm{d}t'}{a(t')}\,. \tag{2.85}$$

This horizon sets the limit for regions in the universe that could ever have been in causal contact.
From this point onward, unless stated otherwise, we work within the framework of the cosmological standard model, known as the ΛCDM model [74, 90]. We therefore now turn to the different components of the cosmic energy density and their scaling behavior with the expansion of the universe. Note, that this discussion may change in the framework of other cosmological models. By inserting the equation of state (2.79) into the continuity equation (2.83) and solving for ρ, we can derive the scaling of the different cosmic energy densities for each component individually. For ordinary and dark matter for which $\omega = 0$, we obtain [91]

$$\rho_{\mathrm{M}} \propto a^{-3}\,, \quad a(t) \propto t^{2/3}\,, \quad d_{\mathrm{H}}(t) \propto t\,. \tag{2.86}$$

In contrast, radiation is characterized by $\omega = 1/3$, implying that its energy density scales as

$$\rho_{\mathrm{r}} \propto a^{-4}\,, \quad a(t) \propto t^{1/2}\,, \quad d_{\mathrm{H}}(t) \propto t^{2/3}\,. \tag{2.87}$$

This faster decrease of the energy density of radiation compared to matter is due not only to the dilution of energy with volume but also to the redshifting of photon energies. As the universe expands, the wavelength of each photon is stretched, resulting in a loss of energy due to the relativistic Doppler effect. The vacuum energy density, associated with the cosmological constant, behaves differently. A constant contribution to the Einstein equations is obtained for $\omega = -1$ and we therefore arrive at

$$\rho_\Lambda = \text{const.}\,, \quad a(t) \propto e^{Ht}\,, \quad d_{\mathrm{H}}(t) = \text{const.} \tag{2.88}$$

From this scaling behavior, we see that different components dominate the energy budget of the universe at different epochs. The time evolution of the respective densities is shown in figure 2.2. As one can see, the universe was radiation-dominated in its early stages. Later, matter took over, leading to a decelerated expansion. Since approximately 4 billion years ago [74], dark energy has become the dominant component, resulting in an accelerated expansion of the universe. In addition to the energy densities, figure 2.2 also shows the evolution of the particle horizon d_{H} as given by equation (2.85). During

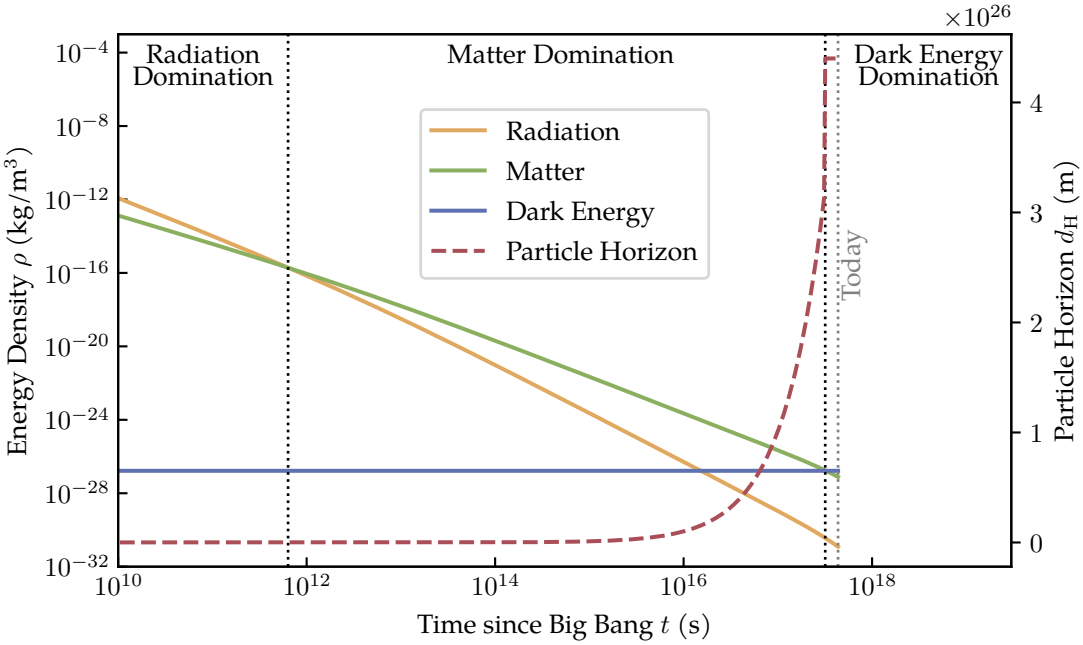

Figure 2.2: Evolution of the energy densities of radiation ρ_r, matter ρ_m, and dark energy ρ_Λ as a function of cosmic time t since the Big Bang. The dashed vertical lines indicate the transitions between radiation-, matter-, and dark energy-dominated eras. Additionally, the gray dashed line marks today. The red curve shows the comoving particle horizon, highlighting the growth of the causally connected region through cosmic history.

the radiation-dominated era, the particle horizon increased only slowly. Once matter dominated the energy budget of the universe, the horizon grew more rapidly, allowing increasingly larger regions to become causally connected. Since the onset of dark energy domination, however, the horizon has remained effectively constant due to the exponential expansion of space, causing the distant regions to become causally disconnected again in the present universe.
While the current accelerated expansion explains why distant regions of the universe are no longer in causal contact, it does not suffice to explain why the universe is so homogeneous on large scales including regions that have never been causally connected, not even before the phase of exponential expansion driven by dark energy. To resolve this so-called horizon problem, the concept of cosmic inflation is introduced [95, 96]. Inflation refers to a phase of extremely rapid expansion shortly after the Big Bang, which dramatically enlarged the particle horizon and brought initially small, causally connected regions to cosmic scales. In most models, this expansion is driven by a scalar field evolving slowly in a sufficiently flat potential. After inflation ends, the energy stored in the field is converted into particles, initiating the process of reheating.
The remarkable homogeneity and isotropy of the universe, which serves as one of the primary motivations for inflation, is strongly supported by observations of the CMB [74, 97], to which we now turn.

2.4.1 Cosmic Microwave Background

The CMB is the oldest electromagnetic radiation in the universe, emitted approximately 370000 years after the end of inflation [74]. In the early universe, conditions were extremely hot and dense, with a plasma consisting primarily of electrons, protons, neutrinos and photons. The photons were constantly scattering off the free electrons, preventing them from propagating freely through space. As the universe expanded, it cooled down. Around 370000 years after the end of inflation, the temperature had dropped to about $T \approx 3000\,\mathrm{K}$, marking the epoch of recombination [74, 98]. During this period, electrons and protons combined to form neutral hydrogen, and the density of free electrons dropped dramatically. As a result, the universe became transparent to photons for the first time. These photons have been traveling largely unimpeded ever since and make up the CMB we observe today. Due to the ongoing expansion of the universe, this light has been redshifted into the microwave region of the electromagnetic spectrum. Today, the CMB has a temperature of $T \approx (2.7255 \pm 0.0006)\,\mathrm{K}$ and follows a nearly perfect blackbody spectrum [99].
The temperature of the CMB is not completely uniform, but exhibits tiny fluctuations of the order $O(10^{-5})$ [100, 101]. These anisotropies play a crucial role in the formation of cosmic structures. There are several sources contributing to the observed anisotropy in the CMB.
The most prominent one is the dipole anisotropy, caused by the motion of our solar system relative to the rest frame of the CMB. Since this is a local effect rather than a cosmological signal, it is typically subtracted from CMB maps in cosmological analyses. There is also the reionization effect: After recombination, the universe was filled with neutral hydrogen and helium. The first stars and galaxies emitted ultraviolet radiation that reionized the helium, freeing electrons once again [74, 102]. These free electrons scattered some of the CMB photons, slightly altering the signal we observe today.
In contrast to these effects, there are also primary anisotropies affecting the CMB.

One such source is the Sachs–Wolfe effect, which describes how radiation from overdense regions is gravitationally redshifted, while radiation from underdense regions is blueshifted [103]. This means the photons lose (or gain) energy while climbing out of gravitational potential wells (or hills), resulting in slightly colder (or hotter) spots in the CMB map. However, the frequency alteration is partially compensated by gravitational time dilation, which alters the rate of photon emission in these regions and reduces the net temperature contrast observed today.
Similar to this effect is the integrated Sachs–Wolfe effect, which describes the influence of time dependent gravitational fields on the photons. Another source is the Doppler shift at last scattering caused by the peculiar velocities of electrons, which induce frequency shifts in the photons as they decouple. An important effect that shapes the observed primary anisotropies is the presence of acoustic oscillations in the baryon–photon fluid prior to last scattering. Initial perturbations in the density field after inflation led to the gravitational attraction of baryons toward dark matter overdensities. As the baryon density increased, so did the photon pressure, which resisted compression and pushed the baryonic matter outward again. This back-and-forth between gravitational attraction and photon pressure led to oscillations in the baryon–photon plasma. The maxima and minima of these oscillations manifest as peaks in the CMB power spectrum. The positions and relative heights of these peaks allow us to infer key cosmological parameters, such as the baryon density, dark matter content, and curvature of the universe.
In addition to temperature anisotropies, the CMB also exhibits polarizations [104–106]. These polarization patterns can be decomposed into two distinct types: E-modes and B-modes. To describe the polarization quantitatively, we introduce the Stokes parameters, which characterize the state of polarization of an electromagnetic wave. For a monochromatic wave propagating in the z-direction, with electric components $E_x = |E_x| e^{i\delta_x}$ and $E_y = \left|E_y\right| e^{i\delta_y}$, the Stokes parameters are given by:

$$I = |E_x|^2 + \left|E_y\right|^2 , \tag{2.89}$$

$$Q = |E_x|^2 - \left|E_y\right|^2 , \tag{2.90}$$

$$U = 2\,|E_x|\left|E_y\right| \cos\varphi\,, \tag{2.91}$$

$$V = 2\,|E_x|\left|E_y\right| \sin\varphi\,, \tag{2.92}$$

where $\varphi = \delta_x - \delta_y$ is the phase difference between the electric field components in the x- and y-directions. Here, I denotes the total intensity, Q and U represent the linearly polarized components, and V describes the degree of circular polarization. Measuring the intensity through polarizers at different angles allows one to determine the Stokes parameters. The resulting, coordinate-dependent polarization field can then be decomposed into a coordinate-independent, curl-free E-mode and a divergence-free B-mode component.
The E-mode polarization arises primarily from Thomson scattering of CMB photons off free electrons. During the epoch of recombination, the radiation field was anisotropic due to the presence of density fluctuations, which gave rise to a net linear polarization. In this scattering process, components of the incoming electric field that are not aligned with the direction of propagation are preferentially scattered, leading to a measurable polarization signal.
Due to their generation mechanism, E-modes are strongly correlated with temperature fluctuations in the CMB. In contrast, B-mode polarization arises from tensor perturbations, such as primordial GWs generated during inflation. These tensor modes introduce

a transverse-shear deformation of spacetime, which imprints a curl-like structure in the polarization pattern. This additional rotational component, not present in scalar density perturbations, is what distinguishes B-modes from E-modes.
Primordial B-modes are considered a "smoking gun" signature of inflation, resulting from quantum fluctuations in the early universe that give rise to a stochastic background of GWs. Secondary B-modes can also be generated at later times via gravitational lensing, as large-scale structures deflect the path of photons and convert some E-mode signals into B-modes.
E-mode polarizations have been measured in great detail by experiments like WMAP [107] and Planck [108], whereas the search for primordial B-modes remains ongoing. Dedicated experiments such as BICEP [109], POLARBEAR [110], and the Simons Observatory [111] are currently pursuing increasingly sensitive observations, particularly on large angular scales, where the primordial signal would be most prominent.
In summary, the anisotropies and polarization patterns observed in the CMB provide a powerful probe of the physical conditions in the early universe. However, to fully understand the origin and growth of cosmic structures, it is essential to go beyond the homogeneous and isotropic background description and consider perturbations to the FLRW spacetime. In the following, we present the theory of linear cosmological perturbations within the framework of GR.

2.4.2 Linear Cosmological Perturbations in General Relativity

As one may suspect, the phenomenon of anisotropy cannot be explained by an exactly homogeneous universe. Instead, the structures observed today can be understood as the result of the growth of small initial fluctuations. To describe this mathematically, we closely follow references [91, 112, 113], and therefore, introduce small perturbations to the metric $g_{\mu\nu}$ and the energy–momentum tensor $T_{\mu\nu}$ in the form of:

$$g_{\mu\nu} = \bar{g}_{\mu\nu} + \delta g_{\mu\nu}(t,x)\,, \qquad T_{\mu\nu} = \bar{T}_{\mu\nu} + \delta T_{\mu\nu}(t,x)\,. \tag{2.93}$$

Here, $\bar{g}_{\mu\nu}$ represents the spatially flat FLRW metric, which takes the following form when perturbations are taken into account

$$\mathrm{d}s^2 = a^2(\eta)\left[-(1+2A)\mathrm{d}\eta^2 + 2B_i\mathrm{d}x^i\mathrm{d}\eta + (\delta_{ij}+2E_{ij})\mathrm{d}x^i\mathrm{d}x^j\right], \tag{2.94}$$

where A, B_i and E_{ij} are functions of spatial coordinates x and conformal time η. We employ the usual Scalar–Vector–Tensor (SVT) decomposition, which results in:

$$B_i = \partial_i B + \hat{B}_i\,, \tag{2.95}$$

$$E_{ij} = C\delta_{ij} + \left(\partial_i\partial_j - \frac{1}{3}\delta_{ij}\nabla^2\right)E + \frac{1}{2}\left(\partial_i\hat{E}_j + \partial_i\hat{E}_i\right) + \hat{E}_{ij}\,. \tag{2.96}$$

Note that the hatted quantities have vanishing divergence. These perturbations are not uniquely defined and depend on the choice of coordinates, which may lead to spurious perturbations or, in other words, physical redundancies. Hence, we must identify the true perturbations. To do this, we consider the coordinate transformation:

$$x^\mu(q) \to \tilde{x}^\mu(q) = x^\mu(q) + \epsilon^\mu(q)\,, \tag{2.97}$$

where ϵ^μ is assumed to be small, allowing it to be treated as a perturbation with

$$\epsilon^0 = T\,, \qquad\qquad \epsilon^i = L^i\,. \tag{2.98}$$

T represents the hypersurfaces of constant time in the new coordinates, and L^i denotes the spatial coordinates on these hypersurfaces. Since only the coordinates are renamed, a scalar field $\phi(\eta, x)$ at each point q remains invariant, i.e., $\phi(x^\mu) = \tilde{\phi}(\tilde{x}^\mu)$. Taylor expanding $\tilde{\phi}(\tilde{x}^\mu)$ around x^μ to first order immediately yields

$$\delta\tilde{\phi} = \delta\phi - \bar{\phi}' T\,. \tag{2.99}$$

For the metric $g_{\mu\nu}$, the transformation rule follows from the requirement that the spacetime interval must remain invariant under the transformation:

$$g_{\mu\nu}(x) = \frac{\partial\tilde{x}^\alpha}{\partial x^\mu}\frac{\partial\tilde{x}^\beta}{\partial x^\nu}\tilde{g}_{\alpha\beta}(\tilde{x})\,. \tag{2.100}$$

Again, Taylor expanding the right handside of equation (2.100) to first order around x^μ, we obtain the transformation rules which in terms of the SVT decomposition read

$$A \to A - T' - \mathcal{H}T\,, \qquad B \to B + T' - L'\,, \qquad \hat{B}_i \to \hat{B}_i - \hat{L}_i'\,, \tag{2.101}$$

$$C \to C - \mathcal{H}T - \frac{1}{3}\nabla^2 L\,, \qquad E \to E - L\,, \qquad \hat{E}_i \to \hat{E}_i - \hat{L}_i\,, \tag{2.102}$$

$$\hat{E}_{ij} \to \hat{E}_{ij}\,. \tag{2.103}$$

Here, the conformal Hubble rate $\mathcal{H}$ is defined as $\mathcal{H} = a'/a$. One can now avoid the gauge problem by introducing the so-called Bardeen variables [114], which remain unchanged under coordinate transformations, and thus, represent the true perturbations of spacetime:

$$\Psi_{\text{Bardeen}} = A + \mathcal{H}(B - E') + (B - E')'\,, \tag{2.104}$$

$$\hat{\Phi}_{\text{Bardeen},i} = \hat{B}_i - \hat{E}_i'\,, \tag{2.105}$$

$$\Phi_{\text{Bardeen}} = -C + \frac{1}{3}\nabla^2 E - \mathcal{H}(B - E')\,. \tag{2.106}$$

Alternatively, one may fix the gauge, which often simplifies calculations. For example, in the Newtonian gauge, one typically sets $B = E = 0$, resulting in a diagonal metric.
The perturbations of the energy–momentum tensor $T^\mu{}_\nu$ are defined as

$$T^0{}_0 = -(\bar{\rho} + \delta\rho)\,, \tag{2.107}$$

$$T^i{}_0 = -(\bar{\rho} + \bar{p})v^i\,, \tag{2.108}$$

$$T^i{}_j = (\bar{p} + \delta p)\delta^i{}_j + \Pi^i{}_j\,, \tag{2.109}$$

where v^i is the bulk velocity and $\Pi^i{}_j$ denotes the anisotropic stress.
In many cosmological contexts, it is useful to introduce the momentum density perturbation:

$$q^i = (\bar{\rho} + \bar{p})v^i\,. \tag{2.110}$$

The total perturbations in $\delta\rho$, δp, q^i and Π^{ij} result from a simple sum over all relevant components. Here, $\delta\rho$ and δp are scalar quantities, while v_i and q_i transform as vectors, and Π_{ij} as a tensor. Thus, all perturbations naturally decompose according to the SVT decomposition introduced earlier. Applying the coordinate transformation from

equation (2.97) and Taylor expanding, we find that the energy–momentum perturbations transform according to:

$$\delta\rho \to \delta\rho - \bar{\rho}'T\,, \qquad \delta p \to \delta p - \bar{p}'T\,, \qquad q_i \to q_i + (\bar{\rho}+\bar{p})L_i'\,, \tag{2.111}$$

$$v_i \to v_i + L_i'\,, \qquad \Pi_{ij} \to \Pi_{ij}\,. \tag{2.112}$$

Having defined both the perturbations of the metric and of the energy–momentum tensor $T^{\mu\nu}$, we now turn to their evolution. These proceed in two distinct ways: the evolution of the metric perturbations is governed by Einstein's equations (2.77), while the evolution of matter perturbations follows from the conservation of the energy–momentum tensor in equation (2.82).

We start with the latter and note that we must expand the conservation equation to linear order in the perturbations to obtain the desired evolution equations. To facilitate the derivation, we adopt the Newtonian gauge, in which the perturbed metric takes the form

$$\mathrm{d}s^2 = a^2(\eta)\left[-(1+2\Psi)\,\mathrm{d}\eta^2 + (1-2\Phi)\,\delta_{ij}\mathrm{d}x^i\mathrm{d}x^j\right]. \tag{2.113}$$

Following reference [112], we have relabeled $A = \Psi$ and $C = -\Phi$ to make contact with the Bardeen potentials. As usual, from the metric, the perturbed Christoffel symbols can be computed. Evaluating the conservation equation $\nabla_\mu T^\mu{}_\nu$ to first order in the perturbation for the component with $\nu = 0$ the perturbed continuity equation follows:

$$\delta\rho' = -3H(\delta\rho + \delta p) - \partial_i q^i + 3\Phi'(\bar{\rho}+\bar{p})\,. \tag{2.114}$$

The first term describes the dilution due to the background expansion, the second term represents local fluid flow and the third captures the change in density induced by the perturbations in the background expansion. The continuity equation can alternatively be expressed as

$$\delta' = -\left(1+\frac{\bar{p}}{\bar{\rho}}\right)(\Delta v - 3\Phi') - 3H\left(\frac{\delta p}{\delta\rho} - \frac{\bar{p}}{\bar{\rho}}\right)\delta\,, \tag{2.115}$$

where $\delta = \delta\rho/\bar{\rho}$ is the density contrast. Next, the spatial part leads to the Euler equation:

$$q_i' = -4Hq_i - (\bar{\rho}+\bar{p})\,\partial_i\Psi - \partial_i\delta p - \partial^j\Pi_{ij}\,, \tag{2.116}$$

which can again be expressed using the momentum density q^i as

$$v_i' = -\left(H + \frac{\bar{p}'}{\bar{\rho}+\bar{p}}\right)v_i - \frac{1}{\bar{\rho}+\bar{p}}\left(\partial_i\delta p + \partial^j\Pi_{ij}\right) - \partial_i\Psi\,. \tag{2.117}$$

Thus, we see that the evolution of matter perturbations is directly influenced by the metric potentials Ψ and Φ.

We now turn to the evolution of the metric perturbations themselves, governed by Einstein's field equation $G^\mu_\nu = 8\pi G T^\mu_\nu$ in Newtonian gauge. Considering the $\mu = \nu = 0$ component, we obtain:

$$\Delta^2\Phi - 3H\left(\Phi^i + H\Psi\right) = 4\pi G a^2\delta\rho\,, \tag{2.118}$$

which can be interpreted as the relativistic generalization of the Poisson equation. For the spatial off-diagonal components ($\mu = i \neq 0$, $\nu = j \neq 0$), we find

$$\left(\partial_i\partial_j - \frac{1}{3}\delta_{ij}\Delta^2\right)(\Phi - \Psi) = 8\pi G a^2\Pi_{ij}\,, \tag{2.119}$$

showing that anisotropic stress sources a difference between Φ and Ψ. For the mixed components ($\mu = 0, \nu = i \neq 0$), we obtain

$$(\Phi' + H\Psi) = -4\pi G a^2 q\,, \tag{2.120}$$

relating the gradient of the metric potentials to the momentum density. Finally, taking the trace over the spatial part results in:

$$\Phi'' + \frac{1}{3}\Delta^2\,(\Psi - \Phi) + \left(2H' + H^2\right)\Psi + H\Psi' + 2H\Phi' = 4\pi G a^2 \delta p\,, \tag{2.121}$$

which links the time evolution of the metric perturbations to the pressure perturbations. Together, all these equations form a closed system of differential equations once the equation of state is specified and the fluid is assumed to evolve adiabatically.
With this, we have outlined the basic theory of linear perturbations. This formalism is essential for connecting primordial fluctuations in the early universe to the anisotropies observed in the CMB today. In principle, one can evolve initial conditions through cosmic history using the perturbation equations derived above to predict the CMB power spectra. However, due to the high complexity of these coupled differential equations, especially when including effects from photon–baryon interactions, and recombination physics, such calculations are rarely carried out analytically. Instead, numerical codes such as CAMB [115, 116] and CLASS [117] are widely used to perform these computations with high precision and efficiency. With all of this in place, we are now ready to address the phenomenology of dark energy and its implications for cosmic structure formation.

2.4.3 Phenomenological Models of Dark Energy

Most discussions in the literature are conducted within the framework of the ΛCDM model, which represents the most widely used cosmological model and which successfully explains a wide range of observational phenomena [74, 112]. Despite its success, there are both conceptual and observational motivations to critically reassess the ΛCDM model.
Among the observational tensions, one of the most important is the so-called Hubble tension [74], which refers to the discrepancy between local measurements of the Hubble constant (e.g., based on supernovae data) and the value inferred from Planck data when interpreted within the ΛCDM framework. Furthermore, recent results from the Dark Energy Spectroscopic Instrument (DESI) survey have gained attention. The DESI experiment provides high-precision measurement of Baryonic Acoustic Oscillations (BAO) over a range of redshifts around $O(1)$ [118]. Analyses of the data show that models with a dynamic dark energy component are preferred with respect to the ΛCDM model.
In both the ΛCDM model and its extensions, dark energy is modeled as a perfect fluid characterized by an energy density ρ and a pressure p, with an associated equation of state parameter $\omega = p/\rho$ [90, 113]. In the ΛCDM model, dark energy is assumed to have a constant equation of state parameter $\omega = -1$, corresponding to a cosmological constant with a time-independent energy density ρ_Λ.
A first generalization consists of treating ω as a free parameter rather than fixing it to -1. This leads to the so-called ωCDM model [90, 112], in which the energy density evolves according to

$$\rho_\Lambda^{\omega\mathrm{CDM}}(a) \propto a^{-3(1+\omega)}\,. \tag{2.122}$$

Inspecting the second Friedmann equation (2.81), it follows that for a matter component with $\omega < -1/3$ this density behaves as dark energy, i.e., yields an accelerated expansion of the universe. Going beyond a constant ω, models with a time-dependent equation of state $\omega(a)$ have been proposed. A commonly used phenomonelogical parametrization is the $\omega_0\omega_a$ model, where ω depends on the scale factor a as [119, 120]:

$$\omega(a) = \omega_0 + \omega_a(1 - a)\,. \tag{2.123}$$

The corresponding evolution of the dark energy density is then governed by:

$$\rho_\Lambda^{\omega_0\omega_a\mathrm{CDM}}(a) \propto a^{-3(1+\omega_0+\omega_a)} \exp\left(-3\omega_a(1-a)\right). \tag{2.124}$$

Such a parametrization provides a flexible framework to capture potential deviations from a cosmological constant and to test observational sensitivity to a dynamic dark energy. In the next chapter, we make use of this approach to explore whether a time-varying dark energy component is supported by observations.

Chapter 3

A Model of Holographic Dark Energy

In this thesis, we search for *traces of gravity* as gravitational imprints in physical systems that are not primarily governed by gravity. Especially in regimes where gravity is no longer negligible, quantum theories such as QFTs tend to break down. These regions therefore provide a natural ground for probing indirect signatures of a deeper gravitational structure. In this chapter, we focus on cosmological scales and investigate dark energy and its potentially holographic origin, as might be motivated by an underlying theory of gravity.

QFTs appear to not provide a sufficient description of nature in the presence of black holes [121–127]. A striking example of this limitation is the way in which DOFs, or equivalently information or entropy, are assigned to regions of spacetime: In QFT, this number scales with the volume of a region, i.e., with L^3 for a box of side length L. In contrast, the holographic principle suggests that the maximal entropy associated with a gravitating system, such as a black hole, scales with the area of the horizon, i.e., with L^2 [121–126]. This mismatch implies that QFT overcounts the number of fundamental DOFs at low energies or on large scales.

From this discrepancy, Cohen, Kaplan and Nelson (CKN) [127] derived a concrete bound to define the domain of validity for an Effective Field Theory (EFT). Assuming that the entropy of any physical system should not exceed the Bekenstein–Hawking entropy S_{BH} of a black hole of the same size, the entropy computed within QFT S_{QFT} is then given by

$$S_{\mathrm{QFT}} = \Lambda_{\mathrm{UV}}^3 L^3 \leq \pi L^2 M_{\mathrm{Pl}}^2 = S_{\mathrm{BH}}\,, \tag{3.1}$$

for a box of side length L, where Λ_{UV} denotes the Ultraviolet (UV) cutoff and M_{Pl} is the Planck mass. For a fixed UV cutoff, this condition also defines a maximal length L_{max}, and thereby an Infrared (IR) cutoff $\Lambda_{\mathrm{IR}} = L_{\mathrm{max}}^{-1}$. While this bound ensures that the number of quantum states is consistent with the information-theoretic limit imposed by black hole thermodynamics, it does not constrain how much energy can be stored in the volume. As a result, it still allows for states whose total energy is large enough that their Schwarzschild radius R_{S} exceeds the size of the box, i.e., $R_{\mathrm{S}} > L$. To prevent the formation of black holes within an EFT, according to CKN a stricter bound must be imposed. This leads to the so-called CKN bound [127]:

$$L \geq R_{\mathrm{S}} \sim \frac{M_{\mathrm{QFT}}}{M_{\mathrm{Pl}}^2} = \frac{\Lambda_{\mathrm{UV}}^4 L^3}{M_{\mathrm{Pl}}^2} \leftrightarrow \Lambda_{\mathrm{UV}}^4 \leq \frac{M_{\mathrm{Pl}}^2}{L^2}\,. \tag{3.2}$$

This condition ensures that no physical state described by the theory corresponds to a black hole, and it establishes a fundamental connection between the UV and IR scales. This bound has wide-ranging implications, including effects on the anomalous magnetic

moment of leptons [128–132], the hierarchy problem [133], and the phenomenology of radiative neutrino mass models [134]. One of its earliest and most prominent applications, which is already discussed in the original CKN paper [127], concerns the cosmological constant problem [46], i.e., the puzzling smallness of the observed dark energy density. In QFT, quantum corrections to the vacuum energy scale as Λ_{UV}^4 [46], where Λ_{UV} is the ultraviolet cutoff of the EFT. A natural question is what value this cutoff should take. In the absence of additional UV physics, the only available scale that remains when combining QFT and gravity is the Planck scale. It marks the energy at which quantum gravitational effects become non-negligible and perturbative QFT breaks down. Hence, in such scenarios, it is common to identify the cutoff with the Planck mass: $\Lambda_{\mathrm{UV}} \sim M_{\mathrm{Pl}}$. However, this leads to an enormous discrepancy: the predicted vacuum energy density is larger than the observed dark energy by about 120 orders of magnitude. However, according to CKN, gravity itself forbids contributions to the energy densities that would lead to the formation of black holes within the EFT already below the Planck scale. Instead, CKN propose to use the Hubble horizon H as the relevant IR scale of the universe, i.e., to identify the size of the box as the Hubble radius, $L_{\mathrm{max}} = 1/H$. Inserting this into the CKN bound in equation (3.2) yields a UV cutoff of $\Lambda_{\mathrm{UV}} \sim 10^{-3}\,\mathrm{eV}$, which corresponds to the observed order of magnitude of today's dark energy density $\rho_\Lambda \sim (10^{-3}\,\mathrm{eV})^4$.
While this scenario offers a natural suppression of the vacuum energy through holographic arguments, it comes with an important consequence: since the Hubble parameter $H = H(t)$ evolves with time, the UV cutoff, and therefore the dark energy density, also becomes time-dependent. This implies that dark energy is not constant, but dynamically evolving, a predicition that is testable with high-precision cosmological observations.
The aim of this chapter is therefore to analyze the implications of a dynamically evolving dark energy component that emerges from gravity-motivated constraints on QFT. This is further motivated by the latest results of the DESI collaboration, providing the first evidence towards a preference of dynamic dark energy models with respect to ΛCDM [5]. First, in section 3.1, we focus on the background dynamics by solving the Friedmann equations with the CKN-modified dark energy term. We then fit the resulting model to the DESI BAO, model independent Hubble measurements and supernovae datasets, comparing its predictions to those of alternative cosmological models. In addition, we investigate trends arising from the comparison of the DESI Year-1 and Year-2 data releases which we from now on refer to as DR1 and DR2, respectively. In section 3.2, we extend the analysis to include linear cosmological perturbations. We formulate the relevant perturbation equations and perform a global fit using additional data from CMB and weak gravitational lensing. The objective is to fully exploit the available cosmological data to rigorously assess the viability of the CKN framework in a precision cosmological setting. Finally, in section 3.3, we summarize our results, compare the findings of the two analyses, and provide an outlook on future directions and potential extensions to this work.

3.1 Background Evolution and Constraints from Late-Universe Data

Recent measurements from DESI BAO, when combined with supernovae and CMB data, show a 4.2 σ preference for models with dynamical dark energy over the standard ΛCDM model [5, 135], see also section 2.4. As argued in the introduction to chapter 3, the CKN bound also leads to a dynamically evolving dark energy. Motivated by this, we now

want to test the resulting model against DESI BAO, supernovae, and Hubble parameter data. To keep the analysis tractable at this stage, we restrict ourselves to background dynamics only in this section, neglecting linear perturbations. This allows us to obtain a first indication of whether the CKN-based model is compatible with observations, before undertaking a more comprehensive analysis.

Starting from equation (3.2), and assuming that the IR cutoff scale is set by the Hubble horizon $L_{\max} = 1/H$, the UV cutoff is given by:

$$\Lambda_{\rm UV}^4 \lesssim H^2(z) M_{\rm Pl}^2 \,, \tag{3.3}$$

where z denotes the redshift, $M_{\rm Pl}$ the Planck mass, and $H(z)$ the Hubble parameter. This leads to a Vacuum Energy Density (VED) at one-loop level given by:

$$\rho_{\rm VED}^{\text{1-loop}} \simeq \nu \frac{\Lambda_{\rm UV}^4}{16\pi^2} = \nu \frac{M_{\rm Pl} H^2(z)}{16\pi^2} \,. \tag{3.4}$$

The case $\nu = 1$ corresponds to the original CKN bound, while $\nu \neq 1$ generalizes it to what we refer to as the νCKN model. This extension allows us to phenomenologically absorb uncertainties, simplifications, and model-dependent details of the underlying derivation. For instance, the 1-loop vacuum energy term may contain additional numerical factors such as a symmetry factor of $1/2$, counting factors for DOFs, or scheme-dependent regularization constants. Moreover, the νCKN framework encompasses the broader class of models from the literature in which the vacuum energy scales as $H^2(z)$, including running vacua models [136–138] and certain holographic dark energy scenarios [139, 140]. Further, in the regime of interest, i.e., $z \lesssim 3.5$, we have $H(z)^4 \ll M_{\rm Pl}^2 H(z)^2$, which allows us to neglect the IR cutoff. Additionally, contributions from heavy particles are neglected whenever their energy exceeds the UV cutoff [127, 128].

Criticism has been raised in the literature against models in which the dark energy density scales as $H^2(z)$. Specifically, assuming that the energy–momentum tensors of matter and dark energy are separately conserved does not lead to an accelerated expansion of the universe [139, 141], which clearly contradicts observations. However, if one instead only assumes the joint energy conservation for the total fluid, the resulting effective equation of state can drive accelerated expansion [142–144] and provides a good fit to observational data up to redshifts $z \sim O(1)$. As we will discuss below, a non-conservation of dark energy is further required for a consistent framework. Another concern is the potential conflict of such models with other cosmological processes at high redshift z, such as large-scale structure formation or the properties of the CMB [141]. These tensions, however, may be alleviated for small values of ν, especially given that the universe is matter dominated for $z \gtrsim 0.4$. Moreover, the true value of ν is entirely unknown. One could in principle consider a redshift-dependent $\nu(z)$, depending on the theoretical framework under study. In the present analysis, however, we restrict ourselves to the case of a constant parameter ν.

To investigate how the CKN bound affects the evolution of the universe, we incorporate the resulting vacuum energy density in equation (3.4) semi-classically into the energy-momentum tensor $T^{\mu\nu}$ [46]:

$$T^{\mu\nu} = T^{\mu\nu}_{\rm classical} + \langle T^{\mu\nu} \rangle, \qquad \text{with} \quad \langle T^{\mu\nu} \rangle = \rho_{\rm VED}^{\text{1-loop}}\, g^{\mu\nu} \,. \tag{3.5}$$

Here, $T_{\rm classical}$ contains the contributions from matter $T^{\mu\nu}_{\rm matter}$, radiation $T^{\mu\nu}_{\rm radiation}$, and a classical cosmological constant Λ:

$$T^{\mu\nu}_{\rm classical} = T^{\mu\nu}_{\rm matter} + T^{\mu\nu}_{\rm radiation} + \Lambda_0 g^{\mu\nu} \,. \tag{3.6}$$

As mentioned earlier, we do not assume separate conservation of the energy–momentum tensor for matter and dark energy. Instead, we allow for the possibility of energy exchange between two components, see for example references [142, 144]. Separate conservation does not only imply a non-expanding universe, but also directly contradicts the assumption of a dynamical dark energy component with $\dot{\rho}_{\text{VED}}^{\text{1-loop}} \neq 0$. If we impose separate conservation laws for matter and dark energy with the covariant conservation of the total energy-momentum tensor, i.e., $\nabla_\mu T^{\mu\nu} = 0$, we have:

$$\nabla_\mu T^{\mu\nu}_{\text{classical}} = 0\,, \quad \text{and} \quad \nabla_\mu \langle T^{\mu\nu} \rangle = 0\,, \tag{3.7}$$

where the second term leads to

$$\nabla_\mu \left(\rho_{\text{VED}}^{\text{1-loop}} g^{\mu\nu} \right) = 0\,, \tag{3.8}$$

$$\leftrightarrow \quad g^{\mu\nu} \nabla_\mu \left(\rho_{\text{VED}}^{\text{1-loop}} \right) + \rho_{\text{VED}}^{\text{1-loop}} \nabla_\mu \left(g^{\mu\nu} \right) = 0\,. \tag{3.9}$$

Using the metric compatibility of the covariant derivative, we arrive at

$$g^{\mu\nu} \nabla_\mu \left(\rho_{\text{VED}}^{\text{1-loop}} \right) = 0\,, \tag{3.10}$$

which implies that $\dot{\rho}_{\text{VED}}^{\text{1-loop}} = 0$. This is incompatible with any dynamical evolution of dark energy, and thus directly contradicts our framework. Therefore, we are compelled to assume a common energy conservation law for dark energy and at least one other matter component.
By combining the $\mu\nu = 00$ and $\mu\nu = ij$ components of Einstein's field equations, we obtain the standard Friedmann equation:

$$H^2(t) = \frac{8\pi G}{3} \left(\rho_{\text{M}}(t) + \rho_{\text{DE}}(t) \right)\,. \tag{3.11}$$

Here, ρ_{M} denotes the matter density, and ρ_{DE} the dark energy density. In what follows, we neglect the contribution of radiation, since we are interested in the matter-dominated epoch. Moreover, we assume a spatially flat universe with $\Omega_{\text{k}} = 0$. Assuming that the total energy density consists of two components, i.e., $\rho_{\text{tot}} = \rho_{\text{M}} + \rho_{\text{DE}}$, and using the corresponding equations of state $p_{\text{M}} = 0$ and $p_{\text{DE}} = -\rho_{\text{DE}}$, the continuity equation (2.83) becomes:

$$\dot{\rho}_{\text{M}}(t) + \dot{\rho}_{\text{DE}}(t) = -3H(t)\rho_{\text{M}}(t)\,. \tag{3.12}$$

Solving the Friedmann equation (3.11) together with the continuity equation (3.12) leads to the following expression for the Hubble parameter:

$$H^2(z) = H_0^2 \left(\Omega_{\text{M}}(z) + \Omega_{\text{DE}}(z) \right)\,, \tag{3.13}$$

where $H_0 = H(z = 0)$ is the present-day Hubble parameter, and

$$\Omega_{\text{M}}(z) = \Omega_{\text{M}}^0 \left(1 + z\right)^{3 - \frac{\nu}{2\pi}}\,, \tag{3.14}$$

$$\Omega_{\text{DE}}(z) = \Omega_{\text{DE}}^0 + \Omega_{\text{M}}^0 \frac{\nu}{6\pi - \nu} \left(\left(1 + z\right)^{3 - \frac{\nu}{2\pi}} - 1 \right)\,, \tag{3.15}$$

with Ω_{M}^0 and Ω_{DE}^0 denoting the current values of the respective energy densities, normalized to the critical density $\rho_{\text{crit},0} = \left(3H_0^2\right) / \left(8\pi G\right)$. To characterize the dynamical

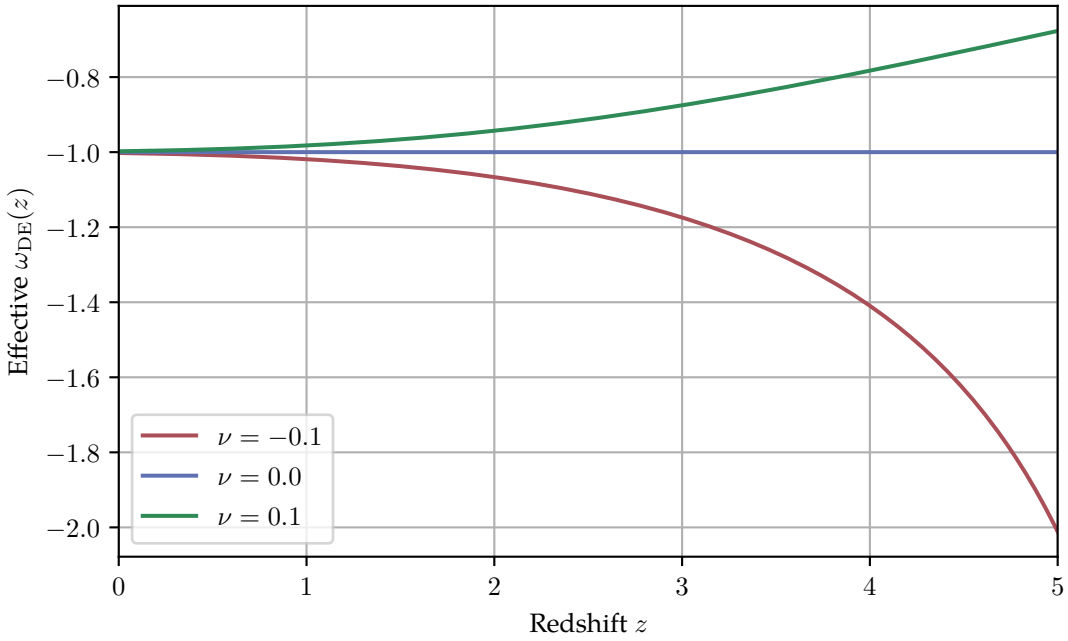

Figure 3.1: Redshift evolution of the effective equation of state parameter $\omega_{\rm DE}(z)$, derived from the redshift dependence of the dark energy density $\rho_{\rm DE}(z)$ in the model under consideration. The different curves correspond to different values of the model parameter ν. We choose the representative values $\Omega_{\rm M}^0 = 0.3$ and $\Omega_{\rm DE}^0 = 0.7$.

behavior of the dark energy component in terms of an effective fluid description, we define a redshift-dependent equation of state parameter $\omega_{\rm DE}(z)$ via the standard continuity equation, i.e., $\dot{\rho}_{\rm DE} = -3H\,(1 + \omega_{\rm DE})\,\rho_{\rm DE}$ by rewriting equation (3.12), where $\omega_{\rm DE}(z)$ is now a function of $\rho_{\rm M}$ and its derivative. This parameter is convenient for interpreting the redshift evolution of $\rho_{\rm DE}(z)$ in analogy to scalar field models. In particular, values of $\omega_{\rm DE}(z) > -1$ are commonly associated with quintessence-like behavior [48], where the dark energy density $\rho_{\rm DE}$ decreases more slowly than in the cosmological constant case, i.e., ΛCDM, while values $\omega_{\rm DE}(z) < -1$ correspond to phantom-like evolution [145]. Figure 3.1 shows the resulting behavior of $\omega_{\rm DE}(z)$ for representative values of the model parameter ν, $\Omega_{\rm M}^0$ and $\Omega_{\rm DE}^0$. For $\nu = 0$, the model reduces to ΛCDM with a constant equation of state parameter $\omega = -1$. Positive values of ν lead to $\omega_{\rm DE}(z) > -1$ at low redshift, whereas negative values result in $\omega_{\rm DE}(z) < -1$. Note, that at high redshift, i.e., $z \gg 1$, the effective equation of state parameter can deviate from -1 and turn positive. However, since $\Omega_{\rm DE} \ll 1$ in this regime, such deviations remain phenomenologically unproblematic and do not affect the background evolution in the matter-dominated era. With this, the (ν)CKN model is fully specified and can be directly compared to the alternative dark energy models introduced in subsection 2.4.3, namely the ΛCDM, ωCDM, and $\omega_0\omega_a$CDM models. In all cases, we assume a spatially flat universe, neglect radiation, i.e., $\Omega_{\rm M}^0 + \Omega_{\rm DE}^0 = 1$, and focus on differences in the dynamical behavior of the dark energy sector.

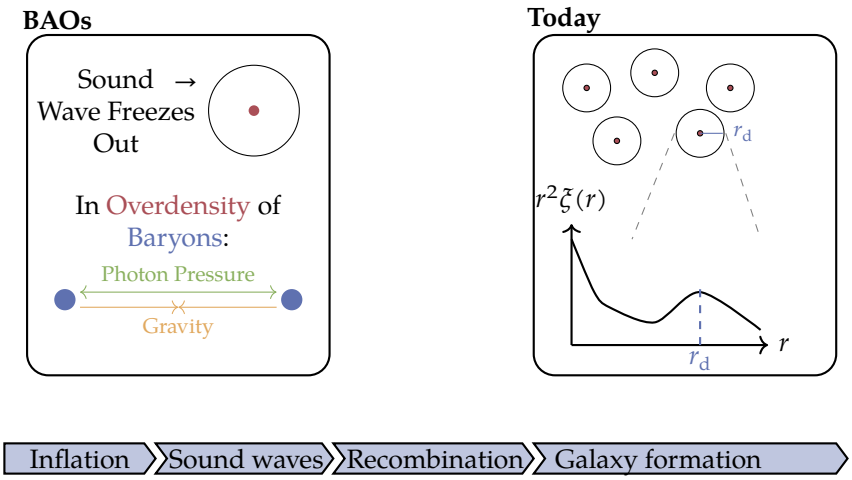

Figure 3.2: Schematic illustration of the BAO freeze-out (left) and the imprinted correlation ξ in today's galaxy distribution (right). The timeline at the bottom highlights key epochs. Note, that the freeze-out of the sound waves happens during recombination.

3.1.1 Observational Data And Statistical Methodology

This subsection presents a quantitative analysis of how well the CKN-inspired modifications align with current cosmological observations, with particular emphasis on the recent BAO measurements from the DESI survey [5, 135]. We start by outlining the observational datasets employed, followed by a detailed description of the statistical methodology before ending with a discussion of the corresponding results.
The statistical analysis relies on a combination of recent cosmological probes. These include the BAO data from DESI [5, 135], model independent measurements of the Hubble expansion rate [146], and two type Ia supernova samples: Pantheon+ [147], and DES-SN5YR [148], referred to as DESY5 throughout this chapter.

DESI BAO: BAOs arise from pressure-driven sound waves that propagated through the tightly coupled photon–baryon fluid in the early universe [149, 150]. Prior to recombination, the high radiation pressure generated by photon scattering counteracted gravitational collapse, leading to oscillatory perturbations in the baryonic component. These perturbations propagate outward from initial overdensities at the sound speed of the relativistic plasma in the matter distribution, which we call the sound horizon [151, 152]. After recombination, when photons decouple and the baryon–photon interactions cease, these oscillations freeze-out, and the perturbation pattern becomes imprinted in the distribution of baryonic matter. This leads to a slight overabundance of galaxies separated by the comoving sound horizon scale r_d, manifesting as a broad peak in the two-point correlation function of matter tracers [153]. Figure 3.2 represents a schematic evolution of this process. The underlying physical mechanism is the same as for the acoustic oscillations in the photon–baryon fluid discussed in the context of the CMB anisotropies in subsection 2.4.1, where these oscillations manifest as the characteristic peak structure in the CMB power spectrum [149]. In practice, BAO measurements exploit this feature to provide a standard ruler for cosmological distance scales. The observable quantities include the transverse comoving distance $D_M(z)$ and the Hubble

distance $D_{\rm H}(z) = c/H(z)$, where c denotes the speed of light, both normalized by the comoving sound horizon at the drag epoch $r_{\rm d}$, which describes the time when baryons effectively decouple from Compton drag due to the interactions with photons. The DESI survey provides BAO measurements extracted from galaxies, quasars, and Lyman-α forest tracers across a wide redshift range [5, 135]. The datasets include values for $D_{\rm M}(z)/r_{\rm d}$ and $D_{\rm H}(z)/r_{\rm d}$, however, in redshift bins with lower statistics, only the angle-averaged distance $D_{\rm V}(z)/r_{\rm d}$ is reported. In this work, we treat the sound horizon at the drag epoch $r_{\rm d}$ as a free parameter. Note, that BAO data primarily constrain the parameter combination $r_{\rm d}H_0$ as well as the matter density $\Omega^0_{\rm M}$ [154]. The DESI sample consists of seven redshift bins with negligible inter-bin correlations, as documented in reference [5, 135].

Supernova: Type Ia supernovae serve as standard candles for mapping the expansion history of the universe. The two datasets used here are Pantheon+ [147] and DESY5 [148]. Unfortunately, broader compilations such as Union3 are not publicly accessible at the time of writing. Physically, these events are thought to originate from white dwarfs in binary systems, which accrete mass from their companion stars [155]. When the white dwarf nears the Chandrasekhar limit, a runaway thermonuclear explosion is triggered. Owing to the uniform mass threshold for ignition, these explosions yield similar intrinsic luminosities. After empirical corrections for stretch and color [156], they behave as standard candles, i.e., as astrophysical light sources with known absolute brightness. This makes it possible to infer their luminosity distance from the observed flux, providing a direct handle on the distance-redshift relation that underpins cosmological inference. For DESY5, we use the published distance moduli and associated covariance matrix. Since type Ia supernovae data constrain the combination of the absolute magnitude M and the Hubble constant H_0, but not each quantity individually, we follow reference [148] in redefining them into the single parameter $\tilde{M} = M + 5\log_{10}(c/H_0)$. This parameter is analytically marginalized over in the likelihood. A similar procedure is applied to the Pantheon+ dataset [147], where we again marginalize over $\tilde{M}$, and restrict the analysis to redshifts $z > 0.01$ in accordance with reference [148].

Model independent Hubble measurements: As a complementary probe, we include Hubble rate measurements obtained via the cosmic chronometer method [157]. These determinations are largely model independent and provide valuable information on the expansion history at intermediate redshifts. The cosmic chronometer approach exploits the fact that the differential age evolution of passively evolving galaxies can be used to estimate the Hubble parameter directly [158]. By measuring the age difference Δt between galaxy populations separated by a small redshift interval Δz, one obtains an estimate for the expansion rate via $H(z) \approx -(1/(1+z))(\Delta z/\Delta t)$. The method relies on selecting massive, early-type galaxies that have undergone minimal star formation since their formation epoch. These systems evolve passively and can thus be treated as "cosmic clocks", enabling a direct inference of $H(z)$ without assuming a specific cosmological model [159]. Since only the covariance matrix of Moresco et al. is available [160] and the corresponding subset dominates the correlations, we neglect inter-correlations among the remaining measurements.

As already stated in the introduction to this chapter, the present subsection focuses exclusively on late-universe observables, and early-universe data such as CMB temperature, polarization, and lensing measurements are not considered at this stage. All

datasets are fitted simultaneously, with only one supernovae sample included at a time. The inclusion of Hubble rate measurements helps to break degeneracies that arise in BAO and supernovae-only analyses.
To evaluate how well the theoretical models, namely CKN and νCKN, reproduce the observational data, we perform a standard χ^2 minimization. The total test statistic is defined as

$$\chi^2 = \left(\vec{O}_{\rm th}\left(\xi_i\right) - \vec{O}_{\rm exp}\right)^T C^{-1} \left(\vec{O}_{\rm th}\left(\xi_i\right) - \vec{O}_{\rm exp}\right), \tag{3.16}$$

where $\vec{O}_{\rm th}$ denotes the vector of theoretical predictions evaluated at model parameters ξ_i, and $\vec{O}_{\rm exp}$ contains the corresponding measurements, with covariance matrix C, which incorporates both statistical and systematic uncertainties provided by the respective datasets. This expression does not yet account for the analytical marginalization performed over the parameter $\tilde{M}$ in the DESY5 and Pantheon+ likelihoods; for technical details see [148, 161]. Despite the Bayesian origin of the data, the use of a frequentist χ^2 approach is justified by the approximately Gaussian nature of the reported uncertainties and the near-linear dependence of observables on the model parameters in the region of interest. Uncertainties on the fit parameters are estimated from the inverse Hessian evaluated at the best-fit point. We also compute Confidence Level (CL) contours by projecting the χ^2 onto subspaces of interest, profiling over all remaining parameters. The numerical minimization and likelihood profiling are implemented in `Mathematica` [162], using a differential evolution algorithm for global optimization. To asses the relative performance of CKN models against other cosmological models like ΛCDM, ωCDM and $\omega_0\omega_a$CDM, we compute the difference in the best-fit χ^2 values:

$$\Delta\chi^2 = \chi^{2,(\nu)\rm CKN}_{\rm min} - \chi^{2,\rm alt.model}_{\rm min}. \tag{3.17}$$

Assuming Wilks' theorem applies [163], $\Delta\chi^2$ approximately follows a χ^2 distribution with DOFs equal to the difference in the number of model parameters, allowing the conversion to significance levels in terms of standard deviations. However, since Wilks' theorem only holds for nested models, such a conversion is only valid when comparing νCKN and ΛCDM. In particular, models such as $\omega_0\omega_a$CDM and νCKN differ not only in parameter number but also in functional form, making them non-nested. For comparisons involving non-nested models, we employ the Akaike Information Criterion (AIC) as an alternative metric for model selection [164]. The AIC provides a more general framework for comparing non-nested models by balancing goodness of fit against model complexity as it penalizes the latter. It is defined as

$$\mathrm{AIC} = \chi^2_{\rm min} + 2k, \tag{3.18}$$

where k is the total number of free parameters in the model.

3.1.2 Results

Table 3.1 and 3.2 summarize the best-fit parameters for the CKN and νCKN models when fitted to DESI BAO DR2 and Hubble data, combined either with the DESY5 or the Pantheon+ supernovae sample. The individual contributions to the total χ^2 for DR2 from each dataset are listed in table 3.3. The resulting $\chi^2_{\rm min}$/DOF values, approximately 0.89 for DESY5 and 0.88 for Pantheon+, indicate good overall agreement between both models and the data. Figure 3.3 displays the angle-averaged distance ratio $D_{\rm V}/\left(r_{\rm d}z^{2/3}\right)$

Table 3.1: Best-fit values for the CKN and νCKN models using the DESI BAO DR2 and Hubble data, combined with either DESY5 or Pantheon+ data. The table lists Hubble-today H_0, the matter density parameter $\Omega_{\rm M}^0$ and the sound horizon at the drag epoch $r_{\rm d}$.

Model/Datasets	H_0/(km/s/Mpc)	$\Omega_{\rm M}^0$	$r_{\rm d}$/Mpc
CKN			
+ DESY5	68.83 ± 2.35	0.352 ± 0.009	144.27 ± 4.85
+ Pantheon+	69.09 ± 2.36	0.347 ± 0.009	144.23 ± 4.85
νCKN			
+ DESY5	68.90 ± 2.38	0.348 ± 0.018	144.26 ± 4.85
+ Pantheon+	69.46 ± 2.40	0.330 ± 0.018	144.21 ± 4.85

Table 3.2: Best-fit values for the CKN and νCKN models using the DESI BAO DR2 and Hubble data, combined with either DESY5 or Pantheon+ data. The table lists the parameter ν and the corresponding minimum $\chi^2_{\rm min}$ per DOF.

Model/Datasets	ν	$\chi^2_{\rm min}$/DOF
CKN		
+ DESY5	–	1674/1871
+ Pantheon+	–	1437/1632
νCKN		
+ DESY5	0.92 ± 0.35	1674/1870
+ Pantheon+	0.64 ± 0.36	1436/1631

Table 3.3: Breakdown of the total χ^2 values for DESI BAO DR2, showing the contributions from the BAO, Hubble, and either DESY5 or Pantheon+ data.

Models	DESY5			Pantheon+		
	$\chi^{2,\rm BAO}_{\rm min}$	$\chi^{2,\rm DESY5}_{\rm min}$	$\chi^{2,\rm Hubble}_{\rm min}$	$\chi^{2,\rm BAO}_{\rm min}$	$\chi^{2,\rm Pantheon+}_{\rm min}$	$\chi^{2,\rm Hubble}_{\rm min}$
CKN	11.51	1649	12.81	11.45	1413	12.71
νCKN	11.23	1649	12.79	10.25	1413	12.64

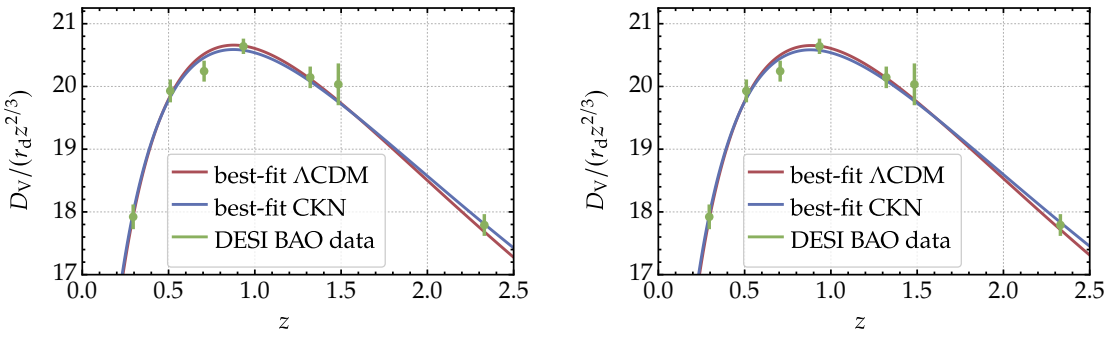

(**a**) Using DESY5

(**b**) Using Pantheon+

Figure 3.3: Angle-averaged distance measure $D_V/(r_d z^{2/3})$ at the best-fit point, compared to DESI data (green) [135], for both the ΛCDM model (red) and the CKN models (blue). Left: using DESY5; right: using Panthon+. The curves for CKN and νCKN are visually indistinguishable.

at the respective best-fit points, compared with the DESI DR2 measurements. Since the CKN and the νCKN predictions are nearly indistinguishable in this observable, only the CKN case is shown. A quantitative comparison of CKN and νCKN with ΛCDM, ωCDM and $\omega_0\omega_a$CDM for DESI BAO DR2 is presented in table 3.4. Differences in χ^2 and in the AIC are provided for both dataset combinations. All alternative models are fitted for DESI BAO DR2 using the same methodology, and the results, shown in table 3.5 and 3.6 are consistent with previous studies [5]. From the $\Delta\chi^2$ values, both CKN and νCKN outperform ΛCDM in terms of fit quality for both dataset combinations. However, for the Pantheon+ data, this improvement is not statistically significant, with the νCKN case corresponding to a marginal significance of -1.75σ. For DESY5, ωCDM and $\omega_0\omega_a$CDM perform slightly better, but the νCKN model still shows a 2.63σ preference over ΛCDM. Interestingly, in the Pantheon+ case, CKN yields an AIC comparable to ωCDM, which has the lowest AIC among all tested models, with the largest difference observed relative to ΛCDM.

Furthermore, the best-fit results presented here allow for a direct comparison between the current DESI DR2 analysis and the previous DR1-based fits, summarized in table 3.7. The overall trend clearly favors models with a time-evolving dark energy component over the standard ΛCDM scenario. This tendency is also reflected in the νCKN framework. For the Pantheon+ dataset in particular, the νCKN model exhibits a more pronounced improvement in the fit between DR1 and DR2 than the standard CKN model. The redshift evolution of the dark energy density $\rho_{DE}(z)$ for the CKN and the νCKN models is compared to that of the alternative models in figures 3.4 and 3.5, respectively. All densities are normalized to the critical density $\rho_{crit}(z)$. Across all scenarios, the qualitative behavior is similar. Lastly, we show the comparison of parameter correlations between DESI BAO DR1 and DR2. The parameter correlations for the CKN model are shown in figure 3.6 for the DESY5 and in figure 3.7 for the Panthon+ dataset. We show the two-dimensional CL for the pairs Ω_M^0–H_0, H_0–r_d, and Ω_M^0–r_d. We also show the comparison between the parameter correlations between DESI BAO DR1 and DR2 for the νCKN model in figure 3.8 for the DESY5 and in figure 3.9 for the Panthon+ dataset. There, we show the correlations with the ν parameter. The observed shrinking of the confidence regions in the correlation plots aligns well with expectations, as increasing

Table 3.4: Relative performance of CKN and νCKN compared to alternative cosmological models for DESI BAO DR2. Shown are the differences in χ^2 and AIC. Negative values indicate a statistical preference of (ν)CKN.

Models	$\Delta\chi^2_{\text{DESY5}}$	$\Delta\text{AIC}_{\text{DESY5}}$	$\Delta\chi^2_{\text{Pantheon+}}$	$\Delta\text{AIC}_{\text{Pantheon+}}$
CKN with				
ΛCDM	-6.90	-6.90	-2.05	-2.05
ωCDM	3.14	1.14	2.26	0.26
$\omega_0\omega_a$CDM	5.74	1.74	2.43	-1.57
νCKN with				
ΛCDM	-6.94	-4.94	-3.07	-1.07
ωCDM	3.09	3.09	1.24	1.24
$\omega_0\omega_a$CDM	5.69	3.69	1.41	-0.59

Table 3.5: Best-fit parameters for the alternative cosmological models ΛCDM, ωCDM and $\omega_0\omega_a$CDM using DESI BAO DR2 and Hubble data combined with DESY5 or Pantheon+. Shown are the results for Hubble-today H_0, the matter density parameter Ω^0_{M}, the sound horizon at the drag epoch r_{d} and the parameter ω_0.

Model /Datasets	H_0 in km/s/Mpc	Ω^0_{M}	r_{d} in Mpc	ω or ω_0
ΛCDM				
+ DESY5	69.77 ± 2.38	0.309 ± 0.008	144.28 ± 4.85	–
+ Pantheon+	70.10 ± 2.39	0.303 ± 0.008	144.21 ± 4.85	–
ωCDM				
+ DESY5	68.71 ± 2.37	0.297 ± 0.009	144.11 ± 4.85	-0.88 ± 0.04
+ Pantheon+	69.32 ± 2.40	0.297 ± 0.008	144.10 ± 4.85	-0.92 ± 0.04
$\omega_0\omega_a$CDM				
+ DESY5	68.69 ± 2.50	0.321 ± 0.013	143.70 ± 5.01	-0.78 ± 0.07
+ Pantheon+	69.49 ± 2.28	0.302 ± 0.017	143.60 ± 4.58	-0.91 ± 0.06

Table 3.6: Best-fit parameters for the alternative cosmological models ΛCDM, ωCDM and $\omega_0\omega_a$CDM using DESI BAO DR2 and Hubble data combined with DESY5 or Pantheon+. Shown are the results for the parameter ω_a, and the corresponding minimal $\chi^2_{\rm min}$/DOF.

Model /Datasets	ω_a	$\chi^2_{\rm min}$/DOF
ΛCDM		
+ DESY5	–	1681/1871
+ Pantheon+	–	1439/1632
ωCDM		
+ DESY5	–	1670/1870
+ Pantheon+	–	1435/1631
$\omega_0\omega_a$CDM		
+ DESY5	-0.77 ± 0.39	1668/1869
+ Pantheon+	-0.11 ± 0.43	1434/1630

Table 3.7: Comparison of the minimum $\chi^2_{\rm min}$ values obtained from fits to DESI BAO DR1 and DR2 $\Delta\chi^2_{\rm DR2-DR1}$, each combined with Hubble rate measurements and either DESY5 or Pantheon+ supernovae dataset, across the different cosmological models considered in this work. We also show the change in the difference between the $\chi^2_{\rm min}$ values of the different models and the $\chi^2_{\rm min}$ of the ΛCDM model $(\Delta\chi^2)^{\Lambda\rm CDM}$ between the two data releases DR1 and DR2.

Models	$\Delta\chi^2_{\rm DR2-DR1}$		$(\Delta\chi^2)^{\Lambda\rm CDM}_{\rm DR2} - (\Delta\chi^2)^{\Lambda\rm CDM}_{\rm DR1}$	
	DESY5	Pantheon+	DESY5	Pantheon+
CKN	-2.85	-2.84	-2.34	-0.90
νCKN	-2.91	-3.76	-2.39	-1.83
ΛCDM	-0.52	-1.93	–	–
ωCDM	-3.72	-3.59	-3.20	-1.66
$\omega_0\omega_a$CDM	-3.29	-3.13	-2.77	-1.20

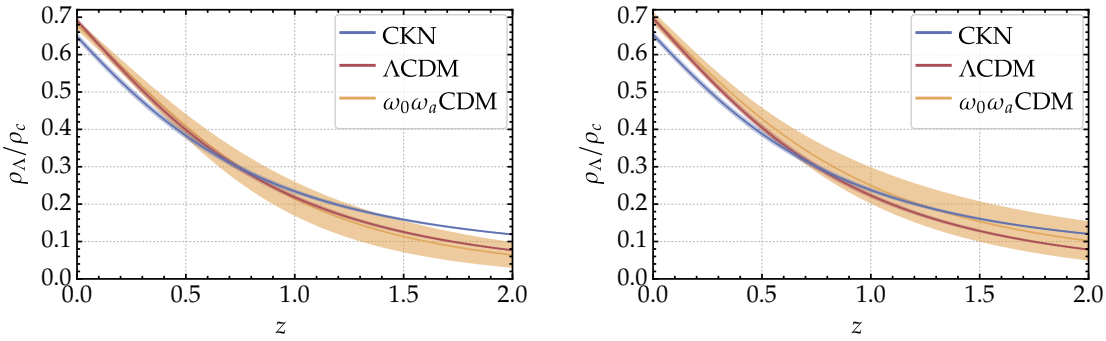

(**a**) Using DESY5 (**b**) Using Pantheon+

Figure 3.4: Evolution of the dark energy density $\rho_{\rm DE}$, normalized to $\rho_{\rm crit}(z)$, for the CKN model and alternative models, fitted to the DESI BAO + Hubble + DESY5 (left) and Pantheon+ (right) datasets.

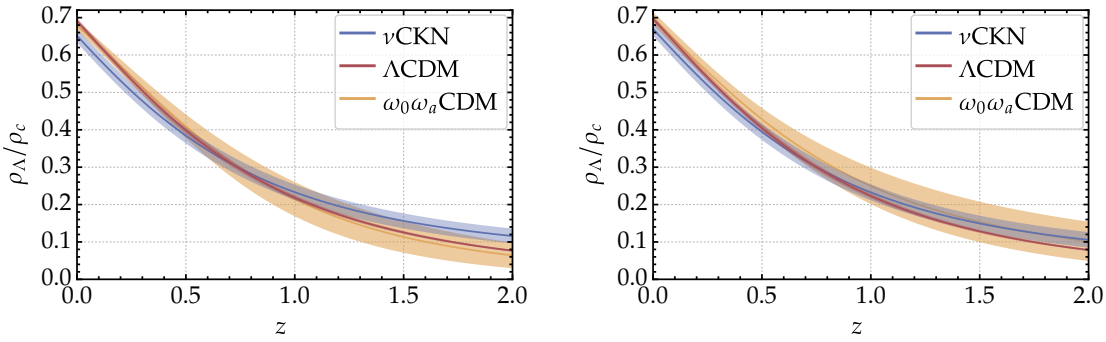

(**a**) Using DESY5 (**b**) Using Pantheon+

Figure 3.5: Same as figure 3.4, but for the νCKN model.

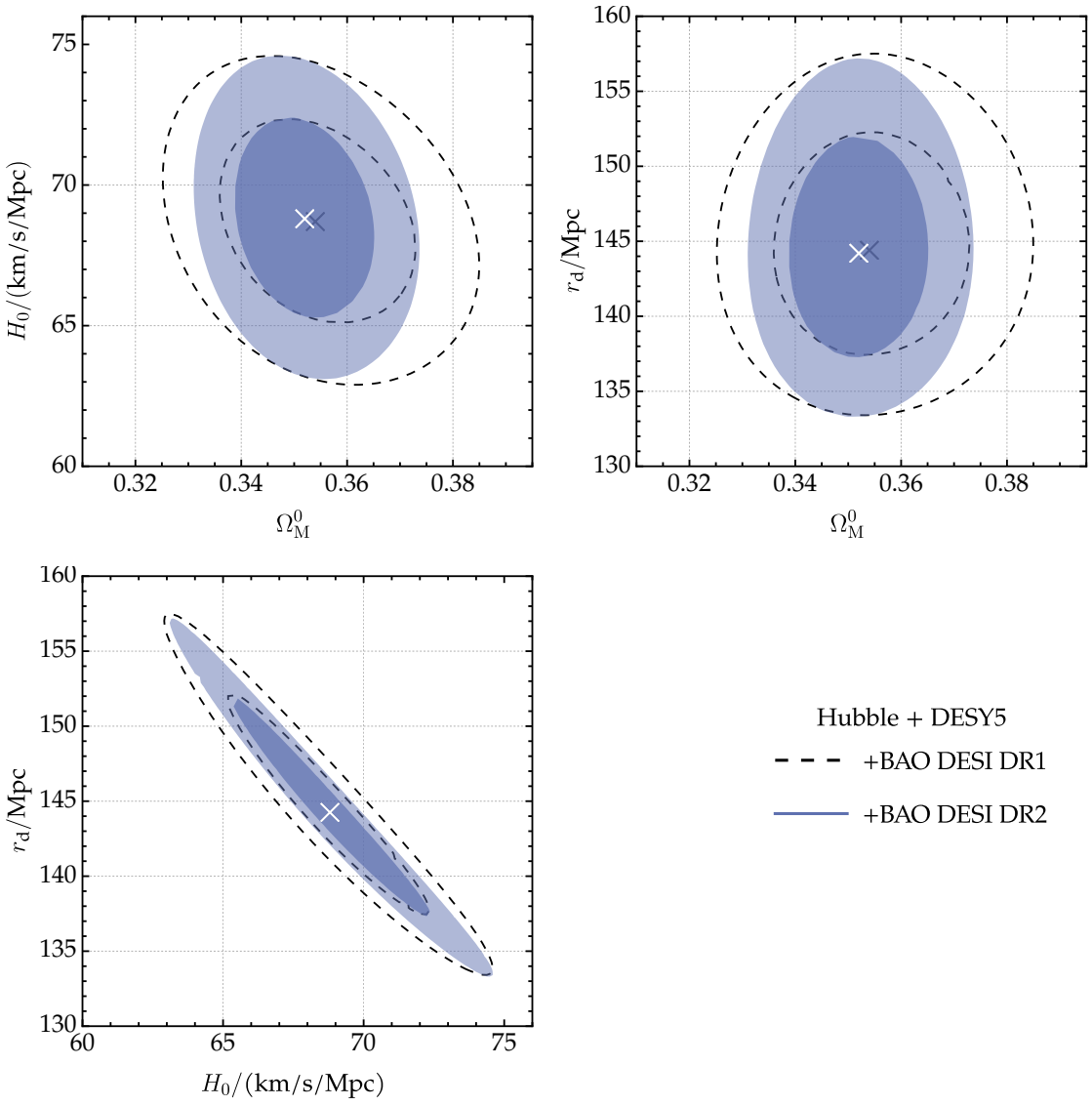

Figure 3.6: Correlations of Ω_M^0–H_0 (top left), Ω_M^0–r_d (top right), H_0–r_d (bottom left) in the CKN model for the DESI BAO+Hubble+DESY5 DR1 (black dashed lines) and DESI BAO+Hubble+DESY5 DR2 (blue area) dataset at the 95 % and 68 % CL.

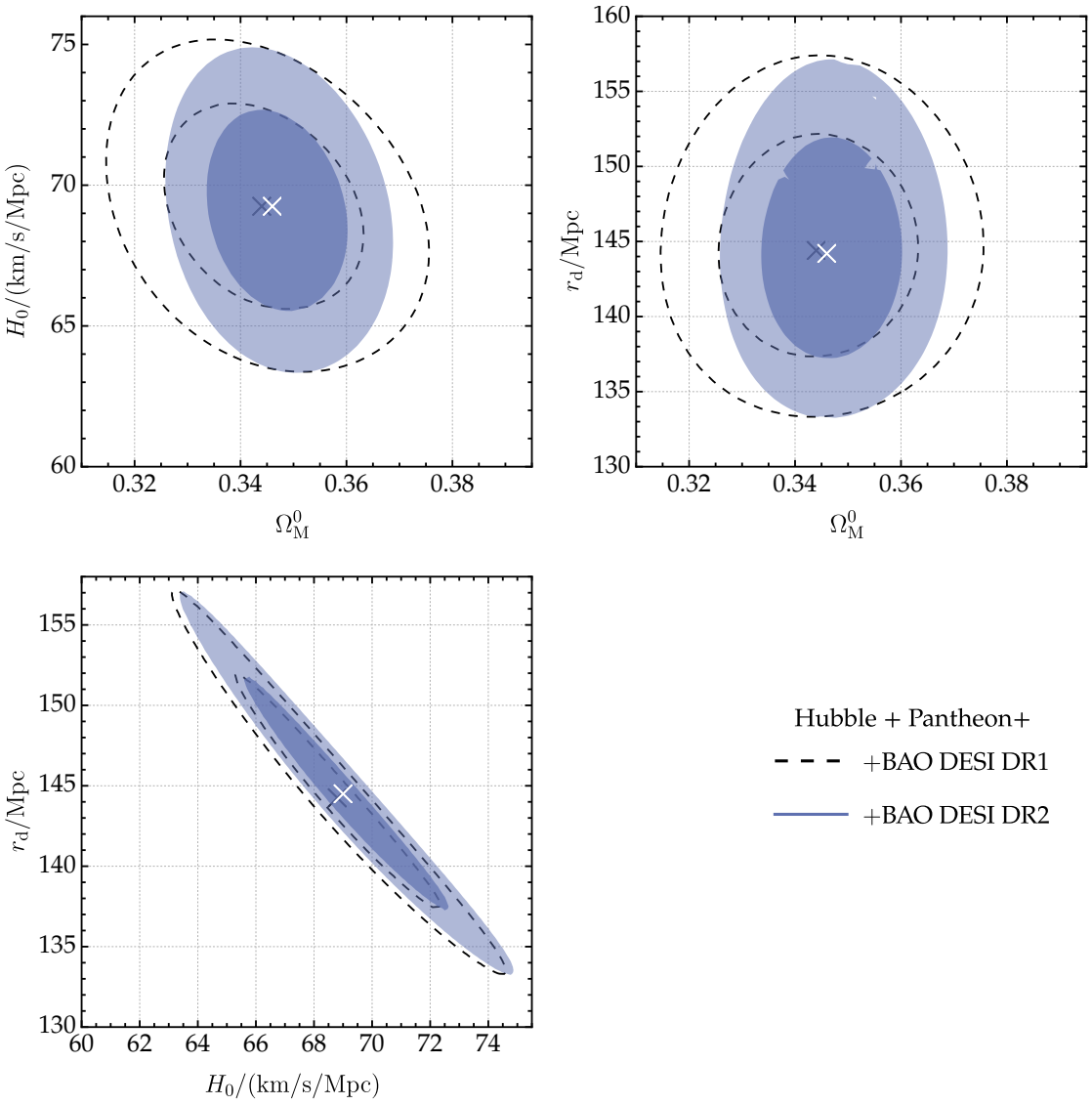

Figure 3.7: Correlations of Ω_M^0–H_0 (top left), Ω_M^0–r_d (top right), H_0–r_d (bottom left) in the CKN model for the DESI BAO+Hubble+Pantheon+ DR1 (black dashed lines) and DESI BAO+Hubble+Pantheon+ DR2 (blue area) dataset at the 95 % and 68 % CL.

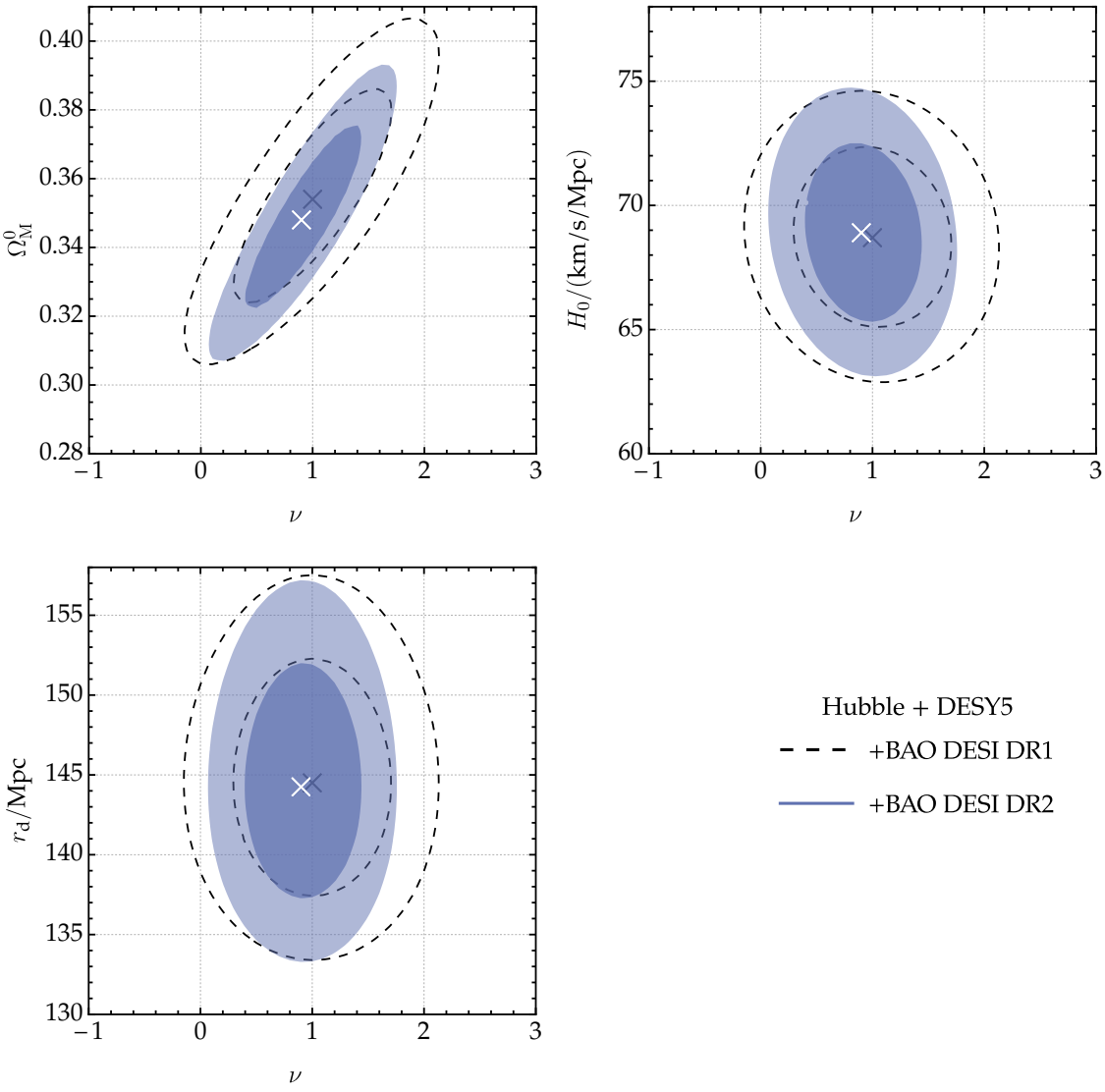

Figure 3.8: Correlations of ν–Ω_M^0 (top left), ν–H_0 (top right), ν–r_d (bottom left) in the νCKN model for the DESI BAO+Hubble+DESY5 DR1 (black dashed lines) and DESI BAO+Hubble+DESY5 DR2 (blue area) dataset at the 95 % and 68 % CL.

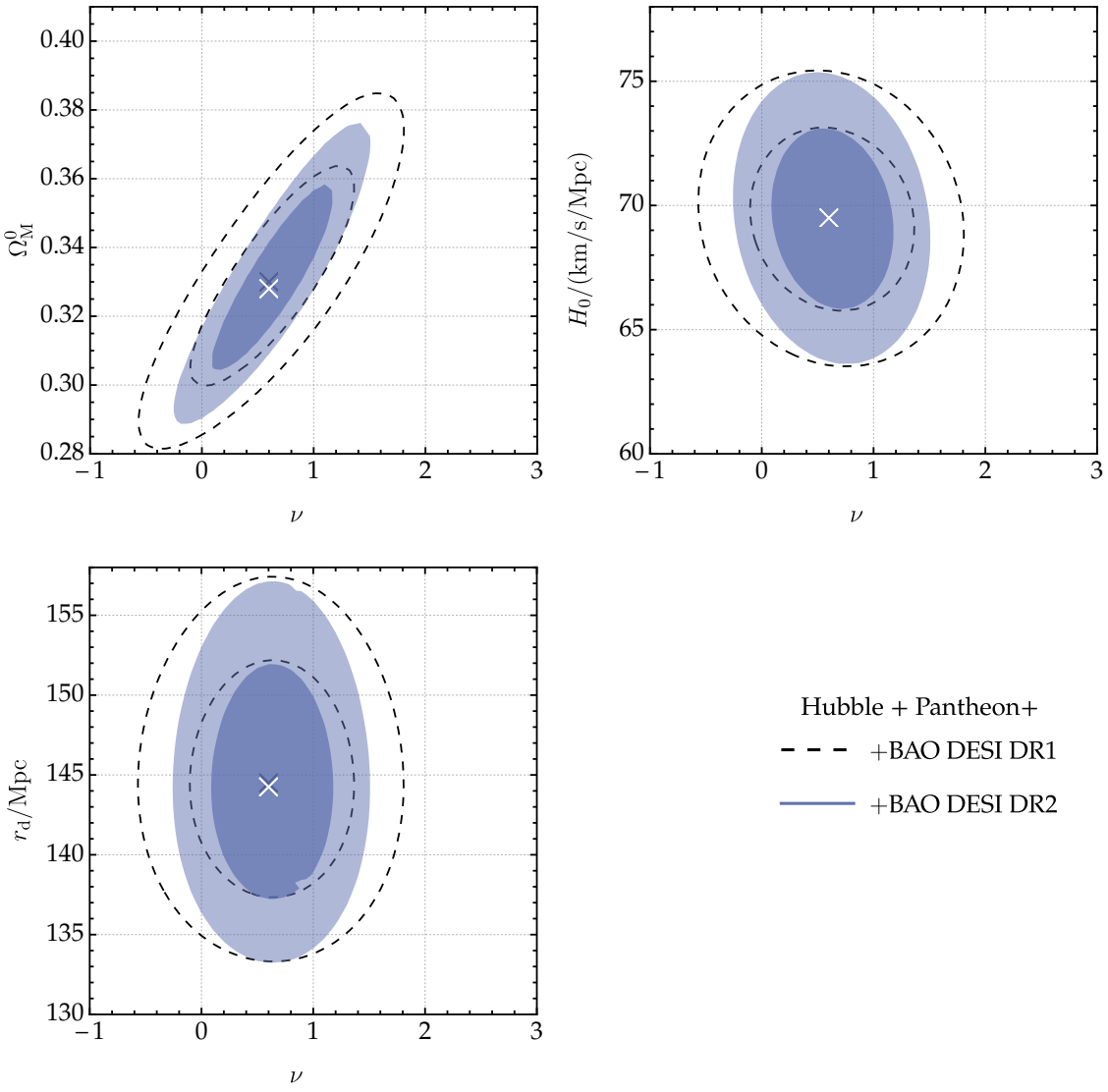

Figure 3.9: Correlations of ν–Ω_M^0 (top left), ν–H_0 (top right), ν–r_d (bottom left) in the νCKN model for the DESI BAO+Hubble+Pantheon+ DR1 (black dashed lines) and DESI BAO+Hubble+Pantheon+ DR2 (blue area) dataset at the 95 % and 68 % CL.

the statistical sample size typically leads to tighter constraints. This trend is particularly interesting and warrants further exploration in light of upcoming observational campaigns. In the coming years, the statistical power of cosmological datasets is expected to increase substantially. The DESI survey will continue operations for approximately two more years [165], while new experiments such as Euclid [166, 167], which began data collection last year, and the Large Synoptic Survey Telescope at the Vera C. Rubin Observatory [168] are set to significantly expand the available data volume. These efforts are anticipated to yield both reduced uncertainties and improved discriminatory power among competing cosmological models. Euclid, in particular, forecasts improvements in parameter uncertainties by up to an order of magnitude [167]. To illustrate the potential impact of these future datasets, we perform a simple projection of the expected χ^2 differences between the (ν)CKN models and alternative cosmological scenarios. For this estimation, we assume that the central values of the observables remain unchanged with respect to DR1, while the uncertainties are reduced. For the DESI BAO measurements, we scale the year-1 uncertainties by a factor of $\sqrt{5}$ to reflect the full five-year survey duration. For the Euclid-based projection, we focus on the anticipated improvements in distance-luminosity measurements and rescale the uncertainties of the DESY5 and Pantheon+ datasets by a conservative factor of 4. This factor is derived from the smallest projected improvement in the parameter uncertainties for the ωCDM model as reported by Euclid [167]. Table 3.8 summarizes the projected $\Delta\chi^2$ values between the (ν)CKN models and the alternatives for three scenarios: DESI-5Y (DESI after five years), Euclid-Unc (uncertainty improvement from Euclid), and the combined projection using both improvements. In table 3.9 we show the reinterpretation of the $\Delta\chi^2$ values in terms of significance for the nested models. As can be seen, assuming unchanged central values, the ωCDM and $\omega_0\omega_a$CDM models would be statistically preferred over the (ν)CKN scenarios. However, it is important to emphasize that the central values of future datasets are likely to differ from those used here, which could change the outcome of such comparisons. Thus, these projections should not be interpreted as predictions about the true cosmological model but rather as indicative uncertainties suggests a potentially strong capability to distinguish ΛCDM from time-varying dark energy models.

To summarize this first part, we have investigated the cosmological implications of the CKN bound, which encodes a gravitational constraint on the validity of QFT, by performing an analysis based on the latest cosmological late-universe data. Specifically, we have analyzed data from the DESI BAO DR1 and DR2 releases in combination with Hubble parameter measurements and one of two supernovae datasets: DESY5 or Pantheon+. To account for unknown prefactors in the original CKN relation and to include broader classes of models in which the dark energy scales with H^2, we extend the CKN scenario to the νCKN model. We find that both the CKN and νCKN models provided good fits to the data, with the CKN model generally performing slightly better when taking into consideration the DOFs of the models under comparison. In particular, for the Pantheon+ dataset, the CKN model outperforms most other cosmological models considered in this section, including ΛCDM, and $\omega_0\omega_a$CDM. Although the νCKN model introduces an additional free parameter, it does not improve the fit substantially over the original CKN model. The results also confirm and strengthen previous findings from DR1: models with a time-dependent dark energy component are preferred over ΛCDM. This trend is visible in the CKN models as well and becomes more pronounced in the transition from DR1 to DR2, particularly for the νCKN scenario combined with Pantheon+ data. The impact of increased statistics is clearly seen in the correlation plots, where confidence

Table 3.8: Projected χ^2 differences between the CKN and νCKN models and the alternative cosmological models considered in this work, based on two future scenarios: DESI-5Y (DESI after five years of data collection) and Euclid-Unc (the expected reduction in uncertainties of distance-luminosity measurements from Euclid). Results are shown for both the DESY5 and Pantheon+ datasets.

Models	DESI-5Y		Euclid-Unc		DESI-5Y + Euclid-Unc	
	$\Delta\chi^2_{\text{DESY5}}$	$\Delta\chi^2_{\text{Pantheon+}}$	$\Delta\chi^2_{\text{DESY5}}$	$\Delta\chi^2_{\text{Pantheon+}}$	$\Delta\chi^2_{\text{DESY5}}$	$\Delta\chi^2_{\text{Pantheon+}}$
CKN with						
ΛCDM	-1.8	3.9	-16.5	-9.4	-42.4	-17.4
ωCDM	7.1	7.4	14.9	1.5	20.4	7.1
$\omega_0\omega_a$CDM	18.4	11.1	47.0	1.5	45.4	8.1
νCKN with						
ΛCDM	-3.7	-1.0	-18.1	-9.4	-43.2	-19.0
ωCDM	5.1	2.5	13.3	1.5	19.6	5.5
$\omega_0\omega_a$CDM	16.4	6.2	45.4	1.5	44.6	6.5

Table 3.9: Future projection of the DESI experiment after five years of data (DESI-5Y) and the expected improvement from the Euclid experiment. The χ^2_{min} differences between the νCKN and the ΛCDM models, shown in table 3.8, are translated into corresponding significance levels Σ.

Models	DESI-5Y		Euclid-Unc		DESI-5Y + Euclid-Unc	
	Σ_{DESY5}	$\Sigma_{\text{Pantheon+}}$	Σ_{DESY5}	$\Sigma_{\text{Pantheon+}}$	Σ_{DESY5}	$\Sigma_{\text{Pantheon+}}$
νCKN with						
ΛCDM	-1.9σ	-1.0σ	-4.3σ	-3.1σ	-6.6σ	-4.4σ

regions shrink, as expected. This behavior reflects the growing constraining power of current and upcoming datasets. Encouragingly, the observed shift in the data releases suggests a future in which the nature of dark energy might be revealed with greater clarity. To illustrate the potential of near-future measurements, we perform a simplified forecast for the model discrimination power achievable by the final DESI dataset and upcoming Euclid observations. Assuming central values remain unchanged with respect to DR1, we estimate that a statistical separation between νCKN and ΛCDM at a level of up to 6.6σ could be achieved. While such projections should not be interpreted as predictions of which model is ultimately correct, they do highlight the discriminating power of future data. Given the promising performance of the CKN model and its physical motivation rooted in gravitational arguments, these findings strongly motivate further study. A next step will be to confront the (ν)CKN scenarios with additional datasets, such as CMB power spectra and weak lensing data. This is the focus of the following section.

3.2 Perturbations and Global Analysis

In this section, we extend the analysis of the previous model, characterized by equation (3.12) and a dark energy density defined as

$$\rho_{\mathrm{DE}} = \Lambda_0 + \nu \frac{M_{\mathrm{Pl}} H^2}{16\pi^2}\,, \tag{3.19}$$

by incorporating early-universe data. Once the early universe is taken into account, several assumptions must be revised: radiation can no longer be neglected, and the interaction between dark energy and both DM and baryonic matter needs to be specified. Consequently, additional assumptions are required to properly describe these interactions.

From equation (3.12) we know that dark energy must couple to matter, either to baryons or to DM. A coupling to baryons, however, is strongly constrained, as it would directly affect Big Bang Nucleosynthesis (BBN). In contrast, the DM sector is far less constrained, making it a natural candidate for such interactions. Exploring a possible dark energy–DM coupling can therefore provide valuable insights, and, given our limited knowledge of DM, it would be premature to exclude such a possibility. Alternative models incorporating a coupling between dark energy and photons are subject to strong observational constraints, since it would directly modify the CMB. Another conceivable option is a coupling to neutrinos, which has been studied in the literature, see, e.g., references [169, 170]. In the present work, we focus on the case of a dark energy–DM interaction.

With these assumptions, the background equations for baryons and radiation remain unchanged with respect to the standard ΛCDM model, cf. section 2.4 or reference [112]. Since we allow for an interaction between dark energy and DM, however, these components are no longer separately conserved. Instead, the covariant derivative of the temporal component of the energy–momentum tensor, $T^{\mu}{}_{0}$, acquires a source term $\bar{Q}$. As the total energy–momentum tensor must still be conserved, the source term for dark energy and DM differ only by a relative sign:

$$\dot{\bar{\rho}}_{\mathrm{DM}} + 3H\bar{\rho}_{\mathrm{DM}} = -\bar{Q}\,, \tag{3.20}$$

$$\dot{\bar{\rho}}_{\mathrm{DE}} = \bar{Q}\,. \tag{3.21}$$

Here, barred quantities denote unperturbed background values, and the dot indicates differentiation with respect to proper time. The background evolution can then be obtained by combining the sum of these two equations with the Friedmann equation,

$$H^2 = \frac{8\pi G}{3}\left(\bar{\rho}_\mathrm{R} + \bar{\rho}_\mathrm{B} + \bar{\rho}_\mathrm{DM} + \bar{\rho}_\mathrm{DE}\right), \tag{3.22}$$

which leads to

$$\bar{\rho}_\mathrm{DE} = \frac{\nu - 6\pi\rho^0_\mathrm{DE}}{\nu - 6\pi} + \nu\frac{(\nu-6\pi)\,\rho^0_\mathrm{R} - a^{1+\frac{\nu}{2\pi}}\left(6\pi\left(\rho^0_\mathrm{B}+\rho^0_\mathrm{DM}\right) + \nu\left(3\rho^0_\mathrm{B} + 3\rho^0_\mathrm{DM} + 4\rho^0_\mathrm{R}\right)\right)}{3a^4\,(\nu-6\pi)\,(\nu+2\pi)}, \tag{3.23}$$

$$\bar{\rho}_\mathrm{DM} = \frac{-3a\,(\nu+2\pi)\,\rho^0_\mathrm{B} - 4\nu\rho^0_\mathrm{R} + a^{1+\frac{\nu}{2\pi}}\left(6\pi\left(\rho^0_\mathrm{B}+\rho^0_\mathrm{DM}\right) + \nu\left(3\rho^0_\mathrm{B} + 3\rho^0_\mathrm{DM} + 4\rho^0_\mathrm{R}\right)\right)}{3a^4\,(\nu+2\pi)}, \tag{3.24}$$

where the superscript zero denotes the values of the quantities today. The anisotropies in the CMB and the growth of the Large Scale Structure (LSS) originate from perturbations to these background quantities. It is therefore necessary to derive the corresponding perturbed equations.
Following the standard treatment in the literature [112, 171] and in analogy to equation (2.93) in section 2.4, we parametrize the perturbations of the metric $g_{\mu\nu}$ and of the energy–momentum tensor $T_{\mu\nu}$ as

$$g_{\mu\nu} = \bar{g}_{\mu\nu} + \delta g_{\mu\nu}(t,x)\,, \qquad T_{\mu\nu} = \bar{T}_{\mu\nu} + \delta T_{\mu\nu}(t,x)\,. \tag{3.25}$$

Here, the symbol δ denotes the perturbation to the corresponding quantities. The background metric $\bar{g}_{\mu\nu}$ refers to the spatially flat FLRW metric, which, upon including perturbations, takes the form given in equation (2.94). The perturbations of the energy–momentum tensor are specified in equation (2.107)–(2.109).
The linearized Einstein equations, together with the covariant conservation of the energy–momentum tensor, lead to a coupled system of differential equations for the perturbed quantities. In order to formulate these equations, it is necessary to provide a covariant parametrization of the background interaction term $\bar{Q}$ between dark energy and DM. The most general covariant form is given by [171, 172]

$$Q^\mu = \left(\bar{Q} + \delta Q\right)u^\mu + F^\mu\,. \tag{3.26}$$

Here, the total energy–momentum transfer is decomposed into a component parallel $\left(\bar{Q}+\delta Q\right)$ and a component orthogonal F^μ to its total four-velocity u^μ. This introduces two new quantities into the system, namely δQ and F^μ. In the following, we set $F^\mu = 0$ in order to construct a minimal model and to ensure that no momentum transfer occurs among the unperturbed background quantities. Otherwise, a preferred spatial direction would be induced, which would violate the observed isotropy of the CMB at the background level.
Recall that $\bar{Q}$ is uniquely determined by our background model and is given by

$$\bar{Q} = \dot{\bar{\rho}}_\mathrm{DE} = \frac{\nu M^2_\mathrm{Pl}\dot{H}H}{8\pi^2}\,. \tag{3.27}$$

The remaining unknown is therefore the perturbation of the background energy transfer, δQ, which we parametrize phenomenologically. A natural choice is to assume that the

dark energy is not perturbed, i.e., $\delta\rho_{\mathrm{DE}} = 0$, motivated by the fact that we consider dark energy to be the sum of the cosmological constant and the Lorentz invariant contribution of vacuum energy in QFT. However, since the fundamental theory underlying the interaction between dark energy and DM remains unknown, the possibility of perturbations in the dark energy density cannot be excluded. In the simplest case, this would correspond to setting $\delta Q = 0$. Another intuitive choice is to relate the perturbations directly to the background transfer rate, $\delta Q \propto \delta\dot{\rho}_{\mathrm{DE}}$, given that $\bar{Q} \propto \dot{\rho}_{\mathrm{DE}}$[1]. In the following, we will concentrate on the first scenario, namely the case where dark energy is assumed to remain unperturbed, $\delta\rho_{\mathrm{DE}} = 0$.
To avoid gauge artifacts and to consistently analyze the behavior of the perturbations, we derive the perturbation equations analogously to subsection 2.4.2 but in a gauge-invariant form [114, 171, 172]:

$$\Delta'_{\mathrm{DM}} = -\Delta_{\mathrm{DM}}\frac{\bar{\rho}'_{\mathrm{DM}}}{\bar{\rho}_{\mathrm{DM}}} - 3\mathcal{H}\Delta_{\mathrm{DM}} - kV_{\mathrm{DM}}\,, \tag{3.28}$$

$$V'_{\mathrm{DM}} = -\frac{V_{\mathrm{DM}}}{\bar{\rho}_{\mathrm{DM}}}\left(\bar{\rho}'_{\mathrm{DM}} + 4\mathcal{H}\bar{\rho}_{\mathrm{DM}}\right) + k\psi - \frac{\bar{\rho}'_{\mathrm{DE}}}{\bar{\rho}_{\mathrm{DM}}}k\mathcal{H}^{-1}\phi\,, \tag{3.29}$$

where the metric potentials in gauge-invariant form are given as

$$\psi = \Psi + \mathcal{H}\left(B - E'\right) + \left(B - E'\right)'\,, \tag{3.30}$$

$$\phi = \Phi - \frac{1}{3}k^2E + \mathcal{H}\left(B - E'\right)\,, \tag{3.31}$$

with the metric potentials Ψ and Φ from subsection 2.4.2. Further, Δ_{DM} denotes the gauge-invariant density contrast, defined as

$$\Delta_{\mathrm{DM}} = \delta_{\mathrm{DM}} + \mathcal{H}^{-1}\frac{\bar{\rho}'_{\mathrm{DM}}}{\bar{\rho}_{\mathrm{DM}}}\left(\Phi - \frac{1}{3}k^2E\right)\,. \tag{3.32}$$

The conformal Hubble parameter is given by $\mathcal{H} = a'/a$, where the prime denotes differentiation with respect to conformal time, and V_{DM} is defined as

$$V_{\mathrm{DM}} = k^{-1}\Theta_{\mathrm{DM}} + k\left(B - E'\right)\,. \tag{3.33}$$

Note, that we already performed the transformation into Fourier space, where these quantities are related to the ones introduced in subsection 2.4.2 through

$$\partial_i \to ik_i\,, \qquad\qquad v_{\mathrm{DM}i} \to -i\frac{k_i}{k}\frac{\Theta_{\mathrm{DM}}}{k}\,, \tag{3.34}$$

with the Fourier transformed velocity divergence Θ_{DM}. All remaining equations coincide with those from the standard ΛCDM model. It is well established in the literature that models with interactions between dark energy and DM can exhibit instabilities in the early universe [172, 173]. In order to rule out such pathological behavior, we perform an initial-conditions analysis in the following section.

[1]Note, for a covariant description one of course has to take into account the correct transformation property of the perturbation.

3.2.1 Early- and Late-Universe Behavior

In this subsection, we examine the behavior of both perturbations and background quantities of our model in the early and late universe. It is well known that large-scale instabilities can arise in the early universe, and we investigate the conditions under which such instabilities may occur. Moreover, the description of density perturbations at early times requires the specification of initial conditions. A common choice are adiabatic initial conditions, which imply that all species evolve in a correlated manner [172]:

$$S_{AB} = -3\mathcal{H}\frac{\rho_A}{\rho_A'}\Delta_A + 3\mathcal{H}\frac{\rho_B}{\rho_B'}\Delta_B\,, \tag{3.35}$$

with $A, B = \gamma, \nu$, DM, b, and possibly DE, and the requirement that the gauge invariant entropy perturbation vanishes, i.e., $S_{AB} = 0$. The motivation for adopting adiabatic initial conditions is twofold. On the theoretical side, models of inflation provide a natural explanation: a single scalar field, referred to as the inflaton, drives the accelerated expansion, and upon its decay, all particle species are produced from the same source [95, 96]. Consequently, their primordial fluctuations share a common origin and are expected to evolve in the same way. On the observational side, the structures observed in the CMB are in excellent agreement with adiabatic initial conditions [174]. In view of this compelling theoretical and observational evidence, we want to be able to impose adiabatic initial conditions in our model as well.
In order to investigate the precise behavior of our model, we expand the perturbation equations (3.28) and (3.29) together with all additional equations corresponding to those of ΛCDM for early times [112, 172], i.e., in the limit of small $k\tau$. The full system of equations before expansion takes the form

$$\frac{\mathrm{d}\Delta_{\mathrm{DM}}}{\mathrm{d}\log(k\tau)} = -k^2\tau^2\tilde{V}_{\mathrm{DM}} - \tau\Delta_{\mathrm{DM}}\left(\mathcal{H} + \frac{\rho_{\mathrm{DM}}'}{\rho_{\mathrm{DM}}}\right), \tag{3.36}$$

$$\frac{\mathrm{d}\tilde{V}_{\mathrm{DM}}}{\mathrm{d}\log(k\tau)} = \psi - \tilde{V}_{\mathrm{DM}} - \frac{\tau}{\rho_{\mathrm{DM}}}\tilde{V}_{\mathrm{DM}}\left(4\mathcal{H}\rho_{\mathrm{DM}} + \rho_{\mathrm{Dm}}'\right) + \frac{\phi\left(3\mathcal{H}\rho_{\mathrm{DM}} - \rho_{\mathrm{DM}}'\right)}{\rho_{\mathrm{DM}}\mathcal{H}}, \tag{3.37}$$

$$\frac{\mathrm{d}\Delta_{\gamma}}{\mathrm{d}\log(k\tau)} = -\frac{4}{3}k^2\tau^2\tilde{V}_{\gamma}\,, \tag{3.38}$$

$$\frac{\mathrm{d}\tilde{V}_{\gamma}}{\mathrm{d}\log(k\tau)} = 2\psi + \frac{1}{4}\Delta_{\gamma} + \Omega_{\nu}\tilde{\Pi}_{\nu} - \tilde{V}\gamma\,, \tag{3.39}$$

$$\frac{\mathrm{d}\Delta_{\mathrm{b}}}{\mathrm{d}\log(k\tau)} = -k^2\tau^2\tilde{V}_{\gamma}\,, \tag{3.40}$$

$$\frac{\mathrm{d}\Delta_{\nu}}{\mathrm{d}\log(k\tau)} = -\frac{4}{3}k^2\tau^2\tilde{V}_{\nu}\,, \tag{3.41}$$

$$\frac{\mathrm{d}\tilde{V}_{\nu}}{\mathrm{d}\log(k\tau)} = 2\psi + \frac{1}{4}\Delta_{\nu} - \frac{1}{6}k^2\tau^2\tilde{\Pi}_{\nu} + \Omega_{\nu}\tilde{\Pi}_{\nu} - \tilde{V}_{\nu}\,, \tag{3.42}$$

$$\frac{\mathrm{d}\tilde{\Pi}_{\nu}}{\mathrm{d}\log(k\tau)} = -2\tilde{\Pi}_{\nu} + \frac{8}{5}\tilde{V}_{\nu}\,, \tag{3.43}$$

with the gauge invariant quantities from equation (3.32) and (3.33), $\tilde{V} = V/(k\tau)$ and $\Omega_{\nu} = \rho_{\nu}/\rho_{\mathrm{tot}}$. Here, the anisotropic stress $\tilde{\Pi} = \Pi/(k\tau)^2$ is related to the anisotropic

stress from subsection 2.4.2 via the following Fourier transformation:

$$\Pi_{ij} \to -p\left(\frac{k_i k_j}{k^2} - \frac{1}{3}\delta_{ij}\right)\Pi\,. \tag{3.44}$$

Note, that in deriving equation (3.37) we replaced ρ_{DE} using the Friedmann equations (3.20) and (3.21). The metric potentials ϕ and ψ are given by the Einstein equations

$$\phi = -\psi - \Omega_\nu \tilde{\Pi}_\nu\,, \tag{3.45}$$

$$\psi = -\frac{\sum_i \Omega_i \left(\Delta_i + 3\left(1+\omega_i\right)\tilde{V}_i\right)}{\sum_i 3\left(1+\omega_i\right)\Omega_i + \frac{2}{3}k^2\tau^2} - \Omega_\nu \tilde{\Pi}_\nu\,, \tag{3.46}$$

where ω is determined by the equation of state and i denotes the matter components. In order to solve this system for early times, all energy densities must be expanded in terms of $k\tau$. For all species that follow standard ΛCDM behavior, this expansion reproduces the well-known early-universe evolution. The only exception is the dark matter component from equation (3.24), which behaves for $\nu \sim O(1)$ in the early universe approximately as

$$\rho_{\mathrm{DM}}(a) \sim -\frac{4}{3\left(\nu + 2\pi\right)}\nu\rho_{\mathrm{R},0}a^{-4}\,. \tag{3.47}$$

This term is taken as the leading contribution in the system of equations. We use $\rho_{\mathrm{tot}} \approx \rho_{\mathrm{R}}$, and expand the remaining quantities accordingly: $\mathcal{H} = 1/\tau$. We rewrite the system of equation into matrix form: $\mathrm{d}u/\mathrm{d}\log k\tau = Au$, where

$$u = \left(\Delta_{\mathrm{DM}}, \tilde{V}_{\mathrm{DM}}, \Delta_\gamma, \tilde{V}_\gamma, \Delta_{\mathrm{b}}, \Delta_\nu, \tilde{V}_\nu, \tilde{\Pi}_\nu\right)^{\mathrm{T}}\,, \tag{3.48}$$

and the resulting matrix A after expansion reads

$$A = \begin{pmatrix}
1 & 0 & 0 & 0 & 0 & 0 & 0 & 0 \\
\varepsilon & -1-3\varepsilon & -2+\frac{1}{8}b & -2+\frac{b}{2} & 0 & -\frac{\Omega_\nu^0}{2} & -2\Omega_\nu^0 & -\Omega_\nu^0 \\
0 & 0 & 0 & 0 & 0 & 0 & 0 & 0 \\
\varepsilon & -3\varepsilon & \frac{1}{4}+\frac{1}{8}b & -3+\frac{b}{2} & 0 & -\frac{\Omega_\nu^0}{2} & -2\Omega_\nu^0 & -\Omega_\nu^0 \\
0 & 0 & 0 & 0 & 0 & 0 & 0 & 0 \\
0 & 0 & 0 & 0 & 0 & 0 & 0 & 0 \\
\varepsilon & -3\varepsilon & -2+\frac{1}{8}b & -2+\frac{b}{2} & 0 & \frac{1}{4}-\frac{1}{2}\Omega_\nu^0 & -1-2\Omega_\nu^0 & -\Omega_\nu^0 \\
0 & 0 & 0 & 0 & 0 & 0 & \frac{8}{5} & -2
\end{pmatrix}\,, \tag{3.49}$$

with

$$\varepsilon = \frac{\nu}{3\pi}\,, \qquad\qquad b = -\nu\frac{2}{\pi} + 4\Omega_\nu^0\,. \tag{3.50}$$

The behavior of the early-universe solution can be determined from the corresponding eigenvalues:

$$\lambda = \mathrm{diag}\left(-1,-1,1,0,0,0,-\frac{5}{2} - \frac{\sqrt{5-32\Omega_\nu^0}}{2\sqrt{5}}, -\frac{5}{2} + \frac{\sqrt{5-32\Omega_\nu^0}}{2\sqrt{5}}\right)\,. \tag{3.51}$$

These values indicate a positive exponential growth of the DM density, which signals an instability in the early universe. This problematic feature originates from the a^{-4} contribution in equation (3.47), and therefore, we must ensure that the corresponding term in this equation does not dominate. For this we expand the energy density $\rho_{\rm DM}$ simultaneously for small ν in the early universe:

$$\rho_{\rm DM}(a) \sim \rho_{\rm DM,0} a^{-3} - \frac{2}{3\pi} \nu \rho_{\rm R,0} a^{-4} \,. \tag{3.52}$$

This requirement constrains the parameter ν to sufficiently small values:

$$\nu < \frac{\rho_{\rm DM,0}}{\rho_{\rm R,0}} a_{\rm ini} \frac{3\pi}{2} \,, \tag{3.53}$$

where $a_{\rm ini}$ denotes the scale factor at the time where we impose the initial conditions. Under this modified behavior, the expanded system takes the form

$$A = \begin{pmatrix}
0 & 0 & 0 & 0 & 0 & 0 & 0 & 0 \\
0 & -2 & -\frac{-1+\Omega^0_{\rm DE}+\Omega^0_\nu}{4\left(-1+\Omega^0_{\rm DE}\right)} & -\frac{-1+\Omega^0_{\rm DE}+\Omega^0_\nu}{-1+\Omega^0_{\rm DE}} & 0 & -\frac{\Omega^0_\nu}{4\left(-1+\Omega^0_{\rm DE}\right)} & -\frac{\Omega^0_\nu}{-1+\Omega^0_{\rm DE}} & -\Omega^0_\nu \\
0 & 0 & 0 & 0 & 0 & 0 & 0 & 0 \\
0 & 0 & -\frac{-1+\Omega^0_{\rm DE}+\Omega^0_\nu}{4\left(-1+\Omega^0_{\rm DE}\right)} & \frac{3-3\Omega^0_{\rm DE}-2\Omega^0_\nu}{-1+\Omega^0_{\rm DE}} & 0 & \frac{\Omega^0_\nu}{-2+2\Omega^0_{\rm DE}} & \frac{2\Omega^0_\nu}{-1+\Omega^0_{\rm DE}} & -\Omega^0_\nu \\
0 & 0 & 0 & 0 & 0 & 0 & 0 & 0 \\
0 & 0 & 0 & 0 & 0 & 0 & 0 & 0 \\
0 & 0 & -\frac{-1+\Omega^0_{\rm DE}+\Omega^0_\nu}{2\left(-1+\Omega^0_{\rm DE}\right)} & \frac{-2+2\Omega^0_{\rm DE}-2\Omega^0_\nu}{-1+\Omega^0_{\rm DE}} & 0 & \frac{-1+\Omega^0_{\rm DE}+2\Omega^0_\nu}{4\left(-1+\Omega^0_{\rm DE}\right)} & \frac{-1-\Omega^0_{\rm DE}+2\Omega^0_\nu}{-1+\Omega^0_{\rm DE}} & -\Omega^0_\nu \\
0 & 0 & 0 & 0 & 0 & 0 & \frac{8}{5} & -2
\end{pmatrix} , \tag{3.54}$$

with eigenvalues given by

$$\lambda = \mathrm{diag}\left(0,0,0,0,-2,-1,-\frac{-25+25\Omega^0_{\rm DE}+c}{10\left(-1+\Omega^0_{\rm DE}\right)}, \frac{25-25\Omega^0_{\rm DE}+c}{10\left(-1+\Omega^0_{\rm DE}\right)}\right) , \tag{3.55}$$

with

$$c = \sqrt{5}\sqrt{-\left(-1+\Omega^0_{\rm DE}\right)^2\left(-5+32\Omega^0_\nu\right)} \,. \tag{3.56}$$

Therefore, the solutions are now well behaved, and the instabilities are avoided as long as ν fulfills equation (3.53). The corresponding eigenvectors are given by

$$\lambda_1 = \left(0, \frac{5}{16} - 4\Omega_\nu^0, \frac{\left(1-\Omega_{\mathrm{DE}}^0\right)\left(15+4\Omega_\nu^0\right)}{4\left(-1+\Omega_{\mathrm{DE}}^0+\Omega_\nu^0\right)}, \frac{-5+\Omega_{\mathrm{DE}}^0\left(5-4\Omega_\nu^0\right)+24\Omega_\nu^0}{16\left(-1+\Omega_{\mathrm{DE}}^0+\Omega_\nu^0\right)}, 0, 0, \frac{5}{4}, 1\right)^T , \tag{3.57}$$

$$\lambda_2 = \left(0, -\frac{1}{16}, \frac{-3+3\Omega_{\mathrm{DE}}^0+4\Omega_\nu^0}{4\left(-1+\Omega_{\mathrm{DE}}^0+\Omega_\nu^0\right)}, \frac{-1+\Omega_{\mathrm{DE}}^0}{16\left(-1+\Omega_{\mathrm{DE}}^0+\Omega_\nu^0\right)}, 0, 1, 0, 0\right)^T , \tag{3.58}$$

$$\lambda_3 = (0,0,0,0,1,0,0,0)^T , \tag{3.59}$$

$$\lambda_4 = (1,0,0,0,0,0,0,0)^T , \tag{3.60}$$

$$\lambda_5 = (0,1,0,0,0,0,0,0)^T , \tag{3.61}$$

$$\lambda_6 = \left(0, -\frac{\Omega_\nu^0}{2}, 0, \frac{\left(9-4\Omega_{\mathrm{DE}}^0\right)\Omega_\nu^0}{8\left(-1+\Omega_{\mathrm{DE}}^0+\Omega_\nu^0\right)}, 0, 0, \frac{5}{8}, 1\right)^T , \tag{3.62}$$

$$\lambda_7 = \left(0, -\frac{5\left(5-16\Omega_\nu^0+\Omega_{\mathrm{DE}}^0\left(-5+16\Omega_\nu^0\right)+c\right)}{8\left(5-5\Omega_{\mathrm{DE}}^0+c\right)}, 0, -d_-, 0, 0, -d_-, 1\right)^T , \tag{3.63}$$

$$\lambda_8 = \left(0, -\frac{5\left(-5+16\Omega_\nu^0+\Omega_{\mathrm{DE}}^0\left(5-16\Omega_\nu^0\right)+c\right)}{8\left(-5+5\Omega_{\mathrm{DE}}^0+c\right)}, 0, d_+, 0, 0, d_+, 1\right)^T \tag{3.64}$$

with

$$d_\pm = \frac{-5+5\Omega_{\mathrm{DE}}^0 \pm c}{-16+16\Omega_{\mathrm{DE}}^0} . \tag{3.65}$$

From these, one observes that an appropriate linear combination allows us to satisfy the condition for adiabatic initial perturbations. We have thus verified the early-universe behavior of the system: for sufficiently small values of ν, the instabilities are avoided, and adiabatic initial conditions can consistently be imposed.
So far, we have focused on the density perturbations in the early universe. These perturbations must have undergone growth in order to give rise to the structures observed today, such as galaxies and galaxy clusters. The evolution of such total matter fluctuations is governed by the so-called growth equation [175, 176]. To investigate the behavior of our model in the late universe, i.e., $z \lesssim 10$, we therefore turn to the perturbation equation for the total matter density denoted with δ_{M} in the Newtonian gauge:

$$\delta_{\mathrm{M}}' = -\frac{\bar{\rho}_{\mathrm{DE}}'}{\bar{\rho}_{\mathrm{M}}}\delta_{\mathrm{M}} + k v_M + 3\Phi' , \tag{3.66}$$

$$v_{\mathrm{M}}' = v_{\mathrm{M}}\left(\frac{\bar{\rho}_{\mathrm{DE}}'}{\bar{\rho}_{\mathrm{M}}} - \mathcal{H}\right) - k\Psi , \tag{3.67}$$

where v_{M} is related to the Fourier transformation of the velocity divergence in equation (3.33) via $v_{\mathrm{M}} = -\Theta_{\mathrm{M}}/k$, where we appropriately adjusted the matter indices. Differentiating equation (3.66) and substituting equation (3.67) into it, we then take the subhorizon limit, i.e., $k \gg \mathcal{H}$. This yields the growth equation

$$D'' - D\left(-\frac{\bar{\rho}_{\mathrm{DE}}''}{\bar{\rho}_{\mathrm{M}}} + \frac{\bar{\rho}_{\mathrm{M}}'\bar{\rho}_{\mathrm{DE}}'}{\bar{\rho}_{\mathrm{M}}^2} + \frac{\bar{\rho}_{\mathrm{DE}}'^2}{\bar{\rho}_{\mathrm{M}}^2} - \frac{\bar{\rho}_{\mathrm{DE}}'}{\bar{\rho}_{\mathrm{M}}}\mathcal{H} + 4\pi G a^2 \bar{\rho}_{\mathrm{M}}\right) + D'\mathcal{H} = 0 , \tag{3.68}$$

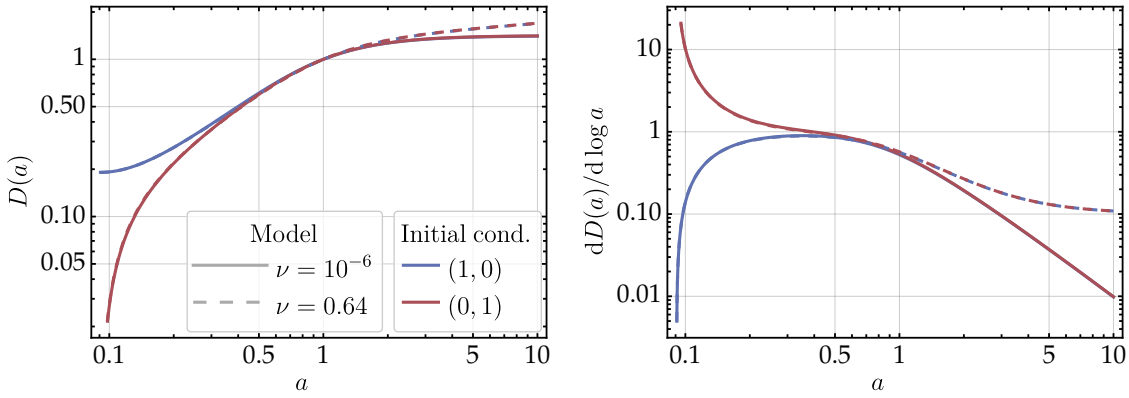

Figure 3.10: Solutions of the growth equation for different values of ν. Left: normalized growth factor $D(a)$ with $D(a_0) = 1$. Right: corresponding growth rates. We show a realistic values, $\nu = 10^{-6}$, and the best-fit value $\nu = 0.64$ from section 3.1. The input parameters are given in table 3.10.

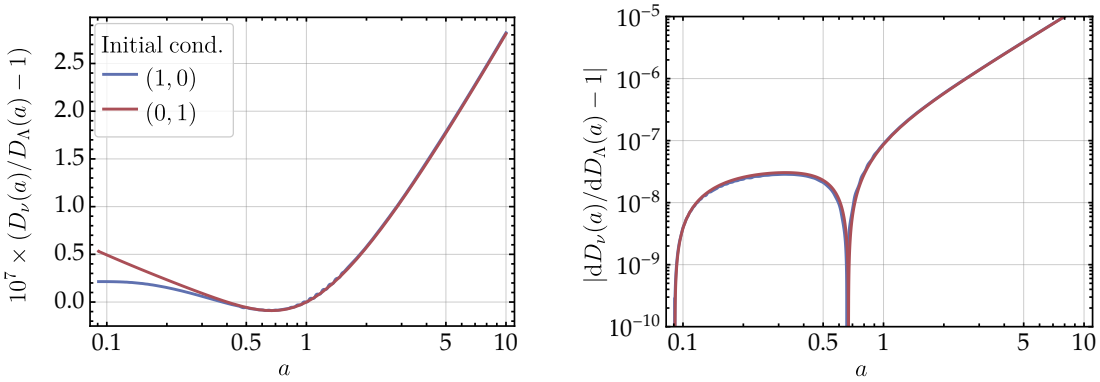

Figure 3.11: Relative deviation between the νCKN model and ΛCDM for $\nu = 10^{-6}$. Left: growth function. Right: absolute value of the relative difference of the growth rates. The input parameters are given in table 3.10.

where we factorised $\delta_{\mathrm{M}}(\vec{k}, t) = \delta_{\mathrm{M}}(\vec{k})D(t)$. To analyze the behavior of the full space of solutions of this equation, we consider two linearly independent initial conditions:

$$D(a_{10}) = 1\,, \qquad D(a_{10}) = 0\,, \tag{3.69}$$
$$D'(a_{10}) = 0\,, \qquad D'(a_{10}) = 1\,, \tag{3.70}$$

where a_{10} denotes the scale factor at redshift $z = 10$. If both of these independent solutions are well behaved, then any other linear combination, and thus any physically admissible solution, will also remain stable. The left panel of figure 3.10 shows the solutions of the growth equation for the chosen initial conditions. Note that all solutions are re-normalized such that $D(a_0) = 1$, where a_0 denotes the present scale factor. The curves are shown for two representative parameter choices: $\nu = 10^{-6}$, which corresponds to a realistic value motivated by the discussion of the initial conditions at $a_{\mathrm{ini}} \approx 10^{-10}$, and $\nu = 0.64$, the best-fit value reported in section 3.1. The right panel of figure 3.10 displays the corresponding growth rates. A vanishing growth rate indicates a stagnation of structure formation. Figure 3.11 illustrates the relative deviation between the νCKN model and ΛCDM for $\nu = 10^{-6}$. The last panel shows the difference in the growth

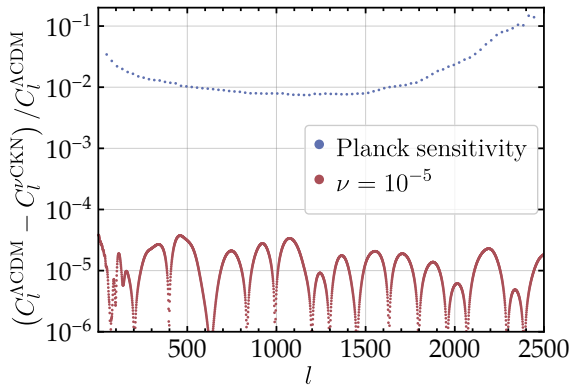

Figure 3.12: Relative deviation in the CMB TT power spectrum between the νCKN model and ΛCDM, computed with the parameter values listed in table 3.10. The dashed line indicates the sensitivity of the Planck experiment [108].

function, while the right panel depicts the absolute value of the relative difference of the growth rates. Although the differences remain very small, one observes that the growth does not approach a constant value in the νCKN scenario.
We thus have demonstrated that for sufficiently small values of ν our model remains well behaved both in the early and in the late universe. However, the deviations from ΛCDM are expected to be small. For this reason, in the following subsection we perform an expected sensitivity analysis based on the CMB power spectrum.

3.2.2 Expected CMB Sensitivity

As discussed in the previous subsection, we do not expect large deviations between the νCKN model and ΛCDM for values of ν that ensure stability in the early universe and satisfy equation (3.53). To obtain a first estimate of whether such differences could be observable at all, it is natural to turn to the most stringent and precise cosmological probe currently available, namely the CMB. In particular, we focus on the variance C_ℓ of the spherical harmonic coefficients of the temperature anisotropies, and more specifically on the TT correlations [108]. These are given by

$$C_\ell = 4\pi \int \mathrm{d}\ln k\, \Theta_\ell^2(k)\, \Delta_R^2(k)\,. \tag{3.71}$$

Here, Δ_R denotes the primordial curvature perturbation, while Θ_ℓ is the transfer function encoding the evolution of the fluctuations in the primordial plasma. To compute the latter, we implement our model, consisting of the background equations together with equation (3.28)–(3.29) in the Newtonian gauge with adiabatic initial conditions, into `CLASS` [117]. For comparison, we determine the predictions of the ΛCDM model using the same setup. Figure 3.12 shows the relative deviation between the two models, with the input parameters summarized in table 3.10. The sensitivity of the Planck satellite [108] is also indicated. As can be seen, the Planck error bars lie at least two orders of magnitude above the predicted deviation. This provides a first indication that the νCKN model cannot be distinguished from ΛCDM at the level of current CMB observations. To further investigate and substantiate this result, we perform a global analysis of cosmological datasets in the next chapter.

Table 3.10: Input parameters used for figures 3.10–3.12.

Parameter	Value
$H_0/(\mathrm{km/s/Mpc})$	68.877
$\Omega_\mathrm{b}h^2$	0.022
$\Omega_\mathrm{DM}h^2$	0.121
$T_\mathrm{CMB}/\mathrm{K}$	2.726
N_ur	3.044
A_s	2.094×10^{-9}
n_s	0.963
ν	10^{-5}

Table 3.11: Best-fit values for the νCKN model using the DESI BAO DR2 and Hubble data, combined with either DESY5 or Pantheon+ data using the methodology of this section. The table lists Hubble-today H_0, the matter density parameter Ω^0_M, the drag epoch r_d and the parameter ν.

$H_0/(\mathrm{km/s/Mpc})$	Ω^0_M	$r_\mathrm{d}/\mathrm{Mpc}$	ν
$70.5^{+2.1}_{-2.2}$	0.310 ± 0.002	$143.0^{+4.5}_{-4.9}$	-1.06×10^{-9}
73.2 ± 0.9	0.312 ± 0.002	$137.0^{+1.9}_{-2.0}$	1.12×10^{-9}

3.2.3 Global Analysis

To investigate the behavior of our model, we implement the background equations together with the perturbation equations from equations (3.28) and (3.29) as well as the growth equation (3.68) with adiabatic initial conditions in the Newtonian gauge within `CLASS` [117]. In order to incorporate the resulting output into a global analysis, we make use of the Markov Chain Monte Carlo (MCMC) sampler `MontePython` [177], which provides an interface to `CLASS`. Within `MontePython`, the cosmological likelihood is constructed, enabling parameter inference based on Bayesian methods [178]. Specifically, we employ the Metropolis–Hastings algorithm to generate the Markov chain.
To verify the consistency of this method with the approach employed in section 3.1, we first perform an analysis using the same datasets, cf. section 3.1.1. The results of this analysis are presented in figures 3.13 and 3.14, with the corresponding best-fit values in table 3.11. As can be seen, the results are in good agreement, while the error bands obtained with the new method become smaller in both cases but especially when the Pantheon data is included. This behavior is expected due to the additional SH0ES calibration applied to the Pantheon sample here. Moreover, both result plots illustrate that the parameter ν is already strongly constrained by the considerations of section 3.2.1, which is reflected in the nearly flat posterior distribution for ν. As a consequence of this

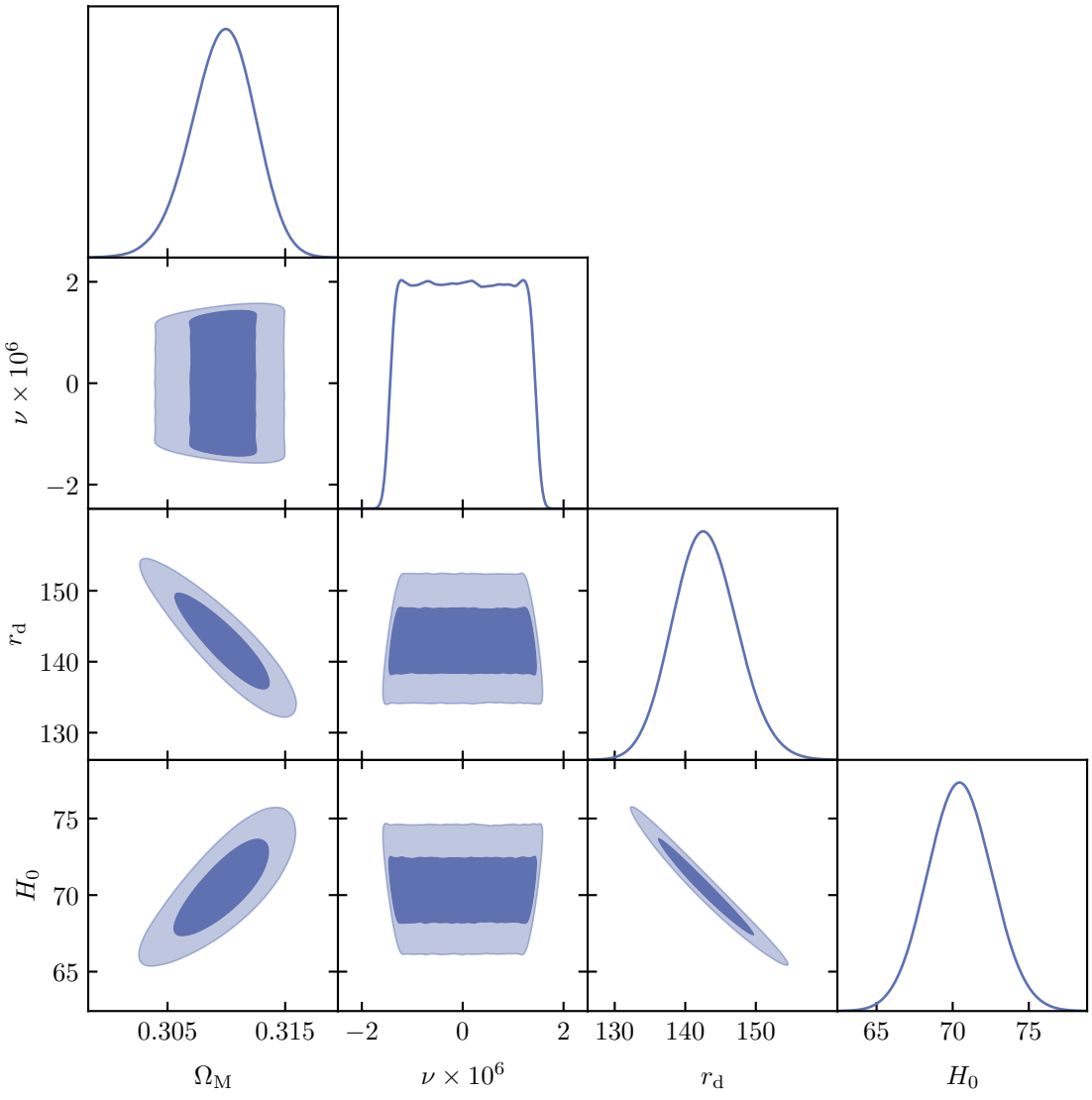

Figure 3.13: Analysis of the late-universe data using DESY5 data with bayesian methods. In dark blue we mark the 68 % and in light blue the 95 % credible regions. H_0 is given in (km/s/Mpc) and r_d in Mpc.

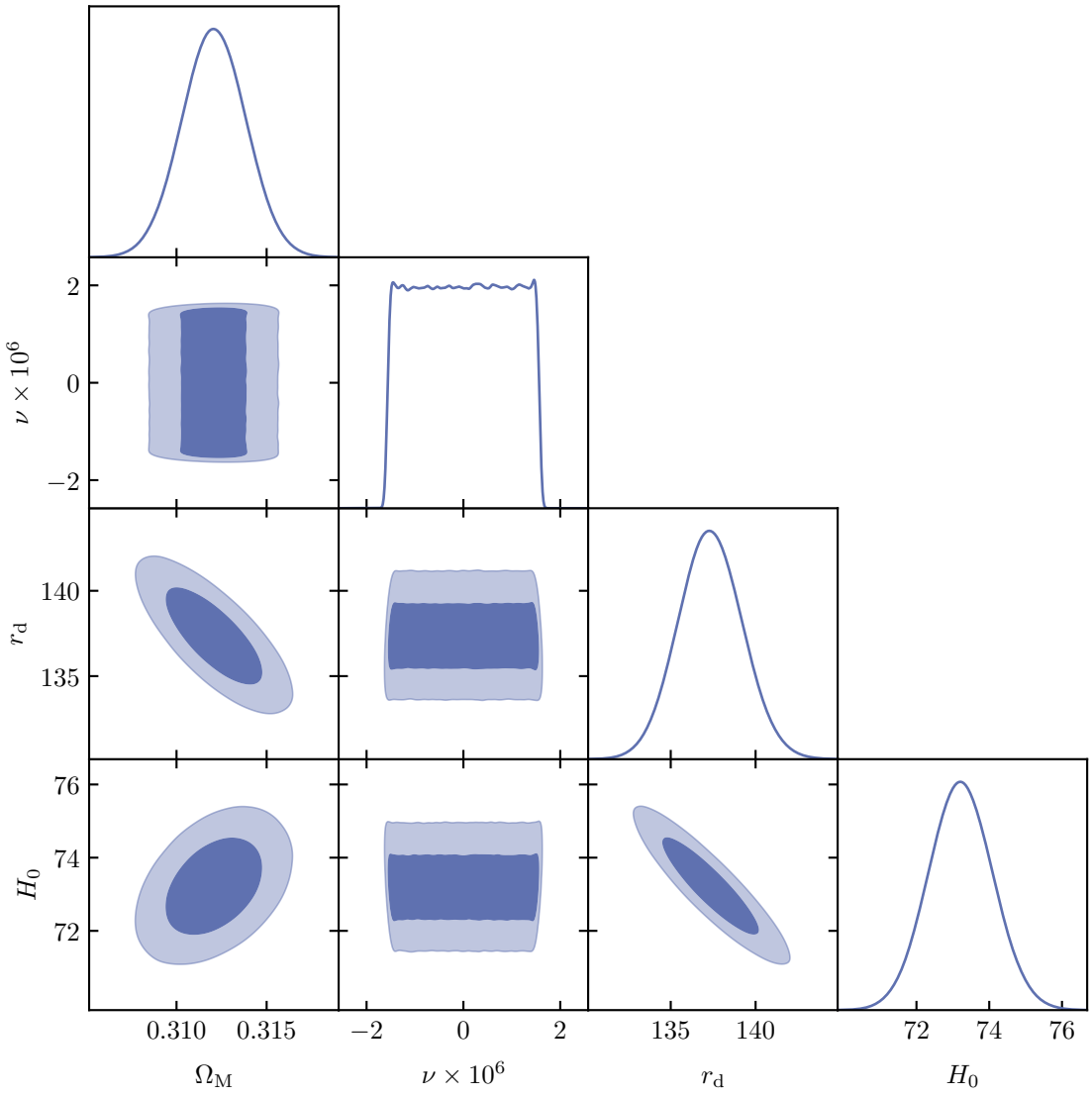

Figure 3.14: Analysis of the late-universe data using Pantheon+SH0ES data with bayesian methods. In dark blue we mark the 68 % and in light blue the 95 % credible regions. H_0 is given in (km/s/Mpc) and r_d in Mpc.

Table 3.12: Best-fit values for the global analysis using the DESI BAO DR2, model independent Hubble measurements, supernovae, CMB, and weak lensing data. The table lists Hubble-today H_0, the DM density parameter $\Omega^0_{\rm DM}$, the baryonic matter parameter $\Omega_{\rm B}h^2$, the dark energy parameter $\Omega_{\rm DE}$ and the parameter ν. We do not provide the $1\,\sigma$ values for ν as it corresponds to the whole theoretically allowed region, see figure 3.15.

Parameter	Value
$H_0/(\mathrm{km/s/Mpc})$	$69.5^{+0.341}_{-0.342}$
$\Omega^0_{\rm DM}h^2$	$0.117 \pm (7 \times 10^{-4})$
$\Omega_{\rm B}h^2$	$(2.27 \pm 0.01) \times 10^{-2}$
$\Omega_{\rm DE}$	0.712 ± 0.004
ν	-3.52×10^{-8}

lack of sensitivity to ν, the remaining parameters are tighter constrained. This behavior is already apparent in section 3.1, when comparing the CKN and νCKN scenarios.
We now extend our analysis by including additional datasets:

Planck CMB data: The Planck satellite measures the CMB [74]. From the total intensity, corresponding to the Stokes parameter I in equation (2.89), one obtains the multipole coefficients which determine $C_\ell^{\rm TT}$ through a spherical-harmonic decomposition [179]. Measurements with different polarization settings provide access to the Stokes parameters Q and U in equations (2.90) and (2.91), respectively. Their decomposition yields the $C_\ell^{\rm EE}$ spectrum, while the cross-correlation with temperature gives the $C_\ell^{\rm TE}$ spectrum. For high- and low-ℓ multipole, Planck employs dedicated instruments optimized for the respective frequency ranges [108].
In our analysis, we use the TTTEEE likelihood at high-ℓ, and the TT and EE likelihoods at low-ℓ. In addition, we include the CMB lensing likelihood provided by Planck, which contains information about the deflection of CMB photons travelling through gravitational potentials.

Weak lensing data: As light propagates through the universe, it is deflected by massive objects. Weak lensing describes the impact of this effect on the light we observe from distant galaxies [180]. Experimentally, the light from a large number of galaxies is used to determine the cosmic shear for each individual galaxy. To average out the statistical fluctuations of the intrinsic galaxy shapes, the two-point shear correlator is computed. What remains is a systematic effect induced by weak lensing. To account for this effect in our analysis, we employ the KiDS-1000 COSEBIs likelihood [181], which decomposes the two-point shear correlators further into E- and B-modes.

In figure 3.15 we present the results of the global analysis including these experimental inputs, while table 3.12 lists the corresponding best-fit values. We find that even with the inclusion of early-universe data, where the impact of ν becomes more pronounced, no sensitivity to ν emerges. This demonstrates that, under the assumptions made, there is no way to distinguish the ΛCDM model from the νCKN scenario with current experi-

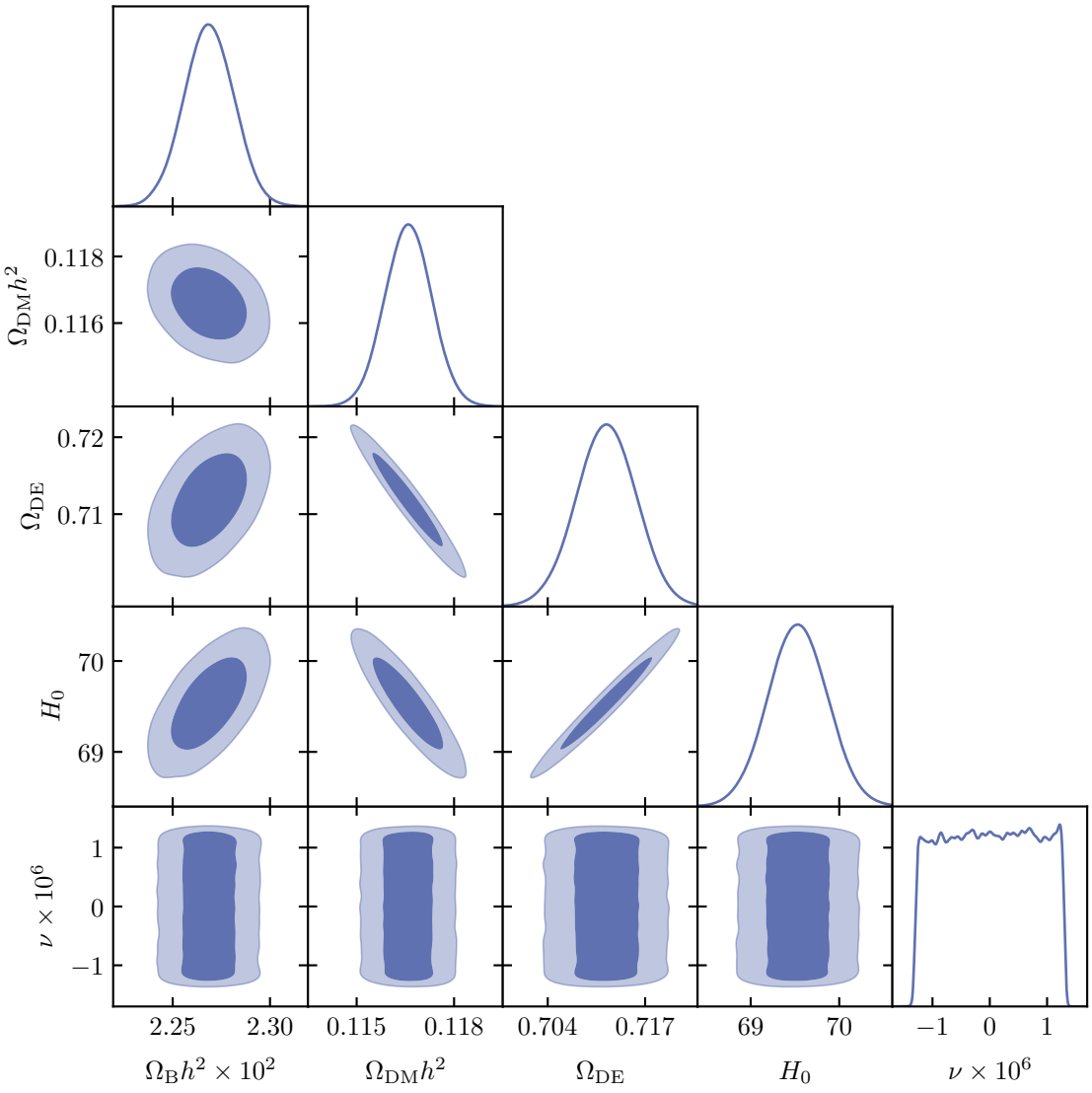

Figure 3.15: Result of the global analysis using DESI BAO DR2, model independent Hubble measurements, Pantheon+SH0ES supernovae dataset, CMB, and weak lensing data. In dark blue we mark the 68 % and in light blue the 95 % credible regions. H_0 is given in (km/s/Mpc).

mental data. Consequently, the νCKN model can neither be conclusively confirmed nor ruled out at present.

3.3 Summary and Discussion

In this chapter, we first have performed an initial analysis of the νCKN model using late-universe observational data, in particular $z \lesssim 3.5$. This model is characterized by time-dependent contributions from the vacuum energy of a QFT, where in turn this time-dependence originates from the CKN bound. This feature provides a natural theoretical motivation, as it directly connects the dynamics of dark energy to fundamental aspects of QFT in a gravitational context. For the first analysis, we employ the DESI BAO DR2, model-independent Hubble measurements, and the Pantheon+ or DESY5 supernovae data. The results indicate that both CKN and νCKN with $\nu \sim O(1)$ are preferred over ΛCDM at the significance of up to $2.6\,\sigma$. A comparable preference is also observed for other models of dynamical dark energy. Furthermore, we discuss future surveys such as Euclid, whose data are expected to significantly increase the statistical power and thereby improve the ability to discriminate between competing scenarios.
These results motivate a global analysis including early-universe data. Since these also comprise CMB observations, it is necessary to formulate the perturbation equations of our model, which requires additional assumptions. Compared to the initial late-universe analysis, the coupling of dark energy to matter must now be specified. To retain the largest possible freedom, we adopt a coupling between dark energy and dark matter, which requires a covariant formulation. Motivated by the fact that dark energy receives a contribution from the vacuum energy, we assume a vanishing dark energy perturbation, i.e., $\delta\rho_{\mathrm{DE}} = 0$. In order to avoid instabilities in the early universe, the parameter ν must then be chosen sufficiently small. Note, that for such values of ν it is not possible to reproduce the best-fit value of section 3.1. And indeed, a first estimate already shows that, under this condition, the difference between the νCKN and ΛCDM lies about two orders of magnitude below the sensitivity of Planck. A subsequent global analysis including both CMB and weak lensing data confirms that νCKN and ΛCDM are observationally indistinguishable.
Even with the inclusion of future data, such as those expected from Euclid, we anticipate at most an order-of-magnitude impovement in sensitivity. However, even under ideal conditions, the sensitivity to C_ℓ is fundamentallly limited by cosmic variance [112, 182]:

$$\sigma(C_\ell) \approx \sqrt{\frac{2}{2\ell+1}} C_\ell \,, \tag{3.72}$$

which further complicates the task of distingushing between the νCKN model and ΛCDM. In principle, a careful choice of binning could allow small deviations in the signal to accumulate into a statistically significant effect. For other ways to get around the limitation of cosmic variance see, e.g., reference [182]. Nevertheless, given the present experimental situation, such an outcome appears unlikely.
In order to translate the preference observed in late-universe data into the early-universe regime, the only remaining option would be to modify our model. However, altering the choice of δQ to one of the other possibilities discussed, inevitably introduces early-universe instabilities. Even if such behavior can be excluded in the early universe, there could be other instabilities manifesting as adiabtic instabilities [172, 173, 183].

As we have seen, the theoretical restriction on ν in order to avoid such instabilities arises from the a^{-4} scaling of DM and/or dark energy components. In principle, it may be possible to extend the coupling of dark energy to matter in such a way that this behavior is eliminated. One conceivable option would be a coupling of dark energy to dark radiation [169, 184, 185]. In addition, computations of the vacuum energy in curved spacetime suggest that its scaling receives further corrections, which could also remove the problematic a^{-4} contribution [186].
Another intriguing possibility is that the universe may have undergone transitions between different cosmological regimes, potentially linked to phase transitions in the early universe [171, 187].
In summary, the parameter ν is constrained so tightly that current cosmological data cannot distinguish ΛCDM from νCKN. Nevertheless, further investigation of the νCKN scenario on different physical scales remains highly interesting. In this chapter, gravity has entered only implicitly, shaping dark energy through the CKN bound. In the next chapter, we turn to an explicit treatment of gravity as a classical background in QFT and explore its impact on neutrino oscillations.

Chapter 4

Neutrino Oscillations in Curved Spacetime

The detection of GW170817 marked the first GW multimessenger observation, combining a GW signal measured by LIGO [188] with electromagnetic counterparts observed by Fermi [189] and INTEGRAL [190]. Earlier multimessenger observations, such as the detection of neutrinos and photons from SN1987a [191–193], had already demonstrated the power of combining distinct messengers. The observation of GW170817 provided a significant impetus for the development of multimessenger astronomy, enabling unprecedented tests of fundamental physics and astrophysical models through the combined observation of GWs, electromagnetic radiations, and neutrinos. Today, multimessenger efforts involve an active interplay between different observational channels: GWs measured by LIGO, Virgo [188], KAGRA [194], and, in the near future, LISA [195]; electromagnetic radiation across the radio, optical and X-ray bands; and neutrinos observed for example by IceCube [196] and KM3NeT [197]. This synergy allows for precise source localization and improved understanding of compact object mergers [198–200], supernovae [201], active galactic nuclei [202], gamma ray bursts [203] and related phenomena [204, 205]. It also allows for independent tests of fundamental physics, including violation of Lorentz symmetry [206], neutrino properties [207, 208], and potential QG effects [209].

Within this broader multimessenger framework, neutrinos occupy a distinct role: They are emitted in many of the afore-mentioned events and, due to their extremly weak interactions, can escape dense astrophysical environments unimpeded, preserving directional and spectral information [210]. Moreover, their flavor composition is measurable and encodes information about the production mechanism, propagation effects and potential signatures of new physics. Unlike other messengers, neutrinos undergo flavor oscillations during propagation. As they traverse cosmic distances, these oscillations could be sensitive to the geometry of spacetime. Gravitational effects can alter the oscillation phase, induce dephasing or wave packet separation, and potentially lead to decoherence [211, 212]. This makes neutrinos interesting messengers that may carry measurable *traces of gravity* from the geometry of spacetime and raises the central question of this chapter: Are such traces observable?

The standard treatment of neutrino oscillations assumes flat spacetime and describes neutrinos as unlocalized plane waves, which is insufficient as we have dicussed in section 2.2. Therefore, we need to take into account realistic production and detection processes, finite wave packet size and coherence, and propagation across cosmological distances through gravitational fields of galaxies, black holes or GW sources. In settings where gravity may influence the propagation, the phase difference in the transition probability is no longer determined solely by the baseline L and energy E, but becomes path-dependent, requiring a proper treatment of propagation along spacetime geodesics.

The theoretical exploration of classical gravitational effects on neutrino oscillations dates back several decades. Early approaches already in the 1970s considered modifications to the oscillation phase in curved spacetime, starting with the seminal work by Stodolsky, who introduced a geometric phase term based on the integral of the four-momentum along a geodesic [213]:

$$\phi_j = \int_\gamma p_j^\mu \mathrm{d}x_\mu \,. \tag{4.1}$$

Several follow-up studies extended this framework to Schwarzschild, Kerr, and FLRW spacetimes using geometric techniques [211, 214–216]. While conceptually insightful, these treatments lack a true QFT foundation and typically describe neutrinos as idealized point particles or plane waves, neglecting their production and detection. A more formal path was taken by studies employing QFT in curved spacetime, which correctly recognize the observer-dependence of particle concepts and make use of the Bogoliubov transformations between Fock spaces [217–219]. However, even these works often rely on the plane wave formalism and do not account for localization, detector response, or wave packet decoherence. In flat spacetime, by contrast, the wave packet formalism is well-developed: both the internal and external wave packet approaches allow for a field-theoretic description of flavor oscillations with localization and finite coherence [58, 220], cf. section 2.2. However, a consistent generalization of this framework to curved spacetime is still lacking.

To bridge the gap between the conceptual treatments above and realistic observational scenarios, we develop a consistent theoretical framework for neutrino oscillations in arbitrary curved spacetimes, where gravitational particle production is negligible, based on localized wave packet states, embedded within the formalism of QFT, and yielding physically interpretable transition probabilities. This framework will allow us to disentangle classical gravitational effects from genuine signatures of new physics and to assess whether *traces* of classical gravity are detectable in neutrino flavor transitions.

In section 4.1, we construct the internal wave packet formalism in curved spacetime, discuss its assumptions and limitations, and derive a general master formula for the flavor transition amplitude. Section 4.2 simplifies this expression in the regime of weak gravitational fields and explores modifications to the oscillation phase, coherence length, and damping behavior. Section 4.3 applies the formalism to terrestrial experiments and time-dependent backgrounds such as GWs and estimates their phenomenological relevance. In section 4.4, we turn to astrophysical neutrinos and investigate whether propagation through curved spacetime modifies the classical deoherence limit. Section 4.5 discusses the experimental limitations to measure gravitational effects on neutrino oscillations. Finally, section 4.6 summarizes the findings.

This chapter thus marks a key step in the broader theme of this dissertation—probing the *traces of gravity* in quantum systems and bridging the gap between microscopic flavor dynamics and the geometry of the cosmos.

4.1 Internal Wave Packet Formalism in Curved Spacetime

To capture the influence of spacetime curvature on these processes, we now construct a general quantum field-theoretic framework based on localized wave packets. Neutrino oscillation experiments always involve a neutrino production location P and a detector D, both of which follow trajectories $X_{\mathrm{P/D}}(\widetilde{J}_{\mathrm{P/D}})$ through spacetime, parameterized by their

respective proper times $\overset{\frown}{\mathcal{J}}_{\mathrm{P}}$ and $\overset{\frown}{\mathcal{J}}_{\mathrm{D}}$. In this chapter, the background geometry is modeled as a global, hyperbolic, four-dimensional Lorentzian manifold $(\mathcal{M}, g)$ with metric tensor g and associated Levi–Cevita connection ∇. By definition global hyperbolicity guarantees the existence of a foliation into Cauchy surfaces, which define coordinate-independent hypersurfaces of constant time. This property is essential for defining well-posed initial value problems for the Dirac equation, and thus, for a consistent description of neutrino evolution. The hypersurfaces serve as the natural stage for defining quantum states and ensuring causality in the evolution of fields. Within the framework of QFT [221–224] particle states are observer-dependent. For neutrinos, these are solutions of the Dirac equation in curved spacetime:

$$0 = \gamma^{\mu}(x)\left(\partial_{\mu} + \Gamma_{\mu}(x)\right)\Psi(x) - m\Psi(x)\,, \tag{4.2}$$

$$\Gamma_{\mu}(x) := \frac{1}{8}\left[\gamma^{\alpha}, \gamma^{\beta}\right] e_{\alpha}{}^{\nu}(x) g_{\nu\rho}(x) \nabla_{\mu} e_{\beta}{}^{\rho}(x)\,. \tag{4.3}$$

Here, Γ_{μ} is the spin connection, e_{α} are vierbeins and $\gamma^{\mu}(x) := \gamma^{\alpha} e_{\alpha}{}^{\mu}(x)$ are the curved-spacetime Dirac matrices. The spinor mode functions ξ_J and ϵ_J provide a complete basis on the spin bundle, where J denotes a set of quantum numbers labeling these modes, with orthonormality relations given by

$$\langle \xi_J, \xi_K \rangle = \langle \epsilon_J, \epsilon_K \rangle = \delta_{JK}\,, \qquad\qquad \langle \xi_J, \epsilon_K \rangle = 0\,, \tag{4.4}$$

with respect to the scalar product

$$\langle \xi, \epsilon \rangle := \int_{\Sigma} \mathrm{d}\sigma_{\mu}(x)\, \bar{\xi}(x) \gamma^{\mu}(x) \epsilon(x)\,, \tag{4.5}$$

where Σ is a Cauchy surface and $\mathrm{d}\sigma_{\mu}$ its directed surface element. Positive- and negative-frequency conditions are defined relative to the observer's proper time $\overset{\frown}{\mathcal{J}}$:

$$\text{positive frequency } (\xi_J(x)): \qquad \frac{\nabla}{\mathrm{d}\overset{\frown}{\mathcal{J}}} \xi_J(x) = -i\omega_J \xi_J(x)\,, \tag{4.6}$$

$$\text{negative frequency } (\epsilon_J(x)): \qquad \frac{\nabla}{\mathrm{d}\overset{\frown}{\mathcal{J}}} \epsilon_J(x) = +i\omega_J \epsilon_J(x)\,. \tag{4.7}$$

Where $\nabla/\mathrm{d}\overset{\frown}{\mathcal{J}}$ denotes the covariant derivative ∇ along the path parameterized by $\overset{\frown}{\mathcal{J}}$. Here, ω_J denotes the energy associated with the mode ξ_J (or ϵ_J), as measured by the observer following proper time $\overset{\frown}{\mathcal{J}}$. A field operator $\Psi(x)$ is then decomposed as

$$\Psi(x) = \sum_{J} \left(a_J \xi_J(x) + b_J^{\dagger} \epsilon_J(x)\right)\,, \tag{4.8}$$

with the usual anticommutation relations for the ladder operators a_J and b_J with normalizations consistent with section 2.2.

For a neutrino experiment, the two relevant observers O_{P} and O_{D} define particle states via their own mode functions at the production and detection, respectively. If their respective notions of particle differ, the mode functions are related by a Bogoliubov transformation:

$$\xi^{\mathrm{P}}_{j;J}(x) = \sum_{J'} \left[\alpha_j(J;J') \xi^{\mathrm{D}}_{j;J'}(x) + \beta_j(J;J') \epsilon^{\mathrm{D}}_{j;J'}(x)\right]\,, \tag{4.9}$$

$$\epsilon^{\mathrm{P}}_{j;J}(x) = \sum_{J'} \left[\alpha^*_j(J;J') \epsilon^{\mathrm{D}}_{j;J'}(x) - \beta^*_j(J;J') \xi^{\mathrm{D}}_{j;J'}(x)\right]\,, \tag{4.10}$$

with

$$\alpha_j(J;J') := \langle \xi^{\mathrm{D}}_{j;J'}, \xi^{\mathrm{P}}_{j;J} \rangle \,, \qquad \beta_j(J;J') := \langle \epsilon^{\mathrm{D}}_{j;J'}, \xi^{\mathrm{P}}_{j;J} \rangle \,. \tag{4.11}$$

The difference in the particle picture reflects the fact that two distinct observers experience different proper times $\mathcal{T}$. This leads to a transformation of the ladder operators

$$a^{\mathrm{P}}_{j;J} = \sum_{J'} \left[\alpha^*_j(J;J') a^{\mathrm{D}}_{j;J'} + \beta^*_j(J;J') b^{\mathrm{D}\dagger}_{j;J'} \right] , \tag{4.12}$$

$$b^{\mathrm{P}}_{j;J} = \sum_{J'} \left[\alpha^*_j(J;J') b^{\mathrm{D}}_{j;J'} - \beta^*_j(J;J') a^{\mathrm{D}\dagger}_{j;J'} \right] . \tag{4.13}$$

As a consequence, the vacuum of O_{D} appears populated with particles in the frame of O_{P} whenever $\beta_j \neq 0$:

$$\langle 0, \mathrm{D}| \, a^{\mathrm{P}\dagger}_{j;J} a^{\mathrm{P}}_{j;J} \, |0, \mathrm{D}\rangle = \sum_{J'} |\beta_j(J;J')|^2 \,. \tag{4.14}$$

The flavor transition amplitude for a neutrino emitted as ν_a and detected as ν_b is defined as

$$\mathcal{A}_{ab} := \langle \nu_b, \mathrm{D} | \nu_a, \mathrm{P} \rangle \,, \tag{4.15}$$

with flavor states expressed as superpositions of mass eigenstates:

$$|\nu_a, \mathrm{P}\rangle := \sum_j U^*_{aj} \sum_J \phi^{\mathrm{P}}_j(J) a^{\mathrm{P}\dagger}_{j;J} \, |0, \mathrm{P}\rangle \,, \tag{4.16}$$

$$|\nu_b, \mathrm{D}\rangle := \sum_j U^*_{bj} \sum_{J'} \phi^{\mathrm{D}}_j(J') a^{\mathrm{D}\dagger}_{j;J'} \, |0, \mathrm{D}\rangle \,, \tag{4.17}$$

where ϕ^{D}_j and ϕ^{P}_j are the wave packets at detection and production, respectively. In general, this amplitude contains not only single-particle contributions but also terms involving particle–antiparticle pair creation. Expressing $\mathcal{A}_{ab}$ in terms of the detector observer's quantities yields:

$$\begin{aligned} \mathcal{A}_{ab} = \sum_j U^*_{aj} U_{bj} \sum_{J,J'} \phi^{\mathrm{D}*}_j(J') \phi^{\mathrm{P}}_j(J) \\ \times \left(\alpha_j(J;J') \, \langle 0, \mathrm{D}|0, \mathrm{P}\rangle + \sum_{K'} \beta_j(J;K') \, \langle \nu_j(J') \bar{\nu}_j(K'), \mathrm{D}|0, \mathrm{P}\rangle \right) . \end{aligned} \tag{4.18}$$

The second term in brackets encodes contributions from gravitationally-induced particle production. For a clean oscillation framework, we must exclude scenarios where gravitational particle production significantly populates the detector vacuum, which requires

$$\sum_{J,K',J'} \phi^{\mathrm{P}}_j(J) \beta_j(J;K') \, \langle \nu_j(J') \bar{\nu}_j(K'), \mathrm{D}|0, \mathrm{P}\rangle \, \phi^{\mathrm{D}*}_j(J') \approx 0 \,. \tag{4.19}$$

This condition is satisfied whenever β_j is negligible on the support of ϕ^{D}_j and ϕ^{P}_j for the quantum numbers J. Under this condition, the full amplitude simplifies to

$$\mathcal{A}_{ab} \approx \langle 0, \mathrm{D}|0, \mathrm{P}\rangle \sum_j U^*_{aj} U_{bj} \sum_{J,J'} \phi^{\mathrm{D}*}_j(J') \phi^{\mathrm{P}}_j(J) \alpha_j(J;J') \,, \tag{4.20}$$

which inserted in the flavor transition probability yields the master formula

$$P_{ab} = \frac{1}{N} \int_{\overset{\frown}{T}_{P1}}^{\overset{\frown}{T}_{P2}} \mathrm{d}\overset{\frown}{T}_{P} \int_{\overset{\frown}{T}_{D1}}^{\overset{\frown}{T}_{D2}} \mathrm{d}\overset{\frown}{T}_{D} \, |\mathcal{A}_{ab}(\overset{\frown}{T}_{P}, \overset{\frown}{T}_{D})|^2 \,, \tag{4.21}$$

$$N = \int_{\overset{\frown}{T}_{P1}}^{\overset{\frown}{T}_{P2}} \mathrm{d}\overset{\frown}{T}_{P} \int_{\overset{\frown}{T}_{D1}}^{\overset{\frown}{T}_{D2}} \mathrm{d}\overset{\frown}{T}_{D} \sum_{b} |\mathcal{A}_{ab}(\overset{\frown}{T}_{P}, \overset{\frown}{T}_{D})|^2 \,. \tag{4.22}$$

Here, $[\overset{\frown}{T}_{P1}, \overset{\frown}{T}_{P2}]$ and $[\overset{\frown}{T}_{D1}, \overset{\frown}{T}_{D2}]$ are the source and detector livetimes, respectively. In the special case of flat spacetime and inertial observers, the Bogoliubov coefficients in equation (4.11) reduce to momentum-conserving delta functions with a phase:

$$\alpha_j(\vec{p}, \sigma; \vec{p}', \sigma') = \delta_{\sigma\sigma'} \delta^{(3)}(\vec{p} - \vec{p}') e^{-ip_\mu (X_D^\mu - X_P^\mu)} \,, \tag{4.23}$$

thereby recovering the standard oscillation formula. As usual, we use the momentum $\vec{p}$ and spin σ as quantum numbers to label the states in flat spacetime. In curved spacetime, however, the decomposition must respect the local geometry and observer-dependent mode definitions, necessitating the general QFT in curved spacetime-based treatment applied here. To ensure consistency, the probability expression in equation (4.21) for the flavor transition is normalized such that it describes the conditional probability for detection, independent of the absolute likelihood that a neutrino reaches the detector. This step is crucial, as $\mathcal{A}_{ab}$ includes geometric and wave packet overlap factors that affect detectability, not just flavor conversion. This formalism now provides a fully general framework for describing flavor transitions of wave packets in arbitrary curved backgrounds, as long as gravitational particle production effects remain negligible. Having established the general formalism, we next consider the regime of weak gravitational fields, where analytic simplifications become possible.

4.2 Application to Weak Gravitational Fields

A central challenge in evaluating the flavor transition amplitude in equation (4.20) in curved spacetime lies in the dependence of the Bogoliubov coefficient α on the global structure of the mode solutions to the Dirac equation. These global mode functions are typically difficult, or even impossible, to determine analytically. To circumvent this issue, we impose additional assumptions to further simplify the amplitude $\mathcal{A}_{ab}$: the neutrino wave packets remain sufficiently localized such that spacetime curvature can be neglected within the spacetime region U_ν occupied by the neutrino wave packets.
In many physically relevant scenarios, the curvature scale is much larger than the size of the neutrino wave packet, allowing us to replace the global problem by a sequence of local flat spacetime evolutions. As shown in reference [225], localized quantum wave packets of massive particles propagate, on average, along classical timelike geodesics. Based on this, we assume that each neutrino mass eigenstate j travels along a classical geodesic c_j from the production to the detection, with initial conditions specifying position and velocity.
Since we are not always able to compute the Bogoliubov coefficient α_j directly, we adopt a stepwise propagation approach: we approximate the full propagation by discretizing a single geodesic c, which connects the production point X_P and the detection point

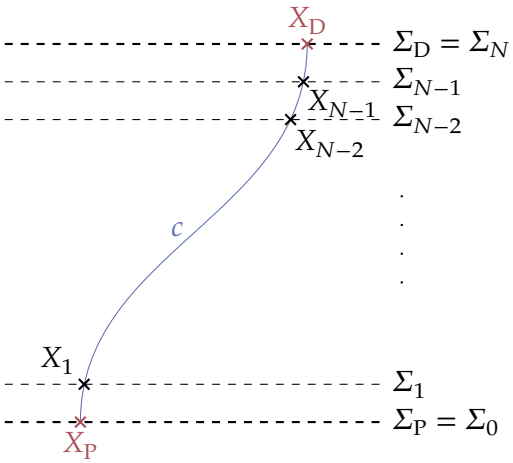

Figure 4.1: Shown is the geodesic c connecting the neutrino production event X_P with the neutrino detection event X_D. We foliate the spacetime region containing the neutrino path by $N+1$ hypersurfaces Σ_k.

X_D. This geodesic needs not to coincide with any of the individual paths c_j of the mass eigenstates. However, since neutrino detection requires overlap of the wave packets, only timelike or lightlike separations contribute to the amplitude. We therefore choose c to lie within the causal region and to minimize the deviation from the mass eigenstate geodesics c_j. Additionally, the path c must be fully contained within the region U_ν which is the region where the wave packets of all mass eigenstates have support. This assumption implicitly restricts the analysis to weak gravitational fields, as strong curvature may lead to widely diverging paths c_j and break the condition of shared support.
To implement the stepwise procedure, we partition the proper time interval τ along c into $N+1$ equal segments

$$0 = \tau_0 < \tau_1 < \ldots < \tau_N = \tau\,, \qquad \Delta\tau := \frac{\tau}{N}\,, \qquad X_k := c(\tau_k)\,, \tag{4.24}$$

and introduce a family of Cauchy surfaces Σ_k that intersect the geodesic at the respective points $X_k = \Sigma_k \cap c\,([0,\tau])$, as shown in figure 4.1. At each step along the neutrino's propagation, we exploit the strong localization of its position-space wave packet around the classical geodesic c_j to invoke the equivalence principle and neglect local gravitational effects by transforming into a locally inertial frame centered at each point X_k. Within this approximation, second and higher-order contributions from the spin connection in the Dirac equation are disregarded. Consequently, gravitationally induced spin precession effects are neglected, as our primary interest lies in the lowest-order non-trivial gravitational corrections arising from the curvature-modified propagation path. At each spacetime point X_k along the geodesic c, we define a local inertial frame with coordinates z^μ_k, whose origin is located at X_k. The associated coordinate basis $\partial/\partial z^\mu_k$ are constructed by parallel transporting the initial basis $\partial/\partial z^\mu_P$ at the production point X_P along the curve c. This yields a set of four mutually orthonormal and parallel vector fields:

$$E_\mu(\tau) := P^c_{0\to\tau}\frac{\partial}{\partial z^\mu_P}(X_P)\,, \tag{4.25}$$

which satisfy

$$E_\mu(\tau_k) = \frac{\partial}{\partial z_k^\mu}(X_k)\,, \tag{4.26}$$

$$E_\mu(\tau_2) = P^c_{\tau_1\to\tau_2} E_\mu(\tau_1)\,, \tag{4.27}$$

where $P^c_{\tau_1\to\tau_2}$ denotes the parallel transport along the geodesic from $c(\tau_1)$ to $c(\tau_2)$.
The first local inertial frame $z_0^\mu \equiv z_\mathrm{P}^\mu$ is taken to coincide with the rest frame of the neutrino production. To formalize the construction of parallel transported frames, we use Fermi normal coordinates along a curve C. When applied to a geodesic c, as done here, this corresponds to the Riemann Normal Coordinate System (RNC) naturally associated with the geodesic. However, the final local inertial frame $z_\mathrm{D} \equiv z_N$ at the detector does not necessarily coincide with the rest frame of the observer O_D, due to the independent motion and orientation of the detection apparatus. Therefore, we introduce a second local inertial frame $\tilde{z}_\mathrm{D}$ at the detector, which is tied to the rest frame of O_D. To correctly describe the detection, the propagated neutrino wave packet must be expanded in terms of the mode functions ξ_j^D defined in this latter frame.
For each mass eigenstate j and each parallel-transported local frame z_k, we define a corresponding set of positive frequency solutions denoted $\xi^{X_\mathrm{P}\to X_k}_{j;\vec{p}\sigma}$, labeled by momentum $\vec{p}$ and spin σ, with $k = 0, \dots, N$. These mode functions are chosen such that they coincide with the flat spacetime solutions, and they take the same form as

$$\xi_{j;\vec{p}\sigma}(z_k) = u_{j\sigma}(\vec{p})\frac{e^{-ip_{j\mu}z_k^\mu}}{\sqrt{(2\pi)^3 2p_j^0}}\,, \qquad p_j^0 = \sqrt{|\vec{p}|^2 + m_j^2}\,, \tag{4.28}$$

when evaluated at X_k in the coordinate frame z_k^μ. This set enables the step-wise propagation outlined above.
Starting from the general amplitude expression in equation (4.20), we insert a complete set of mode functions $\xi^\mathrm{D}_{j;\vec{p}\sigma}$ defined in the detector frame:

$$\mathcal{A}_{ab}(X_\mathrm{D}, X_\mathrm{P}) = \sum_j U^*_{aj}U_{bj} \sum_{\sigma,\sigma'=\pm 1/2} \int \mathrm{d}^3\vec{p} \int \mathrm{d}^3\vec{p}\,'\, \phi_j^{\mathrm{D}*}(\vec{p},\sigma)\phi_j^\mathrm{P}(\vec{p}\,',\sigma') \underbrace{\alpha_j(\vec{p}\,',\sigma';\vec{p},\sigma)}_{=\langle \xi^\mathrm{D}_{j;\vec{p}\sigma}, \xi^\mathrm{P}_{j;\vec{p}\,'\sigma'}\rangle}\,. \tag{4.29}$$

Using the position-space wave packets

$$\psi_j^\mathrm{P}(x) := \sum_{\sigma=\pm 1/2} \int \mathrm{d}^3\vec{p}\, \phi_j^\mathrm{P}(\vec{p},\sigma)\xi^\mathrm{P}_{j;\vec{p}\sigma}(x)\,, \tag{4.30}$$

$$\psi_j^\mathrm{D}(x) := \sum_{\sigma=\pm 1/2} \int \mathrm{d}^3\vec{p}\, \phi_j^\mathrm{D}(\vec{p},\sigma)\xi^\mathrm{D}_{j;\vec{p}\sigma}(x)\,, \tag{4.31}$$

we obtain a compact expression:

$$\mathcal{A}_{ab}(X_\mathrm{D}, X_\mathrm{P}) = \sum_j U^*_{aj}U_{bj}\langle \psi_j^\mathrm{D}, \psi_j^\mathrm{P}\rangle \tag{4.32}$$

$$= \sum_j U^*_{aj}U_{bj} \sum_{\sigma=\pm 1/2} \int \mathrm{d}^3\vec{p}\, \langle \psi_j^\mathrm{D}, \xi^{X_\mathrm{P}\to X_\mathrm{D}}_{j;\vec{p}\sigma}\rangle\langle \xi^{X_\mathrm{P}\to X_\mathrm{D}}_{j;\vec{p}\sigma}, \psi_j^\mathrm{P}\rangle\,. \tag{4.33}$$

The motivation for expressing the amplitude in terms of position-space wave packets lies in their strong spatial localization along the curve c. Even wave packets with non-compact support are admissible, provided they decay rapidly outside a characteristic width σ_j, such that their effective support is compact within the spacetime region U_ν. This localization allows for the scalar products to be evaluated over the finite region U_ν. We now turn to how the wave packet is propagated and how it is expressed in the natural basis of the detector. Therefore, the next steps consist of:

1. Computing the propagated momentum-space wave packet,

$$\phi^{\mathrm{P}\to\mathrm{D}}_{j\sigma}(\vec{p}) := \langle \xi^{X_\mathrm{P}\to X_\mathrm{D}}_{j;\vec{p}\sigma}, \psi^{\mathrm{P}}_j \rangle \,, \tag{4.34}$$

   which is performed in subsection 4.2.1, and

2. Matching the detected wave packet to the same mode basis,

$$\tilde{\phi}^{\mathrm{D}}_{j\sigma}(\vec{p}) := \langle \xi^{X_\mathrm{P}\to X_\mathrm{D}}_{j;\vec{p}\sigma}, \psi^{\mathrm{D}}_j \rangle \,, \tag{4.35}$$

   which will be addressed in subsection 4.2.2.

A schematic flowchart of the derivation steps is shown in figure 4.2. Finally, we summarize the assumptions that underlie the calculations:

1. Each mass eigenstate wave packet approximately follows a timelike geodesic c_j.
2. The curvature of spacetime is sufficiently weak such that all mass eigenstate wave packets intersect the detector during the detection window, and gravitational effects can be neglected on the intersection of U_ν with any Cauchy surface Σ_k.
3. The wave packets are localized tightly enough that the mode functions $\xi^{X_\mathrm{P}\to X_k}_j$ can be well approximated by their flat spacetime counterparts within each local frame z_k. Curvature-induced corrections of order z_k^2 across U_ν are assumed to be negligible, both locally and in terms of their cumulative effect along the geodesic c.

For clarity, we omit the mass eigenstate index j in the following discussion, as the computations proceed analogously for each j.

4.2.1 Propagating the Initial Momentum Space Wave Packet

In this subsection, we demonstrate that, under the approximations introduced earlier, the propagation of the initial neutrino wave packet in momentum space is given by

$$\phi^{\mathrm{P}\to\mathrm{D}}_{\sigma}(\vec{p}) = \exp\left(-i\int_0^\tau \mathrm{d}\tau'\, g_{\mu\nu}(c(\tau'))\dot{c}^\mu(\tau')p^\nu(\tau')\right)\phi^{\mathrm{P}}_{\sigma}(\vec{p}) + O\left(\int \mathrm{d}\tau\, R\sigma_\tau^2\right), \tag{4.36}$$

in the limit of infinitely many infinitesimal propagation steps, $N \to \infty$. Here, $p^\nu(\tau')$ denotes the parallel-transported momentum, R is the spacetime curvature scalar, and $\sigma_\tau := \sigma(\Sigma_\tau \cap U_\nu)$ is the spatial diameter of the region U_ν intersected with the Cauchy

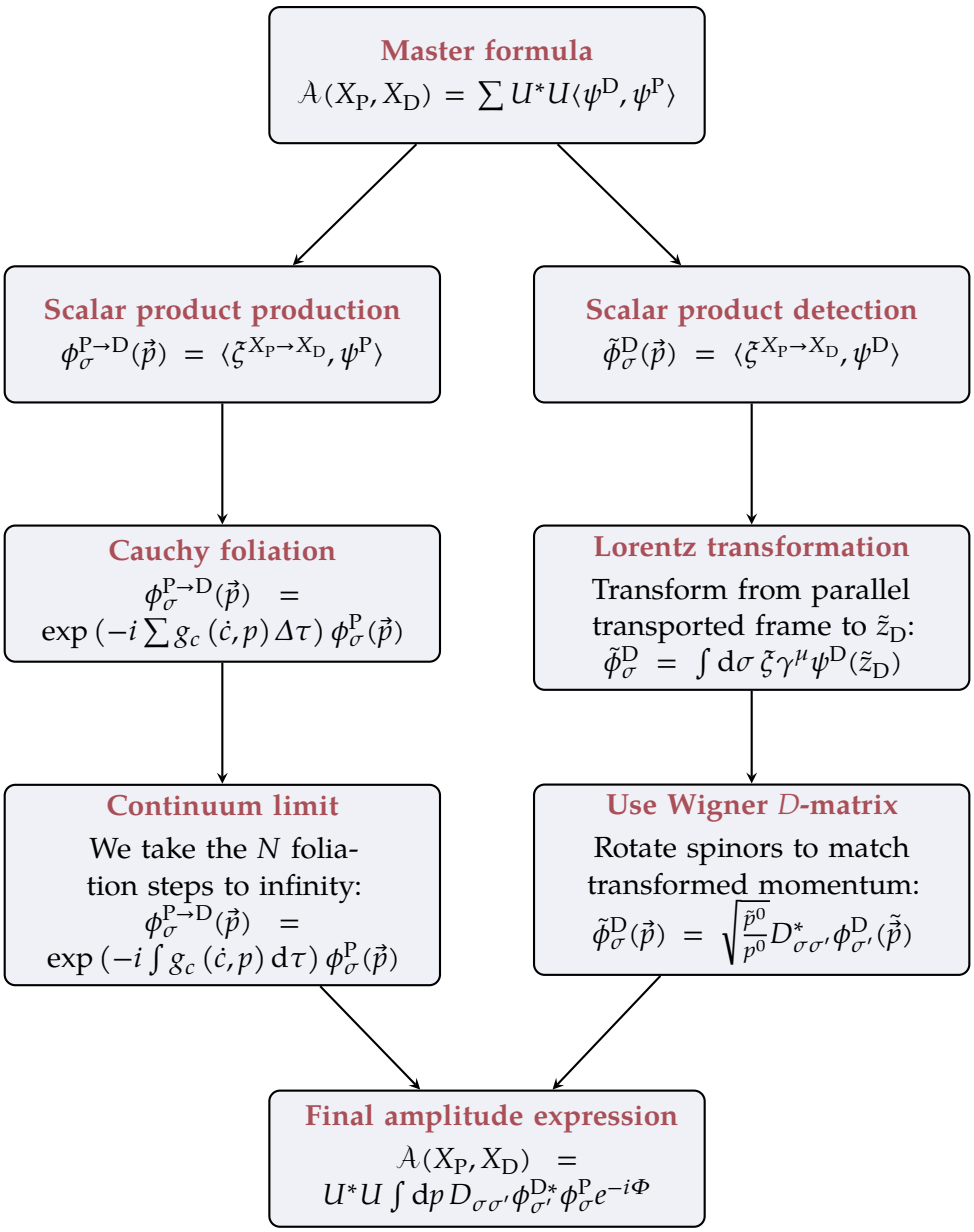

Figure 4.2: Schematic flowchart illustrating the probability derivation. The procedure involves a Lorentz transformation of the local frame, rewriting the spinor overlap, the application of a Wigner D-matrix to match spinor representations, cauchy foliations and the continuum limit $N \to \infty$.

surface Σ_τ[1]. To establish this result, we first prove by induction in appendix B that the wave packet after N finite steps is given by

$$\phi_\sigma^{\mathrm{P}\to\mathrm{D}}(\vec{p}) = \exp\left(-i\sum_{k=0}^{N} g_{\mu\nu}(c(\tau_k))\dot{c}^\mu(\tau_k)p^\nu(\tau_k)\Delta\tau + O(\Delta\tau^2)\right)\phi_\sigma^{\mathrm{P}}(\vec{p}) + O\left(\sum_{k=0}^{N} R_k\sigma_{\tau_k}^2\Delta\tau\right). \tag{4.37}$$

There, the inductive step builds on the relation between the propagated wave packet at step $k+1$

$$\phi_\sigma^{\mathrm{P}\to k+1}(\vec{p}) := \langle \xi_{\vec{p}\sigma}^{X_{\mathrm{P}}\to X_{k+1}}, \psi^{\mathrm{P}}\rangle, \tag{4.38}$$

and the one at step k. We evaluate this scalar product on the Cauchy surface Σ_k in the local coordinates z_k, yielding

$$\phi_\sigma^{\mathrm{P}\to k+1}(\vec{p}) = \int\limits_{\Sigma_k\cap U_\nu} \mathrm{d}\sigma_\mu(z_k)\,\bar{\xi}_{\vec{p}\sigma}^{X_{\mathrm{P}}\to X_{k+1}}(z_{k+1}(z_k))\gamma^\mu(z_k)\psi^{\mathrm{P}}(z_k). \tag{4.39}$$

Crucially, the integral only extends over the region U_ν, which contains the support of all mass eigenstate wave packets. This localization allows us to invoke the equivalence principle and approximate the mode functions by their flat spacetime expressions:

$$\phi_\sigma^{\mathrm{P}\to k+1}(\vec{p}) \approx \int\limits_{\Sigma_k\cap U_\nu} \mathrm{d}\sigma_\mu(z_k)\,\frac{e^{ig_{X_{k+1}}(p,z_{k+1}(z_k))}}{\sqrt{(2\pi)^3 2p^0}}\bar{u}_\sigma(\vec{p})\gamma^\mu\psi^{\mathrm{P}}(z_k). \tag{4.40}$$

This approximation holds because we choose N large enough that consecutive points X_k and X_{k+1} lie within the local region where curvature corrections are negligible. The scalar product $g(p,z)$ appearing in the phase factor is written in a coordinate-independent form by expressing both p and z_{k+1} in the parallel-transported basis $E_\mu(\tau_{k+1})$. This allows the phase to be reexpressed on the tangent space at X_k via:

$$g_{X_{k+1}}(p, z_{k+1}(z_k)) = g_{X_k}(P^c_{\tau_{k+1}\to\tau_k}p, P^c_{\tau_{k+1}\to\tau_k}z_{k+1}(z_k)). \tag{4.41}$$

Using the parallel-transport properties of the frame E_μ, we find that the components of the momentum remain constant:

$$P^c_{\tau_{k+1}\to\tau_k}p = p^\mu E_\mu(\tau_k), \tag{4.42}$$

Thus, the phase factor becomes:

$$g_{X_{k+1}}(p, z_{k+1}(z_k)) = \eta_{\mu\nu}p^\mu\left(P^c_{\tau_{k+1}\to\tau_k}z_{k+1}(z_k)\right)^\nu. \tag{4.43}$$

To determine how the coordinate vector $z_{k+1}(z_k)$ changes under parallel transport to X_k, we perform a Taylor expansion of the composition of exponential maps involved in the transition between the local inertial frames at X_{k+1} and X_k. This is achieved by constructing a geodesic variation with fixed endpoints and solving the associated Jacobi equation with boundary conditions determined by the neutrino trajectory. Using the

[1]We define the diameter of a spacelike subset $A \subset \mathcal{M}$ as $\sigma(A) := \sup_{x,y\in A}\mathrm{d}(x,y)$, where d is the distance function induced by the positive-definite Riemann metric $-g|_A$.

assumption that the gravitational field is approximately homogeneous across the wave packet support, the Jacobi field can be computed analytically to leading order. The result reads

$$\left(P^{c}_{k+1\to k} z_{k+1}(z_k)\right)^{\nu} = z_k^{\nu} - \dot{c}_k^{\nu}\Delta\tau + O(\Delta\tau^2, Rz^2)\,, \tag{4.44}$$

where $\dot{c}_k^{\nu}$ denotes the tangent vector of the geodesic at X_k, and z_k^{ν} the coordinates of the point in the local inertial frame. A detailed derivation is given in appendix A.
Substituting this into the scalar product in equation (4.40) yields:

$$\begin{aligned}
\phi_{\sigma}^{\mathrm{P}\to k+1}(\vec{p}) &= \int\limits_{\Sigma_k\cap U_\nu} \mathrm{d}\sigma_\mu(z_k)\, e^{-ip_\mu \dot{c}^\mu(\tau_k)\Delta\tau + O(\Delta\tau^2)} \underbrace{\frac{e^{ip_\mu z_k^\mu}}{\sqrt{(2\pi)^3 2p^0}}\bar{u}_\sigma(\vec{q})\,\gamma^\mu(z_k)\psi^{\mathrm{P}}(z_k)}_{\approx \bar{\xi}^{X_\mathrm{P}\to X_k}_{\vec{p}\sigma}(z_k)} \\
&\quad + O(R_k\sigma^2_{\tau_k}\Delta\tau) && (4.45)\\
&= e^{-ip_\mu\dot{c}^\mu(\tau_k)\Delta\tau + O(\Delta\tau^2)}\langle \xi^{X_\mathrm{P}\to X_k}_{\vec{p}\sigma}, \psi^{\mathrm{P}}\rangle + O(R_k\sigma^2_{\tau_k}\Delta\tau) && (4.46)\\
&= e^{-ip_\mu\dot{c}^\mu(\tau_k)\Delta\tau + O(\Delta\tau^2)}\phi_\sigma^{\mathrm{P}\to k}(\vec{p}) + O(R_k\sigma^2_{\tau_k}\Delta\tau)\,. && (4.47)
\end{aligned}$$

Here, we have truncated all terms of order Rz_k^2 and used the fact that $z_k^2 \lesssim \sigma_{\tau_k}$ due to the wave packet localization. This recursive relation completes the inductive proof of equation (4.37), as outlined in detail in appendix B. Iterating this step from Σ_P to Σ_D, we arrive at

$$\begin{aligned}
\phi_\sigma^{\mathrm{P}\to\mathrm{D}}(\vec{p}) &= \exp\left(-i\sum_{k=0}^{N}\eta_{\mu\nu}\dot{c}^\mu(\tau_k)p^\nu\Delta\tau + O(\Delta\tau^2)\right)\phi_\sigma^{\mathrm{P}}(\vec{p}) + O\left(\sum_k R_k\sigma^2_{\tau_k}\Delta\tau\right) && (4.48)\\
&= \exp\left(-i\sum_{k=0}^{N} g_{\mu\nu}(c(\tau_k))\dot{c}^\mu(\tau_k)p^\nu(\tau_k)\Delta\tau + O(\Delta\tau^2)\right)\phi_\sigma^{\mathrm{P}}(\vec{p}) \\
&\quad + O\left(\sum_k R_k\sigma^2_{\tau_k}\Delta\tau\right)\,. && (4.49)
\end{aligned}$$

In the second line, we have expressed all quantities in general coordinates, making the parallel transport of the momentum explicit via the time-dependent components $p^\mu(\tau)$. Taking the limit $N\to\infty$ then yields the result stated in equation (4.36).

4.2.2 Relating the Propagated and Detected Neutrino Wave Packets

The second key step in deriving the neutrino oscillation formula in weakly curved spacetime is to relate the detected momentum-space wave packet $\tilde{\phi}^{\mathrm{D}}_\sigma(\vec{p})$ to the propagated mode functions $\xi^{X_\mathrm{P}\to X_\mathrm{D}}$, rather than to the natural detection modes ξ^{D}. This is necessary since the propagation through spacetime is governed by the former, whereas the detection process projects onto the latter. The central object of interest is therefore the overlap integral from equation (4.35), which we now evaluate by expressing $\xi^{X_\mathrm{P}\to X_\mathrm{D}}$ in terms of ξ^{D}, and identifying a relation between the wave packets in both bases.
Both local inertial frames z_D and $\tilde{z}_\mathrm{D}$, constructed at the detection event X_D, are related by a local Lorentz transformation Λ. This follows from the definition of normal coordinates, which satisfy

$$g_{X_\mathrm{D}}\left(\frac{\partial}{\partial z^\mu_\mathrm{D}}(X_\mathrm{D}), \frac{\partial}{\partial z^\nu_\mathrm{D}}(X_\mathrm{D})\right) = \eta_{\mu\nu} = g_{X_\mathrm{D}}\left(\frac{\partial}{\partial \tilde{z}^\mu_\mathrm{D}}(X_\mathrm{D}), \frac{\partial}{\partial \tilde{z}^\nu_\mathrm{D}}(X_\mathrm{D})\right)\,, \tag{4.50}$$

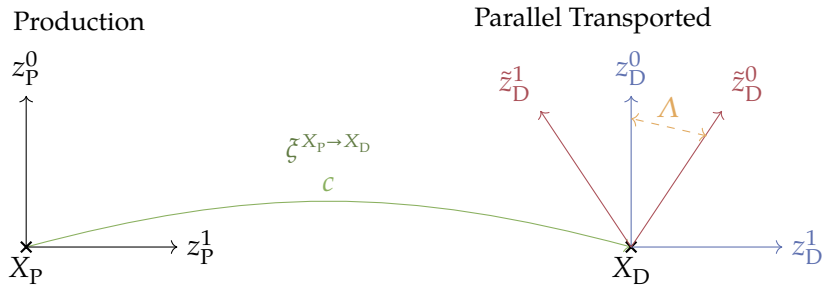

Figure 4.3: Illustration of the mismatch between the natural local frame $\tilde{z}_D$ associated with the detector and the parallel transported frame z_D used to define the propagated mode functions. The frames are related by a local Lorentz transformation Λ, which also induces a transformation of the spinor components. This transformation must be taken into account when evaluating the overlap integral between the propagated and detected neutrino wave packets.

and thus imply $z_D^\mu(\tilde{z}_D) = [\Lambda^{-1}]^\mu{}_\nu \tilde{z}_D^\nu$. See figure 4.3 for a schematic sketch of the different coordinate systems.
We choose the tetrad basis $\tilde{e}_\alpha$ associated with the detector observer O_D to coincide with the natural orthonormal basis of $\tilde{z}_D$ at X_D. This basis is related to the previously used propagation frame basis e_α by the same Lorentz transformation Λ:

$$\tilde{e}_\alpha(\tilde{z}_D) = [\Lambda^{-1}]^\beta{}_\alpha(\tilde{z}_D) e_\beta(z_D(\tilde{z}_D)) \,. \tag{4.51}$$

This transformation also acts on spinor fields with spin-1/2 representation $\Lambda_{1/2}(\tilde{z})$. In order to express the propagated mode function $\xi^{X_P \to X_D}(z_k)$ in terms of spinors evaluated in the detector frame $\tilde{z}_D$, we must apply $\Lambda_{1/2}$ appropriately. Using these relations, we now rewrite the inner product from equation (4.35) that defines the detected wave packet. We express everything in the frame $\tilde{z}_D$, where the detection process naturally takes place. The propagated mode function $\xi^{X_P \to X_D}(z_k)$ must first be evaluated in this frame, which requires a transformation of both its spacetime and spinor arguments. The resulting expression for the detected wave packet in momentum space reads

$$\tilde{\phi}_\sigma^D(\vec{p}) = \int_{\Sigma_D \cap U_\nu} \mathrm{d}\sigma_\mu(\tilde{z}_D)\, \bar{\xi}_{\vec{p}\sigma}^{X_P \to X_D}(z_D(\tilde{z}_D)) \gamma^\mu(\tilde{z}_D) \psi^D(\tilde{z}_D) \,. \tag{4.52}$$

Since all fields are localized around X_D, we neglect correction of order $O\left(\tilde{z}_D^2\right)$, as in the propagation step. This allows us to approximate the spinor transformation by a constant Lorentz transformation $\Lambda_{1/2}^{-1}(0)$, and the mode function becomes

$$\tilde{\phi}_\sigma^D(\vec{p}) \approx \int_{\Sigma_D \cap U_\nu} \mathrm{d}\sigma_\mu(\tilde{z}_D) \frac{e^{i p_\mu [\Lambda^{-1}]^\mu{}_\rho \tilde{z}_D^\rho}}{\sqrt{(2\pi)^3 2p^0}} \bar{u}_\sigma(\vec{p}) \Lambda_{1/2}^{-1}(0) \gamma^\mu \psi^D(\tilde{z}_D) \,, \tag{4.53}$$

where the spinor $\bar{u}_\sigma(\vec{p})$ is defined with respect to the propagation frame. To express the integral entirely in the detection frame, we relate this spinor to the standard spinor defined in $\tilde{z}_D$ via the spin-1/2 representation of the Lorentz transformation. This relation reads

$$\Lambda_{1/2} u_\sigma(\vec{p}) = \sum_{\sigma' = \pm 1/2} D^{1/2}_{\sigma\sigma'}(\Lambda, p) u_{\sigma'}(\tilde{\vec{p}}) \,, \qquad \tilde{p}^\mu := \Lambda^\mu{}_\nu p^\nu \,, \tag{4.54}$$

with the Wigner D-matrix $D^{1/2}_{\sigma\sigma'}$. Inserting this identity into equation 4.53 and absorbing the normalization factor, we obtain the final form of the detected wave packet in the detection frame:

$$\tilde{\phi}^{\mathrm{D}}_{\sigma}(\vec{p}) \approx \sqrt{\frac{\tilde{p}^0}{p^0}} \sum_{\sigma'=\pm 1/2} D^{1/2*}_{\sigma\sigma'}(\Lambda, p)\phi^{\mathrm{D}}_{\sigma'}(\tilde{\vec{p}})\,. \tag{4.55}$$

A summary of these derivation steps is shown in figure 4.2. To complete the transition from the initial to the final frame, we emphasize that physical measurements are usually performed only in the local rest frames of the source and the detector, represented by the coordinates z^μ_{P} and $\tilde{z}^\mu_{\mathrm{D}}$, respectively. Consequently, all tangent vectors defined at the detection point X_{D} and expressed in the parallel transported frame z^μ_{D} originate from the production frame and have been carried along the geodesic c via parallel transport. Due to the specific construction of the local frames z^μ_{D} and z^μ_{P} as RNC with parallel-transported bases, a given tangent vector will have the same component representation in both bases. This allows us to express the Lorentz transformation between the local detector frame $\tilde{z}^\mu_{\mathrm{D}}$ and the parallel transported frame z^μ_{D} as:

$$\Lambda^\alpha{}_\beta = \left.\frac{\partial \tilde{z}^\alpha_{\mathrm{D}}}{\partial x^\sigma}\right|_{X_{\mathrm{D}}} [P^c_{0\to\tau}]^\sigma{}_\rho \left.\frac{\partial x^\rho}{\partial z^\beta_{\mathrm{P}}}\right|_{X_{\mathrm{P}}}\,, \tag{4.56}$$

where $P^c_{0\to\tau}$ denotes the parallel transport operator along the curve c, written in arbitrary coordinates x^μ. This Lorentz transformation not only aligns the frames but also encapsulates possible gravitational redshift and Doppler effects arising from curved spacetime or the relative motion between production and detection.
The full neutrino flavor transition amplitude for strongly localised wave packets then takes the form:

$$\mathcal{A}_{ab}(X_{\mathrm{P}}, X_{\mathrm{D}}) \approx \sum_j U^*_{aj}U_{bj} \sum_{\sigma,\sigma'=\pm 1/2} \int \mathrm{d}^3\vec{p} \sqrt{\frac{\tilde{p}^0_j}{p^0_j}} D^{1/2}_{\sigma\sigma'}(\Lambda, p_j)\phi^{\mathrm{D}*}_{j\sigma'}(\tilde{\vec{p}}_j)\phi^{\mathrm{P}}_{j\sigma}(\vec{p}) e^{-i\Phi_j(p_j, X_{\mathrm{P}}, X_{\mathrm{D}})}\,, \tag{4.57}$$

where we made the mass eigenstate label j explicit again, and with the oscillation phase

$$\Phi_j(p_j, X_{\mathrm{P}}, X_{\mathrm{D}}) = \int_0^\tau \mathrm{d}\tau'\, g_{\mu\nu}(c(\tau'))\dot{c}^\mu(\tau')p^\nu_j(\tau')\,. \tag{4.58}$$

An equivalent expression is obtained by expressing all quantities in the detector frame using the momentum q^μ_j defined in $\tilde{z}_{\mathrm{D}}$:

$$\mathcal{A}_{ab}(X_{\mathrm{P}}, X_{\mathrm{D}}) \approx \sum_j U^*_{aj}U_{bj} \sum_{\sigma,\sigma'=\pm 1/2} \int \mathrm{d}^3\vec{q} \sqrt{\frac{\hat{q}^0_j}{q^0_j}} D^{1/2*}_{\sigma'\sigma}(\Lambda^{-1}, q_j)\phi^{\mathrm{D}*}_{j\sigma'}(\vec{q})\phi^{\mathrm{P}}_{j\sigma}(\hat{\vec{q}}_j) e^{-i\Phi'_j(q_j, X_{\mathrm{P}}, X_{\mathrm{D}})}\,, \tag{4.59}$$

where

$$\Phi'_j(q_j, X_{\mathrm{P}}, X_{\mathrm{D}}) = \int_0^\tau \mathrm{d}\tau'\, g_{\mu\nu}(c(\tau'))\dot{c}^\mu(\tau')q^\nu_j(\tau')\,, \tag{4.60}$$

and with the momentum $\hat{q}_j^\mu := [\Lambda^{-1}]^\mu{}_\nu q_j^\nu$ transformed back to the parallel transported frame.
The expressions in equation (4.57) and (4.59) represent the central result of this work: a fully covariant generalization of the plane wave formalism for neutrino oscillations in curved spacetime, originally formulated using the Stodolsky phase [211, 213, 226], to the case of propagating neutrino wave packets. To recover the standard plane wave description, we consider wave packets sharply peaked in momentum space around the mean four-momentum

$$\bar{p}_j^\mu = m_j \dot{c}_j^\mu(0)\,, \tag{4.61}$$

where $\dot{c}_j^\mu(0)$ denotes the initial velocity of mass-j geodesic and is related to the mean momentum by $\bar{p}_j^\mu/m_j$. In this limit, the oscillation phase Φ_j varies slowly over the width of the momentum distribution, allowing us to apply the mean value theorem and evaluate Φ_j at $\bar{p}_j$, pulling it out of the momentum integral in equation (4.57). This yields

$$\Phi_j(\bar{p}_j, X_\mathrm{P}, X_\mathrm{D}) \approx m_j \int_0^\tau \mathrm{d}\tau'\, \dot{c}_j^\mu(\tau') g_{\mu\nu}(c(\tau'))\dot{c}^\nu(\tau')\,. \tag{4.62}$$

Since the parallel-transported velocity $P^c_{0\to\tau}\dot{c}_j(0)$ approximately equals $\dot{c}_j(\tau)$ for $c_j(\tau) \approx c(\tau)$, this expression reduces to the familiar Stodolsky phase in curved spacetime.
Given that neutrinos are produced and detected through Lorentz-covariant weak interactions, it is natural to assume that the associated wave packets transform consistently under Lorentz transformations. Within our normalization, this is expressed as

$$\phi^\mathrm{R}_{j\sigma}(\vec{p}) = \frac{\varphi^\mathrm{R}_{j\sigma}(p_j)}{\sqrt{(2\pi)^3 2p_j^0}}\,, \quad \text{with} \qquad \tilde{\varphi}^\mathrm{R}_{j\sigma}(p_j) = \varphi^\mathrm{R}_{j\sigma}(\Lambda^{-1}p_j)\,, \tag{4.63}$$

for $\mathrm{R} \in \{\mathrm{P}, \mathrm{D}\}$. Considering a simple class of neutrino wave packets specified by a mean momentum $P^\mu_{\mathrm{R}j}$ and a width tensor

$$\Sigma^{\mu\nu}_{\mathrm{R}j} := \sum_{\sigma=\pm 1/2} \int \mathrm{d}^3\vec{p}\, |\phi^\mathrm{R}_{j\sigma}(\vec{p})|^2 p_j^\mu p_j^\nu - P^\mu_{\mathrm{R}j} P^\nu_{\mathrm{R}j}\,, \tag{4.64}$$

and inserting it into equation (4.59), we obtain the detection-frame respresentation:

$$\begin{aligned}\mathcal{A}_{ab}(X_\mathrm{P}, X_\mathrm{D}) \approx \sum_j U^*_{aj}U_{bj} \sum_{\sigma,\sigma'=\pm 1/2} \int \frac{\mathrm{d}^3\vec{q}}{(2\pi)^3 2q_j^0} D^{1/2*}_{\sigma'\sigma}(\Lambda^{-1}, q_j) \\ \times \varphi^{\mathrm{D}*}_{j\sigma'}(q_j; P_{\mathrm{D}j}, \Sigma_{\mathrm{D}j}) \varphi^\mathrm{P}_{j\sigma}(q_j; \Lambda P_{\mathrm{P}j}, \Lambda^T \Sigma_{\mathrm{P}j}\Lambda) e^{-i\Phi'_j(q_j, X_\mathrm{P}, X_\mathrm{D})}\,.\end{aligned} \tag{4.65}$$

An analogous expression follows in the source-based description.
In neutrino oscillation experiments, the neutrino spin is typically not measured. We therefore average the squared amplitude $|\mathcal{A}_{ab}|^2$ over initial spin states. In the common case where the quantization axis is chosen so that only one spin state $\bar{\sigma}$ is produced and detected, the averaged squared amplitude simplifies to:

$$\overline{|\mathcal{A}_{ab}|^2} = \sum_{jk} U^*_{aj}U_{bj}U_{ak}U^*_{bk} \frac{1}{2} \sum_{\bar{\sigma}\bar{\sigma}'} D^{1/2*}_{\bar{\sigma}\bar{\sigma}'}(\Lambda, p_j) D^{1/2}_{\bar{\sigma}\bar{\sigma}'}(\Lambda, q_k) \mathcal{J}_{jk\bar{\sigma}\bar{\sigma}'}\,, \tag{4.66}$$

where $\mathcal{J}_{jk}\bar{\sigma}\bar{\sigma}'$ denotes the remaining momentum integrals over the product of wave packet shapes and oscillation phases. For sharply peaked distributions, the Wigner D-matrices can be evaluated at the mean momenta $\bar{p}_j$ and $\bar{q}_k$, yielding only small corrections of order $O(\Delta\bar{p}_{jk})$. These corrections are neglected here, since they are not enhanced by macroscopic propagation distances.
Finally, the oscillation phase Φ'_j from equation (4.60) can be recast in a form closely resembling the flat spacetime case. Using the constancy of the scalar product $g_{\mu\nu}\dot{c}^\mu q_j^\nu$ along the geodesic, the phase evaluates to

$$\Phi'_j(q_j, X_\mathrm{P}, X_\mathrm{D}) = \underbrace{\eta_{\mu\nu}\dot{\bar{c}}^\mu(\tau)\tau}_{=L_\nu}\, q_j^\nu\,, \tag{4.67}$$

where all quantities are expressed in the local inertial frame of the detector O_D, which is the natural reference for an experimental analysis.
The derivation above provides the complete expression for neutrino flavor transition amplitudes in weak gravitational fields, incorporating the full wave packet structure and the effects of parallel transport, Lorentz transformation, and spinor rotations. Importantly, the resulting formulas naturally reduce to their flat spacetime counterparts in the appropriate limit. Moreover, they reproduce the familiar Stodolsky phase.
With this framework established, we are now equipped to explore specific metrics and experimental configurations, assessing the magnitude and observability of the predicted effects.

4.3 Gravitational Influence on Terrestrial Neutrino Experiments

Neutrino oscillation studies can be broadly divided into two regimes:

1. Experiments where both production and detection occur within the vicinity of Earth.
2. Observations of neutrinos originating from astrophysical or cosmological sources.

In the following, we focus on the first class, terrestrial experiments, which includes current and upcoming setups covering short- and long-baseline accelerator experiments as well as atmospheric neutrino measurements. Such experiments, due to their controlled conditions and precisely known baselines, provide an ideal setting to quantify possible gravitational corrections with minimal astrophysical uncertainties.
To evaluate possible gravitational effects in this regime, we apply equation (4.59) to neutrinos propagating near Earth. The relevant spacetime geometry can be accurately described in the linear gravity approximation, i.e., by expanding the metric as

$$g_{\mu\nu} = \eta_{\mu\nu} + \varepsilon h_{\mu\nu} + O(\varepsilon^2)\,, \tag{4.68}$$

where $\varepsilon \ll 1$ quantifies the gravitational field strength. This framework is not only valid for Earth's gravitational field but also extends to weak perturbations from GWs or smooth large-scale potentials such as galactic fields [227]. Even though we focus on terrestrial experiments, the treatment is general enough to also allow us the discussion of possible effects on astrophysical neutrinos.
Since we do not track spin in the considered set-ups, the spin label is omitted. We work with a Lorentz-covariant formulation for neutrino mass eigenstates as in equations (4.63),

which allows us to use the locally inertial form in equation (4.65) for the amplitude $\mathcal{A}_{ab}$. The production and detection wave packets are taken as Gaussian in momentum space [61, 228, 229]

$$\phi_j(\vec{p}) := \{(2\pi)^3 \det(\Sigma_j)\}^{-\frac{1}{4}} \exp\left(-\frac{1}{2}(\vec{p}-\vec{P}_j)^T \Sigma_j^{-1}(\vec{p}-\vec{P}_j)\right), \tag{4.69}$$

with mean momenta $\vec{P}_j = \tilde{\vec{P}}_{\mathrm{P}j}, \vec{P}_{\mathrm{D}j}$ and width tensors $\Sigma_j = \tilde{\Sigma}_{\mathrm{P}j}, \Sigma_{\mathrm{D}j}$. We now compute the gravitationally corrected amplitude by integrating over momentum space in analogy to the flat spacetime case. The integration reveals three distinct signatures through which gravity could, in principle, affect the oscillation signal: momentum mismatch damping, longitudinal-transverse separation and gravitational redshift of mean momenta. Carrying out the momentum integration analogous to the flat spacetime case yields

$$\begin{aligned}\mathcal{A}_{ab}(X^\mu_{\mathrm{P}}, X^\mu_{\mathrm{D}}) = \sum_j U^*_{aj} U_{bj} \left(\sigma^3_{\mathrm{P}j}\sigma^3_{\mathrm{D}j}\det(\Sigma_j)\right)^{-\frac{1}{2}} \\ \times \exp\left(-\frac{(\tilde{\vec{P}}_{\mathrm{P}j} - \vec{P}_{\mathrm{D}j})^2}{4(\sigma^2_{\mathrm{P}j}+\sigma^2_{\mathrm{D}j})} - \frac{1}{2}(\bar{\vec{v}}_j L^0 - \vec{L})^T \Sigma_j^{-1}(\bar{\vec{v}}_j L^0 - \vec{L})\right) \exp\left(-iL_\mu \bar{p}^\mu_j\right),\end{aligned} \tag{4.70}$$

where $\Sigma_{\mathrm{R}j} = \sigma^2_{\mathrm{R}j}\mathbb{1}$ for $\mathrm{R} = \mathrm{P}, \mathrm{D}$ and the Lorentz boost of $\tilde{\sigma}_{\mathrm{P}j}$ has been neglected, as the relative velocities between production and detector are taken non-relativistic. Here, the average four-momentum $\bar{p}^\mu_j$ and the group velocity $\bar{\vec{v}}_j$ are

$$\bar{p}^0_j := \bar{E}_j := \sqrt{\bar{\vec{p}}_j^{\,2} + m_j^2}, \qquad \bar{\vec{p}}_j := \frac{\sigma^2_{\mathrm{D}j}\tilde{\vec{P}}_{\mathrm{P}j} + \sigma^2_{\mathrm{P}j}\vec{P}_{\mathrm{D}j}}{\sigma^2_{\mathrm{P}j}+\sigma^2_{\mathrm{D}j}}, \qquad \bar{\vec{v}}_j := \frac{\bar{\vec{p}}_j}{\bar{E}_j}. \tag{4.71}$$

The position-space covariance,

$$\Sigma_j := \left(\frac{1}{\sigma^2_{\mathrm{P}j}} + \frac{1}{\sigma^2_{\mathrm{D}j}}\right)\mathbb{1} + \frac{iL^0}{\bar{E}_j}(\mathbb{1} - \bar{\vec{v}}_j \bar{\vec{v}}_j^{\,T}), \tag{4.72}$$

controls the overlap between production and detection wave packets. Only states with $\bar{\vec{v}}_j L^0 \sim \vec{L}$ within the uncertainty given by Σ_j contribute significantly. The same factor enforces approximate mean momentum conservation and includes potential gravitational redshift effects on $\tilde{\vec{P}}_{\mathrm{P}j}$.

To simplify the general three-dimensional description of the amplitude in equation (4.70), it is instructive to diagonalise the position-space covariance matrix Σ_j. By construction, one eigenvector corresponds to the mean propagation direction of the j-th mass eigenstate, $\hat{v}^\parallel_j := \bar{\vec{p}}_j/|\bar{\vec{p}}_j|$, while the remaining two eigenvectors, denoted $\hat{v}^\perp_{j1}$ and $\hat{v}^\perp_{j2}$, form an orthonormal basis of the plane orthogonal to $\hat{v}^\parallel_j$. In this eigenbasis, the longitudinal and transverse eigenvalues of Σ_j are given by

$$\sigma^2_{\parallel j} := \frac{1}{2}\left(\frac{1}{\sigma^2_{\mathrm{P}j}} + \frac{1}{\sigma^2_{\mathrm{D}j}}\right) + \frac{iL^0}{\bar{E}_j}(1 - \bar{\vec{v}}_j^{\,2}), \quad \sigma^2_{\perp 1j} = \sigma^2_{\perp 2j} = \sigma^2_{\perp j} := \frac{1}{2}\left(\frac{1}{\sigma^2_{\mathrm{P}j}} + \frac{1}{\sigma^2_{\mathrm{D}j}}\right) + \frac{iL^0}{\bar{E}_j}. \tag{4.73}$$

These quantities determine the spatial extent of the overlap region between production and detection wave packets. In particular, the real parts of their inverses define the coherence length scales in the parallel and perpendicular directions. The baseline vector $\vec{L}$ can be decomposed into parallel and perpendicular components with respect to $\hat{v}_j^{\parallel}$,

$$\vec{L} = \vec{L}_{\parallel} + \vec{L}_{\perp}\,, \quad \vec{L}_{\parallel} \parallel \hat{v}_j^{\parallel}\,, \quad \vec{L}_{\perp} \perp \hat{v}_j^{\parallel}\,. \tag{4.74}$$

From the Gaussian factor in equation (4.70), one finds that the amplitude is significantly suppressed whenever

$$|\vec{L}_{\perp}|^2 \lesssim \mathrm{Re}(\sigma_{\perp j}^{-2})^{-1} \ll |\vec{L}|^2\,. \tag{4.75}$$

Since in all realistic set-ups $\mathrm{Re}(\sigma_{\perp j}^{-2})^{-1} \ll |\vec{L}|^2$, this condition implies that $\vec{L} \approx \vec{L}_{\parallel}$, or equivalently $\vec{L}_{\perp} \approx 0$, up to corrections negligible in the present approximation scheme. This observation has an important practical consequence: for the purpose of evaluating the oscillation probability, the geometry effectively reduces to an one-dimensional propagation along the average momentum direction. All vector quantities in the problem can therefore be replaced by their absolute values, $\vec{a} \to a := |\vec{a}|$, without loss of accuracy, except for the mean production and detection momenta $\vec{\tilde{P}}_{\mathrm{P}j}$ and $\vec{P}_{\mathrm{D}j}$. These remain as full three-vectors, since they may still differ slightly in direction due to gravitational redshift or small effects, and are not yet fixed by the overlap condition.
In oscillation experiments, interference between different mass eigenstates occurs only if their central momenta and wave packet shapes are sufficiently similar. This allows us to impose the simplifying assumption $\sigma_{\mathrm{P}j} \equiv \sigma_{\mathrm{P}}$ and $\sigma_{\mathrm{D}j} \equiv \sigma_{\mathrm{D}}$ for all mass eigenstates j.
Let p and E denote, the momentum and energy, respectively, of a massless neutrino arriving at the detector. For each mass eigenstate, we define small deviations

$$\Delta p_j := \bar{p}_j - p\,, \qquad\qquad \Delta E_j := \bar{E}_j - E\,, \tag{4.76}$$

where $\bar{p}_j$ and $\bar{E}_j$ are the averaged momentum and energy introduced earlier. Since terrestrial and astrophysical neutrinos are highly relativistic, these deviations scale as

$$\frac{\Delta p_j}{p} \sim \frac{m_j^2}{2p^2}\,, \qquad\qquad \frac{\Delta E_j}{E} \sim \frac{m_j^2}{2E^2}\,, \tag{4.77}$$

which are small compared to unity. In the following, we introduce the ultra-relativistic expansion parameter

$$\varepsilon_{\mathrm{UR}} \sim \frac{\Delta p_j}{p} \sim \frac{m_j^2}{p^2}\,, \tag{4.78}$$

and treat gravitational corrections through the separate small parameter ε from equation (4.68).
All expressions are expanded consistently up to $O(\varepsilon_{\mathrm{UR}}^2 \varepsilon)$, that is, second order in the ultra-relativistic deviations multiplied by first order in the gravitational perturbation. Terms of higher order in either $\varepsilon_{\mathrm{UR}}$ or ε are neglected. This expansion regime ensures that:

1. Kinematic effects from the small neutrino masses are retained to the extent that they can influence gravitational phase shifts.

2. No higher-order gravitational corrections beyond the linear approximation are included, which is consistent with equation (4.68).

With these simplifications, the subsequent derivation of the oscillation probability can be performed analytically, retaining explicit dependence on both Δp_j and ΔE_j where needed for phase and coherence effects.
To obtain the neutrino oscillation probability, the final step consists in evaluating the time integrals along the worldlines of the source and detector, as indicated in equation (4.21). We assume both the neutrino production point and the detector to be at rest with respect to the same coordinate system, where the metric takes the form given in equation (4.68). Accordingly, we parameterize their trajectories $X^\mu_{\mathrm{P}}(\overset{\frown}{T_{\mathrm{P}}})$ and $X^\mu_{\mathrm{D}}(\overset{\frown}{T_{\mathrm{D}}})$ by the corresponding coordinate times $\overset{\frown}{T}_{\mathrm{P/D}} \equiv T_{\mathrm{P/D}}$ as

$$X^\mu_{\mathrm{P}}(T_{\mathrm{P}}) \equiv \begin{pmatrix} T_{\mathrm{P}} \\ \vec{X}_{\mathrm{P}} \end{pmatrix}, \qquad X^\mu_{\mathrm{D}}(T_{\mathrm{D}}) \equiv \begin{pmatrix} T_{\mathrm{D}} \\ \vec{X}_{\mathrm{D}} \end{pmatrix}. \tag{4.79}$$

As shown in appendix C, the physical spacetime separation vector can be expressed as

$$L^\mu = \left(\delta^\mu{}_\nu + \frac{\varepsilon}{2}\delta l^\mu{}_\nu\right)\Delta X^\nu, \tag{4.80}$$

with

$$\begin{aligned}\delta l^\mu{}_\nu =& \langle h^\mu{}_\nu \circ c_0\rangle - \left[h^\mu{}_\nu(X_{\mathrm{D}}) - \langle h^\mu{}_\nu \circ c_0\rangle\right] \\ &+ \left[\langle \partial^\mu h_{\sigma\nu} \circ c_0\rangle - \left\langle \tau' \mapsto \int_0^{\tau'} \frac{\mathrm{d}\tau''}{\tau}\partial^\mu h_{\sigma\nu}(c_0(\tau''))\right\rangle\right]\Delta X^\sigma .\end{aligned} \tag{4.81}$$

Here, the average of a function f along the geodesic is defined as

$$\langle f\rangle \equiv \langle \tau' \mapsto f(\tau')\rangle := \int_0^\tau \frac{\mathrm{d}\tau'}{\tau} f(\tau'). \tag{4.82}$$

The Lorentz transformation contained in $\tilde{P}_{\mathrm{P}j}$ simplifies to

$$\Lambda^\mu{}_\nu = \delta^\mu{}_\nu - \frac{\varepsilon}{2}\lambda^\mu{}_\nu, \tag{4.83}$$

$$\lambda^\mu{}_\nu := \left[\langle \partial_\nu h^\mu{}_\rho \circ c_0\rangle - \langle \partial^\mu h_{\nu\rho} \circ c_0\rangle\right]\Delta X^\rho, \tag{4.84}$$

see appendix C. This confirms our earlier statement: in this regime the Lorentz transformation reduces to a small, non-relativistic boost with velocity proportional to the gravitational perturbation strength $\varepsilon \ll 1$.
With the amplitude $\mathcal{A}_{ab}$ at hand, the oscillation probability given in equation (4.21) then reads

$$P_{ab}(\vec{X}_{\mathrm{P}}, \vec{X}_{\mathrm{D}}, E) = \frac{\sum_{jk} U^*_{aj}U_{ak}U_{bj}U^*_{bk}I_{jk}(\vec{X}_{\mathrm{P}}, \vec{X}_{\mathrm{D}}, E)}{\sum_j |U_{aj}|^2 I_{jj}(\vec{X}_{\mathrm{P}}, \vec{X}_{\mathrm{D}}, E)}, \tag{4.85}$$

where the time integral I_{jk} containing the livetime intervals $[T_{\mathrm{P1}}, T_{\mathrm{P2}}]$ and $[T_{\mathrm{D1}}, T_{\mathrm{D2}}]$ of the neutrino production and detection, respectively, is given as

$$\begin{aligned} I_{jk}(\vec{X}_{\mathrm{P}}, \vec{X}_{\mathrm{D}}, E) \approx & \int_{T_{\mathrm{P1}}}^{T_{\mathrm{P2}}} \mathrm{d}T_{\mathrm{P}} \int_{T_{\mathrm{D1}}}^{T_{\mathrm{D2}}} \mathrm{d}T_{\mathrm{D}} \exp\left(-\frac{(\tilde{\vec{P}}_{\mathrm{P}j} - \vec{P}_{\mathrm{D}j})^2}{2\sigma_P^2} - \frac{(\tilde{\vec{P}}_{\mathrm{P}k} - \vec{P}_{\mathrm{D}k})^2}{2\sigma_P^2} \right) \\ & \times \exp\left(-\frac{(\bar{v}_j L^0 - L)^2}{2\sigma_{\|j}^2} - \frac{(\bar{v}_k L^0 - L)^2}{2\sigma_{\|k}^{2*}} \right) \\ & \times \exp\left(-i(\Delta E_{jk} L^0 - \Delta p_{jk} L) \right) . \end{aligned} \tag{4.86}$$

Here, $\Delta p_{jk} = \bar{p}_j - \bar{p}_k$ is the difference between the mean momenta. Corrections from the position-space covariance Σ_j are neglected since, for ultra-relativistic neutrinos, the only mass-index–dependent contribution comes from $\mathrm{Im}\left(I_{jk}\right)$, which is suppressed and not enhanced by the propagation distance.
Changing integration variables from $(T_{\mathrm{P}}, T_{\mathrm{D}})$ to $(\Delta T, T_{\mathrm{D}})$ with $\Delta T := T_{\mathrm{D}} - T_{\mathrm{P}}$, allows us to exploit the time-translation invariance of the amplitude at order $O(\varepsilon)$. Breaking of this invariance arises only at $O(\varepsilon)$ through a possible time dependence of the perturbation $h_{\mu\nu}$. Expanding the exponent around the point of maximal wave packet overlap $\Delta T_{jk}^{\star}$ and performing the Gaussian ΔT integral yields the final expression for the probability in linearly perturbed Minkowski spacetime

$$P_{ab}(\vec{X}_{\mathrm{P}}, \vec{X}_{\mathrm{D}}, E) = \int_{T_{\mathrm{D1}}}^{T_{\mathrm{D2}}} \frac{\mathrm{d}T_{\mathrm{D}}}{T_{\mathrm{D2}} - T_{\mathrm{D1}}} \hat{P}_{ab}(\vec{X}_{\mathrm{P}}, \vec{X}_{\mathrm{D}}, T_{\mathrm{D}}, E) , \tag{4.87}$$

$$\begin{aligned} \hat{P}_{ab}(\vec{X}_{\mathrm{P}}, \vec{X}_{\mathrm{D}}, T_{\mathrm{D}}, E) := & \sum_{jk} U_{aj}^* U_{ak} U_{bj} U_{bk}^* \exp\left(-i \frac{\Delta m_{jk}^2}{2E} \left[1 - \frac{\Delta p_j + \Delta p_k}{2E} \right] L(T_{\mathrm{D}}) \right) \\ & \times \exp\left(-\left[\frac{L(T_{\mathrm{D}})}{L_{jk}^{\mathrm{coh}}(T_{\mathrm{D}})} \right]^2 \right) \exp\left(-\frac{1}{2} \left[\frac{\Delta E_{jk}}{\sigma_E} \right]^2 \right) , \end{aligned} \tag{4.88}$$

with the effective energy width σ_E, the coherence length L_{jk}^{coh} and the mean energy differences ΔE_{jk} given as

$$L_{jk}^{\mathrm{coh}}(T_{\mathrm{D}}) := \sqrt{2}\sigma_X \left[\frac{(\Delta v_{jk}^+)^2}{1 + \chi_j^2 (L^0)^2 (T_{\mathrm{D}})} + \frac{(\Delta v_{jk}^-)^2}{1 + \chi_k^2 (L^0)^2 (T_{\mathrm{D}})} \right] = 4\sqrt{2}\sigma_X \frac{E^2}{|\Delta m_{jk}^2|} + O(\varepsilon_{\mathrm{UR}}^2) , \tag{4.89}$$

$$\Delta E_{jk} := \Delta p_{jk} + \frac{\Delta m_{jk}^2}{2E} - \frac{\Delta p_j m_j^2 - \Delta p_k m_k^2}{2E^2} - \frac{\Delta m_{jk}^4}{8E^3} , \tag{4.90}$$

$$\sigma_E := \sigma_X^{-1} . \tag{4.91}$$

In this expression, σ_X denotes the spatial width of the wave packet, $\Delta v_{jk}^{\pm}$ represent the effective velocity differences between the mass eigenstates j and k, and χ_j accounts for the spatial spreading of the wave packet associated with the j-th mass eigenstate. These

quantities are given by

$$\sigma_X := \frac{1}{4}\left(\frac{1}{\sigma_P^2} + \frac{1}{\sigma_D^2}\right), \tag{4.92}$$

$$\Delta v_{jk}^{\pm} = \mp\frac{\Delta m_{jk}^2}{4E^2} + \varepsilon\left(\frac{\delta v_{j0} + \delta v_{k0}}{2}\right) \pm \frac{\Delta p_j m_j^2 - \Delta p_k m_k^2}{2E^3} \pm \frac{\Delta m_{jk}^4}{8E^4} \mp \left(\frac{\Delta m_{jk}^2}{4E^2}\right)^2, \tag{4.93}$$

$$\chi_j = \frac{1}{2\sigma_X^2}\left(\frac{m_j^2}{E^3} - \frac{3\Delta p_j m_j^2}{E^4} - \frac{3m_j^4}{2E^5}\right). \tag{4.94}$$

Furthermore, the propagation time at which the overlap between the j-th and k-th neutrino mass eigenstates reaches its maximum is given by

$$L^0(\Delta T_{jk}^\star) = \frac{L(\Delta T_{jk}^\star)}{\tilde{v}_{jk}}, \tag{4.95}$$

$$\frac{1}{\tilde{v}_{jk}} := 1 + \frac{m_j^2 + m_k^2}{4E^2} + \varepsilon\frac{\delta v_{j0} + \delta v_{k0}}{2} - \frac{\Delta p_j m_j^2 + \Delta p_k m_k^2}{2E^3} - \frac{(\Delta m_{jk}^2)^2}{8E^4} - \frac{m_j^4 + m_k^4}{16E^4}, \tag{4.96}$$

and the geometric velocity shifts δv_{j0} at $\Delta T_{jk}^\star$ are defined by

$$\varepsilon\delta v_{j0} := -\frac{\varepsilon}{2}\frac{\sigma_D^2}{\sigma_P^2 + \sigma_D^2}\frac{m_j^2}{E^2}\frac{(\vec{\ell}\cdot\vec{e}_k)\lambda^k{}_\beta p^\beta}{E} = \frac{\sigma_D^2}{\sigma_P^2 + \sigma_D^2}\frac{m_j^2}{E^2}\left(\vec{P}_{Dj} - \vec{P}_{Pj}\right)\cdot\vec{\ell}. \tag{4.97}$$

Here, p^α denotes the four-momentum of a massless neutrino with $p = E$, propagating in the direction $\vec{\ell} = \vec{L}/L$ and $\lambda^k{}_\beta$ is defined in equation (4.83). These velocity shifts characterize the deviation of the geodesics c_j of the individual neutrino mass eigenstates from the reference geodesic c connecting X_P and X_D. Further details on the calculation are provided in appendix D.

For static gravitational fields, such as Earth-bound experiments, the integral over T_D becomes trivial since the amplitude depends only on ΔT. If the baseline satisfies $L \ll L_{jk}^{coh}$, the oscillation pattern is unaffected by gravity up to order $O\left(\varepsilon_{UR}^2\varepsilon\right)$. For $L \sim L_{jk}^{coh}$, geodesic deviations between different mass eigenstates affect the onset of decoherence via wave packet separation. Higher-order terms in ε and ε_{UR} can in principle modify the oscillation phase through geometric velocity shifts δv_{j0}, but these effects are too small to be measurable with current or near-future terrestrial experiments. The only potentially observable gravitational effect is the parallel transport of the initial momentum distribution, which could distort the length dependence of oscillations, though even this is negligible for laboratory baselines.

In contrast, for time-dependent perturbations $h_{\mu\nu}$ such as GWs, the T_D integration produces a non-trivial averaging over the oscillatory terms, which can act as a source of decoherence. This effect is only relevant if the variation of the baseline during the detector livetime is comparable to the oscillation length

$$L_{jk}^{osc} := 4\pi\frac{E}{\Delta m_{jk}^2}\left[1 - \frac{\Delta p_j + \Delta p_k}{2E}\right]^{-1}. \tag{4.98}$$

Given typical GWs strains of order $\Delta L/L \sim 10^{-20}$ [230], the resulting decoherence is negligible for terrestrial experiments and could only play a role for cosmic neutrinos. However, as discussed in reference [3] and in the following sections, their oscillations cannot be resolved, hiding such an effect.
Since we have shown that terrestrial experiments cannot probe gravitational corrections, one might turn to neutrinos traveling over astrophysical distances, where cumulative effects could in principle become relevant.

4.4 Gravitational Influence on Astrophysical Neutrinos

In the following, we turn to the second main class of neutrino sources: neutrinos originating from the Sun or from astrophysical and cosmological distances. For such sources, oscillatory signatures are unobservable with present or foreseeable experimental capabilities. The underlying reason is the enormous baseline L involved, which demands an exceptionally fine relative energy resolution

$$\frac{\Delta E}{E} \lesssim \frac{L^{\mathrm{osc}}_{jk}}{L}\,, \tag{4.99}$$

where ΔE is the absolute energy bin width, E the neutrino energy, and L^{osc}_{jk} the oscillation length defined in equation (4.98). Within this regime, our weak-field master formula from equation (4.57) or (4.59) simplifies substantially: the interference term with $j \neq k$ vanishes, leaving only the incoherent contributions

$$\begin{aligned} P_{ab} &= \sum_j \frac{|U_{aj}|^2|U_{bj}|^2}{N} \int_{\mathcal{J}_{\mathrm{D1}}}^{\mathcal{J}_{\mathrm{D2}}} \mathrm{d}\mathcal{J}_{\mathrm{D}} \int_{\mathcal{J}_{\mathrm{P1}}}^{\mathcal{J}_{\mathrm{P2}}} \mathrm{d}\mathcal{J}_{\mathrm{P}} \left| \int \mathrm{d}^3\vec{q} \sqrt{\frac{\hat{q}^0}{q^0}} \phi_j^{\mathrm{D}*}(\vec{q}) \phi_j^{\mathrm{P}}(\hat{\vec{q}}_j) e^{-iq_j^\mu L_\mu} \right|^2 \\ &= \sum_j \frac{|U_{aj}|^2|U_{bj}|^2}{N} \int_{\mathcal{J}_{\mathrm{D1}}}^{\mathcal{J}_{\mathrm{D2}}} \mathrm{d}\mathcal{J}_{\mathrm{D}} \int_{\mathcal{J}_{\mathrm{P1}}}^{\mathcal{J}_{\mathrm{P2}}} \mathrm{d}\mathcal{J}_{\mathrm{P}} \left| \langle \psi_j^{\mathrm{D}}, \psi_j^{\mathrm{P}} \rangle \right|^2 . \end{aligned} \tag{4.100}$$

As argued in reference [61], results derived for Gaussian wave packets apply more generally to sharply peaked wave packets of arbitrary shape. In this limit, the probability reduces to purely real damping factors enforcing approximate momentum matching $P^\mu_{\mathrm{D}j} \sim \tilde{P}^\mu_{\mathrm{P}j}$, and the localization condition $\vec{L} \sim \vec{\bar{v}}_j L^0$, where $\vec{\bar{v}}_j$ denotes the group velocity of the j-th mass eigenstate. If all eigenstates are nearly degenerate, $\Delta m^2_{jk} \ll E^2$, their production wave packets are centered at almost identical mean momenta, and therefore follow essentially the same geodesic trajectories. In this situation, the factors $|\langle \psi_j^{\mathrm{D}}, \psi_j^{\mathrm{P}} \rangle|^2$ are effectively independent of j and can thus be taken outside the sum in equation (4.100), and cancel against the normalization N. The resulting expression reproduces the well-known flat spacetime decoherence limit:

$$P_{ab} \to P^{\mathrm{deco}}_{ab} = \sum_j |U_{aj}|^2 |U_{bj}|^2 \,. \tag{4.101}$$

By the equivalence principle, mass eigenstate wave packets with the same initial velocity share the same geodesic path. In general, different masses imply slightly different initial group velocities, but as long as the gravitational field gradients along the trajectory are small, their paths remain aligned and the above result remains valid even within the

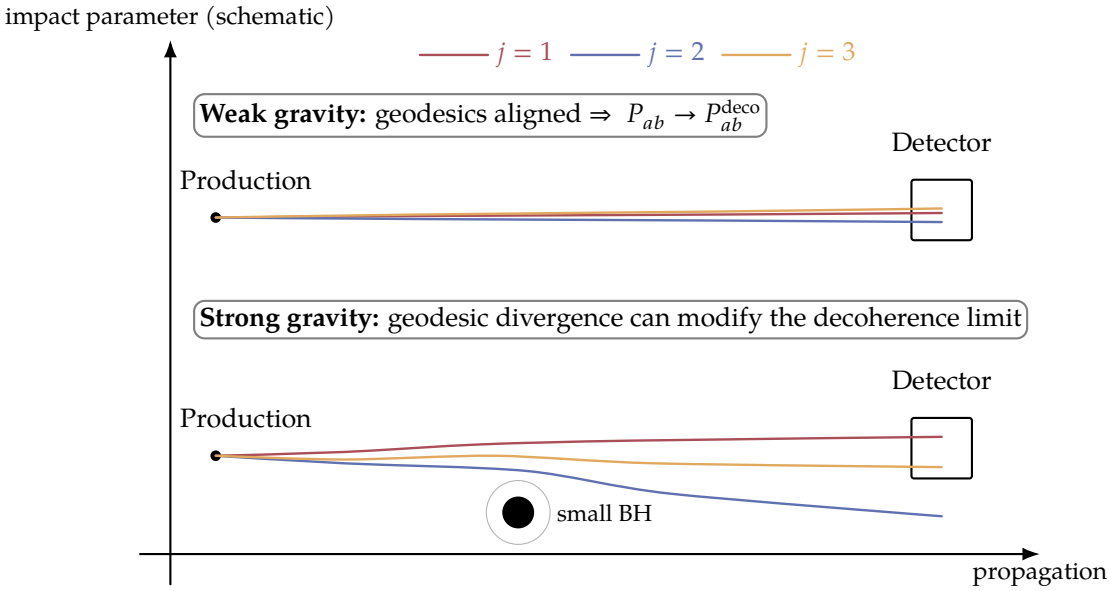

Figure 4.4: Schematic illustration of mass-eigenstate–dependent geodesics between production and detector. Upper (weak gravity): geodesics are nearly coincident, so the decoherence limit P_{ab}^{deco} remains valid. Lower (strong gravity; small black hole near the path): geodesics can diverge such that some mass eigenstates miss the detector while other might reconverge, making the scalar overlaps j-dependent.

general framework of equation (4.20). In such cases, gravitational corrections to flavor evolution can be safely neglected.

The situation changes in strong-field environments. Near compact objects such as small black holes, the geodesic of different mass eigenstates may separate so much that some never intersect the detector world volume within the experiment's livetime, effectively yielding $\psi_j^{\mathrm{D}} \approx 0$ for certain mass eigenstates j. Alternatively, the geodesic may diverge substantially during propagation but reconverge within the detector, leading to j-dependent overlaps $\langle \psi_j^{\mathrm{D}}, \psi_j^{\mathrm{P}} \rangle$ that break the factorization above. A schematic illustration is shown in figure 4.4. In practice, however, astrophysical neutrinos are typically produced in the vicinity of supermassive black holes, where the curvature is relatively mild [231]. The likelihood of encountering regions of extreme curvature, e.g., near microscopic black holes, during their journey to Earth is even smaller than that of traversing dense matter regions. For a recent assessment of black hole mass densities, see reference [232]. Consequently, the assumptions leading to equation (4.101) should hold for the overwhelming majority of cosmic neutrinos observed at Earth.

While this shows that static weak fields along astrophysical baselines fail to yield measurable deviations, time-dependent backgrounds such as GWs combined with astrophysical distances might appear more promising. In the following section we discuss under which circumstances this would yield measurable effects.

4.5 Estimation of Gravitational Wave Effects on Neutrino Oscillations

In our earlier work [3], we investigated two weak-field, time-dependent scenarios: a passing monochromatic GW and the Stochastic Gravitational Wave Background (SGWB).

Although the arguments in section 4.3 and 4.4 indicate that gravitational effects are unlikely to be observable for realistic sources and detectors, it is still worthwhile to estimate their possible size and to identify the parameter ranges in which they could become significant. In the monochromatic GW case, a varying production–detection distance can shift the oscillation pattern or, if the detection period exceeds the GW period, lead to gravitationally induced decoherence. Such signatures require low GW frequencies and very long baselines, as only then can the modulation become comparable to the oscillation length. For the SGWB, the relevant effect is an additional averaging over stochastic metric perturbations, which can further suppress oscillatory features depending on the background amplitude and correlation properties.
In reference [3], we developed a simple, intuitive model based on deviations from the static trajectory approximation to estimate these effects and compare them to standard decoherence mechanisms such as wave packet separation and finite energy resolution. We start from the standard expression for the flavor transition probability including a generic decoherence term $\mathcal{D}_{jk}$ accounting for wave packet separation

$$\hat{P}_{ab}(E,L) = \sum_j |U_{aj}|^2|U_{bj}|^2 + 2\sum_{j<k} \mathrm{Re}\left(U^*_{aj}U_{bj}U_{ak}U^*_{bk} \exp\left[-2\pi i \frac{L}{L^{\mathrm{osc}}_{jk}} - \mathcal{D}_{jk}(E,L) \right] \right) . \tag{4.102}$$

A GW modifies the propagation distance L by perturbing the neutrino geodesic. In the ultrarelativistic limit, the effect can be written as

$$L(t) = L_0 + \Delta L(t) \,, \tag{4.103}$$

where $\Delta L(t)$ encodes the GW induced variation of the production–detection separation and depends on the GW strain h, the frequency f and propagation direction. Note, that L_0 is the coordinate distance measured at a reference time t_0, for details see reference [3]. For a monochromatic plane wave, $\Delta L(t)$ oscillates at the GW frequency ω and vanishes in the flat spacetime limit and is given as

$$\begin{aligned} \Delta L(t) \approx -\frac{1}{2} \sum_{r\in\{+,\times\}} \int \mathrm{d}^3\vec{k}\, \psi^r(\vec{k}) \frac{A^r_\parallel(\varphi,\theta)}{\tilde{\omega}} \\ \times \left\{ \sin(\tilde{\omega}L_0)\cos(\omega t + \phi^r) + [\cos(\tilde{\omega}L_0) - 1]\sin(\omega t + \phi^r) \right\} , \end{aligned} \tag{4.104}$$

where ψ^r are real, positive momentum space wave packets and ϕ^r denote the phase shifts of the corresponding modes. Further, the reduced GW frequency $\tilde{\omega}$ and projected polarization tensors $A^r_\parallel$ are given as

$$\tilde{\omega} = \omega\,(1 - \cos\,(\theta))\;, A^+_\parallel(\varphi,\theta) = \sin^2\,(\theta)\cos\,(2\varphi)\,, \quad A^\times_\parallel(\varphi,\theta) = \sin^2\,(\theta)\sin\,(2\varphi)\,. \tag{4.105}$$

Since most oscillation experiments do not resolve individual production and detection times, we again need to average the probability over the data-taking period T,

$$P_{ab}(E,L_0) = \frac{1}{T}\int_0^T \hat{P}_{ab}(E, L_0 + \Delta L(t))\,\mathrm{d}t\,. \tag{4.106}$$

This time averaging suppresses the oscillatory term whenever the GW period is shorter than T, acting as an additional source of decoherence. This decoherence effect increases

with strain and baseline, and becomes significant only for low GW frequencies. Further details on the derivation of $\Delta L(t)$, including the solution of the perturbed geodesic equation and the role of GW polarization, can be found in reference [3].
Having established how GWs perturb the neutrino path length L and thereby modify the oscillation probability through time averaging, we now turn to the question of observability. Detecting such an effect in a real experiment requires a specific interplay between oscillation dynamics, detector capabilities, and source properties. We identify five general conditions:

1. **Oscillation length comparability:** The GW-induced modulation ΔL must be comparable to at least one neutrino oscillation length L_{jk}^{osc}; otherwise, the time averaging in equation (4.106) produces only a negligible change.

2. **Dominance over wave packet decoherence:** Loss of coherence due to wave packet separation must occur at longer baselines (or lower energies) than the GW effect, ensuring that the latter is not hidden.

3. **Energy resolution:** The energy bin width ΔE must be small enough such that oscillations are not washed out by averaging within a bin.

4. **Source localization:** The spatial extent Σ_{P} of the neutrino production region must be much smaller than the oscillation length L_{jk}^{osc}.

5. **Free separation:** The physical distance between production and detection must be modulated by the GW; rigid connections or mechanical forces suppress the effect.

Criteria 1. and 3. are in tension: oscillations must be fast enough for ΔL to vary significantly over the run time, but not so fast that finite ΔE erases them. To quantify this, we first consider the maximal GW induced change in baseline for a monochromatic plane wave in the low frequency regime $\tilde{\omega} \ll L_0^{-1}$, equation (4.104) reduces to

$$\max_{\omega t \in [0,2\pi)} |\Delta L(t)| = \frac{hL_0}{2}\,, \tag{4.107}$$

where h is an effective strain depending on the GW polarization and relative orientation between the GW and neutrino path. We conservatively assume that a discernible modulation requires

$$r = \frac{\max_{t\in\tau} |\Delta L(t)|}{L_{jk}^{\mathrm{osc}}} = \frac{\Delta m_{jk}^2}{4\pi E}\frac{hL_0}{2}\,, \tag{4.108}$$

to reach at least $r \approx 0.1$, ensuring that the ν_j–ν_k interference term is significantly damped. This sets a minimal baseline for a given neutrino energy E and GW strain h

$$L_{\min}(E) = 8\pi r \frac{E}{h\Delta m_{jk}^2} < L_0\,. \tag{4.109}$$

At the same time, wave packet coherence demands $L_0 < L_{jk}^{\mathrm{coh}}$, with

$$L_{jk}^{\mathrm{coh}} = \frac{4\sqrt{2}E^2}{\Delta m_{jk}^2}\sigma_x\,. \tag{4.110}$$

where σ_x is the wave packet width in position space. The observable range is therefore

$$8\pi r \frac{E}{h\Delta m^2_{jk}} < L_0 < \frac{4\sqrt{2}E^2}{\Delta m^2_{jk}}\sigma_x \,. \tag{4.111}$$

Even with this baseline window, the detector must resolve the oscillations in energy. For the (jk) channel this requires

$$\Delta E \lesssim \frac{2}{\Delta m^2_{jk}} \frac{E^2}{L_0} \,. \tag{4.112}$$

or, in terms of the relative energy resolution

$$\delta E := \Delta E/E \lesssim \frac{L^{\text{osc}}_{jk}}{2\pi L_0} \,. \tag{4.113}$$

Similarly, the source size Σ_{P} must satisfy

$$\Sigma_{\text{P}} \ll L^{\text{osc}}_{jk} \,, \tag{4.114}$$

to avoid spatial averaging of the oscillations.
To detect GW induced modulations, the production–detection separation must respond freely to spacetime distortions, analogous to the freely suspended mirrors in LIGO [85]. Astrophysical neutrino sources naturally satisfy this, since both the production region and the detector are in free fall within their gravitational fields. Promising candidates as such neutrino sources include the Sun, possible decays of DM particles bound in gravitational wells inside celestial bodies, and distant compact objects such as pulsars, blazars, or supernovae.
We can also combine criteria 1. and 3., which yields a link between the minimal detectable strain h_{min} and the experimental energy resolution:

$$h_{\text{min}} = 2r\frac{L^{\text{osc}}_{jk}}{L_0} = 4\pi r \delta E \,. \tag{4.115}$$

Even with optimistic values $\delta E_{\text{thr}} \sim 1\,\%$ and $r \approx 0.1$ [233], this gives

$$h_{\text{min}} \sim 1.3 \times 10^{-2} \,, \tag{4.116}$$

many orders of magnitude above the $\sim 10^{-20}$ sensitivity of current laser interferometers [234]. Achieving comparable sensitivity with neutrino oscillation experiments would therefore require an energy resolution δE at the $10^{-18}\,\%$ level, which is well beyond foreseeable capabilities [233]. Additional limitations arise if the GW coherence time T_{GW} is shorter than the experimental run time T_{exp}, which will suppress the time-averaged signal. Thus neutrino-based detection of coherent GWs appears feasible only for extremely long-lived, monochromatic signals, such as those from Supermassive Black Hole Binariess (SMBHB) [235] or Extreme Mass Ratio Inspirals (EMRI) [236], which can persist for $O\,(10\,\text{yr})$ or more [237].
Taking all constraints into account, coherent GW detection via neutrino oscillations is unlikely to compete with dedicated GW observatories. This conclusion is consistent with the indications from the previous sections, where order-of-magnitude estimates already suggested that the effect would be far below realistic detection thresholds. The

detailed criteria and sensitivity estimates developed here make this conclusion even more robust: they show quantitatively how the combined requirements on baseline, coherence, resolution, and signal duration confine the parameter space to a regime far beyond the reach of current or planned neutrino experiments.
In contrast to plane waves of well-defined astrophysical origin, the SGWB consists of an ensemble of coherent GWs, expected to populate the nanohertz frequency range. The recent evidence reported by pulsar timing array collaborations [238, 239] has triggered increased interest in its possible implications, including potential effects on neutrino oscillations [240, 241]. While the decoherence mechanism is qualitatively different from the coherent case and may evade some of the limitations identified above, we do not expect a significant influence on neutrino oscillations. Since the SGWB merely represents an ensemble of such GWs, it appears unlikely that the sensitivity would be substantially higher so as to render the effect observable. Nevertheless, earlier studies have explored this connection mainly at a qualitative level, highlighting the interplay between SGWB-induced decoherence and other damping mechanisms with promising results. Here, we follow a more quantitative route and subject the scenarios in reference [241] to a sophisticated analysis.
To this end, we define the decoherence term introduced in equation (4.102) by including both the standard wave packet separation and an additional contribution originating from the SGWB,

$$\mathcal{D}_{jk}(E, L_0) = \left(\frac{L_0}{L_{jk}^{\mathrm{coh}}} \right)^2 + \Gamma_{jk}^{\mathrm{SGWB}}(E) \,. \tag{4.117}$$

This modification rests on the same physical idea as before—namely, that gravitational perturbations alter the coherence properties of propagating neutrinos—but is formulated within the density matrix approach, see e.g. reference [240]. Since we have shown that averaging over the running time of a typical neutrino experiment yields negligible impact, we now focus exclusively on the stochastic perturbations introduced by the SGWB through which the system propagates.
The SGWB-induced damping factor is given by [241]

$$\Gamma_{jk}^{\mathrm{SGWB}}(E, L_0) = \left(\frac{3H_0}{8\pi L_{jk}^{\mathrm{osc}}} \right)^2 \int_{f_{\min}}^{f_{\max}} \frac{\mathrm{d}f}{f^5} \sin^2(\pi f L_0) \Omega_{\mathrm{GW}}(f) \,, \tag{4.118}$$

where $\Omega_{\mathrm{GW}}(f)$ denotes the fractional GW energy density, H_0 the Hubble constant today, and $f_{\min}$ and $f_{\max}$ the boundaries of the GW spectrum. The latter is typically modeled in terms of the characteristic strain $h_{\mathrm{c}}(f)$, parametrized by a power-law form,

$$h_{\mathrm{c}}(f) = A_* \left(\frac{f}{f_{\mathrm{yr}}} \right)^{\frac{3-\gamma}{2}} \,, \tag{4.119}$$

with $f_{\mathrm{yr}} = 1\,\mathrm{yr}^{-1} \approx 31.7\,\mathrm{nHz}$ as reference frequency, spectral index γ, and amplitude A_*. This leads to the energy density spectrum

$$\Omega_{\mathrm{GW}}(f) = \frac{2\pi^2}{3H_0^2} f_{\mathrm{yr}}^2 |A_*|^2 \left(\frac{f}{f_{\mathrm{yr}}} \right)^{1-\gamma} \,. \tag{4.120}$$

Since the UV part of the spectrum is strongly suppressed, we may safely take the upper limit $f_{\max} \to \infty$ as in reference [241]. Under this assumption, the SGWB contribution

Table 4.1: Values for the oscillation length L_{jk}^{osc} for different neutrino energies E and mass splitting of $\Delta m_{jk}^2 \sim 10^{-3}\,\mathrm{eV}^2$.

E	L_{jk}^{osc} / km
keV	2.4×10^{-3}
MeV	2.4
GeV	2.4×10^{3}
TeV	2.4×10^{6}
PeV	2.4×10^{9}
EeV	2.4×10^{12}

simplifies to

$$\Gamma_{jk}^{\mathrm{SGWB}} = \frac{3}{64}\left(\frac{|A_*|}{f_{\mathrm{yr}} L_{jk}^{\mathrm{osc}}}\right)^2 \left(\frac{f_{\mathrm{min}}}{f_{\mathrm{yr}}}\right)^{1-\gamma} \left(\frac{1}{(\gamma-1)} - \mathrm{Re}\left(E_\gamma(2\pi i f_{\mathrm{min}} L_0)\right)\right), \tag{4.121}$$

with $E_\gamma(z)$ being the exponential integral of order γ. In total, this description introduces three free parameters: the lower cutoff frequency f_{min}, the spectral ampltiude A_*, and the index γ.

In order to identify promising environments for probing the impact of the SGWB on neutrino oscillations, we now turn to possible neutrino sources ranging from terrestrial experiments to astrophysical emitters. The general criteria 2. to 5. remain applicable in this case, while criterion 1., formulated for coherent GW signals, is no longer valid in the stochastic case.

Starting with long-baseline experiments, we find that criterion 5. is not satisfied, which excludes sensitivity to SGWB-induced decoherence. The same conclusion holds for atmospheric neutrinos. Solar neutrinos, produced in the $\sim 100\,\mathrm{keV}$–MeV range, are also unsuitable: the production region would need to be localized on meter–kilometer scales to avoid averaging effects, see table 4.1, far below the size of the solar core. Hypothetical neutrinos originating from DM decays within gravitational wells are likewise unpromising, as no such signals have been observed. Astrophysical sources beyond the solar system appear more promising at first sight. Supernovae [242] are intense emitters of MeV neutrinos [243], but the localization requirement again proves prohibitive, since the source region would need to be known at the kilometer scale. Blazars, i.e., active galactic nuclei with jets pointing towards the Earth, could in principle emit neutrinos up to the EeV scale [244, 245]. At such high energies, the production region could extend to $\sim 10^{14}\,\mathrm{km}$ without fully averaging out the oscillation signal. However, the expected flux is far too low for statistical significance [246].

Therefore, the most promising candidates that remain are Galactic pulsars [247–257] such as Vela, Crab or Cas A [258–260], which are expected to produce comparatively high neutrino fluxes of order $30\,\mathrm{km}^{-2}\,\mathrm{yr}^{-1}$. For future telescopes with effective areas of $\sim 100\,\mathrm{km}^2$ and data-taking periods of ~ 20 years, event counts of $N \sim 10^4$ may be achievable. Neutrinos are likely generated in the pulsar magnetosphere or the surrounding wind nebula, where protons are accelerated and interact with ambient photons or

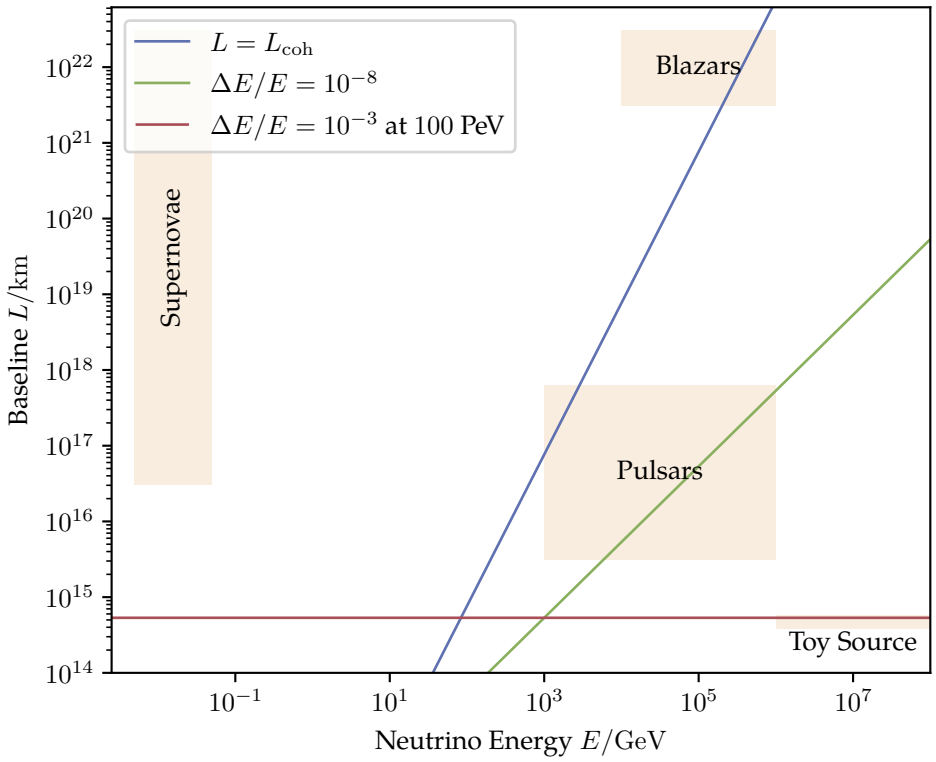

Figure 4.5: Energy–baseline parameter space for potential astrophysical neutrino sources and a toy source from reference [241]. Shaded regions indicate typical ranges for supernovae, pulsars and blazars. The blue line shows the coherence length L_{coh}, while the green and red curves represent different energy resolutions. Regions above the lines are subject to decoherence or energy smearing, indicating that no realistic astrophysical sources lie in a regime where such effects could be avoided.

baryons to produce pions, and hence, neutrinos [247–257, 261, 262]. With predicted energies in the range $E \sim 100\,\mathrm{TeV}$–$2\,\mathrm{PeV}$ [256], the oscillation lengths are larger than the estimated source size, cf. table 4.1. Even if the production region is not much smaller than L_{jk}^{osc}, partial averaging would merely induce additional damping, without fully erasing the oscillation signal. Pulsars thus emerge as the most plausible sources for a phenomenological analysis.

A compact overview of this discussion is shown in figure 4.5: shaded bands indicate the characteristic energy–baseline ranges of the source classes, i.e., supernovae, blazars and pulsars. The blue curve shows the coherence length L_{coh} (here for $\sigma_x = 1\,\mathrm{nm}$), so configurations above this line tend to lose wave packet coherence before reaching the detector. The green curve marks the energy-averaging threshold for a nominal resolution of $\Delta E/E = 10^{-8}$, i.e., combinations above this line are additionally suppressed by energy smearing. The red line illustrates an energy resolution of $\Delta E/E = 10^{-3}$ at 100 PeV. Source regions that lie below both curves at their relevant energies remain viable for observing oscillatory structure; those that sit predominantly above one (or both) curves are effectively washed out. To quantify the sensitivity to SGWB effects, we perform an analysis following the scenarios of reference [241]. We model an idealized experimental setup in which neutrino events are binned in energy and originate from a source at

distance L_0. The event distribution for a flavor b is then predicted as

$$\rho_b(E) = \sum_a \varphi_a(E) P_{ab}(E, L_0)\,, \tag{4.122}$$

with φ_a the source spectrum and P_{ab} the oscillation probability. We adopt a power-law spectrum $\varphi \propto E^{-2}$. For the statistical treatment we employ a Poisson likelihood,

$$\mathcal{L}(A_*, \gamma, f_{\min} \mid \vec{n}) = \prod_{b=1}^{n_f} \prod_{i=1}^{n} \mathrm{Pois}(n_{ib}, \eta_{ib}(A_*, \gamma, f_{\min}))\,, \tag{4.123}$$

where η_{ib} is the predicted event number in bin i, flavor b and n_{ib} is the observed count. The toy datasets are generated under the null hypothesis $\Gamma_{jk}^{\mathrm{SGWB}} = 0$, i.e., flat spacetime. The likelihood ratio tests are then performed in the (A_*, γ) and $(A_*, f_{\min})$ parameter planes for fixed values of $f_{\min}$ or γ, respectively. With the negative logarithmic likelihood ratio

$$\Lambda(\vec{n})|_{f_{\min}=f_{\min}^{\mathrm{fix}}} = -2 \ln \left(\frac{\mathcal{L}(A_{*0}, \gamma_0, f_{\min}^{\mathrm{fix}})}{\sup_{(A_*,\gamma)\in\mathbb{R}^2} \left(\mathcal{L}(A_*, \gamma, f_{\min}^{\mathrm{fix}})\right)} \right), \tag{4.124}$$

$$\Lambda(\vec{n})|_{\gamma=3} = -2 \ln \left(\frac{\mathcal{L}(A_{*0}, 3, f_{\min,0})}{\sup_{(A_*,f_{\min})\in\mathbb{R}^2} \left(\mathcal{L}(A_*, 3, f_{\min})\right)} \right), \tag{4.125}$$

on a grid in a region of our parameter space, where (A_{*0}, γ_0) and $(A_{*0}, f_{\min,0})$ denote the corresponding grid points, respectively. We now turn to the specific pulsar scenario from reference [241], assuming neutrinos with $E \in [1, 100]$ PeV emitted at a distance $L_0 \sim 50$ ly. With an energy resolution $\delta E/E \sim 0.1\,\%$ at 100 PeV, this choice avoids the unrealistic sub-$10^{-6}\,\%$ resolution that would be required for known pulsars such as Vela, see figure 4.5. Nevertheless, there is no known pulsar with this configuration. We assume $N \simeq 2 \times 10^4$ events and a flat E^{-2} spectrum, corresponding to an optimistic upper bound on the event rate. While astrophysical observations typically suggest softer spectra, e.g. $E^{-3.2}$ for NGC1068 [263] or $E^{-2.53}$ for the diffuse flux [264], we maintain the flat spectrum to maximize statistics at the highest energies. For simplicity, we further assume a pure ν_e flux and include wave packet decoherence with $\sigma_x \sim 1$ nm.
The resulting exclusion regions in the γ–A_* plane are displayed in figure 4.6, alongside the NANOGrav 15-year 68 % (95 %) credible region results in dark (light) green [238]. Our contours qualitatively reproduce the behavior of reference [241], but are quantitatively weaker since we refrain from expanding $\Gamma_{jk}^{\mathrm{SGWB}}$ in the $L_0 \gg 1/f_{\min}$ limit, which does not apply to the present configuration. The full expression reveals a strong cancellation between terms, effectively erasing sensitivity to the SGWB. Even in this optimistic setup, deviations from standard oscillations do not exceed $\sim 1.5\,\sigma$, far below significance. Moreover, the parameter regions excluded in our analysis are already ruled out by CMB bounds on Ω_{GW}, see e.g. reference [265].
For completeness, we also show exclusion limits in the $f_{\min}$–h_c plane for a flat spectrum ($\gamma = 3$) in figure 4.7. The limits are of order $O(0.1)$, comparable to those obtained for coherent GW signals, and remain many orders of magnitude less stringent than current astrophysical and cosmological constraints. Finally, we note that for much larger cutoff frequencies, $f_{\min} \sim 10^{-12}$–10^{-9} Hz, one would require MeV neutrinos, e.g. from supernovae. However, in this case decoherence due to wave packet separation has already occurred, and no SGWB signature could be expected unless coherence is

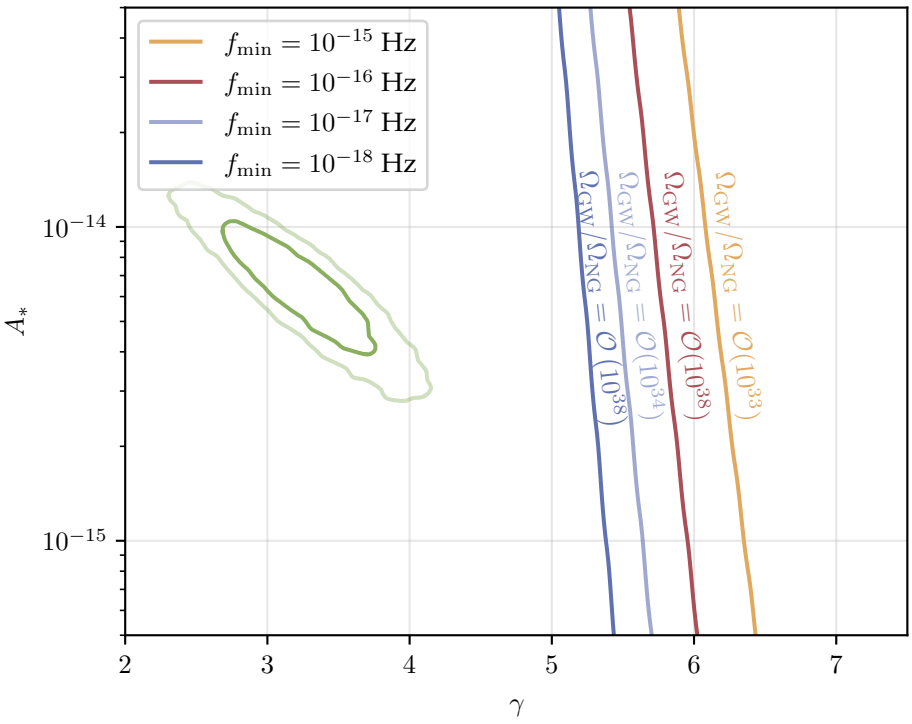

Figure 4.6: Dark (light) green: 68 % (95 %) credible regions of the NANOGrav 15-year result [238]. The lines show 68 % CL limits on the GW amplitude A_* and spectral index γ for $f_{\min} \in \{10^{-18}, 10^{-17}, 10^{-16}, 10^{-15}\}$. For each line we also indicate $\Omega_{\rm GW}/\Omega_{\rm NG}$ at the NANOGrav best-fit amplitude, corresponding to $\gamma \in \{5, 5, 6, 6\}$ from left to right.

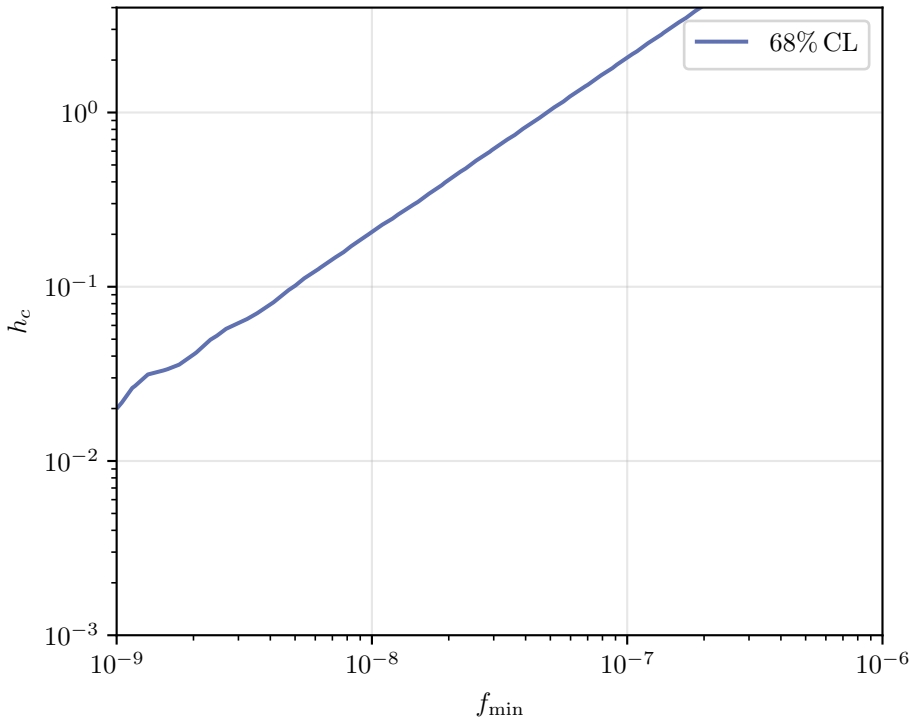

Figure 4.7: The blue line correspond to the limits at 68 % CL on the GW strain h_c and the minimal frequency $f_{\min}$ for a flat spectrum, i.e., $\gamma = 3$. Parameter configurations above this line are excluded if the effect of the SGWB is not observed in neutrino oscillation experiments at baselines $L_0 \sim 50\,\text{lyr}$, energies $E \in [1\,\text{PeV}, 100\,\text{PeV}]$, bin widths $\Delta E \lesssim 0.1\text{PeV}$ and neutrino wave packet widths $\sigma_x \sim 1\,\text{nm}$.

somehow restored, e.g. via matter effects [266]. Even if such mechanisms operated, the required energy resolution would be unrealistically stringent, and uncertainties in the source distance would further diminish prospects.

4.6 Summary and Discussion

In this chapter, we have investigated the impact of curved spacetime on neutrino oscillations from complementary perspectives. Our analysis combined a general theoretical framework with concrete applications: on the one hand, we extend the Lorentz-covariant internal wave packet formalism known from flat spacetime to arbitrary weakly curved spacetimes, yielding a master expression for the oscillation amplitude. On the other hand, we have applied this formalism in a simplified form to specific time-dependent geometries sourced by GWs. Moreover, we reasses the effect of the SGWB on neutrino oscillations.

The two approaches converge on a common conclusion: under realistic circumstances, classical gravitational effects on neutrino oscillations are exceedingly small. For terrestrial experiments in the weak-field limit, the formal influence of gravity reduces to a parallel transport of the neutrino momentum and an apparent correction to the coherence length. However, these terms do not lead to any observable change in the oscillation probability, rendering the prediction effectively indistinguishable from the flat spacetime case. For astrophysical baselines, although gravitational curvature could in principle influence the decoherence limit, the weak-field approximation ensures that mass eigenstates remain on nearly coincident geodesics. Only in extreme environments, such as trajectories intersecting compact objects of microscopic scale, could curvature effects significantly alter coherence. Such situations, however, are not expected to play a role for the vast majority of neutrinos reaching Earth.

The case of GWs highlights these limitations even more clearly. Because the observable effect of a GW is constrained by the experimental energy resolution, the minimal strain accessible to neutrino oscillation experiments is bounded from below at the level of today's percent-level resolution. This translates into sensitivity requirements of strains $h \sim O\left(10^{-2}\right)$. In turn this means for realistic strains that the required sensitivity is many orders of magnitude beyond current capabilities and not competitive with laser interferometry or pulsar timing techniques. Even highly idealized scenarios involving extreme astrophysical neutrino sources confirm that the required event statistics, energy spectra, and resolutions cannot be realized in practice.

Taken together, these results demonstrate that standard general-relativistic effects on neutrino oscillations are, for all practical purposes, unobservable. This conclusion has two important implications. First, it provides a robust theoretical benchmark: future oscillation experiments can safely neglect classical spacetime curvature in the interpretation of their data, except in highly contrived scenarios. Second, it sharpens the perspective for searches beyond the standard paradigm. If any deviation from the expected oscillation pattern is to be detected, our analysis makes clear that it cannot be attributed to ordinary gravitational backgrounds. Instead, such a signal is a compelling indication of new physics, such as QG-induced decoherence mechanism or interactions with exotic dark-sector fields.

This perspective naturally sets the stage for the following chapter, where we turn to precisely such possibilities. By applying the theory of open quantum systems, we will investigate how QG fluctuations or spacetime foam could leave imprints on the decoherence limit of neutrino osillations. In this sense, the negligible role of classical gravity strengthens the case for neutrinos as sensitive messengers of *traces of gravity*: any observable effect in oscillation data would not arise from standard curvature effects, but rather from subtle quantum features of spacetime itself.

Chapter 5

Tracing Quantum Gravity with Neutrinos

Through this thesis, we search for *traces of gravity*: subtle imprints of gravitational phenomena across vastly different energy regimes. While gravity is notoriously hard to probe at the quantum level, some of its signatures may be hidden in systems we can observe. This chapter focuses on the potential to detect such effects in neutrino oscillations occurring over astrophysical and atmospheric distances.

Here, the focus lies on QG-induced effects in neutrino oscillations. Neutrinos are uniquely suited as probes due to their long, mostly unperturbed propagation paths, which make them sensitive to even tiny deviations from oscillation probabilities given in standard QFTs. These properties make them an excellent candidate for investigating even weak QG effects. Our approach follows a bottom-up approach: rather than deriving predictions from a specific QG theory, we formulate an effective, low-energy description of how QG might influence an otherwise well-understood quantum system. One natural framework for this is that of open quantum systems [267, 268], where the quantum DOFs, in this case neutrinos, interact with an unobserved environment, here associated with the QG sector. Such interactions can lead to decoherence, i.e., a loss of coherence and entanglement, which could in principle result in measurable modifications to neutrino oscillation patterns.

A central theoretical motivation for QG-induced decoherence comes from the so-called no-hair theorem [125, 269, 270]. This principle states that black holes, as solutions of classical GR, can be completely characterized by just three conserved quantities: mass, electric charge, and angular momentum. All other information, such as the flavor of infalling particles, is effectively lost behind the event horizon. If this concept is extended to QG and it is treated as an environment interacting with the quantum system, it suggests that flavor information of neutrinos may likewise be lost through such interactions. This loss of information underpins the idea of QG-induced flavor decoherence [271–275].

Within this framework, only conserved gauge quantum numbers are protected from decoherence. As a result, transition to new, electrically neutral states, so-called dark fermions, become possible. These could represent DM candidates, such as sterile neutrinos [276, 277], WIMPs [276, 278], feebly interacting massive particles [279, 280], or others [281]. Over long distances, flavor information becomes increasingly diluted, and the transition probabilities between standard neutrino flavors and dark fermions approach equal values. This means that any initially pure neutrino system will inevitably develop a dark fermion component over time. One observable consequence is the modification to the flavor composition, and thus the expected oscillation pattern.

In our analysis, we focus on atmospheric rather than astrophysical neutrinos. While we expect enhanced effects at higher energies and longer propagation baselines, the low statistics of astrophysical neutrinos and poorly known production mechanisms limit their

constraining power, see subsection 2.2.3 for more details. Currently, the strongest bounds on decoherence parameters stem from the IceCube Collaboration, using high-energy atmospheric neutrinos [282]. Further improvements are expected from KM3NeT [197], an underwater neutrino telescope under construction in the Mediterranean Sea. It consists of two components: ORCA [283], designed to detect neutrinos above $\approx$ 1 GeV and benefit from matter effects to enhance sensitivity, and ARCA [284], which targets high-energy neutrinos in the TeV–PeV regime and beyond. Together, they will provide comprehensive coverage across different energy scales.
IceCube has released an extensive public dataset [285], which we use to estimate the potential sensitivity of the detector to the model under consideration. Beyond that, we perform a data-driven analysis to set experimental bounds on the model parameters. In doing so, we extend existing IceCube studies by allowing for a variable number of dark fermions. In section 5.1, we introduce the theoretical framework of open quantum systems and explain how it is employed in this work to develop a phenomenological description of QG-induced decoherence in the neutrino sector. Section 5.2 presents the details of our analysis along with the corresponding results, highlighting both the expected sensitivity of (future) neutrino telescopes to the decoherence parameters and the current limits derived from IceCube data. Finally, section 5.3 provides a summary and places the findings into the broader context of this thesis.

5.1 Imprints of Gravity: Decoherence Effects in the Neutrino Sector

To model potential QG-induced modifications of neutrino oscillations, we adopt the formalism of open quantum systems [274, 286]. This framework allows us to describe the influence of an unknown quantum environment on an otherwise well-understood quantum system, without assuming a specific microscopic theory of QG. The essential idea is to treat the QG DOFs as an unobserved environment and to track their effective impact on the system by introducing non-unitary terms in the evolution equations [274, 286]. The most prominent effect is the occurrence of decoherence. For a general overview of decoherence, see references [287, 288].
Open quantum systems are naturally described by a density operator ρ, which encodes statistical mixtures and loss of purity due to interactions with the environment. In our setup, the system consists of standard neutrino flavor states, extended by possible additonal fermionic DOFs, referred to as dark fermions. They share the same unbroken gauge quantum numbers, such as electric and color charge and their masses must remain within the kinematically accessible range, but are otherwise unconstrained.
This is motivated by the no-hair theorem, which asserts only its mass and charges like electric charge and angular momentum are preserved for black hole solutions. By analogy, we assume that QG interactions violate all other global quantum numbers, such as lepton flavor, potentially leading to irreversible flavor decoherence and mixing with dark fermions. As a result, a pure initial neutrino state may evolve into a mixed state involving both standard and dark components.
Such a scenario could alter the expected oscillation pattern and be detectable in neutrino telescopes. In particular, the probability distribution among flavors would flatten over long baselines, with transitions to dark states washing out coherence. These effects are expected to be enhanced at higher energies and over long propagation distances, making long-baseline experiments especially sensitive probes. In the remainder of this section, we develop the theoretical framework underlying this decoherence scenario.

We assume Markovian time evolution, meaning that the dynamics of the system are entirely determined by its current state, without memory effects from the past. Under this assumption, the time evolution of a general open quantum system is governed by the Lindblad master equation:

$$\dot{\rho}_S = -i\,[H_S, \rho_S] + D\,[\rho_S]\,. \tag{5.1}$$

The first term on the right-hand side is the usual von Neumann equation, describing the unitary evolution of the system's density matrix ρ_S under the system Hamiltonian H_S. The second term represents the non-unitary contribution from the interaction with the environment. Here, the dissipator $D\,[\rho_S]$ encodes the influence of the environmental DOFs on the system and is therefore responsible for decoherence.
We consider ultra-relativistic neutrinos propagating through the Earth. As described in subsection 2.2.2, the Hamiltonian in this case takes a form analogous to equation (2.62)

$$H = H_0 + H_{\text{Matter}}\,, \quad \text{with} \qquad H_0 = \frac{\Delta M^2}{2E}\,, \quad \text{and} \qquad H_{\text{Matter}} = U^\dagger V U\,. \tag{5.2}$$

However, this equation must be generalized, since we do not necessarily assume the number of neutrino flavors to be $n_f = 3$, but rather allow for $n_f \geq 3$, since we also include dark fermions that share the same unbroken gauge quantum numbers. As a consequence, the squared mass mixing matrix is extended to $\Delta M^2 = \text{diag}\left(0, \Delta m^2_{21}, \Delta m^2_{31}, \dots, \Delta m^2_{n_f 1}\right)$ with $\Delta m^2_{ij} = m^2_i - m^2_j$.
By choosing this form of the Hamiltonian, we implictly assume that the dark fermions are also ultra-relativistic at the energy scales relevant for atmospheric neutrinos. Moreover, since we assume that QG conserves the four-momentum, the center-of-mass energy of the system remains unchanged as well. This conservation of energy, together with the fact that the neutrino energy is defined with an uncertainty $\Delta E \sim 1/\Delta t$ (arising from the finite spatial extension of the wave packet), implies that a neutrino can only mix with other states whose masses lie within this energy uncertainty range. Consequently, the masses of the dark fermions must be of the same order of magnitude as those of the active neutrino generations.
Note, that the previous considerations hold only if QG indeed preserves energy and momentum. If this assumption fails, heavy mass states could in principle be produced. In such a case, the Hamiltonian would take the modified form

$$\left\langle \psi_j | H_0 | \psi_j \right\rangle = \sqrt{\vec{p}^2 + m^2_{\psi_j}} + \delta E_{\text{QG}}\,, \tag{5.3}$$

where additional particle states $|\psi_j\rangle$ with larger masses contribute. Their energy eigenvalues are then shifted by a QG correction term δE_{QG}, which may originate from Lorentz violation or other non-standard dispersion effects.
However, in this work, we are only interested in flavor oscillations among active neutrinos. Assuming that the dark-sector states couple only weakly to the active neutrinos, the Lindblad equation (5.1) ensures that the active-to-active transition rates remain unaffected by the specific structure of the Hamiltonian components associated with the dark sector. Under this assumption, we may consistently adopt the Hamiltonian form given in equation (5.2), even if four-momentum conservation is violated at the fundamental level.
The matter potential in this context differs slightly from the case discussed in subsection 2.2.2. It now takes the form

$$V = \text{diag}\left(V_{\text{CC}} + V_{\text{NC}}, V_{\text{NC}}, V_{\text{NC}}, 0, \dots, 0\right)\,. \tag{5.4}$$

Here, V_{CC} affects only electron neutrinos, as explained in subsection 2.2.2, while V_{NC} contributes equally to all neutrino flavors. The dark-sector states, in contrast, do not couple to ordinary matter, and therefore, do not experience a matter potential. A transformation to the mass basis V_{Mass} is analogously performed via

$$U = U_{\mathrm{PMNS}} \otimes \mathbb{1}_{(n_f-3)\times(n_f-3)}\,, \tag{5.5}$$

where U_{PMNS} denotes the PMNS matrix introduced in equation (2.24). The dark sector is not rotated by this transformation, as we assume only a small mixing between active and dark states. However, this framework remains valid even in the presence of significant active–dark mixing. In that case, the mixing matrix U would no longer be block-diagonal. Nevertheless, the matter potential acts exclusively within the active subspace.
The dissipator introduced in equation (5.1) can be split into two contributions:

$$D\left[\rho_{\mathrm{S}}\right] = D_{\mathrm{Matter}}\left[\rho_{\mathrm{S}}\right] + D_{\mathrm{QG}}[\rho_{\mathrm{S}}]\,. \tag{5.6}$$

The term D_{Matter} encodes known dissipative effects due to scattering with ordinary matter, such as incoherent ν_τ regeneration and energy loss through inelastic interactions. These effects are well studied and described in the literature [289, 290]. In contrast, D_{QG} captures decoherence effects induced by QG. It can be expressed in the form [291]

$$D_{\mathrm{QG}}\left[\rho_{\mathrm{S}}\right] = \sum_{i,j=0}^{n_f^2-1} \mathcal{D}^i_{\mathrm{QG}j}\rho^j\lambda_i \quad \text{with} \quad \mathcal{D}_{\mathrm{QG}} = \mathrm{diag}\left(0,\Gamma,\ldots,\Gamma\right)\,, \tag{5.7}$$

where Γ is a phenomenological parameter encoding the decoherence rate induced by QG. Here, the density matrix ρ_{S} is expanded in terms of the SU$\left(n_f\right)$ generators λ_i with coefficients

$$\rho_{\mathrm{S}} = \sum_i \rho^i\lambda_i\,. \tag{5.8}$$

This choice of basis provides a systematic and complete parametrization of states and dissipative processes in an n_f-dimensional Hilbert space. The trace-preserving property $\mathrm{Tr}\left[\rho_{\mathrm{S}}\right] = 1$ ensures that the identity component is left invariant, while all other components are exponentially damped by the decoherence parameters γ_i. This damping suppresses coherent flavor oscillations and gradually drives the system toward a maximally mixed state, without inducing net particle loss or creation.
Many QG models suggest, see e.g., references [292, 293], that decoherence arises because the environment selects preferred basis states, causing superpositions to decohere. Since the full theory of QG is not yet known, we cannot predict the exact structure of the damping parameter Γ. Nevertheless, we can model them phenomenologically by parametrizing their energy dependence as [275, 294, 295]

$$\Gamma(E_\nu) = \gamma_0\left(\frac{E_\nu}{E_0}\right)^n\,. \tag{5.9}$$

Here, E_0 denotes a reference energy, which we set to 1 TeV in accordance with the energy peak of the neutrino flux observed by the IceCube experiment. The parameter γ_0 sets the decoherence strength at this reference scale, and n characterizes the energy dependence of the decoherence rate.
Positive values of n are motivated by the expectation that QG effects become more significant at shorter wavelengths, i.e., higher energies. When neutrino wavelengths

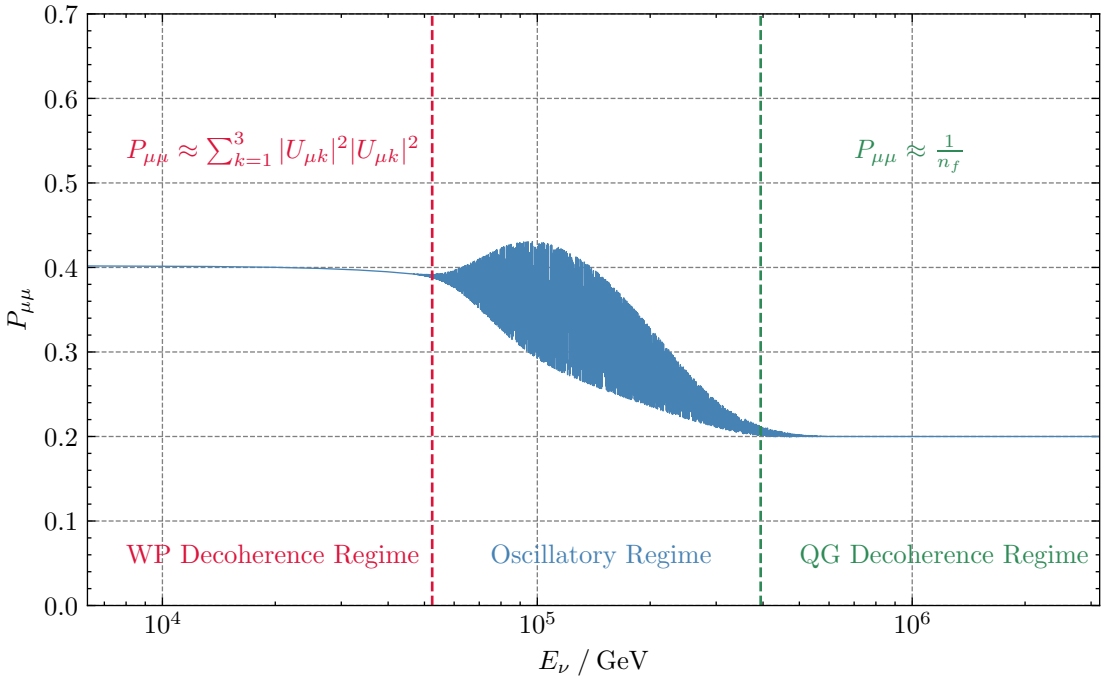

Figure 5.1: Oscillation probability for the channel $\nu_\mu \to \nu_\mu$ assuming a baseline of $L = 14.4\,\mathrm{MPc}$, corresponding to the distance to NGC1068, a wave packet width of $\sigma_x = 10^{-9}\,\mathrm{m}$, a QG parameter of $\gamma_0 = 10^{-35}\,\mathrm{eV}$, and a fermion number of $n_f = 5$. The quadratic decoherence model ($n = 2$) is applied. Mass-squared differences and mixing parameters are taken from reference [298], rounded to the first significant digit not affected by experimental uncertainties.

approach the Planck scale, these effects can no longer be neglected, and the decoherence becomes appreciable. However, there are also theoretical scenarios in which the damping is stronger at lower energies and vanishes at high energies. Such behavior may arise in models featuring UV/IR mixing or in non-local theories of gravity, where short- and long-distance physics become intertwined [296]. In such scenarios, low-energy phenomena can be sensitive to Planck-scale effects, leading to enhanced decoherence at small energies.

According to reference [297], the probability for neutrino oscillation in vacuum in the presence of a dissipator of the form given in equation (5.7), and assuming a baseline L and a decoherence rate Γ, takes the form

$$\begin{aligned} P(\nu_\alpha \to \nu_\beta) = \frac{1}{n_f}\left(1 - \exp\left(-\Gamma(E_\nu)L\right)\right) + \left(\sum_{k=1}^{3} |U_{\alpha k}|^2 |U_{\beta k}|^2\right) \exp\left(-\Gamma(E_\nu)L\right) \\ + 2\sum_{j>i=1}^{3} \mathrm{Re}\left[U^*_{\alpha j} U_{\alpha i} U_{\beta j} U^*_{\beta i}\right] \exp\left(-\Gamma(E_\nu)L - \left(\frac{L}{L^{\mathrm{coh}}_{ij}}\right)^2\right) \cos\left(\frac{\Delta m^2_{ij} L}{2E_\nu}\right) \\ - 2\sum_{j>i=1}^{3} \mathrm{Im}\left[U^*_{\alpha j} U_{\alpha i} U_{\beta j} U^*_{\beta i}\right] \exp\left(-\Gamma(E_\nu)L - \left(\frac{L}{L^{\mathrm{coh}}_{ij}}\right)^2\right) \sin\left(\frac{\Delta m^2_{ij} L}{2E_\nu}\right). \end{aligned} \tag{5.10}$$

Figure 5.1 shows the vacuum oscillation probability from equation (5.10) for a baseline of $L = 14.4\,\mathrm{MPc}$, providing a schematic illustration of the qualitative behavior of neutrino

oscillations in the presence of quantum decoherence. At low energies, the differences in group velocity between the mass eigenstates are so large that wave packet separation leads to complete decoherence, suppressing oscillations. At very high energies, oscillations are also suppressed, but this time due to *QG* effects, leading to an asymptotic flavor distribution of $1/n_f$, as previously discussed. In the intermediate regime, coherent oscillations can still occur. Provided that neutrino telescopes achieve sufficiently high energy resolution, i.e.,

$$\frac{\Delta E_\nu}{E_\nu} \lesssim \frac{2E_\nu}{\Delta m^2 L}\,, \tag{5.11}$$

these oscillatory features could, in principle, be observable.
In cases where $n \neq 0$, it is useful to introduce the coherence energy E_{QG},

$$\Gamma(E_{\mathrm{QG}})L \stackrel{!}{=} 1 \qquad \Leftrightarrow \qquad E_{\mathrm{QG}} = E_0 \left(\frac{1}{\gamma_0 L}\right)^{\frac{1}{n}}\,, \tag{5.12}$$

which marks the energy scale at which decoherence effects become significant and begin to damp oscillations noticeably. Since the decoherence factor enters the oscillation probability as an exponential $\exp(\Gamma L)$, the impact of QG grows rapidly with increasing baseline. This makes astrophysical neutrinos the most promising probe for such effects. However, as discussed in section 2.2, wave packet decoherence becomes relevant at astrophysical distances as well. Therefore, the full oscillation probability must include an additional exponential damping term governed by the coherence length. In contrast, for atmospheric neutrinos, this term is negligible due to the much shorter travel distances, and will hence be neglected in the corresponding part of our analysis.
To summarize, our discussion makes clear that astrophysical neutrinos would in principle offer the most sensitive probe for QG decoherence. However, due to the currently limited statistics in the astrophysical channel, atmospheric neutrinos remain the most practicle and statistically robust source of data for such searches at present.

5.2 Sensitivity and Constraints on the Decoherence Parameter

In this section, we investigate the sensitivity of the IceCube Neutrino Observatory to QG-induced decoherence effects in the presence of new fermionic particles. In addition, we derive current experimental constraints on the corresponding QG parameters. The sensitivity analysis is based on a publicly available Monte Carlo (MC) simulation sample used in reference [209] and includes all systematic effects discussed in reference [209] and references therein. To obtain the current experimental limits, we make use of the measured IceCube data from reference [209]. We begin in subsection 5.2.1 by describing the detail of the MC sample and the construction of the theoretical model predictions. In subsection 5.2.2, we then explain the statistical methodology in detail. The resulting sensitivity estimates and experimental limits are presented in subsection 5.2.3. Finally, subsection 5.2.4 discusses possible future analyses and the achievable sensitivities.

5.2.1 Flux Propagation and Detector Response Modeling

In this analysis, we focus on high-energy atmospheric neutrinos as a probe for the decoherence models introduced in section 5.1. At these energies, neutrino propagation

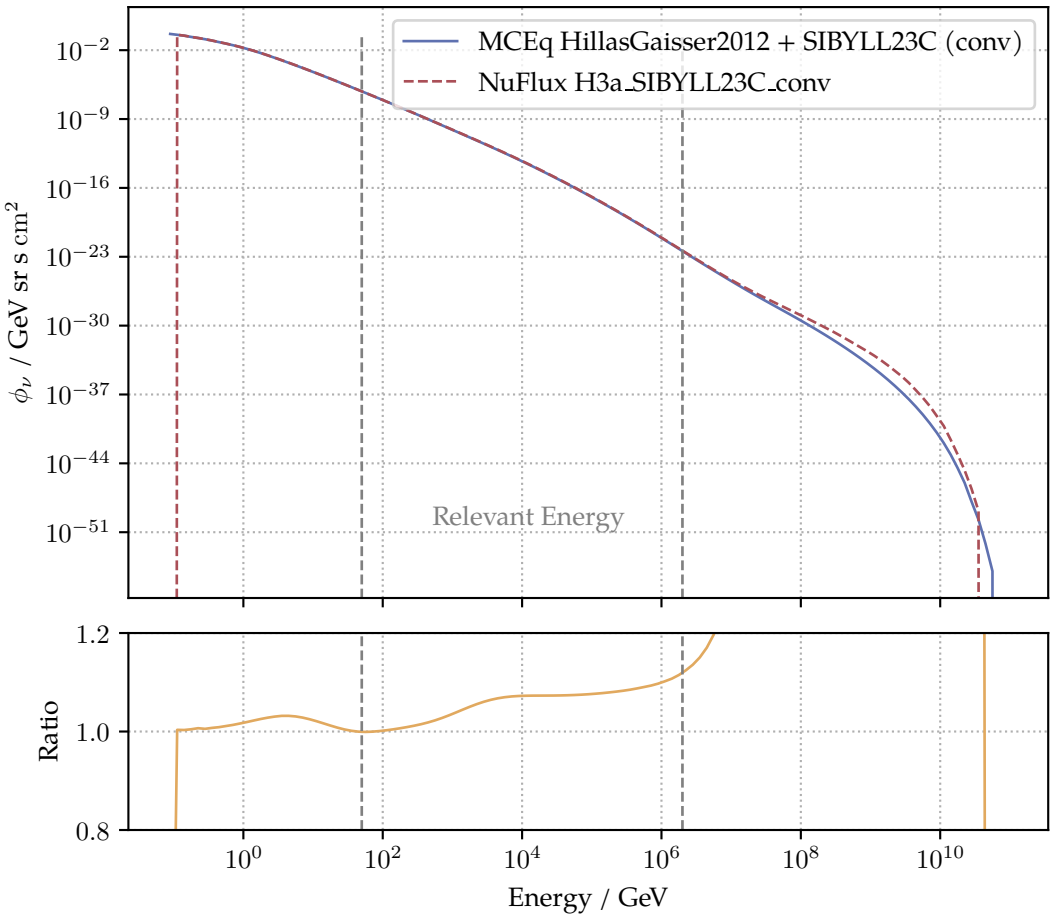

Figure 5.2: Fluxes (upper) and their ratio (lower) between the atmospheric ν_μ fluxes predicted by `MCEq` and `nuflux` for the H3a+SIBYLL23C model combination for $\theta = 90°$. In dashed gray we also mark the energy range relevant for this analysis.

through the Earth is dominated by incoherent interactions with the Earth's matter, leading to neutrino absorption [299], energy loss and, in the case of tau neutrinos, regeneration effects [300, 301]. For details on the underlying theory see subsection 2.2.2. To account for these effects in the sensitivity analysis, we use the publicly available software `NuSQuIDS` [73], which we extend to include an additional decoherence term from equation (5.7) to model potential interactions with dark fermionic states. As input fluxes, we use conventional atmospheric neutrino fluxes computed with `MCEq` [302] based on the `H3a` primary cosmic ray model [303] in combination with the `SIBYLL23C` hadronic interaction model [304]. This choice replaces the previously employed flux predictions from the `nuflux` package [305], which were used in our earlier analysis [4]. As shown in figure 5.2, the `nuflux`-based fluxes exhibit significant deviations from the `MCEq` prediction in the PeV range. While the differences in the energy region relevant for our analysis are more moderate, they are still non-negligible and can impact the interpretation of potential decoherence effects. To ensure consistency and reliability of the theoretical input, we therefore use the `MCEq`-based fluxes in the following. The astrophysical contribution is described by an unbroken power-law spectrum with a spectral index of -2.5 [306]. The propagation of these fluxes is performed for varying numbers of additional fermionic species n_f and across different decoherence scenarios where we assume different energy

powerlaw dependencies n. To incorporate the dependence on the QG parameter γ_0, fluxes are computed for several values of γ_0 and then interpolated accordingly.
To translate the resulting fluxes into observable events in the IceCube detector, we rely on the publicly released MEOWS MC sample [285], which provides the necessary tools for connecting flux predictions to detected events, following the procedure described in reference [209]. This MC sample corresponds to a total livetime of $T = 7.6$ years and contains 24 902 627 unweighted track-like events, i.e., ν_μ and $\bar{\nu}_\mu$, and provides both true and reconstructed values of the energy and the cosine of the zenith angle θ_{zenith}. The reconstruction achieves an energy resolution of $\sigma \log_{10}(E_{\nu_\mu}) \sim 0.3$, and an angular resolution $\sigma_{\cos\theta_{\text{zenith}}}$ ranging from 0.005 to 0.015, depending on the energy [307]. The effect of decoherence is incorporated by reweighting the MC events with the expected fluxes computed using `NuSQuIDS`. Additionally, systematic uncertainties from both the detector and the input fluxes are accounted for through a set of nuisance parameters $\vec{\eta}$. These parameters rescale the MC weights and are treated following the approach outlined in references [209, 307]. Table 5.1 provides an overview of all considered nuisance parameters, including their nominal values, uncertainties, and applied constraints. The Icecube dataset employed here to determine the experimental constraints on the QG parameters includes 305 735 only track-like events and is taken from reference [307].

5.2.2 Statistical Methodology

To evaluate the sensitivity of IceCube to decoherence effects induced by QG, as well as to derive exclusion limits based on observed data, we adopt a likelihood-based statistical framework. This approach allows for a consistent treatment of both MC fluctuations and systematic uncertainties. The core of the method is a likelihood ratio test based on the binned event counts. The expected event distribution is derived from reweighted MC simulations, as outlined in subsection 5.2.1. To incorporate systematic uncertainties, including detector effects and flux modeling, we construct a profile likelihood function by maximizing over a set of nuisance parameters:

$$\mathcal{L}_{\text{profile}}(\gamma_0|\vec{X}) := \sup_{\vec{\eta}} \mathcal{L}_{\text{bin}}(\gamma_0, \vec{\eta}|\vec{X}) \Pi(\vec{\eta}) \,, \tag{5.13}$$

where $\vec{X}$ denotes the given dataset, $\vec{\eta}$ is the vector of nuisance parameters, and $\Pi(\vec{\eta})$ represents prior constraints on $\vec{\eta}$ in the form of independent Gaussian distributions:

$$\Pi(\vec{\eta}) = \prod_{j=1}^{N_{\text{sys}}} \frac{\exp\left(-\frac{(\eta_j - \bar{\eta}_j)^2}{2\sigma_{\eta_j}^2}\right)}{\sqrt{2\pi\sigma_{\eta_j}^2}} \,, \tag{5.14}$$

with nominal values $\bar{\eta}_j$ and standard deviations σ_{η_j} taken from reference [307] and given in table 5.1. In addition, the likelihood $\mathcal{L}_{\text{bin}}$ describes the statistical fluctuations in each bin and is modelled following the effective likelihood introduced in reference [308], which properly accounts for uncertainties from finite MC statistics:

$$\mathcal{L}(\gamma_0, \vec{\eta}|\vec{X}) = \prod_{l=1}^{n_{\text{bins}}} \mathcal{L}_{\text{eff}}(n_{\mu,l}(\gamma_0, \vec{\eta}), \sigma_l(\gamma_0, \vec{\eta})|X_l) \,, \tag{5.15}$$

Table 5.1: A list of all nuisance parameters η_j, their nominal values $\bar{\eta}_j$, standard deviations σ_{η_j} and box constraints taken into account in this analysis. Entries marked "NA" indicate that no explicit constraint is applied for the corresponding parameter. For more details see references [209, 307].

Parameter η_j	Nominal value $\bar{\eta}_j$	Standard deviation σ_{η_j}	Box constraint
DOM efficiency	0.97	0.1	$[0.94, 1.03]$
Bulk ice gradient 0	0.0	1.0	NA
Bulk ice gradient 1	0.0	1.0	NA
Forward hole ice (p_2)	-1.0	10.0	$[-5, 3]$
Normalization ($\Phi_{\text{conv.}}$)	1.0	0.4	NA
Spectral shift ($\Delta\gamma_{\text{conv.}}$)	0.00	0.03	NA
Atm. Density	0.0	1.0	NA
Barr WM	0.0	0.40	$[-0.5, 0.5]$
Barr WP	0.0	0.40	$[-0.5, 0.5]$
Barr YM	0.0	0.30	$[-0.5, 0.5]$
Barr YP	0.0	0.30	$[-0.5, 0.5]$
Barr ZM	0.0	0.12	$[-0.25, 0.5]$
Barr ZP	0.0	0.12	$[-0.2, 0.5]$
Normalization (Φ_{astro})	0.787	0.36	NA
Spectral shift ($\Delta\gamma_{\text{astro}}$)	0.0	0.36	NA
Cross section σ_{ν_μ}	1.00	0.03	$[0.5, 1.5]$
Cross section $\sigma_{\bar{\mu}_\mu}$	1.000	0.075	$[0.5, 1.5]$
Kaon energy loss σ_{KA}	0.0	1.0	NA

where n_{bins} is the total number of bins and X_l is the measured number of events in the bin l. Furthermore, $n_{\mu,l}(\gamma_0, \vec{\eta})$ denotes the expected number of events in bin l, and $\sigma_{\text{MC},l}(\gamma_0, \vec{\eta})$ is the associated MC uncertainty. Both are computed from the MC weights ω_i^l in the respective bin as:

$$n_{\mu,l}(\gamma_0, \vec{\eta}) = \sum_{i=1}^{N_l} \omega_i^l(\gamma_0, \vec{\eta}) \,, \qquad \sigma^2_{\text{MC},l}(\gamma_0, \vec{\eta}) = \sum_{i=1}^{N_l} \left[\omega_i^l(\gamma_0, \vec{\eta})\right]^2 \,. \tag{5.16}$$

Here, the summation runs over all MC weights assigned to the l-th bin. The bin-wise likelihood function $\mathcal{L}_{\text{eff}}$ is a modified Poisson likelihood designed to account for statistical fluctuations due to finite MC statistics. It was first introduced in reference [308] and ensures a more accurate treatment of bin-wise uncertainties in the presence of weighted simulated events.
To test the compatibility of a given decoherence parameter γ_0 with the data, we define the test statistics as the logarithmic likelihood ratio:

$$\ln \Lambda := -2 \ln \left(\frac{\sup_{\gamma_0 \in \Theta_0} \mathcal{L}_{\text{profile}}(\gamma_0 | \vec{X})}{\sup_{\gamma_0 \in \Theta} \mathcal{L}_{\text{profile}}(\gamma_0 | \vec{X})} \right) , \tag{5.17}$$

where the null hypothesis space Θ_0 contains a single reference value γ_0^0 (typically $\gamma_0^0 = 0$) and $\Theta = \mathbb{R}$ denotes the full parameter space for each combination (n_f, n) considered here. For the sensitivity study, we define the pseudo-data $\vec{X}$ to be the standard model prediction with no decoherence, i.e., $\vec{X} = \vec{n}_\mu^{\text{std}} = \vec{n}_\mu(\gamma_0 = 0, \vec{\eta})$. In this case, the expected event rates are independent of the specific decoherence model, as $\gamma_0 = 0$ effectively restores standard oscillations. In addition to these sensitivity estimates, we also compute exclusion limits by applying the same statistical formalism to the observed IceCube data [285]. This provides direct bounds on γ_0 under each tested decoherence scenario. In the limit of large event counts, the test statistics $\ln \Lambda$ converges to a χ^2 distribution with one DOF [308], and the likelihood ratio test simplifies to

$$\ln \Lambda(\gamma_0) \to \chi^2(\gamma_0) = \min_{\vec{\eta}} \sum_{l=1}^{n_{\text{bins}}} \frac{(n_{\mu,l}^{\text{std}} - n_{\mu,l}(\gamma_0, \vec{\eta}))^2}{n_{\mu,l}(\gamma_0, \vec{\eta}) + \sigma^2_{\text{MC},l}(\gamma_0, \vec{\eta})} + \sum_{j=1}^{N_{\text{sys}}} \frac{(\eta_j - \bar{\eta}_j)^2}{\sigma^2_{\eta_j}} \,. \tag{5.18}$$

According to Wilks' theorem, this enables a direct interpretation of the χ^2 values in terms of the CL for allowed values of γ_0.

5.2.3 Expected Sensitivities and Observed Limits for the IceCube Neutrino Observatory

In this section, we present the sensitivity of the IceCube Neutrino Observatory to the QG induced decoherence effects introduced in section 5.1. We also derive exclusion limits on the QG parameter γ_0 based on observed data, in addition to the expected sensitivity derived from pseudo data.
To obtain an initial estimate of the expected sensitivity as a function of reconstructed energy and zenith angle, we evaluate the signed χ^2 values per bin, defined by

$$\text{signed}\,\chi^2_l = \frac{(n_{\mu,l}^{\text{QG}} - n_{\mu,l}^{\text{std}})|n_{\mu,l}^{\text{QG}} - n_{\mu,l}^{\text{std}}|}{n_{\mu,l}^{\text{QG}}} \,, \tag{5.19}$$

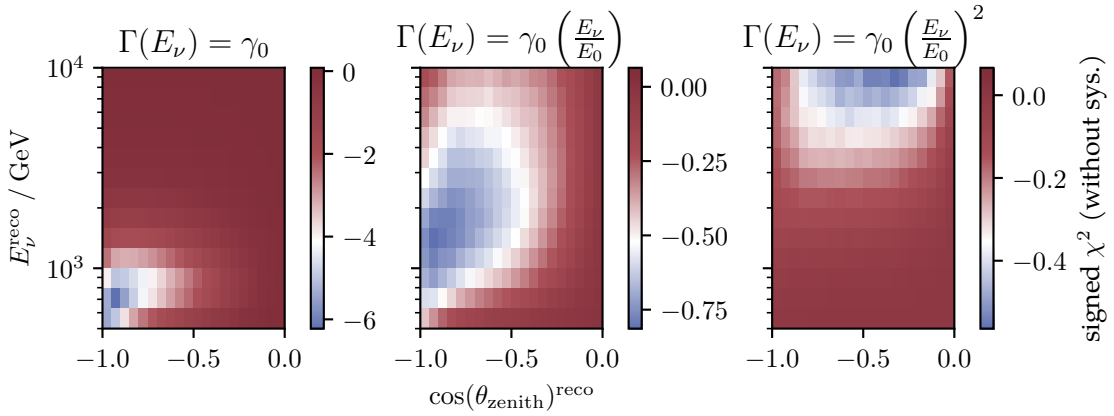

Figure 5.3: Signed χ^2 values (without systematic effects) for $n_\mathrm{f} = 4$ and the three energy dependencies as a function of the reconstructed zenith angle $\cos\left(\theta_{\mathrm{zenith}}\right)^{\mathrm{reco}}$ and reconstructed energy E_ν^{reco}, corresponding to the upper limits on γ_0 at 90 % CL: $\gamma_0 \in \{1.18 \times 10^{-15}, 2.83 \times 10^{-16}, 1.17 \times 10^{-17}\}$ eV (from left to right).

where $n_{\mu,l}^{\mathrm{QG}}$ denotes the binned number of events predicted by a given decoherence model for a fixed QG parameter γ_0 and $n_{\mu,l}^{\mathrm{std}}$ corresponds to the binned number of events in the standard scenario without decoherence. Figure 5.3 shows the resulting signed χ^2 distributions based on the nominal MC event weights, i.e., without including any systematic effects. The panels correspond to $n_f = 4$ and each of the three energy dependencies $n \in 0, 1, 2$ as a function of the reconstructed zenith angle $\cos\left(\theta_{\mathrm{zenith}}\right)^{\mathrm{reco}}$ and reconstructed energy E_ν^{reco}. The value of γ_0 is chosen such that the global test statistic satisfies $\chi^2 = 2.86$, corresponding to a 90 % CL. Figure 5.4 presents an analogous quantity derived from the binned true ν_μ fluxes, i.e., before reconstruction. The shown values are rescaled such that their minima match those of the corresponding signed χ^2 distributions. A comparison between figures 5.3 and 5.4 reveals the impact of detector resolution effects. In particular, the regions of highest sensitivity tend to shift towards larger reconstructed energies and zenith angles, as a consequence of smearing. For the energy-independent decoherence model ($n = 0$), the sensitivity is concentrated at lower energies and in the up-going region, i.e., small zenith angle, which is consistent with the higher event statistics in that domain. In contrast, for the energy-dependent models ($n = 1, 2$), the sensitivity progressively shifts to higher energies, where the impact of decoherence increases.

To assess how systematic uncertainties affect these sensitivity patterns, we repeat the analysis using rescaled MC weights, evaluated at the best-fit nuisance parameter vector $\vec{\eta}$ obtained via profile likelihood maximization. The resulting signed χ^2 maps are shown in figure 5.5 for the same setting as before. From the comparison of the signed χ^2 distributions with and without systematic effects, i.e., figures 5.3 and 5.5, we observe that the systematic effects can induce significant deviations between the naively expected and the actual regions of the highest sensitivity. Across all decoherence models we see that the overall sensitivity is drastically reduced due to the rescaling of the nominal MC weights which is of course expected as we minimize χ^2 on the set of nuisance parameters. For the energy-independent decoherence model ($n = 0$), we still see that the largest (negative) deviation of signed χ_l^2, caused by the model effects, is located in the up-going, low-energy bins as expected, but we also find a region of positive deviation caused by the application of bin-wise scale factors describing the systematic effects after minimizing

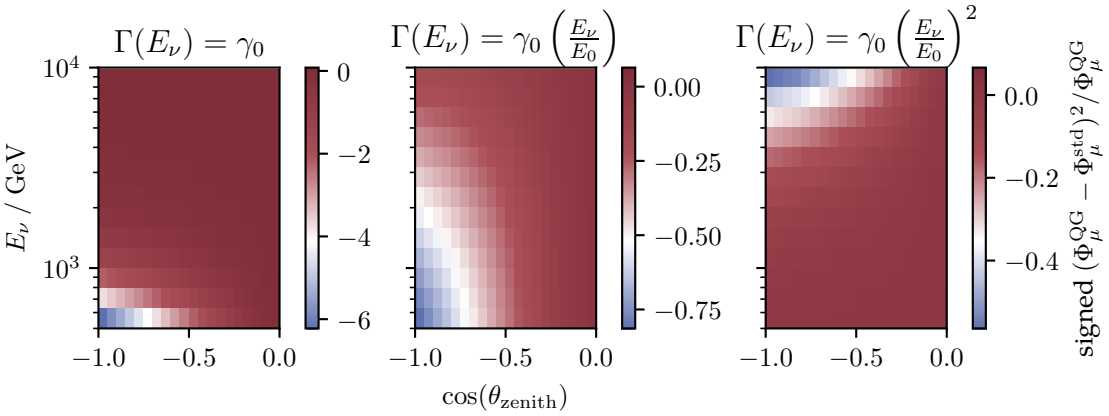

Figure 5.4: Cross-checks for the signed χ^2 distributions ($n_f = 4$) in terms of the binned, true ν_μ fluxes in the energy E_ν and cosine zenith angle $\cos(\theta_{\mathrm{zenith}})$ plane, scaled such that the minimum of the shown quantity and that of the associated signed χ^2 match. Each panel corresponds to a different energy dependence of the underlying QG model, i.e., $n \in \{0, 1, 2\}$ (from left to right) and for the associated to the upper limits on γ_0 at 90 % CL: $\gamma_0 \in \{1.18 \times 10^{-15}, 2.83 \times 10^{-16}, 1.17 \times 10^{-17}\}$ eV.

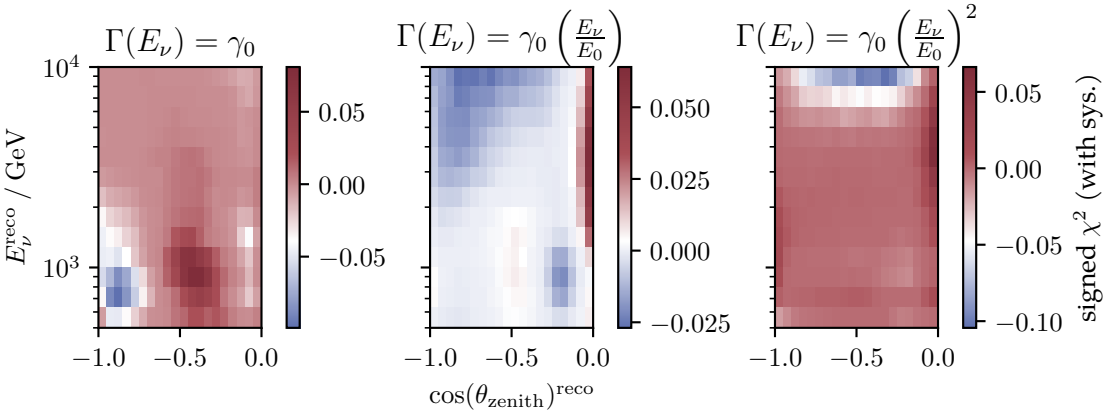

Figure 5.5: Signed χ^2 values (with systematic effects) for $n_{\mathrm{f}} = 4$ and the three energy dependencies as a function of the reconstructed zenith angle $\cos\left(\theta_{\mathrm{zenith}}\right)^{\mathrm{reco}}$ and reconstructed energy E_ν^{reco}, corresponding to the upper limits on γ_0 at 90 % CL: $\gamma_0 \in \{1.18 \times 10^{-15}, 2.83 \times 10^{-16}, 1.17 \times 10^{-17}\}$ eV (from left to right).

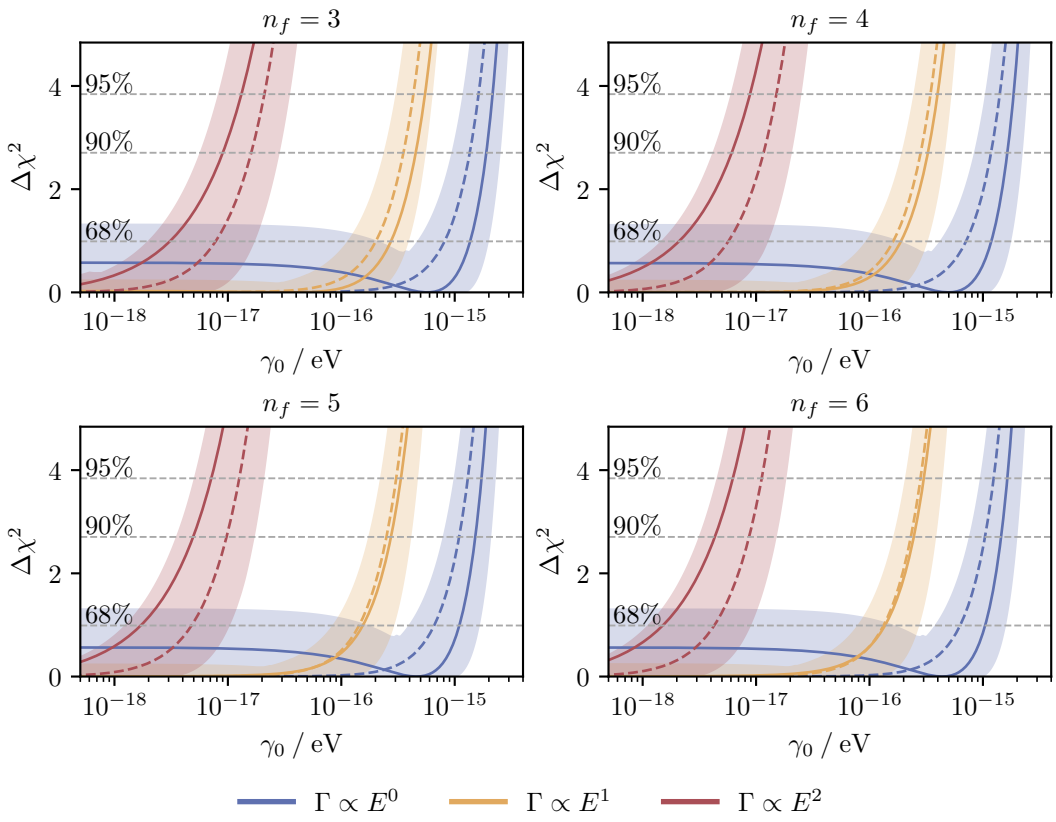

Figure 5.6: Estimated IceCube sensitivity (colored dashed lines) and observed limits for γ_0 (solid colored lines) for $T = 7.6$ years of livetime. The panels are grouped by fermion number n_f, and within each panel the results for the three decoherence models under consideration are shown. Gray dashed lines indicate the χ^2 thresholds for the 68 %, 90 % and 95 % CLs. In addition, their 2σ variations, derived from the distribution of best-fit parameters in 100 toy experiments, are displayed to illustrate the expected spread of sensitivities.

χ^2 with respect to the set of nuisance parameters. In case of the $n = 1$ decoherence model, we find that after applying the systematic effects at the best fit point $\vec{\eta} = \vec{\eta}_{\text{opt}}$, the region of maximal sensitivity is further smeared across all energy and cosine zenith bins. Lastly, for the quadratically energy-dependent decoherence model, as in the case $n = 0$, the region of highest sensitivity remains mostly intact compared to the corresponding region shown in figure 5.3.

After identifying the regions in energy and zenith angle where sensitivities are to be expected and understanding the influence of detector-related systematic uncertainties, figure 5.6 illustrates the dependence of χ^2 on the decoherence parameter γ_0 for the various decoherence models introduced in section 5.1 and for different numbers of fermionic species n_f. The 68 %, 90 % and 95 % CL are indicated by gray dashed lines. The expected sensitivities are shown as colored dashed lines, while the limits obtained from real data are represented by solid colored lines. In addition, their 2σ variations are shown. They were obtained from the ensemble of 100 toy experiments by determining, for each mock dataset, the best-fit parameters and calculating the resulting χ^2 distribution. Table 5.2 summarizes the 90 % CL values for the QG parameter γ_0, both for the

Table 5.2: The γ_0/eV sensitivity limits and observed upper limits at 90 % CL for the different energy dependencies and $n_f \in \{3, 4, 5, 6\}$. In parentheses we report the idealized bounds obtained in a statistics-only approach, i.e., neglecting systematic effects.

n_f	$\Gamma(E_\nu)$ for γ_0	
	Sensitivities	Observed Limits
3	1.36×10^{-15} (1.52×10^{-16})	1.90×10^{-15}
4	1.18×10^{-15} (1.33×10^{-16})	1.64×10^{-15}
5	1.09×10^{-15} (1.24×10^{-16})	1.52×10^{-15}
6	1.04×10^{-15} (1.18×10^{-16})	1.45×10^{-15}
	$\Gamma(E_\nu)$ for $\gamma_0\,(E_\nu/1\text{TeV})$	
3	3.53×10^{-16} (5.30×10^{-17})	4.53×10^{-16}
4	2.83×10^{-16} (4.49×10^{-17})	3.27×10^{-16}
5	2.50×10^{-16} (4.12×10^{-17})	2.74×10^{-16}
6	2.31×10^{-16} (3.90×10^{-17})	2.46×10^{-16}
	$\Gamma(E_\nu)$ for $\gamma_0\,(E_\nu/1\text{TeV})^2$	
3	1.61×10^{-17} (2.77×10^{-18})	9.02×10^{-18}
4	1.17×10^{-17} (2.12×10^{-18})	6.10×10^{-18}
5	9.74×10^{-18} (1.83×10^{-18})	4.94×10^{-18}
6	8.68×10^{-18} (1.66×10^{-18})	4.33×10^{-18}

sensitivity projections and for the limits derived from data, and varying energy dependence. Additionally, for the sensitivity estimates, we report the values that would be obtained without incorporating systematic uncertainties, in order to assess their impact. A comparison with the literature [209] is possible only for $n_f = 3$, where our results show good agreement. Overall, the analysis consistently shows that both the sensitivity and the actual limits on the QG parameter become stronger as the number of considered fermions increases. This trend is expected, since the decoherence limit increasingly deviates from the standard scenario with a higher number of fermions, as illustrated in figure 5.7. Moreover, the sensitivity improves, and the resulting bounds become more stringent, for models with stronger energy dependence. This is consistent with the expectation that energy-dependent decoherence models cause the largest deviations at high energies. As seen in figure 5.7, at the 90 % CL upper limits derived in this analysis, the deviation from the standard $\nu_\mu \to \nu_\mu$ survival probability reaches approximately 5 % at $E_\nu \sim 10\,\text{TeV}$. Another key comparison made possible within the scope of this work is the one between the sensitivity curves and the actual limits derived from the analysis of observed events. It is notable that, for the $n = 2$ decoherence model, the observed limits are more stringent than the predicted sensitivities, unlike as in the other models, where

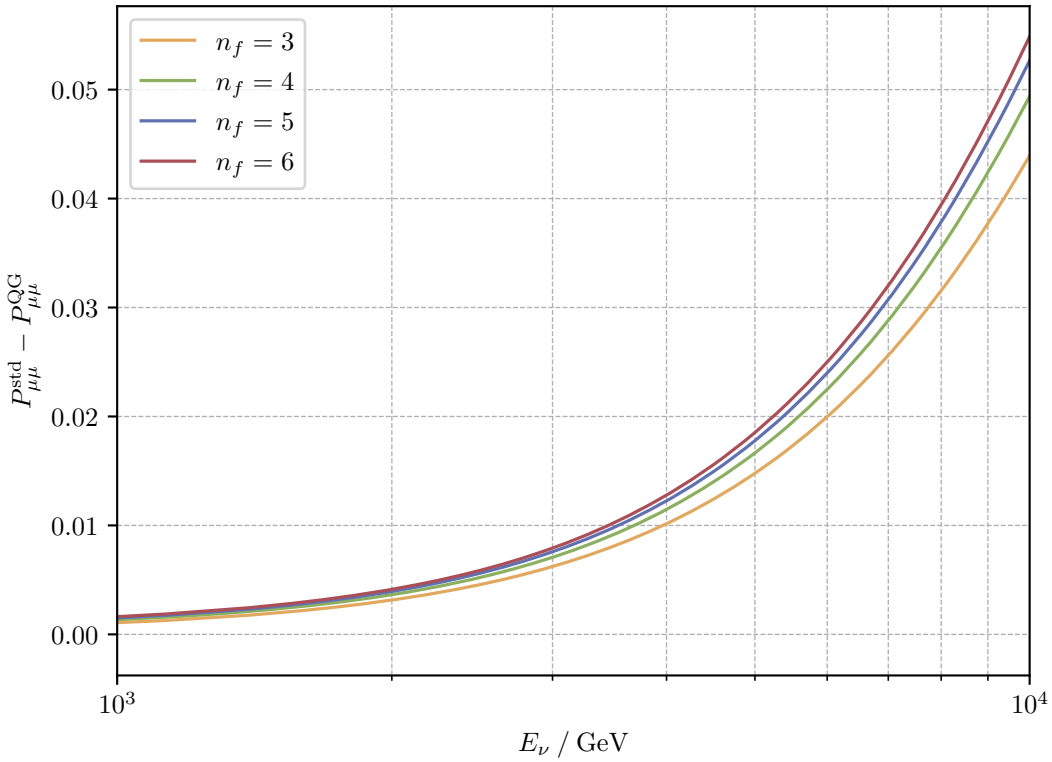

Figure 5.7: Difference between the standard and QG model prediction of the $\nu_\mu \to \nu_\mu$ transition probability, $P^{\mathrm{std}}_{\mu\mu}$ and $P^{\mathrm{QG}}_{\mu\mu}$, for various numbers of fermions in the quadratic decoherence model, with $\cos\theta_{\mathrm{zenith}} = -1$, corresponding to a baseline equal to the Earth diameter. Here, the model probabilities are evaluated at the 90 % CL $\gamma_0 = 1.61 \times 10^{-17}$ eV for $n_f = 3$ and $n = 2$.

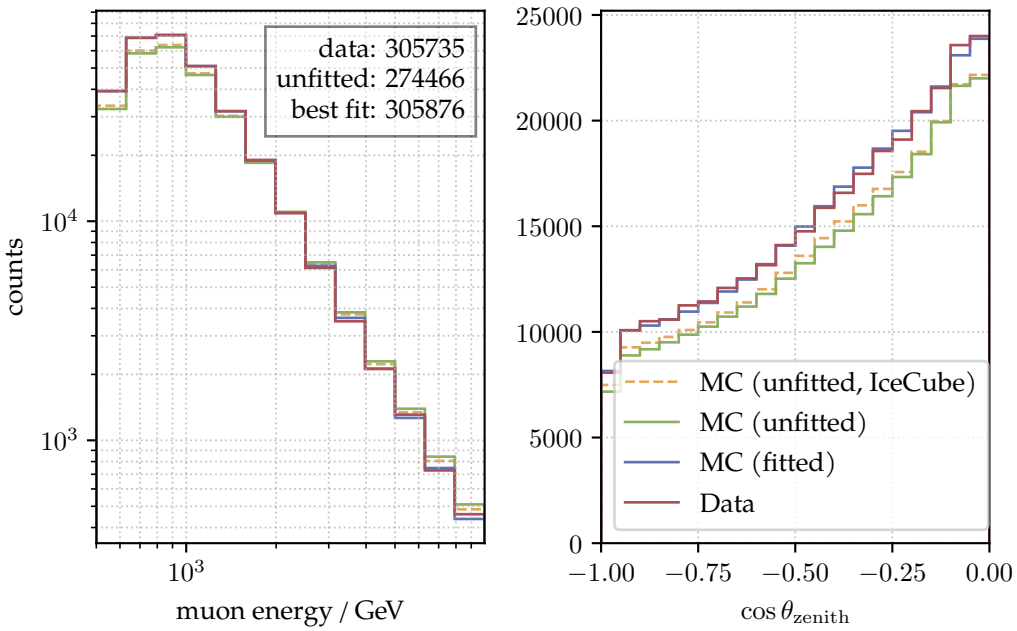

Figure 5.8: Binned event counts as a function of reconstructed muon energy and zenith angle $\cos\theta_{\text{zenith}}$. The MC predictions are shown before (MC unfitted) and after (MC fitted) applying the best-fit γ_0 and the best-fit nuisance parameters obtained from the fit to real data. We also report the MC predictions before applying the best-fit nuisance parameters obtained by the IceCube Collaboration. The line labeled "Data" corresponds to the bin counts from the actual IceCube data.

the sensitivity curves and data-based limits lie much closer together and even overlap partially. In the model with no energy dependence, an additional distinctive feature emerges: the χ^2 value reaches a minimum for all considered numbers of fermions at $\gamma_0 \sim O(10^{-16}\,\text{eV})$, before increasing again toward smaller values of γ_0. This behavior sets the energy-independent model apart from the other energy dependencies and reveals a feature that has not been discussed in the literature.

To validate our analysis and enable a direct comparison with the results from reference [209], figure 5.8 presents the fitted binned event counts for the energy-independent model and for $n_f = 3$ as a function of muon energy (left) and zenith angle (right). Here, "MC (unfitted)" refers to the MC prediction before applying the best-fit nuisance parameters, while "MC (fitted)" indicates the result after including them. The data line corresponds to the binned event counts. We observe a slight discrepancy between the "MC (unfitted)" results from our analysis and those from the official IceCube data release. This may arise from differences in the modeling of the standard predictions for the neutrino events. Nonetheless, once the fitted nuisance parameters are applied, our MC prediction shifts in the expected direction and closely follows the shape of the binned event counts of the data. This confirms that the inclusion of nuisance parameters in our sensitivity analysis behaves as intended. Moreover, the overall agreement with the IceCube analysis is very good, with only minor deviations, as of the small differences observed between our derived limits and those reportes by IceCube for $n_f = 3$ [209].

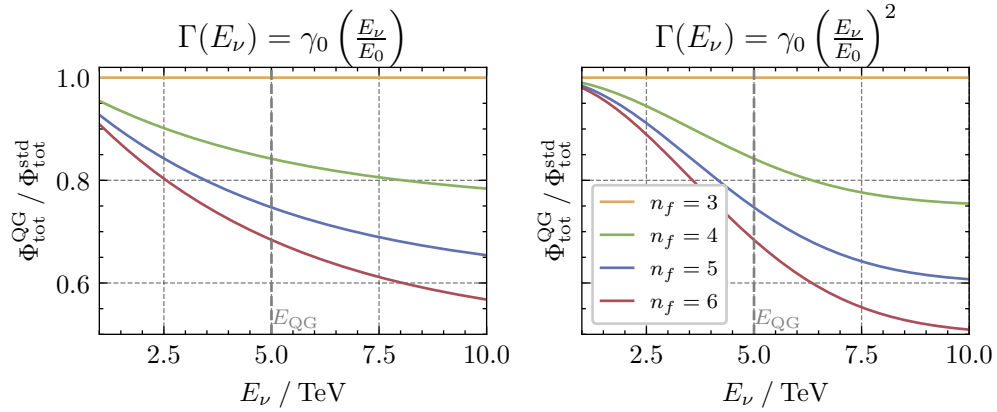

Figure 5.9: Total neutrino flux Φ^{QG}_{tot}, normalized to the corresponding total standard flux Φ^{std}_{tot} assuming a baseline of $L = 14.4\,\text{Mpc}$ for the $n = 1$ and $n = 2$ decoherence models under the condition $E_{min} < E_{QG} = 5\,\text{TeV} < E_{max}$ and for an initial neutrino flavor composition $(1 : 2 : 0)$ neutrino flavor ratio.

5.2.4 Future Prospects for Constraining Quantum Decoherence Effects

As discussed in section 5.1, astrophysical neutrinos provide an attractive avenue for probing quantum decoherence effects, due to their extremely long propagation distances and high energies. However, the current statistical limitations in astrophysical neutrino datasets make such analyses unfeasible at this time. For instance, the nine-year time-integrated IceCube dataset, analyzed in reference [309], identified only a few astrophysical sources with notable pre-trial local significance: NGC1068 with 79 signal events at 5.2σ, PSK 1424+420 with 77 events at 3.7σ, and TXS 0506+056 with 5 events at 3.5σ. Among these, NGC1068 is of particular interest due to the clustering of detected events in the narrow energy range between approximately 1 and 10 TeV. In figure 5.9, we illustrate the impact of quantum decoherence on the total expected flux from this source, expressed as the ratio $\phi^{QG}_{tot}/\phi^{std}_{tot}$ in the $[1, 10]$ TeV region for a representative QG scale $E_{QG} = 5$ TeV and γ_0 determined with equation (5.12). The total flux arriving at Earth is calculated as

$$\phi_{tot} := \sum_\alpha \phi^{Earth}_\alpha = \sum_{\alpha\beta} P_{\beta\alpha} \phi^{source}_\beta \,, \tag{5.20}$$

where $P_{\beta\alpha}$ denotes the flavor transition probability from ν_β to ν_α. The source flux is modeled as a power-law spectrum for each flavor $\phi^{source}_\alpha = c_\alpha \Phi_0 E^{-\sigma}$, assuming normalized flavor weights $\sum_\alpha c_\alpha = 1$, common spectral index σ, and amplitude Φ_0. Under these assumptions, the shown flux ratio is independent of Φ_0, σ, and the initial flavor composition c_α, and serves as a purely theoretical diagnostic to illustrate the deviation introduced by quantum decoherence. When E_{QG} falls within the energy range of observed neutrinos, the total flux in the QG scenario exhibits a noticeable suppression, trending toward the asymptotic limit $\phi^{QG}_{tot} \to (3/n_f)\phi^{std}_{tot}$. This behavior, clearly visible in figure 5.9, offers a potential signature for an energy-dependent decoherence analysis. However, any realistic analysis would require fitting both standard and QG flux models independently to the data, each with potentially different best-fit parameters, rendering the simplified ratio inapplicable to real data without further modeling.
If, instead, E_{QG} lies outside the observed energy range, the impact changes:

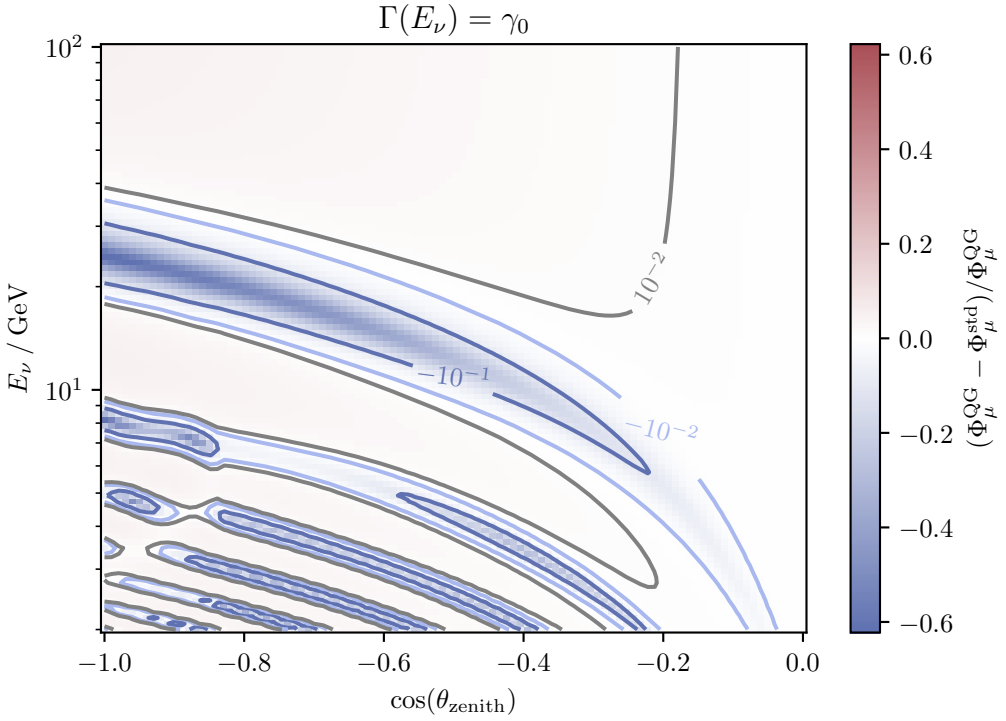

Figure 5.10: Muon neutrino oscillogram for $n_f = 4$ for the constant decoherence model ($n = 0$), using the corresponding 90 % CL upper limit $\gamma_0 = 1.18 \times 10^{-15}$ eV. The plot displays the relative deviation of the muon neutrino flux as a function of the energy E_ν and the zenith angle $\cos\theta_{\text{zenith}}$.

- For $E_{\text{QG}} \gg E_{\text{max}}$, decoherence effects are negligible and the flux prediction remains standard.

- For $E_{\text{QG}} \ll E_{\text{min}}$, the system is already fully decohered, and the total flux is simply rescaled to its asymptotic value. In such a regime, decoherence would merely alter the normalization of the flux and not be disentangled from amplitude-related uncertainties.

Overall, the limited number of signal events and the required long observation periods suggest that dedicated astrophysical decoherence studies will remain challenging in the near future.
Instead, a promising intermediate goal would be a joint atmospheric neutrino analysis combining IceCube and KM3NeT data. Such a combined effort would benefit from both enhanced statistics and complementary systematic uncertainties, increasing the robustness and sensitivity of the resulting constraints on quantum decoherence parameters.
Within the KM3NeT infrastructure, ARCA is generally the more suitable detector for high-energy studies; however, for energy-independent decoherence scenarios, ORCA may also provide valuable sensitivity. Figure 5.10 illustrates the expected deviations of neutrino fluxes under the constant decoherence model for $n_f = 4$, using the 90 % CL upper limit $\gamma_0 = 1.18 \times 10^{-15}$ eV. Here, the fluxes have been calculated with `nuflux`, and again propagated with our modified `NuSQuIDS` version. The plot highlights significant flux modifications below 20 GeV, particularly in the region below 10 GeV, which is the

energy range for which ORCA is optimized. In addition, DeepCore [310] could serve as another viable platform for probing such effects, given its operational threshold around 10 GeV. Results for ARCA are not displayed, as its expected signal characteristics are qualitatively similar to those observed in IceCube, see figure 5.4.

5.3 Summary and Discussion

In this chapter, we have investigated the impact of QG on atmospheric neutrino oscillations in the presence of hypothetical dark fermions. Given the current lack of a complete theory of QG, we refrain from specifying a particular model and instead adopt an effective approach within the framework of open quantum systems. In this context, we assume that neutrino flavor eigenstates become entangled with unknown DOFs associated with QG during propagation. While these QG-related DOFs are not accessible to current experiments, the flavor subsytem of the neutrinos remain observable. As a result of this interaction, the flavor subsystem evolves into a mixed state, reflecting the entanglement with the unmeasured QG environment.
A key assumption underlying this analysis is that QG leads to maximal violation of quantum numbers associated with global symmetries, while preserving unbroken gauge charges, angular momentum, and energy. As a consequence of QG-induced decoherence, an initially pure neutrino state may evolve to include a non-zero admixture of additional, potentially undetected fermionic states. In the asymptotic limit, where lepton flavor is no longer conserved, the transition probabilities are expected to approach a universal value of $1/n_f$, with $n_f \geq 3$ denoting the total number of fermionic species. Hypothetical candidates for such dark-sector fermions include for example sterile neutrinos [53, 80, 311, 312].
We have explored several decoherence scenarios, each characterized by a distinct power-law dependence of the decoherence parameter, $\Gamma \propto \gamma_0 E_\nu^n$, on the neutrino energy E_ν, and by the total number of fermionic states n_f, which defines the dimensionality of the extended flavor space. A statistical analysis is performed to estimate the sensitivity of the IceCube Neutrino Observatory to the QG-induced decoherence parameter γ_0, using publicly available MC simulations.
The expected sensitivities are obtained by reweighting the public IceCube MC sample to incorporate the predicted decoherence effects, while accounting for systematic uncertainties arising from the detector response and the modeling of the atmospheric neutrino flux. The analysis also identifies the energy and zenith-angle regions where IceCube is expected to be most sensitive to such effects.
In addition to the sensitivity predictions, we derive current exclusion limits on γ_0 by applying the analysis framework to recent IceCube data. A comparison between the expected and observed bounds reveals that, in the $n = 2$ decoherence model, the experimental limits are even more stringent than the predicted sensitivities. For energy-dependent models ($n = 1, 2$), the limits and sensitivities are generally in close agreement. Notably, in the energy-independent case ($n = 0$), the χ^2 distribution exhibits a minimum around $\gamma_0 \sim O(10^{-16}\,\text{eV})$, followed by a rise at smaller values of γ_0. Therefore, in this case, a non-zero value of γ_0 is preferred by the data, albeit with low statistical significance.
We always consider several values of n_f, confirming the theoretical expectation that the sensitivity improves with increasing fermion multiplicity. This behavior highlights the potential of atmospheric neutrino experiments to probe the structure of the dark sector

and discriminate between models involving different numbers of dark fermions.
While astrophysical neutrinos, due to their much longer propagation distances, would be even more sensitive to such decoherence effects, the current event statistics remain insufficient for a full analysis. Nevertheless, we anticipate that future analyses combining astrophysical and atmospheric neutrino data, particularly from IceCube and KM3NeT, could significantly enhance the statistical power and also minimize systematic uncertainties. A joint fit using both datasets may ultimately allow for the simultaneous determination of multiple model parameters, including the total number of fermion species n_f.
All these results highlight the potential of neutrino observatories to probe signatures of QG across different energy scales. Although the underlying theory remains unknown, effective frameworks, such as the open quantum system framework, enable us to explore its possible phenomenological consequences. By analyzing both atmospheric and astrophysical neutrinos, we have demonstrated that complementary regimes provide access to different parameter ranges, and that the interplay between them can be used to constrain the structure of new physics scenarios, even in the absence of full knowledge about the theory. This illustrates that tracing the subtle imprints of gravity on quantum systems is not only feasible, but offers a meaningful path towards uncovering the interface between quantum mechanics and gravity.

Chapter 6

Conclusion and Outlook

The guiding idea of this thesis was to investigate how the subtle *traces of gravity* manifest themselves in order to deepen our understanding of the underlying theory. We have approached this question on different scales and within distinct theoretical frameworks. In chapter 3, the central question was whether the Cohen, Kaplan and Nelson (CKN) bound, motivated by gravitational arguments, can form the basis of a consistent cosmological model. We then investigated whether such a model can explain the DESI BAO data, which prefers time-dependent dark energy. Together with model independent Hubble measurements, and supernovae data, we found a mild preference for the (ν)CKN model over ΛCDM. However, once CMB and weak lensing data are included and the early-time dynamics are examined, the only additional parameter ν, which is introduced to absorb model dependencies such as the particle content of the underlying theory, gets constrained to be $\nu \lesssim O\left(10^{-5}\right)$. In this regime, a global analysis shows no measurable deviation from ΛCDM. In this context, gravity acts only implicitly, constraining the energy content through the CKN bound. While the model remains conceptually motivated and consistent, it is experimentally difficult to distinguish it from the standard cosmological model. However, it is not unlikely that the (ν)CKN model with its current assumptions is only valid for the late universe as the parameter ν is unkown and might exhibit a time dependence itself. A further investigation of such a behavior and its compatibility with the DESI data would be interesting.
In chapter 4, we discussed whether the curvature of spacetime induced by gravity has an observable effect on the oscillation process of neutrinos. To address this, we extend the internal wave packet formalism that accounts for both neutrino production and detection, and adapted it to weakly curved spacetimes. For the first time, we derived a general covariant form of the oscillation amplitude in these spacetimes incorporating the wave packet nature of neutrinos. Known results from the plane wave formalism and flat spacetime were correctly recovered in the corresponding limits, while gravitational corrections manifested themselves through modified phases. Therefore, gravity acted explicitly on quantum phases and oscillation patterns of neutrinos. Yet, the derived effects lie far beyond current experimental reach: both weak static fields and time-dependent scenarios such as Gravitational Waves (GW) or the Stochastic Gravitational Wave Background (SGWB) require experimental sensitivities well beyond today's reach. Thus, the formalism provides a consistent theoretical framework, but the observability of the resulting effect remains highly constrained. Importantly, if deviations from the expected neutrino oscillation pattern are observed, these results immediately imply that classical gravitational effects can be excluded as their cause with high confidence. Instead, the origin has to lie in new physics, beyond the Standard Model (SM) formulated on a classical curved background, such as Quantum Gravity (QG).

In chapter 5, we shifted our focus to precisely such QG effects on high-energy neutrinos. We employed the open quantum system formalism to model the influence of an unknown quantum gravitational environment on neutrino oscillations. This influence was parametrized through a damping rate $\Gamma(E)$ with different energy scalings. The underlying idea is that gravity may act as an effective environment reducing flavor coherence. Next, we carried out a sensitivity analysis for IceCube on the QG parameter γ_0 for different numbers of neutrino species and different powerlaws for the energy dependence. These constraints are derived under the assumption that more than three active neutrino species exist, with the additional states comprising all particles that carry the same quantum numbers as neutrinos. Moreover, we determined experimental bounds on the QG parameter γ_0 with current IceCube data at the level of $O(10^{-15})$, with the bound improving as the number of fermions increases. This demonstrates that neutrinos are a promising experimental probe of QG effects.
To summarize, this thesis shows that gravity does leave traces, although they are often extremely difficult to access experimentally. Looking ahead, however, a future experimental landscape promises to address this challenge. With KM3NeT, both the ORCA and ARCA configurations will provide substantially improved sensitivities to neutrino oscillations and to high-energy astrophysical fluxes. IceCube is currently being upgraded to IceCube-Gen2, which will open an entirely new window on extragalactic neutrinos. On the cosmological side, Euclid and the Rubin Observatory are expected to deliver data of unprecedented precision, enabling much sharper tests of dark-energy models allowing their discrimination from ΛCDM.
Beyond these specific experiments, it remains worthwhile to continue searching for further, possibly exotic, signatures of gravity across different areas of physics, with the hope of deepening our understanding of this fundamental interaction.
This work illustrates how combining theory and experiment may gradually bring the *traces of gravity* into sharper focus. The very difficulty of this task underscores how softly gravity speaks in physics—rarely in direct signals, but almost always through its traces. Thus, this thesis ends where it began: with the faintest patterns that gravity imprints, which are nonetheless decisive for our comprehension of the cosmos.

We traced these patterns through the deep,
Their echoes stirred, their silence steep.
Though hidden, still they softly call,
The timeless voice that governs all.

Appendix A

Change of Local Inertial Coordinates

Consider a timelike curve

$$c : [\tau_{\mathrm{P}}, \tau_{\mathrm{D}}] \to \mathcal{M} \tag{A.1}$$

in the Lorentzian manifold $(\mathcal{M}, g)$, and introduce an equidistant partition $\{\tau_j\}_{j=0}^{N}$ of the proper time interval $[\tau_{\mathrm{P}}, \tau_{\mathrm{D}}]$, with $\tau_{\mathrm{P}} = \tau_0 < \tau_1 < ... < \tau_N = \tau_{\mathrm{D}}$. The corresponding points along the curve are denoted by $X_j := c(\tau_j)$ for $j = 0, \dots, N$. The exponential map at $p \in \mathcal{M}$ is defined as

$$\exp_p : \mathcal{E}_p \subset T_p\mathcal{M} \to \mathcal{M}\,, \tag{A.2}$$

which assigns to a tangent vector v the point

$$q = \exp_p(v) := \varsigma_{(p,v)}(1)\,, \tag{A.3}$$

where $\varsigma_{(p,v)}$ denotes the unique geodesic starting at p with inital velocity v. This is the mathematical notion of going straight in curved spacetime, i.e., the path of shortest distance in a given direction. Let $U_p \subset \mathcal{E}_p$ be the domain on which $\exp_p$ is a diffeomorphism onto its image $V_p := \exp_p[U_p] \subset \mathcal{M}$. Given an orthonormal basis $E_\alpha^p \in T_p\mathcal{M}$, Riemann Normal Coordinate Systems (RNC) centered at p are defined by

$$\chi_p^\mu : V_p \to \mathbb{R}^4\,, \qquad\qquad q \mapsto z^\mu = \chi_p^\mu(q)\,, \tag{A.4}$$

such that $q = \exp_p(z^\mu E_\mu^p)$. In these coordinates, spacetime locally looks flat, with curvature effects entering only at quadratic order. Parallel transport along a curve $\tilde{c} : [a, b] \to \mathcal{M}$ is denoted

$$P^{\tilde{c}}_{t_1 \to t_2} : T_{\tilde{c}(t_2)}\mathcal{M} \to T_{\tilde{c}(t_2)}\mathcal{M}\,. \tag{A.5}$$

As discussed in the main text, we now expand the function

$$\zeta : (-\epsilon, \epsilon) \to T_{X_j}\mathcal{M}\,, \qquad \delta\tau \mapsto P^{c}_{\tau_j+\delta\tau\to\tau_j}\left(\exp^{-1}_{c(\tau_j+\delta\tau)}\left(\exp_{X_j}\left(z_j^\mu E_\mu^{X_j}\right)\right)\right)\,, \tag{A.6}$$

in a Taylor series about $\delta\tau = 0$, retaining terms up to first order. Here, z_j^μ are the RNC at X_j. For convenience, we define

$$Q := \exp_{X_j}(z_j^\mu E_\mu^{X_j})\,. \tag{A.7}$$

We choose $\epsilon > 0$ small enough so that

$$Q \in V_{c(\tau_j)} \cap V_{c(\tau_j+\delta\tau)} \tag{A.8}$$

for all $|\delta\tau| < \epsilon$. Since Q lies within the integration domain in equation (4.40), and hence within the compact support of the neutrino wave packet, this condition is satisfied provided the partition size $\Delta\tau = \tau_{j+1} - \tau_j$ obeys $\Delta\tau < \epsilon$. The zeroth order is straightforward since we have no time shift and therefore no change in the coordinates:

$$\zeta(0) = P^{c}_{\tau_j \to \tau_j}\left(\exp^{-1}_{c(\tau_j)}(Q)\right) = \exp^{-1}_{X_j}(Q) = z_j^{\mu} E_{\mu}^{X_j}\,. \tag{A.9}$$

The first order term requires computing

$$\left.\frac{\mathrm{d}\zeta}{\mathrm{d}\delta\tau}\right|_{\delta\tau=0} = \left.\frac{\mathrm{D}}{\mathrm{d}\delta\tau}\right|_{\delta\tau=0} \exp^{-1}_{c(\tau_j+\delta\tau)}(Q)\,. \tag{A.10}$$

This corresponds to asking: How does the initial velocity of the geodesic connecting $c(\tau_j+\delta\tau)$ and Q vary with $\delta\tau$ at $\delta\tau = 0$? To answer this, consider the geodesic variation

$$\sigma : (-\epsilon, \epsilon) \times [0,1] \to \mathcal{M}\,, \tag{A.11}$$

$$(\delta\tau, t) \mapsto \exp_{c(\tau_j+\delta\tau)}(t \exp^{-1}_{c(\tau_j+\delta\tau)}(Q))\,, \tag{A.12}$$

which interpolates between $c(\tau_j + \delta\tau)$ at $t = 0$ and Q at $t = 1$. The associated variational vector field

$$J[0,1] \to \mathfrak{X}(\mathcal{M})\,, \tag{A.13}$$

$$t \mapsto \left.\frac{\partial}{\partial\delta\tau}\right|_{\delta\tau=0} \sigma(\delta\tau, t)\,, \tag{A.14}$$

is a Jacobi field satisfying

$$\frac{\mathrm{D}^2}{\mathrm{d}t^2} J(t) + R_{\varsigma(t)}\left(J(t), \frac{\mathrm{d}\varsigma}{\mathrm{d}t}(t)\right)\frac{\mathrm{d}\varsigma}{\mathrm{d}t}(t) = 0\,, \tag{A.15}$$

with $\varsigma(t) := \sigma(0,t)$ and boundary conditions

$$J(0) = \left.\frac{\mathrm{d}c}{\mathrm{d}\tau}\right|_{\tau=\tau_j}, \qquad J(1) = 0\,. \tag{A.16}$$

and is sketched in figure A.1 together with the variation σ. The Jacobi equation measures how neighboring geodesics deviate due to spacetime curvature, whether they converge or spread apart. By evaluating $\mathrm{D}J/\mathrm{d}t$ at $t = 0$ and using the torsion-free property of the Levi–Civita connection, one finds that

$$\left.\frac{\mathrm{D}}{\mathrm{d}t}\right|_{t=0} J(t) = \left.\frac{\mathrm{D}}{\mathrm{d}\delta\tau}\right|_{\delta\tau=0} \exp^{-1}_{c(\tau_j+\delta\tau)}(Q)\,, \tag{A.17}$$

i.e., solving the Jacobi equation with the boundary values in equation (A.16) directly yields the desired first order Taylor coefficient.
To proceed, we introduce a set of parallel-propagated basis vectors $\hat{E}_{\mu}(t)$ along $\varsigma(t)$, with $\hat{E}_{\mu}(0) = E_{\mu}^{X_j}$, and express equation (A.15) in components:

$$\frac{\mathrm{d}^2 J^{\mu}}{\mathrm{d}t^2}(t) + R^{\mu}{}_{\rho\lambda\nu}(\varsigma(t))\frac{\mathrm{d}\varsigma^{\rho}}{\mathrm{d}t}(t)\frac{\mathrm{d}\varsigma^{\lambda}}{\mathrm{d}t}(t) J^{\nu}(t) = 0\,. \tag{A.18}$$

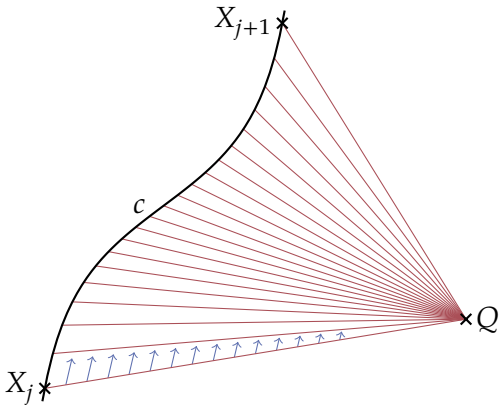

Figure A.1: The neutrino wave packet approximately follows the geodesic c. Illustrated is the geodesic variation (in red) and its Jacobi vector field (blue).

Since $\dot{\varsigma}^\rho(t) = z_j^\rho$ is constant in this basis, and assuming the wave packet is sufficiently localized so that curvature variations across its support can be neglected, the combination

$$A^\mu{}_\nu := -R^\mu{}_{\rho\lambda\nu}(\varsigma(t))z_j^\rho z_j^\lambda \equiv -R^\mu{}_{\rho\lambda\nu}(X_j)z_j^\rho z_j^\lambda + O(z_j^3)\,, \tag{A.19}$$

is approximately constant. This is equivalent to saying the graviational field looks uniform across the entire spatial extent of the wave packet. The Jacobi equation then reduces to

$$\frac{\mathrm{d}^2 J^\mu}{\mathrm{d}t^2}(t) = A^\mu{}_\nu J^\nu(t)\,. \tag{A.20}$$

Since $A_{\mu\nu} := \eta_{\mu\sigma}A^\sigma{}_\nu$ is symmetric, it can be diagonalized by a Lorentz transformation. The solution consistent with the boundary conditions yields, to lowest non-trivial order,

$$J^\mu(t) = -\delta^\mu_\nu \dot{c}^\nu(\tau_j) + O\left(z_j^2\right)\,. \tag{A.21}$$

Finally, substituting back into the Taylor expansion gives

$$\zeta(\delta\tau) = \left(z_j^\mu - \dot{c}^\nu(\tau_j)\delta\tau\right)E_\mu^{X_j} + O(z_j^2, \delta\tau^2)\,. \tag{A.22}$$

This is the linear relation between the local inertial coordinates and the proper-time shift along the neutrino's trajectory, with curvature effects entering only at higher order.

Appendix B

Induction for the Step-By-Step Propagation Procedure

In the main part, we established that the neutrino wave packet expressed in terms of the modes $\xi^{X_P \to X_{k+1}}$ is related to that in terms of $\xi^{X_P \to X_k}$ via

$$\phi_\sigma^{P\to k+1}(\vec{p}) = \exp\left(-ip_\mu \dot{c}^\mu(\tau_k)\Delta\tau + O(\Delta\tau^2)\right)\phi_\sigma^{P\to k}(\vec{p}) + O(R_k\sigma_x^2\Delta\tau)\,, \tag{B.1}$$

where R_k denotes the characteristic curvature scale at step k and σ_x is the wave packets spatial width. So each small propagation step adds a phase proportional to the four-momentum p_μ dotted with the local four-velocity $\dot{c}^\mu$. We now prove by induction that this relation implies the general propagation formula

$$\phi_\sigma^{P\to l}(\vec{p}) = \exp\left(-i\sum_{k=0}^{l-1}\eta_{\mu\nu}\dot{c}^\mu(\tau_k)p^\nu\Delta\tau + O(\Delta\tau^2)\right)\phi_\sigma^{P}(\vec{p}) + O\left(\sum_{k=0}^{l-1}R_k\sigma_x^2\Delta\tau\right). \tag{B.2}$$

For $l = 1$, equation (B.1) reads

$$\phi_\sigma^{P\to 1}(\vec{p}) = \exp\left(-ip_\mu \dot{c}^\mu(\tau_0)\Delta\tau + O(\Delta\tau^2)\right)\phi_\sigma^{P\to 0}(\vec{p}) + O(R_0\sigma_x^2\Delta\tau)\,. \tag{B.3}$$

By definition, $\phi_\sigma^{P\to 0}(\vec{p}) \equiv \phi_\sigma^{P}(\vec{p})$. Inserting this into equation (B.2) with $l = 1$ yields exactly the same expression as equation (B.3).
Assume that equation (B.2) holds for some $l \geq 1$, i.e.,

$$\phi_\sigma^{P\to l}(\vec{p}) = \exp\left[-i\sum_{k=0}^{l-1}\eta_{\mu\nu}\,\dot{c}^\mu(\tau_k)\,p^\nu\,\Delta\tau + O(\Delta\tau^2)\right]\phi_\sigma^{P}(\vec{p}) + O\left(\sum_{k=0}^{l-1}R_k\,\sigma_x^2\,\Delta\tau\right). \tag{B.4}$$

From equation (B.1) for $k = l$, we have

$$\phi_\sigma^{P\to l+1}(\vec{p}) = \exp\left[-i\,p_\mu\,\dot{c}^\mu(\tau_l)\,\Delta\tau + O(\Delta\tau^2)\right]\phi_\sigma^{P\to l}(\vec{p}) + O\left(R_l\,\sigma_x^2\,\Delta\tau\right). \tag{B.5}$$

Substituting the induction hypothesis into the above expression gives

$$\begin{aligned}\phi_\sigma^{P\to l+1}(\vec{p}) = {}& \exp\left[-i\,p_\mu\,\dot{c}^\mu(\tau_l)\,\Delta\tau + O(\Delta\tau^2)\right] \\ & \times\left[\exp\left(-i\sum_{k=0}^{l-1}\eta_{\mu\nu}\,\dot{c}^\mu(\tau_k)\,p^\nu\,\Delta\tau + O(\Delta\tau^2)\right)\phi_\sigma^{P}(\vec{p}) + O\left(\sum_{k=0}^{l-1}R_k\,\sigma_x^2\,\Delta\tau\right)\right] \\ & + O\left(R_l\,\sigma_x^2\,\Delta\tau\right).\end{aligned} \tag{B.6}$$

Multiplying the exponentials and combining the remainder terms yields

$$\phi_\sigma^{P\to l+1}(\vec{p}) = \exp\left[-i\sum_{k=0}^{l}\eta_{\mu\nu}\,\dot{c}^\mu(\tau_k)\,p^\nu\,\Delta\tau + O(\Delta\tau^2)\right]\phi_\sigma^{P}(\vec{p}) + O\left(\sum_{k=0}^{l}R_k\,\sigma_x^2\,\Delta\tau\right). \tag{B.7}$$

This is precisely equation (B.2) with $l \to l+1$, which completes the induction. □

Appendix C

Propagation Distance and Coordinate Transformations in Linearized Gravity

To employ the weak-field expression for the neutrino oscillation amplitude, we require explicit formulas for two key ingredients:

1. The effective spacetime displacement vector L^μ introduced in equation (4.67).
2. The Lorentz transformation that relates the detector's local inertial frame to the global coordinates.

Determining these quantities necessitates solving the geodesic equation in general coordinates for a linearly perturbed spacetime and obtaining an explicit representation of the parallel transport operator. In addition, we must specify the coordinate transformations between the global coordinate system x^μ, where the metric is given in equation (4.68), and the local inertial frames at the production and at the detector.
Both the geodesic solution and the parallel transport operator depend on the Christoffel symbols from equation (2.72), where we plug in the metric (4.68) to get to the Christoffel symbols in linearized gravity. The transformation between the local inertial coordinates z^α at a spacetime point X_0 and the global coordinates x^μ takes the form

$$\left.\frac{\partial z^\alpha}{\partial x^\mu}\right|_{X_0} = \delta^\alpha{}_\mu + \frac{\varepsilon}{2}\eta^{\alpha\rho}h_{\rho\mu}(X_0) + O(\varepsilon^2)\,, \tag{C.1}$$

$$\left.\frac{\partial x^\mu}{\partial z^\alpha}\right|_{X_0} = \delta^\mu{}_\alpha - \frac{\varepsilon}{2}\eta^{\mu\rho}h_{\rho\alpha}(X_0) + O(\varepsilon^2)\,. \tag{C.2}$$

Equation (C.1) and (C.2) implicitly assume that the coordinate axes of z^μ and x^μ coincide at zeroth order in ε. This condition is satisfied in the situation considered in section 4.3, where both production and detector are approximately at rest in the global frame x^μ. Consequently, no additional Lorentz transformation is required to align the local inertial frames with the global coordinates.
We begin by solving the geodesic equation (2.71) for the curve c^μ with the boundary conditions

$$c^\mu(0) = X_\mathrm{P}^\mu\,, \qquad\qquad c^\mu(\tau) = X_\mathrm{D}^\mu\,. \tag{C.3}$$

We adopt the perturbative ansatz

$$c^\mu(\lambda) = c_0^\mu(\lambda) + \varepsilon c_1^\mu(\lambda) + O(\varepsilon^2)\,, \tag{C.4}$$

and insert it into equation (2.71). Matching coefficients at each order in ε yields

$$\frac{\mathrm{d}^2 c_0^\mu}{\mathrm{d}\lambda^2}(\lambda) = 0\,, \tag{C.5}$$

$$\frac{\mathrm{d}^2 c_1^\mu}{\mathrm{d}\lambda^2}(\lambda) = -\hat{\Gamma}^\mu_{\sigma\rho}(c_0(\lambda))\frac{\mathrm{d}c_0^\sigma}{\mathrm{d}\lambda}(\lambda)\frac{\mathrm{d}c_0^\rho}{\mathrm{d}\lambda}(\lambda)\,, \tag{C.6}$$

where $\Gamma^\mu_{\sigma\rho} =: \varepsilon\hat{\Gamma}^\mu_{\sigma\rho}$ by definition. The zeroth order equation (C.5) is solved by a straight-line trajectory $c_0^\mu(\lambda) = u^\mu\lambda + x_0^\mu$. Integrating equation (C.6) twice with respect to λ yields

$$c_1^\mu(\lambda) = \int_0^\lambda \mathrm{d}\lambda' \int_0^{\lambda'} \mathrm{d}\lambda'' a^\mu(\lambda'') + u_1^\mu\lambda + x_1^\mu\,, \tag{C.7}$$

where the geodesic acceleration is defined as

$$a^\mu(\lambda) := -\hat{\Gamma}^\mu_{\sigma\rho}u^\sigma u^\rho\,. \tag{C.8}$$

Applying the boundary conditions in equation (C.3) and matching coefficients order-by-order yields

$$c_0^\mu(\lambda) = u^\mu\lambda + X_\mathrm{P}^\mu\,, \qquad u^\mu = \frac{X_\mathrm{D}^\mu - X_\mathrm{P}^\mu}{\tau}\,, \tag{C.9}$$

$$c_1^\mu(\lambda) = \int_0^\lambda \mathrm{d}\lambda' \int_0^{\lambda'} \mathrm{d}\lambda'' a^\mu(\lambda'') - \frac{\lambda}{\tau}\int_0^\tau \mathrm{d}\lambda' \int_0^{\lambda'} \mathrm{d}\lambda'' a^\mu(\lambda'')\,. \tag{C.10}$$

To determine L^μ, only the derivative $\mathrm{d}c^\mu/\mathrm{d}\lambda$ transformed to the detector's local inertial frame, is required:

$$L^\mu = \left.\frac{\partial z^\mu}{\partial x^\nu}\right|_{X_\mathrm{D}} \frac{\mathrm{d}c^\nu}{\mathrm{d}\lambda}(\tau)\tau\,. \tag{C.11}$$

The derivative of c^μ times τ is

$$\frac{\mathrm{d}c^\nu}{\mathrm{d}\lambda}(\tau)\tau = \Delta X^\mu + \varepsilon\left[\tau\int_0^\tau \mathrm{d}\lambda a^\mu(\lambda) - \int_0^\tau \mathrm{d}\lambda\int_0^\lambda \mathrm{d}\lambda' a^\mu(\lambda')\right]. \tag{C.12}$$

The integrated geodesic acceleration evaluates to

$$\int_0^\lambda \mathrm{d}\lambda' a^\mu(\lambda') = -\frac{1}{2}\int_0^\lambda \mathrm{d}\lambda' \left(2\partial_\sigma h^\mu{}_\rho(c_0(\lambda')) - \partial^\mu h_{\sigma\rho}(c_0(\lambda'))\right)u^\sigma u^\rho \tag{C.13}$$

$$= -\frac{1}{2}\int_0^\lambda \mathrm{d}\lambda' \left(2\frac{\mathrm{d}}{\mathrm{d}\lambda'}\left[h^\mu{}_\rho(c_0(\lambda'))u^\rho\right] - \partial^\mu h_{\sigma\rho}(c_0(\lambda'))u^\sigma u^\rho\right) \tag{C.14}$$

$$= -u^\rho\left[h^\mu{}_\rho(c_0(\lambda)) - h^\mu{}_\rho(X_\mathrm{P})\right] + \frac{1}{2}\int_0^\lambda \mathrm{d}\lambda'\partial^\mu h_{\sigma\rho}(c_0(\lambda'))u^\sigma u^\rho\,. \tag{C.15}$$

Substituting this back gives

$$\begin{aligned}\frac{\mathrm{d}c^\nu}{\mathrm{d}\lambda}(\tau)\tau = \Delta X^\mu + \varepsilon\Bigg[&- u^\rho\tau\left[h^\mu{}_\rho(X_\mathrm{D}) - h^\mu{}_\rho(X_\mathrm{P})\right] + \frac{\tau}{2}\int_0^\tau \mathrm{d}\lambda'\partial^\mu h_{\sigma\rho}(c_0(\lambda'))u^\sigma u^\rho \\ &+ u^\rho\int_0^\tau \mathrm{d}\lambda\left[h^\mu{}_\rho(c_0(\lambda)) - h^\mu{}_\rho(X_\mathrm{P})\right] \\ &- \frac{1}{2}\int_0^\tau \mathrm{d}\lambda\int_0^\lambda \mathrm{d}\lambda'\partial^\mu h_{\sigma\rho}(c_0(\lambda'))u^\sigma u^\rho\Bigg]\end{aligned} \tag{C.16}$$

$$\begin{aligned}= \Delta X^\mu + \varepsilon\Bigg[&- \Delta X^\rho h^\mu{}_\rho(X_\mathrm{D}) + \Delta X^\rho h^\mu{}_\rho(X_\mathrm{P}) + \frac{1}{2}\left\langle\partial^\mu h_{\sigma\rho}\circ c_0\right\rangle\Delta X^\sigma\Delta X^\rho \\ &+ \Delta X^\rho\left\langle h^\mu{}_\rho\circ c_0\right\rangle - \Delta X^\rho h^\mu{}_\rho(X_\mathrm{P}) \\ &- \frac{1}{2}\left\langle\lambda\mapsto\int_0^\lambda \mathrm{d}\lambda'\partial^\mu h_{\sigma\rho}(c_0(\lambda'))\right\rangle\Delta X^\sigma\Delta X^\rho\Bigg]\end{aligned} \tag{C.17}$$

$$\begin{aligned}= \Delta X^\mu + \frac{\varepsilon}{2}\Bigg[&- 2\Delta X^\rho h^\mu{}_\rho(X_\mathrm{D}) + 2\Delta X^\rho\left\langle h^\mu{}_\rho\circ c_0\right\rangle \\ &+ \left\{\left\langle\partial^\mu h_{\sigma\rho}\circ c_0\right\rangle - \left\langle\lambda\mapsto\int_0^\lambda \mathrm{d}\lambda'\partial^\mu h_{\sigma\rho}(c_0(\lambda'))\right\rangle\right\}\Delta X^\sigma\Delta X^\rho\Bigg],\end{aligned} \tag{C.18}$$

where $\Delta X^\mu := X^\mu_\mathrm{D} - X^\mu_\mathrm{P}$, and

$$\langle f\rangle \equiv \langle\tau'\mapsto f(\tau')\rangle := \int_0^\tau f(\tau')\frac{\mathrm{d}\tau'}{\tau}\,, \tag{C.19}$$

denotes the average of a function along the unperturbed geodesic c_0. Finally, multiplying by $\partial z^\mu/\partial x^\nu$ gives

$$L^\mu = \left(\delta^\mu{}_\nu + \frac{\varepsilon}{2}\delta\ell^\mu{}_\nu\right)\Delta X^\nu\,, \tag{C.20}$$

$$\begin{aligned}\delta\ell^\mu{}_\nu = \Bigg[&\left\langle h^\mu{}_\nu\circ c_0\right\rangle - \left\{h^\mu{}_\nu(X_\mathrm{D}) - \left\langle h^\mu{}_\nu\circ c_0\right\rangle\right\} \\ &+ \left\{\left\langle\partial^\mu h_{\sigma\nu}\circ c_0\right\rangle - \left\langle\lambda\mapsto\int_0^\lambda \mathrm{d}\lambda'\partial^\mu h_{\sigma\nu}(c_0(\lambda'))\right\rangle\right\}\Delta X^\sigma\Bigg].\end{aligned} \tag{C.21}$$

With this derived, we go on to the Lorentz transformation which is given in equation (4.56). We now need to obtain the parallel transport operator in the global coordinates x^μ to first order in ε. Let w^μ be a tangent vector at $T_{X_\mathrm{P}}\mathcal{M}$, expressed in the x^μ basis. The corresponding parallel vector field $W^\mu(\lambda)$ along the geodesic c is given by

$$W^\mu(\lambda) = [P^c_{0\to\lambda}]^\mu{}_\nu w^\nu\,, \tag{C.22}$$

and satisfies the parallel transport equation

$$\frac{\mathrm{D}}{\mathrm{d}\lambda}W^\mu(\lambda) \equiv 0\,, \qquad\qquad W^\mu(0) = w^\mu\,. \tag{C.23}$$

Solving this initial value problem for arbitrary w^μ determines the operator $P^c_{0\to\lambda}$. In local coordinates, equation (C.23) reads

$$\frac{\mathrm{d}W^\mu}{\mathrm{d}\lambda}(\lambda) = -\Gamma^\mu_{\sigma\nu}(c(\lambda))\frac{\mathrm{d}c^\sigma}{\mathrm{d}\lambda}(\lambda)W^\nu\,. \tag{C.24}$$

The corresponding integral form is

$$W^\mu(\lambda) = w^\mu - \int_0^\lambda \mathrm{d}\lambda' \Gamma^\mu_{\sigma\nu}(c(\lambda'))\frac{\mathrm{d}c^\sigma}{\mathrm{d}\lambda'}(\lambda')W^\nu(\lambda')\,. \tag{C.25}$$

Iterating this solution and discarding $O(\varepsilon^2)$ terms yields

$$W^\mu(\lambda) = \left(\delta^\mu{}_\nu - \int_0^\lambda \mathrm{d}\lambda' \Gamma^\mu_{\sigma\nu}(c_0(\lambda'))u^\sigma\right)w^\nu + O(\varepsilon^2)\,. \tag{C.26}$$

Thus, the parallel transport operator becomes

$$[P^c_{0\to\lambda}]^\mu{}_\nu = \delta^\mu{}_\nu - \int_0^\lambda \mathrm{d}\lambda' \Gamma^\mu_{\sigma\nu}(c_0(\lambda'))u^\sigma + O(\varepsilon^2) \tag{C.27}$$

$$= \delta^\mu{}_\nu - \frac{\varepsilon}{2}\int_0^\lambda \mathrm{d}\lambda' \left(\partial_\sigma h^\mu{}_\nu + \partial_\nu h^\mu{}_\sigma - \partial^\mu h_{\sigma\nu}\right)u^\sigma + O(\varepsilon^2) \tag{C.28}$$

$$= \delta^\mu{}_\nu - \frac{\varepsilon}{2}[h^\mu{}_\nu(c_0(\lambda)) - h^\mu{}_\nu(X_\mathrm{P})] - \frac{\varepsilon}{2}\int_0^\lambda \mathrm{d}\lambda' \left(\partial_\nu h^\mu{}_\sigma - \partial^\mu h_{\sigma\nu}\right)u^\sigma + O(\varepsilon^2)\,. \tag{C.29}$$

Evaluating this expression at $\lambda = \tau$ and transforming the lower index to the local inertial frame at the source, and the upper index to that at the detector, gives

$$\Lambda^\alpha{}_\beta = \delta^\alpha{}_\beta - \frac{\varepsilon}{2}\left[\langle\partial_\beta h^\alpha{}_\sigma \circ c_0\rangle - \langle\partial^\alpha h_{\sigma\beta}\circ c_0\rangle\right]\Delta X^\sigma + O(\varepsilon^2)\,. \tag{C.30}$$

The inverse transformation is

$$\Lambda_\alpha{}^\beta = \delta^\alpha{}_\beta + \frac{\varepsilon}{2}\left[\langle\partial_\alpha h^\beta{}_\sigma \circ c_0\rangle - \langle\partial^\beta h_{\sigma\alpha}\circ c_0\rangle\right]\Delta X^\sigma + O(\varepsilon^2)\,. \tag{C.31}$$

Since the deviation from the identity is of order $\varepsilon \ll 1$, the associated rotation angles and boost velocities are small. In particular, the boost component of Λ corresponds to a non-relativistic transformation.

Appendix D

Propagation Time Integration in Linearized Gravity

In this appendix, we evaluate the integral over the neutrino propagation time ΔT that emerges when rewriting equation (4.86) in terms of the alternative variables

$$\begin{pmatrix} \Delta T(T_\mathrm{P}, T_\mathrm{D}) \\ T_\mathrm{D}(T_\mathrm{P}, T_\mathrm{D}) \end{pmatrix} = \begin{pmatrix} T_\mathrm{D} - T_\mathrm{P} \\ T_\mathrm{D} \end{pmatrix} . \tag{D.1}$$

With this change of variables, the time integral takes the form

$$I_{jk}(\vec{X}_\mathrm{P}, \vec{X}_\mathrm{D}, E) = \int_{T_{\mathrm{D}1}}^{T_{\mathrm{D}2}} \mathrm{d}T_\mathrm{D} \int_{T_\mathrm{D}-T_{\mathrm{P}2}}^{T_\mathrm{D}-T_{\mathrm{P}1}} \mathrm{d}\Delta T \exp\left(\Xi_{jk}(\Delta T, T_\mathrm{D})\right) . \tag{D.2}$$

Since the integrand is sharply peaked around its maximum at $\Delta T^\star_{jk}$, the integration limits in ΔT can be extended to the full real line,

$$I_{jk}(\vec{X}_\mathrm{P}, \vec{X}_\mathrm{D}, E) \approx \int_{T_{\mathrm{D}1}}^{T_{\mathrm{D}2}} \mathrm{d}T_\mathrm{D} \int_{-\infty}^{\infty} \mathrm{d}\Delta T \exp\left(\Xi_{jk}(\Delta T, T_\mathrm{D})\right) , \tag{D.3}$$

provided the production livetime is chosen such that $\Delta T^\star_{jk} \in [T_\mathrm{D} - T_{\mathrm{P}2}, T_\mathrm{D} - T_{\mathrm{P}1}]$ for all T_D within the considered interval.
The exponent Ξ_{jk} reads

$$\begin{aligned} \Xi_{jk}(\Delta T(T_\mathrm{P}, T_\mathrm{D}), T_\mathrm{P}) = &- \frac{(\tilde{\vec{P}}_{\mathrm{P}j} - \vec{P}_{\mathrm{D}j})^2}{2\sigma_P^2} - \frac{(\tilde{\vec{P}}_{\mathrm{P}k} - \vec{P}_{\mathrm{D}k})^2}{2\sigma_P^2} \\ &- \frac{(\bar{v}_j L^0 - L)^2}{2\sigma_{\|j}^2} - \frac{(\bar{v}_k L^0 - L)^2}{2\sigma_{\|k}^{2*}} - i(\Delta E_{jk} L^0 - \Delta p_{jk} L) , \end{aligned} \tag{D.4}$$

where $\bar{v}_{j,k}$ are the mean group velocities, L the spatial separation between production and detection, and L^0 the corresponding propagation time in the absence of spreading effects. The real part of Ξ_{jk} determines the envelope of the integrand $|\exp\left(\Xi_{jk}\right)| = \exp\left(\mathrm{Re}(\Xi_{jk})\right)$, which attains its maximum at $\Delta T^\star_{jk}$, corresponding to the point of maximal spatial overlap between the wave packets of mass eigenstates j and k at the detector.

Separating Ξ_{jk} into real and imaginary part, one finds

$$\mathrm{Re}(\Xi_{jk}) = -\frac{(\bar{v}_j L^0 - L)^2}{2\Theta^2\left(1+\chi_j^2 (L^0)^2\right)} - \frac{(\bar{v}_k L^0 - L)^2}{2\Theta^2\left(1+\chi_k^2 (L^0)^2\right)} - \frac{(\tilde{\vec{P}}_{\mathrm{P}j} - \vec{P}_{\mathrm{D}j})^2}{2\sigma_P^2} - \frac{(\tilde{\vec{P}}_{\mathrm{P}k} - \vec{P}_{\mathrm{D}k})^2}{2\sigma_P^2}\,, \tag{D.5}$$

$$\mathrm{Im}(\Xi_{jk}) = +\chi_j L^0 \frac{(\bar{v}_j L^0 - L)^2}{2\Theta^4\left(1+\chi_j^2 (L^0)^2\right)} - \chi_k L^0 \frac{(\bar{v}_k L^0 - L)^2}{2\Theta^4\left(1+\chi_k^2 (L^0)^2\right)} - (\Delta E_{jk} L^0 - \Delta p_{jk} L)\,. \tag{D.6}$$

Here, we have introduced the parametrization of the longitudinal wave packet widths,

$$\sigma_{\|j}^2 = \Theta^2\left(1 + i\chi_j L^0\right)\,, \qquad \Theta^2 := \frac{1}{2}\left(\frac{1}{\sigma_{\mathrm{P}j}^2} + \frac{1}{\sigma_{\mathrm{D}j}^2}\right)\,, \qquad \chi_j := \frac{(1-\bar{\vec{v}}_j^{\,2})}{\bar{E}_j \Theta^2}\,. \tag{D.7}$$

Having set up the expression for Ξ_{jk}, we now determine the propagation time $\Delta T_{jk}^\star$ corresponding to the maximal overlap of the j-th and k-th wave packets at the detector. To this end, we first expand the relevant quantities, i.e., the physical propagation time L^0, the physical separation L, and the parallel-transported source momentum $\tilde{\vec{P}}_j$, to linear order in ε:

$$L^0 = \Delta T + \varepsilon \delta\Delta T(\Delta T, T_{\mathrm{D}})\,, \tag{D.8}$$

$$L = \Delta X + \varepsilon \delta\Delta X(\Delta T, T_{\mathrm{D}})\,, \tag{D.9}$$

$$\tilde{\vec{P}}_{\mathrm{P}j} = \vec{p} + \Delta\vec{P}_{\mathrm{P}j} + \varepsilon\delta\vec{P}_{\mathrm{P}j}(\Delta T, T_{\mathrm{D}}) =: \vec{p} + \Delta\tilde{\vec{P}}_{\mathrm{P}j}(\Delta T, T_{\mathrm{D}})\,, \tag{D.10}$$

with $\vec{p} := p\vec{\ell} := p\vec{L}/|\vec{L}|$. The mean momentum of the j-th mass eigenstate wave packet then takes the form

$$\bar{p}_j = p + \Delta p_j \tag{D.11}$$

$$= p + \frac{\sigma_{\mathrm{D}}^2 \Delta\tilde{\vec{P}}_{\mathrm{P}j} + \sigma_{\mathrm{P}}^2 \Delta\vec{P}_{\mathrm{D}j}}{\sigma_{\mathrm{P}}^2 + \sigma_{\mathrm{D}}^2}\cdot\vec{\ell} \tag{D.12}$$

$$= \underbrace{p + \frac{\sigma_{\mathrm{D}}^2 \Delta\vec{P}_{\mathrm{P}j} + \sigma_{\mathrm{P}}^2 \Delta\vec{P}_{\mathrm{D}j}}{\sigma_{\mathrm{P}}^2 + \sigma_{\mathrm{D}}^2}\cdot\vec{\ell}}_{\bar{p}_{j0}} + \underbrace{\varepsilon\,\frac{\sigma_{\mathrm{D}}^2}{\sigma_{\mathrm{P}}^2 + \sigma_{\mathrm{D}}^2}\delta\vec{P}_{\mathrm{P}j}\cdot\vec{\ell}}_{\delta\bar{p}_{j0}}\,. \tag{D.13}$$

The associated group velocity is given by

$$\bar{v}_j = \bar{v}_{j0} + \varepsilon\delta\bar{v}_{j0}\,, \qquad \bar{v}_{j0} = \frac{\bar{p}_{j0}}{E_{j0}}\,, \qquad \delta\bar{v}_{j0} = \frac{\delta\bar{p}_{j0} m_j^2}{p^3} + O(\varepsilon_{\mathrm{UR}}^2)\,. \tag{D.14}$$

Here, we have dropped terms beyond first order in $\varepsilon_{\mathrm{UR}}$, since such contributions would appear only at $O(\varepsilon\varepsilon_{\mathrm{UR}}^2)$, which are neglected in our approximation.
The time $\Delta T_{jk}^\star$ follows from the condition

$$0 = \left.\frac{\mathrm{dRe}(\Xi_{jk})}{\mathrm{d}\Delta T}\right|_{\Delta T = \Delta T_{jk}^\star}\,. \tag{D.15}$$

We adopt the perturbative ansatz $\Delta T^\star_{jk} = \Delta T^\star_{jk,0} + \varepsilon \Delta T^\star_{jk,1} + O(\varepsilon^2)$, insert it into equation (D.15), and expand to first order in ε. The zeroth order solution is

$$T^\star_{jk,0} = \Delta X \left(1 + \frac{m_j^2 + m_k^2}{4p^2} - \frac{\Delta p_j m_j^2 + \Delta p_k m_k^2}{2p^3} - \frac{(\Delta m_{jk}^2)^2}{8p^4} - \frac{m_j^4 + m_k^4}{16p^4} \right) + O(\varepsilon_{\mathrm{UR}}^3) \,, \tag{D.16}$$

which is accurate to second order in $\varepsilon_{\mathrm{UR}}$. The first order correction reads

$$\Delta T^\star_{jk,1} = -\frac{\partial^2 \mathrm{Re}(\Xi_{jk})}{\partial \Delta T^2}\bigg|^{-1}_{\substack{\varepsilon=0 \\ \Delta T = \Delta T^\star_{jk,0}}} \frac{\partial^2 \mathrm{Re}(\Xi_{jk})}{\partial \varepsilon \partial \Delta T}\bigg|_{\substack{\varepsilon=0 \\ \Delta T = \Delta T^\star_{jk,0}}} \tag{D.17}$$

$$\begin{aligned} = -\frac{1}{v_{j0}^2 + v_{k0}^2} \Bigg\{ \frac{\Delta X}{v_{jk,0}} \Bigg[\left(v_{j0} - v_{jk,0}\right) \left(\frac{\Delta X}{v_{jk,0}} \delta \dot{v}_{j0} + v_{j0} \delta \Delta \dot{T} + \delta v_{j0} - \delta \Delta \dot{X} \right) \\ + \left(v_{k0} - v_{jk,0}\right) \left(\frac{\Delta X}{v_{jk,0}} \delta \dot{v}_{k0} + v_{k0} \delta \Delta \dot{T} + \delta v_{k0} - \delta \Delta \dot{X} \right) \Bigg] \\ + v_{j0} \left(\frac{\Delta X}{v_{jk,0}} \delta v_{j0} + v_{j0} \delta \Delta T - \delta \Delta X \right) \\ + v_{k0} \left(\frac{\Delta X}{v_{jk,0}} \delta v_{k0} + v_{k0} \delta \Delta T - \delta \Delta X \right) \Bigg\} \,, \end{aligned} \tag{D.18}$$

with $v_{jk,0} = (v_{j0}^2 + v_{k0}^2)/(v_{j0} + v_{k0})$. This can be simplified using $\delta v_{j0} = O(\varepsilon_{\mathrm{UR}})$, $v_{j0} - v_{jk,0} = O(\varepsilon_{\mathrm{UR}})$, and

$$\left(v_{j0} - v_{jk,0}\right) + \left(v_{k0} - v_{jk,0}\right) = \frac{\Delta m_{jk}^2}{4p^2} + \frac{\Delta m_{kj}^2}{4p^2} + O(\varepsilon_{\mathrm{UR}}^2) = O(\varepsilon_{\mathrm{UR}}^2) \,, \tag{D.19}$$

which yields

$$\varepsilon \Delta T^\star_{jk,1} = -\left(\varepsilon \delta \Delta T - \left[1 + \frac{m_j^2 + m_k^2}{4p^2} \right] \varepsilon \delta \Delta X + \varepsilon \frac{\delta v_{j0} + \delta v_{k0}}{2} \Delta X \right) + O(\varepsilon^2, \varepsilon \varepsilon_{\mathrm{UR}}^2) \,. \tag{D.20}$$

Combining zeroth and first order results, the maximal overlap time can be written as

$$\Delta T^\star_{jk} = \frac{L}{\tilde{v}_{jk}}\bigg|_{\Delta T = \Delta T^\star_{jk}} - \varepsilon \delta \Delta T\big|_{\Delta T = \Delta T^\star_{jk}} \,, \tag{D.21}$$

$$\frac{1}{\tilde{v}_{jk}} := 1 + \frac{m_j^2 + m_k^2}{4p^2} + \varepsilon \frac{\delta v_{j0} + \delta v_{k0}}{2} - \frac{\Delta p_j m_j^2 + \Delta p_k m_k^2}{2p^3} - \frac{(\Delta m_{jk}^2)^2}{8p^4} - \frac{m_j^4 + m_k^4}{16p^4}\bigg|_{\Delta T = \Delta T^\star_{jk}} \,. \tag{D.22}$$

Substituting $\Delta T^\star_{jk}$ into L^0 yields

$$L^0(\Delta T^\star_{jk}) = \frac{L}{\tilde{v}_{jk}}\bigg|_{\Delta T = \Delta T^\star_{jk}} \,, \tag{D.23}$$

where $\tilde{v}_{jk}$ is the gravitationally corrected mean group velocity of the two mass eigenstates. In deriving these expressions, we have implicitly used

$$\tilde{\vec{P}}_{\mathrm{P}j}\Big|_{\Delta T=\Delta T^{\star}_{jk}} \overset{!}{\approx} \vec{P}_{\mathrm{D}j}\,, \tag{D.24}$$

so that momentum conservation terms in $\mathrm{Re}\left(\Xi_{jk}\right)$ do not contribute to $\Delta T^{\star}_{jk}$. At zeroth order in ε, this follows trivially from the time-independence of the respective terms; at first order, the potentially non-vanishing pieces vanish due to (D.24).
Expanding Ξ_{jk} to second order about its maximum $\Delta T^{\star}_{jk}$ and evaluating the Gaussian integral over ΔT in equation (D.2) yields

$$\begin{aligned}\int_{-\infty}^{\infty} \mathrm{d}\Delta T \exp\left(\Xi_{jk}(\Delta T, T_{\mathrm{D}})\right) \approx \sqrt{\frac{2\pi}{-\ddot{\Xi}_{jk}(\Delta T^{\star}_{jk}, T_{\mathrm{D}})}} \exp\left(\Xi_{jk}(\Delta T^{\star}_{jk}, T_{\mathrm{D}})\right) \\ \times \exp\left(\frac{\mathrm{Im}(\dot{\Xi}_{jk}(\Delta T^{\star}_{jk}, T_{\mathrm{D}}))^2}{2\mathrm{Re}(\ddot{\Xi}_{jk}(\Delta T^{\star}_{jk}, T_{\mathrm{D}}))}\right).\end{aligned} \tag{D.25}$$

As in flat spacetime, the real part of the first exponential governs decoherence due to wave packet separation, while the imaginary part encodes both the oscillation phase and an additional phase from wave packet spreading. The last exponential in equation (D.25) enforces the production and detection coherence condition: the energy differences between mass eigenstates must not be resolveable for oscillations to be observable.
To confirm that this interpretation carries over to curved spacetime, we examine the individual terms in detail. A recurring quantity is

$$\begin{aligned}\bar{v}_j L^0 - L = &\left(1 - \frac{m_j^2}{2p^2} + \frac{\Delta p_j m_j^2}{p^3} + \frac{3m_j^4}{8p^4}\right) \\ &\times \left(1 + \frac{m_j^2 + m_k^2}{4p^2} + \varepsilon\frac{\delta v_{j0} + \delta v_{k0}}{2} - \frac{\Delta p_j m_j^2 + \Delta p_k m_k^2}{2p^3} - \frac{(\Delta m_{jk}^2)^2}{8p^4} - \frac{m_j^4 + m_k^4}{16p^4}\right) L \\ &- L\end{aligned} \tag{D.26}$$

$$\begin{aligned}= &\left[-\frac{\Delta m_{jk}^2}{4p^2} + \varepsilon\left(\frac{\delta v_{j0} + \delta v_{k0}}{2}\right) + \frac{\Delta p_j m_j^2 - \Delta p_k m_k^2}{2p^3} + \frac{\Delta m_{jk}^4}{8p^4} - \left(\frac{\Delta m_{jk}^2}{4p^2}\right)^2\right] L \\ &+ O(\varepsilon^2, \varepsilon\varepsilon_{\mathrm{UR}}^2, \varepsilon_{\mathrm{UR}}^3)\,.\end{aligned} \tag{D.27}$$

Here, the momentum conservation condition from equation (D.24) has been used, leading to

$$\bar{p}_j = p + \Delta P_{\mathrm{D}j} \equiv p + \Delta p_j \tag{D.28}$$

$$\Rightarrow \bar{v}_j = 1 - \frac{m_j^2}{2p^2} + \frac{\Delta p_j m_j^2}{p^3} + \frac{3m_j^4}{8p^4} + O(\varepsilon_{\mathrm{UR}}^3)\,. \tag{D.29}$$

The energy splitting between two mass eigenstates is given by

$$\Delta E_{jk} = \frac{\Delta m_{jk}^2}{2p} + \Delta p_{jk} - \frac{\Delta p_j m_j^2 - \Delta p_k m_k^2}{2p^2} - \frac{\Delta m_{jk}^4}{8p^3} + O(\varepsilon_{\mathrm{UR}}^3)\,. \tag{D.30}$$

Defining the spatial wave packet width

$$\mathrm{Re}(\Xi_{jk}) = -\left(\frac{L}{L_{jk}^{\mathrm{coh}}}\right)^2 , \tag{D.31}$$

$$L_{jk}^{\mathrm{coh}} = 2\sigma_X \left[\left(\frac{\Delta v_{jk}^{+}}{1+\chi_j^2 (L^0)^2}\right)^2 + \left(\frac{\Delta v_{jk}^{-}}{1+\chi_k^2 (L^0)^2}\right)^2\right]^{-\frac{1}{2}} , \tag{D.32}$$

$$\Delta v_{jk}^{\pm} = \mp\frac{\Delta m_{jk}^2}{4p^2} + \varepsilon\left(\frac{\delta v_{j0}+\delta v_{k0}}{2}\right) \pm \frac{\Delta p_j m_j^2 - \Delta p_k m_k^2}{2p^3} \pm \frac{\Delta m_{jk}^4}{8p^4} \mp \left(\frac{\Delta m_{jk}^2}{4p^2}\right)^2 , \tag{D.33}$$

at leading order, L_{jk}^{coh} reproduces the flat spacetime result

$$L_{jk}^{\mathrm{coh}} \approx 4\sqrt{2}\sigma_X \frac{p^2}{\Delta m_{jk}^2} , \tag{D.34}$$

while higher order terms account for wave packet spreading and gravitational corrections.
The gravitational corrections are described by

$$\varepsilon\delta v_{j0} = \varepsilon\frac{\delta p_{j0} m_j^2}{p^3} + O(\varepsilon^2, \varepsilon\varepsilon_{\mathrm{UR}}^2) . \tag{D.35}$$

with δp_{j0}, using momentum conservation, given by

$$\varepsilon\delta p_{j0} = -\frac{\varepsilon}{2}\frac{\sigma_{\mathrm{D}}^2}{\sigma_{\mathrm{P}}^2+\sigma_{\mathrm{D}}^2}(\vec{\ell}\cdot\vec{e}_k)\lambda^k{}_\beta p^\beta + O(\varepsilon^2, \varepsilon\varepsilon_{\mathrm{UR}}) = \frac{\sigma_{\mathrm{D}}^2}{\sigma_{\mathrm{P}}^2+\sigma_{\mathrm{D}}^2}\left(\Delta\vec{P}_{\mathrm{D}j} - \Delta\vec{P}_{\mathrm{P}j}\right)\cdot\vec{\ell} . \tag{D.36}$$

with $p^\alpha := p(1,\vec{\ell})$. The imaginary part of Ξ_{jk} can be decomposed as

$$\mathrm{Im}(\Xi_{jk}) = \Delta\Phi_{jk}(L) + \Delta\tilde{\Phi}_{jk}(L) , \tag{D.37}$$

$$\Delta\Phi_{jk}(L) = -\frac{\Delta m_{jk}^2}{2p}\left[1 - \frac{\Delta p_j + \Delta p_k}{2p}\right]L , \tag{D.38}$$

$$\Delta\tilde{\Phi}_{jk}(L) = \frac{L^2}{8\sigma_X^4}\left[(\Delta v_{jk}^{+})^2\frac{\chi_j L^0}{1+\chi_j^2(L^0)^2} - (\Delta v_{jk}^{-})^2\frac{\chi_k L^0}{1+\chi_k^2(L^0)^2}\right] . \tag{D.39}$$

Here, $\Delta\Phi_{jk}(L)$ is the standard oscillation phase with $O(\varepsilon_{\mathrm{UR}}^2)$ corrections, while $\Delta\tilde{\Phi}_{jk}(L)$ arises from wave packet spreading and is of order $O(\varepsilon_{\mathrm{UR}}^3)$. The second exponential in equation (D.25) and the source-root prefactor can be expressed as

$$\pi_{jk} = -\frac{1}{2}\left(\frac{\Delta E_{jk}}{\sigma_E}\right)^2 + O(\varepsilon^2, \varepsilon\varepsilon_{\mathrm{UR}}^2, \varepsilon_{\mathrm{UR}}^3) , \tag{D.40}$$

with $\sigma_E = 1/\sigma_X$. Keeping only the lowest non-vanishing order in the prefactor, the final result is

$$I_{jk}(\vec{X}_{\mathrm{P}}, \vec{X}_{\mathrm{D}}, E) = \sqrt{\frac{2\pi}{\sigma_E^2}}\int_{T_{\mathrm{D1}}}^{T_{\mathrm{D2}}} \mathrm{d}T_{\mathrm{D}} \exp\left(-\left(\frac{L}{L_{jk}^{\mathrm{coh}}}\right)^2 - i\Delta\Phi_{jk} - i\Delta\tilde{\Phi}_{jk} - \frac{1}{2}\left(\frac{\Delta E_{jk}}{\sigma_E}\right)^2\right) . \tag{D.41}$$

This expression closely parallels the flat spacetime result, but includes geometric corrections in both the propagation distance L and the coherence length L_{jk}^{coh}.

Bibliography

[1] Patrick Adolf, Martin Hirsch, Sara Krieg, Heinrich Päs, and Mustafa Tabet. "Fitting the DESI BAO data with dark energy driven by the Cohen-Kaplan-Nelson bound". In: *JCAP* 08 (2024), p. 048. DOI: 10.1088/1475-7516/2024/08/048. arXiv: 2406.09964 [astro-ph.CO].

[2] Patrick Adolf, Martin Hirsch, Sara Krieg, Heinrich Päs, and Mustafa Tabet. "Addendum: Fitting the DESI BAO Data with Dark Energy Driven by the Cohen-Kaplan-Nelson Bound". In: *JCAP* (Apr. 2025). arXiv: 2504.15332 [astro-ph.CO].

[3] Dominik Hellmann, Sara Krieg, Heinrich Päs, and Mustafa Tabet. "Neutrino oscillations as a gravitational wave detector?" In: *JCAP* 05 (2025), p. 075. DOI: 10.1088/1475-7516/2025/05/075. arXiv: 2405.05000 [hep-ph].

[4] Alba Domi, Thomas Eberl, Dominik Hellmann, Sara Krieg, and Heinrich Päs. "Potential of neutrino telescopes to detect quantum gravity-induced decoherence in the presence of dark fermions". In: *JCAP* 01 (2025), p. 063. DOI: 10.1088/1475-7516/2025/01/063. arXiv: 2409.12633 [hep-ph].

[5] M. Abdul Karim et al. "DESI DR2 Results II: Measurements of Baryon Acoustic Oscillations and Cosmological Constraints". In: (Mar. 2025). arXiv: 2503.14738 [astro-ph.CO].

[6] R. Brandelik et al. "Evidence for Planar Events in e+ e- Annihilation at High-Energies". In: *Phys. Lett. B* 86 (1979), pp. 243–249. DOI: 10.1016/0370-2693(79)90830-X.

[7] G. Arnison et al. "Experimental Observation of Isolated Large Transverse Energy Electrons with Associated Missing Energy at $\sqrt{s} = 540$ GeV". In: *Phys. Lett. B* 122 (1983), pp. 103–116. DOI: 10.1016/0370-2693(83)91177-2.

[8] G. Arnison et al. "Experimental Observation of Lepton Pairs of Invariant Mass Around 95-GeV/c**2 at the CERN SPS Collider". In: *Phys. Lett. B* 126 (1983), pp. 398–410. DOI: 10.1016/0370-2693(83)90188-0.

[9] G. Alexander et al. "Electroweak parameters of the Z^0 resonance and the Standard Model: the LEP Collaborations". In: *Phys. Lett. B* 276 (1992), pp. 247–253. DOI: 10.1016/0370-2693(92)90572-L.

[10] F. Abe et al. "Observation of top quark production in $\bar{p}p$ collisions". In: *Phys. Rev. Lett.* 74 (1995), pp. 2626–2631. DOI: 10.1103/PhysRevLett.74.2626. arXiv: hep-ex/9503002.

[11] Georges Aad et al. "Observation of a new particle in the search for the Standard Model Higgs boson with the ATLAS detector at the LHC". In: *Phys. Lett. B* 716 (2012), pp. 1–29. DOI: 10.1016/j.physletb.2012.08.020. arXiv: 1207.7214 [hep-ex].

[12] Serguei Chatrchyan et al. "Observation of a New Boson at a Mass of 125 GeV with the CMS Experiment at the LHC". In: *Phys. Lett. B* 716 (2012), pp. 30–61. DOI: 10.1016/j.physletb.2012.08.021. arXiv: 1207.7235 [hep-ex].

[13] Q. R. Ahmad et al. "Measurement of the rate of $\nu_e + d \rightarrow p + p + e^-$ interactions produced by ^{8}B solar neutrinos at the Sudbury Neutrino Observatory". In: *Phys. Rev. Lett.* 87 (2001), p. 071301. DOI: 10.1103/PhysRevLett.87.071301. arXiv: nucl-ex/0106015.

[14] Vera C. Rubin and W. Kent Ford Jr. "Rotation of the Andromeda Nebula from a Spectroscopic Survey of Emission Regions". In: *Astrophys. J.* 159 (1970), pp. 379–403. DOI: 10.1086/150317.

[15] A. D. Sakharov. "Violation of CP Invariance, C asymmetry, and baryon asymmetry of the universe". In: *Pisma Zh. Eksp. Teor. Fiz.* 5 (1967), pp. 32–35. DOI: 10.1070/PU1991v034n05ABEH002497.

[16] David J. Griffiths. *INTRODUCTION TO ELEMENTARY PARTICLES*. 1987. ISBN: 978-0-471-60386-3, 978-3-527-61846-0. DOI: 10.1002/9783527618460.

[17] Kenneth G. Wilson. "Confinement of Quarks". In: *Phys. Rev. D* 10 (1974). Ed. by J. C. Taylor, pp. 2445–2459. DOI: 10.1103/PhysRevD.10.2445.

[18] C. S. Wu, E. Ambler, R. W. Hayward, D. D. Hoppes, and R. P. Hudson. "Experimental Test of Parity Conservation in β Decay". In: *Phys. Rev.* 105 (1957), pp. 1413–1414. DOI: 10.1103/PhysRev.105.1413.

[19] Geoffrey B. West. "Electron Scattering from Atoms, Nuclei and Nucleons". In: *Phys. Rept.* 18 (1975), pp. 263–323. DOI: 10.1016/0370-1573(75)90035-6.

[20] Michael E. Peskin and Daniel V. Schroeder. *An Introduction to quantum field theory*. Reading, USA: Addison-Wesley, 1995. ISBN: 978-0-201-50397-5, 978-0-429-50355-9, 978-0-429-49417-8. DOI: 10.1201/9780429503559.

[21] Steven Weinberg. "A Model of Leptons". In: *Phys. Rev. Lett.* 19 (1967), pp. 1264–1266. DOI: 10.1103/PhysRevLett.19.1264.

[22] Peter W. Higgs. "Broken Symmetries and the Masses of Gauge Bosons". In: *Phys. Rev. Lett.* 13 (1964). Ed. by J. C. Taylor, pp. 508–509. DOI: 10.1103/PhysRevLett.13.508.

[23] G. S. Guralnik, C. R. Hagen, and T. W. B. Kibble. "Global Conservation Laws and Massless Particles". In: *Phys. Rev. Lett.* 13 (1964). Ed. by J. C. Taylor, pp. 585–587. DOI: 10.1103/PhysRevLett.13.585.

[24] Makoto Kobayashi and Toshihide Maskawa. "CP Violation in the Renormalizable Theory of Weak Interaction". In: *Prog. Theor. Phys.* 49 (1973), pp. 652–657. DOI: 10.1143/PTP.49.652.

[25] Nicola Cabibbo. "Unitary Symmetry and Leptonic Decays". In: *Phys. Rev. Lett.* 10 (1963), pp. 531–533. DOI: 10.1103/PhysRevLett.10.531.

[26] Ling-Lie Chau and Wai-Yee Keung. "Comments on the Parametrization of the Kobayashi-Maskawa Matrix". In: *Phys. Rev. Lett.* 53 (1984), p. 1802. DOI: 10.1103/PhysRevLett.53.1802.

[27] B. Pontecorvo. "Mesonium and anti-mesonium". In: *Sov. Phys. JETP* 6 (1957), p. 429.

[28] B. Pontecorvo. "Inverse beta processes and nonconservation of lepton charge". In: *Zh. Eksp. Teor. Fiz.* 34 (1957), p. 247.

[29] Ziro Maki, Masami Nakagawa, and Shoichi Sakata. "Remarks on the unified model of elementary particles". In: *Prog. Theor. Phys.* 28 (1962), pp. 870–880. DOI: 10.1143/PTP.28.870.

[30] Y. Fukuda et al. "Evidence for oscillation of atmospheric neutrinos". In: *Phys. Rev. Lett.* 81 (1998), pp. 1562–1567. DOI: 10.1103/PhysRevLett.81.1562. arXiv: hep-ex/9807003.

[31] Murray Gell-Mann, Pierre Ramond, and Richard Slansky. "Complex Spinors and Unified Theories". In: *Conf. Proc. C* 790927 (1979), pp. 315–321. arXiv: 1306.4669 [hep-th].

[32] C. Patrignani et al. "Review of Particle Physics". In: *Chin. Phys. C* 40.10 (2016), p. 100001. DOI: 10.1088/1674-1137/40/10/100001.

[33] D. Walsh, R. F. Carswell, and R. J. Weymann. "0957 + 561 A, B - Twin quasistellar objects or gravitational lens". In: *Nature* 279 (1979), pp. 381–384. DOI: 10.1038/279381a0.

[34] Oliver James, Eugenie von Tunzelmann, Paul Franklin, and Kip S. Thorne. "Gravitational Lensing by Spinning Black Holes in Astrophysics, and in the Movie Interstellar". In: *Class. Quant. Grav.* 32.6 (2015), p. 065001. DOI: 10.1088/0264-9381/32/6/065001. arXiv: 1502.03808 [gr-qc].

[35] D. N. Spergel et al. "Wilkinson Microwave Anisotropy Probe (WMAP) three year results: implications for cosmology". In: *Astrophys. J. Suppl.* 170 (2007), p. 377. DOI: 10.1086/513700. arXiv: astro-ph/0603449.

[36] Gerard Jungman, Marc Kamionkowski, and Kim Griest. "Supersymmetric dark matter". In: *Phys. Rept.* 267 (1996), pp. 195–373. DOI: 10.1016/0370-1573(95)00058-5. arXiv: hep-ph/9506380.

[37] John Preskill, Mark B. Wise, and Frank Wilczek. "Cosmology of the Invisible Axion". In: *Phys. Lett. B* 120 (1983). Ed. by M. A. Srednicki, pp. 127–132. DOI: 10.1016/0370-2693(83)90637-8.

[38] Joachim Kopp. "Sterile neutrinos as dark matter candidates". In: *SciPost Phys. Lect. Notes* 36 (2022), p. 1. DOI: 10.21468/SciPostPhysLectNotes.36. arXiv: 2109.00767 [hep-ph].

[39] P. A. Zyla et al. "Review of Particle Physics". In: *PTEP* 2020.8 (2020), p. 083C01. DOI: 10.1093/ptep/ptaa104.

[40] David Camarena and Valerio Marra. "Local determination of the Hubble constant and the deceleration parameter". In: *Phys. Rev. Res.* 2.1 (2020), p. 013028. DOI: 10.1103/PhysRevResearch.2.013028. arXiv: 1906.11814 [astro-ph.CO].

[41] M. Fukugita and T. Yanagida. "Baryogenesis Without Grand Unification". In: *Phys. Lett. B* 174 (1986), pp. 45–47. DOI: 10.1016/0370-2693(86)91126-3.

[42] S. Perlmutter et al. "Measurements of Ω and Λ from 42 High Redshift Supernovae". In: *Astrophys. J.* 517 (1999), pp. 565–586. DOI: 10.1086/307221. arXiv: astro-ph/9812133.

[43] S. Perlmutter et al. "Discovery of a supernova explosion at half the age of the Universe and its cosmological implications". In: *Nature* 391 (1998), pp. 51–54. DOI: 10.1038/34124. arXiv: astro-ph/9712212.

[44] Sean M. Carroll. "The Cosmological constant". In: *Living Rev. Rel.* 4 (2001), p. 1. DOI: 10.12942/lrr-2001-1. arXiv: astro-ph/0004075.

[45] J. B. Hartle and S. W. Hawking. "Wave Function of the Universe". In: *Phys. Rev. D* 28 (1983). Ed. by Li-Zhi Fang and R. Ruffini, pp. 2960–2975. DOI: 10.1103/PhysRevD.28.2960.

[46] Steven Weinberg. "The Cosmological Constant Problem". In: *Rev. Mod. Phys.* 61 (1989). Ed. by Jong-Ping Hsu and D. Fine, pp. 1–23. DOI: 10.1103/RevModPhys.61.1.

[47] R. R. Caldwell, Rahul Dave, and Paul J. Steinhardt. "Cosmological imprint of an energy component with general equation of state". In: *Phys. Rev. Lett.* 80 (1998), pp. 1582–1585. DOI: 10.1103/PhysRevLett.80.1582. arXiv: astro-ph/9708069.

[48] Shinji Tsujikawa. "Quintessence: A Review". In: *Class. Quant. Grav.* 30 (2013), p. 214003. DOI: 10.1088/0264-9381/30/21/214003. arXiv: 1304.1961 [gr-qc].

[49] W. Pauli. "Dear radioactive ladies and gentlemen". In: *Phys. Today* 31N9 (1978), p. 27.

[50] F. Reines and C. L. Cowan. "Detection of the free neutrino". In: *Phys. Rev.* 92 (1953), pp. 830–831. DOI: 10.1103/PhysRev.92.830.

[51] G. Danby et al. "Observation of High-Energy Neutrino Reactions and the Existence of Two Kinds of Neutrinos". In: *Phys. Rev. Lett.* 9 (1962), pp. 36–44. DOI: 10.1103/PhysRevLett.9.36.

[52] K. Kodama et al. "Observation of tau neutrino interactions". In: *Phys. Lett. B* 504 (2001), pp. 218–224. DOI: 10.1016/S0370-2693(01)00307-0. arXiv: hep-ex/0012035.

[53] B. Pontecorvo. "Neutrino Experiments and the Problem of Conservation of Leptonic Charge". In: *Zh. Eksp. Teor. Fiz.* 53 (1967), pp. 1717–1725.

[54] Raymond Davis Jr., Don S. Harmer, and Kenneth C. Hoffman. "Search for neutrinos from the sun". In: *Phys. Rev. Lett.* 20 (1968), pp. 1205–1209. DOI: 10.1103/PhysRevLett.20.1205.

[55] Kate Scholberg. "Atmospheric neutrinos at Super-Kamiokande". In: *8th International Workshop on Neutrino Telescopes*. Feb. 1999, pp. 183–201. arXiv: hep-ex/9905016.

[56] J. M. Carmona, J. L. Cortes, and J. Indurain. "Interpretation of neutrino oscillations based on new physics in the infrared". In: *JHEP* 06 (2008), p. 033. DOI: 10.1088/1126-6708/2008/06/033. arXiv: 0709.2267 [hep-ph].

[57] Z. Maki, M. Nakagawa, and S. Sakata. "Remarks on the unified model of elementary particles". In: *11th International Conference on High-energy Physics*. 1962, pp. 663–666.

[58] Carlo Giunti and Chung W. Kim. *Fundamentals of Neutrino Physics and Astrophysics*. 2007. ISBN: 978-0-19-850871-7. DOI: 10.1093/acprof:oso/9780198508717.001.0001.

[59] S. Navas et al. "Review of particle physics". In: *Phys. Rev. D* 110.3 (2024), p. 030001. DOI: 10.1103/PhysRevD.110.030001.

[60] C. Giunti. "Neutrino wave packets in quantum field theory". In: *JHEP* 11 (2002), p. 017. DOI: 10.1088/1126-6708/2002/11/017. arXiv: hep-ph/0205014.

[61] Evgeny Kh. Akhmedov and Alexei Yu. Smirnov. "Paradoxes of neutrino oscillations". In: *Phys. Atom. Nucl.* 72 (2009), pp. 1363–1381. DOI: 10.1134/S1063778809080122. arXiv: 0905.1903 [hep-ph].

[62] M. Beuthe. "Towards a unique formula for neutrino oscillations in vacuum". In: *Phys. Rev. D* 66 (2002), p. 013003. DOI: 10.1103/PhysRevD.66.013003. arXiv: hep-ph/0202068.

[63] Evgeny Kh. Akhmedov and Joachim Kopp. "Neutrino Oscillations: Quantum Mechanics vs. Quantum Field Theory". In: *JHEP* 04 (2010). [Erratum: JHEP 10, 052 (2013)], p. 008. DOI: 10.1007/JHEP04(2010)008. arXiv: 1001.4815 [hep-ph].

[64] Boris Kayser. "On the quantum mechanics of neutrino oscillation". In: *Phys. Rev. D* 24 (1 July 1981), pp. 110–116. DOI: 10.1103/PhysRevD.24.110. URL: https://link.aps.org/doi/10.1103/PhysRevD.24.110.

[65] D. V. Naumov and V. A. Naumov. "Quantum Field Theory of Neutrino Oscillations". In: *Phys. Part. Nucl.* 51.1 (2020), pp. 1–106. DOI: 10.1134/S1063779620010050.

[66] L. Wolfenstein. "Neutrino Oscillations in Matter". In: *Phys. Rev. D* 17 (1978), pp. 2369–2374. DOI: 10.1103/PhysRevD.17.2369.

[67] S. P. Mikheyev and A. Yu. Smirnov. "Resonance Amplification of Oscillations in Matter and Spectroscopy of Solar Neutrinos". In: *Sov. J. Nucl. Phys.* 42 (1985), pp. 913–917.

[68] Per Osland and Tai Tsun Wu. "Solar Mikheev-Smirnov-Wolfenstein effect with three generations of neutrinos". In: *Phys. Rev. D* 62 (2000), p. 013008. DOI: 10.1103/PhysRevD.62.013008. arXiv: hep-ph/9912540.

[69] Guido Altarelli. "Models of neutrino masses and mixings". In: *61st Scottish Universities Summer School in Physics: Neutrinos in Particle Physics, Astrophysics and Cosmology (SUSSP61)*. Nov. 2006, pp. 91–115. arXiv: hep-ph/0611117.

[70] C. W. Kim and A. Pevsner. *Neutrinos in physics and astrophysics*. Vol. 8. 1993.

[71] S. M. Bilenky and C. Giunti. "Neutrinoless Double-Beta Decay: a Probe of Physics Beyond the Standard Model". In: *Int. J. Mod. Phys. A* 30.04n05 (2015), p. 1530001. DOI: 10.1142/S0217751X1530001X. arXiv: 1411.4791 [hep-ph].

[72] K. Abe et al. "Constraint on the matter–antimatter symmetry-violating phase in neutrino oscillations". In: *Nature* 580.7803 (2020). [Erratum: Nature 583, E16 (2020)], pp. 339–344. DOI: 10.1038/s41586-020-2177-0. arXiv: 1910.03887 [hep-ex].

[73] Carlos A. Argüelles, Jordi Salvado, and Christopher N. Weaver. "nuSQuIDS: A toolbox for neutrino propagation". In: *Comput. Phys. Commun.* 277 (2022), p. 108346. DOI: 10.1016/j.cpc.2022.108346. arXiv: 2112.13804 [hep-ph].

[74] N. Aghanim et al. "Planck 2018 results. VI. Cosmological parameters". In: *Astron. Astrophys.* 641 (2020). [Erratum: Astron.Astrophys. 652, C4 (2021)], A6. DOI: 10.1051/0004-6361/201833910. arXiv: 1807.06209 [astro-ph.CO].

[75] Zelimir Djurcic et al. "JUNO Conceptual Design Report". In: (Aug. 2015). arXiv: 1508.07166 [physics.ins-det].

[76] V. Hewes et al. "Deep Underground Neutrino Experiment (DUNE) Near Detector Conceptual Design Report". In: *Instruments* 5.4 (2021), p. 31. DOI: 10.3390/instruments5040031. arXiv: 2103.13910 [physics.ins-det].

[77] J. D. Vergados, H. Ejiri, and F. Simkovic. "Theory of Neutrinoless Double Beta Decay". In: *Rept. Prog. Phys.* 75 (2012), p. 106301. DOI: 10.1088/0034-4885/75/10/106301. arXiv: 1205.0649 [hep-ph].

[78] Stefano Dell'Oro, Simone Marcocci, Matteo Viel, and Francesco Vissani. "Neutrinoless double beta decay: 2015 review". In: *Adv. High Energy Phys.* 2016 (2016), p. 2162659. DOI: 10.1155/2016/2162659. arXiv: 1601.07512 [hep-ph].

[79] Peter Minkowski. "$\mu \to e\gamma$ at a Rate of One Out of 10^9 Muon Decays?" In: *Phys. Lett. B* 67 (1977), pp. 421–428. DOI: 10.1016/0370-2693(77)90435-X.

[80] Rabindra N. Mohapatra and Goran Senjanovic. "Neutrino Mass and Spontaneous Parity Nonconservation". In: *Phys. Rev. Lett.* 44 (1980), p. 912. DOI: 10.1103/PhysRevLett.44.912.

[81] Muhammad Sharif, ed. *Proceedings, International Conference on Relativistic Astrophysics : Celebrating 100 Years of Einstein's Theory of General Relativity: Lahore, Pakistan, 10-14 Feb 2015*. Lahore: Punjab U., 2015.

[82] A. Einstein. "Über den Einfluß der Schwerkraft auf die Ausbreitung des Lichtes". In: *Annalen Phys.* 340.10 (1911), pp. 898–908. DOI: 10.1002/andp.19113401005.

[83] Hermann Minkowski. *Raum und zeit*. Springer, 1988.

[84] Albert Einstein. "The foundation of the general theory of relativity." In: *Annalen Phys.* 49.7 (1916). Ed. by Jong-Ping Hsu and D. Fine, pp. 769–822. DOI: 10.1002/andp.19163540702.

[85] B. P. Abbott et al. "Observation of Gravitational Waves from a Binary Black Hole Merger". In: *Phys. Rev. Lett.* 116.6 (2016), p. 061102. DOI: 10.1103/PhysRevLett.116.061102. arXiv: 1602.03837 [gr-qc].

[86] José P. S. Lemos. "Shadow of the Moon and general relativity: Einstein, Dyson, Eddington and the 1919 light deflection". In: *Rev. Bras. Ens. Fis.* 41.suppl.1 (2019), e20190260. DOI: 10.1590/1806-9126-rbef-2019-0260. arXiv: 1912.05587 [physics.hist-ph].

[87] Karl Schwarzschild. "On the gravitational field of a mass point according to Einstein's theory". In: *Sitzungsber. Preuss. Akad. Wiss. Berlin (Math. Phys.)* 1916 (1916), pp. 189–196. arXiv: physics/9905030.

[88] Charles W. Misner, K. S. Thorne, and J. A. Wheeler. *Gravitation*. San Francisco: W. H. Freeman, 1973. ISBN: 978-0-7167-0344-0, 978-0-691-17779-3.

[89] J. A. Peacock. *Cosmological physics*. 1999.

[90] Steven Weinberg. *Cosmology*. 2008. ISBN: 978-0-19-852682-7.

[91] Scott Dodelson. *Modern Cosmology*. Amsterdam: Academic Press, 2003. ISBN: 978-0-12-219141-1.

[92] Albert Einstein. "Kosmologische Betrachtungen zur allgemeinen Relativitätstheorie". In: *Sitzungsberichte der Königlich Preussischen Akademie der Wissenschaften* (Jan. 1917), pp. 142–152.

[93] P. J. E. Peebles and Bharat Ratra. "The Cosmological Constant and Dark Energy". In: *Rev. Mod. Phys.* 75 (2003). Ed. by Jong-Ping Hsu and D. Fine, pp. 559–606. DOI: 10.1103/RevModPhys.75.559. arXiv: astro-ph/0207347.

[94] Adam G. Riess et al. "Observational evidence from supernovae for an accelerating universe and a cosmological constant". In: *Astron. J.* 116 (1998), pp. 1009–1038. DOI: 10.1086/300499. arXiv: astro-ph/9805201.

[95] Alan H. Guth. "The Inflationary Universe: A Possible Solution to the Horizon and Flatness Problems". In: *Phys. Rev. D* 23 (1981). Ed. by Li-Zhi Fang and R. Ruffini, pp. 347–356. DOI: 10.1103/PhysRevD.23.347.

[96] Andrew R. Liddle and D. H. Lyth. *Cosmological inflation and large scale structure*. 2000. ISBN: 978-0-521-57598-0, 978-0-521-82849-9. DOI: 10.1017/CBO9781139175180.

[97] G. F. Smoot et al. "Structure in the COBE Differential Microwave Radiometer First-Year Maps". In: 396 (Sept. 1992), p. L1. DOI: 10.1086/186504.

[98] P. J. E. Peebles. "Recombination of the Primeval Plasma". In: *Astrophys. J.* 153 (1968), p. 1. DOI: 10.1086/149628.

[99] D. J. Fixsen. "The Temperature of the Cosmic Microwave Background". In: 707.2 (Dec. 2009), pp. 916–920. DOI: 10.1088/0004-637X/707/2/916. arXiv: 0911.1955 [astro-ph.CO].

[100] Wayne Hu and Scott Dodelson. "Cosmic Microwave Background Anisotropies". In: *Ann. Rev. Astron. Astrophys.* 40 (2002), pp. 171–216. DOI: 10.1146/annurev.astro.40.060401.093926. arXiv: astro-ph/0110414.

[101] N. Aghanim et al. "Planck 2018 results. I. Overview and the cosmological legacy of Planck". In: *Astron. Astrophys.* 641 (2020), A1. DOI: 10.1051/0004-6361/201833880. arXiv: 1807.06205 [astro-ph.CO].

[102] Xiao-Hui Fan, C. L. Carilli, and Brian G. Keating. "Observational constraints on cosmic reionization". In: *Ann. Rev. Astron. Astrophys.* 44 (2006), pp. 415–462. DOI: 10.1146/annurev.astro.44.051905.092514. arXiv: astro-ph/0602375.

[103] R. K. Sachs and A. M. Wolfe. "Perturbations of a cosmological model and angular variations of the microwave background". In: *Astrophys. J.* 147 (1967), pp. 73–90. DOI: 10.1007/s10714-007-0448-9.

[104] Marc Kamionkowski, Arthur Kosowsky, and Albert Stebbins. "A Probe of primordial gravity waves and vorticity". In: *Phys. Rev. Lett.* 78 (1997), pp. 2058–2061. DOI: 10.1103/PhysRevLett.78.2058. arXiv: astro-ph/9609132.

[105] Matias Zaldarriaga and Uros Seljak. "An all sky analysis of polarization in the microwave background". In: *Phys. Rev. D* 55 (1997), pp. 1830–1840. DOI: 10.1103/PhysRevD.55.1830. arXiv: astro-ph/9609170.

[106] Wayne Hu and Martin J. White. "A CMB polarization primer". In: *New Astron.* 2 (1997), p. 323. DOI: 10.1016/S1384-1076(97)00022-5. arXiv: astro-ph/9706147.

[107] C. L. Bennett et al. "Nine-year Wilkinson Microwave Anisotropy Probe (WMAP) Observations: Final Maps and Results". In: 208.2, 20 (Oct. 2013), p. 20. DOI: 10.1088/0067-0049/208/2/20. arXiv: 1212.5225 [astro-ph.CO].

[108] N. Aghanim et al. "Planck 2018 results. V. CMB power spectra and likelihoods". In: *Astron. Astrophys.* 641 (2020), A5. DOI: 10.1051/0004-6361/201936386. arXiv: 1907.12875 [astro-ph.CO].

[109] P. A. R. Ade et al. "Improved Constraints on Primordial Gravitational Waves using Planck, WMAP, and BICEP/Keck Observations through the 2018 Observing Season". In: *Phys. Rev. Lett.* 127.15 (2021), p. 151301. DOI: 10.1103/PhysRevLett.127.151301. arXiv: 2110.00483 [astro-ph.CO].

[110] Lalitha Sairam et al. "New methods for radial-velocity measurements of double-lined binaries, and detection of a circumbinary planet orbiting TIC 172900988". In: 527.2 (Jan. 2024), pp. 2261–2278. DOI: 10.1093/mnras/stad3136. arXiv: 2310.07527 [astro-ph.EP].

[111] Adrian Lee et al. "The Simons Observatory". In: *Bulletin of the American Astronomical Society*. Vol. 51. Sept. 2019, 147, p. 147. DOI: 10.48550/arXiv.1907.08284. arXiv: 1907.08284 [astro-ph.IM].

[112] Daniel Baumann. *Cosmology*. Cambridge University Press, July 2022. ISBN: 978-1-108-93709-2, 978-1-108-83807-8. DOI: 10.1017/9781108937092.

[113] V. Mukhanov. *Physical Foundations of Cosmology*. Oxford: Cambridge University Press, 2005. ISBN: 978-0-521-56398-7. DOI: 10.1017/CBO9780511790553.

[114] James M. Bardeen. "Gauge Invariant Cosmological Perturbations". In: *Phys. Rev. D* 22 (1980), pp. 1882–1905. DOI: 10.1103/PhysRevD.22.1882.

[115] Antony Lewis, Anthony Challinor, and Anthony Lasenby. "Efficient computation of CMB anisotropies in closed FRW models". In: *Astrophysical Journal* 538 (2000), pp. 473–476. DOI: 10.1086/309179. arXiv: astro-ph/9911177 [astro-ph].

[116] Cullan Howlett, Antony Lewis, Alex Hall, and Anthony Challinor. "CMB power spectrum parameter degeneracies in the era of precision cosmology". In: *Journal of Cosmology and Astroparticle Physics* 1204 (2012), p. 027. DOI: 10.1088/1475-7516/2012/04/027. arXiv: 1201.3654 [astro-ph.CO].

[117] Julien Lesgourgues. "The Cosmic Linear Anisotropy Solving System (CLASS) I: Overview". In: *arXiv e-prints*, arXiv:1104.2932 (Apr. 2011), arXiv:1104.2932. DOI: 10.48550/arXiv.1104.2932. arXiv: 1104.2932 [astro-ph.IM].

[118] Shadab Alam et al. "Completed SDSS-IV extended Baryon Oscillation Spectroscopic Survey: Cosmological implications from two decades of spectroscopic surveys at the Apache Point Observatory". In: *Phys. Rev. D* 103.8 (2021), p. 083533. DOI: 10.1103/PhysRevD.103.083533. arXiv: 2007.08991 [astro-ph.CO].

[119] Michel Chevallier and David Polarski. "Accelerating universes with scaling dark matter". In: *Int. J. Mod. Phys. D* 10 (2001), pp. 213–224. DOI: 10.1142/S0218271801000822. arXiv: gr-qc/0009008.

[120] Eric V. Linder. "Exploring the expansion history of the universe". In: *Phys. Rev. Lett.* 90 (2003), p. 091301. DOI: 10.1103/PhysRevLett.90.091301. arXiv: astro-ph/0208512.

[121] Jacob D. Bekenstein. "Black holes and entropy". In: *Phys. Rev. D* 7 (1973), pp. 2333–2346. DOI: 10.1103/PhysRevD.7.2333.

[122] Jacob D. Bekenstein. "Generalized second law of thermodynamics in black hole physics". In: *Phys. Rev. D* 9 (1974), pp. 3292–3300. DOI: 10.1103/PhysRevD.9.3292.

[123] Jacob D. Bekenstein. "A Universal Upper Bound on the Entropy to Energy Ratio for Bounded Systems". In: *Phys. Rev. D* 23 (1981), p. 287. DOI: 10.1103/PhysRevD.23.287.

[124] Jacob D. Bekenstein. "Entropy bounds and black hole remnants". In: *Phys. Rev. D* 49 (1994), pp. 1912–1921. DOI: 10.1103/PhysRevD.49.1912. arXiv: gr-qc/9307035.

[125] S. W. Hawking. "Particle Creation by Black Holes". In: *Commun. Math. Phys.* 43 (1975). Ed. by G. W. Gibbons and S. W. Hawking. [Erratum: Commun.Math.Phys. 46, 206 (1976)], pp. 199–220. DOI: 10.1007/BF02345020.

[126] S. W. Hawking. "Black Holes and Thermodynamics". In: *Phys. Rev. D* 13 (1976), pp. 191–197. DOI: 10.1103/PhysRevD.13.191.

[127] Andrew G. Cohen, David B. Kaplan, and Ann E. Nelson. "Effective field theory, black holes, and the cosmological constant". In: *Phys. Rev. Lett.* 82 (1999), pp. 4971–4974. DOI: 10.1103/PhysRevLett.82.4971. arXiv: hep-th/9803132.

[128] Andrew G. Cohen and David B. Kaplan. "Gravitational contributions to the electron g-factor". In: (Mar. 2021). arXiv: 2103.04509 [hep-ph].

[129] Tom Banks and Patrick Draper. "Remarks on the Cohen-Kaplan-Nelson bound". In: *Phys. Rev. D* 101.12 (2020), p. 126010. DOI: 10.1103/PhysRevD.101.126010. arXiv: 1911.05778 [hep-th].

[130] Joseph Bramante and Elizabeth Gould. "Anomalous anomalies from virtual black holes". In: *Phys. Rev. D* 101.5 (2020), p. 055007. DOI: 10.1103/PhysRevD.101.055007. arXiv: 1911.04456 [hep-ph].

[131] Nikita Blinov and Patrick Draper. "Densities of states and the Cohen-Kaplan-Nelson bound". In: *Phys. Rev. D* 104.7 (2021), p. 076024. DOI: 10.1103/PhysRevD.104.076024. arXiv: 2107.03530 [hep-ph].

[132] Joseph Bramante and Elizabeth Gould. "Material matter effects in gravitational UV/IR mixing". In: *Phys. Rev. D* 101.8 (2020), p. 084022. DOI: 10.1103/PhysRevD.101.084022. arXiv: 1910.07905 [hep-th].

[133] Thomas W. Kephart and Heinrich Päs. "UV/IR mixing, causal diamonds and the electroweak hierarchy problem". In: *Mod. Phys. Lett. A* 40.21n22 (2025), p. 2550076. DOI: 10.1142/S0217732325500762. arXiv: 2209.03305 [hep-ph].

[134] Patrick Adolf, Martin Hirsch, and Heinrich Päs. "Radiative neutrino masses and the Cohen-Kaplan-Nelson bound". In: *JHEP* 11 (2023), p. 078. DOI: 10.1007/JHEP11(2023)078. arXiv: 2306.15313 [hep-ph].

[135] A. G. Adame et al. "DESI 2024 VI: cosmological constraints from the measurements of baryon acoustic oscillations". In: *JCAP* 02 (2025), p. 021. DOI: 10.1088/1475-7516/2025/02/021. arXiv: 2404.03002 [astro-ph.CO].

[136] Mehdi Rezaei, Mohammad Malekjani, and Joan Sola. "Can dark energy be expressed as a power series of the Hubble parameter?" In: *Phys. Rev. D* 100.2 (2019), p. 023539. DOI: 10.1103/PhysRevD.100.023539. arXiv: 1905.00100 [gr-qc].

[137] Mehdi Rezaei, Joan Solà Peracaula, and Mohammad Malekjani. "Cosmographic approach to Running Vacuum dark energy models: new constraints using BAOs and Hubble diagrams at higher redshifts". In: *Mon. Not. Roy. Astron. Soc.* 509.2 (2021), pp. 2593–2608. DOI: 10.1093/mnras/stab3117. arXiv: 2108.06255 [astro-ph.CO].

[138] Ilya L. Shapiro and Joan Sola. "Scaling behavior of the cosmological constant: Interface between quantum field theory and cosmology". In: *JHEP* 02 (2002), p. 006. DOI: 10.1088/1126-6708/2002/02/006. arXiv: hep-th/0012227.

[139] Miao Li. "A Model of holographic dark energy". In: *Phys. Lett. B* 603 (2004), p. 1. DOI: 10.1016/j.physletb.2004.10.014. arXiv: hep-th/0403127.

[140] Eirini C. Telali and Emmanuel N. Saridakis. "Power-law holographic dark energy and cosmology". In: *Eur. Phys. J. C* 82.5 (2022), p. 466. DOI: 10.1140/epjc/s10052-022-10411-z. arXiv: 2112.06821 [gr-qc].

[141] Stephen D. H. Hsu. "Entropy bounds and dark energy". In: *Phys. Lett. B* 594 (2004), pp. 13–16. DOI: 10.1016/j.physletb.2004.05.020. arXiv: hep-th/0403052.

[142] Joan Sola. "Cosmological constant and vacuum energy: old and new ideas". In: *J. Phys. Conf. Ser.* 453 (2013). Ed. by Taxiarchis Papakostas and Demetrios A Pliakis, p. 012015. DOI: 10.1088/1742-6596/453/1/012015. arXiv: 1306.1527 [gr-qc].

[143] Cristian Moreno-Pulido and Joan Sola Peracaula. "Equation of state of the running vacuum". In: *Eur. Phys. J. C* 82 (2022), p. 1137. DOI: 10.1140/epjc/s10052-022-11117-y. arXiv: 2207.07111 [gr-qc].

[144] Diego Pavon and Winfried Zimdahl. "Holographic dark energy and cosmic coincidence". In: *Phys. Lett. B* 628 (2005), pp. 206–210. DOI: 10.1016/j.physletb.2005.08.134. arXiv: gr-qc/0505020.

[145] Kevin J. Ludwick. "The viability of phantom dark energy: A review". In: *Mod. Phys. Lett. A* 32.28 (2017), p. 1730025. DOI: 10.1142/S0217732317300257. arXiv: 1708.06981 [astro-ph.CO].

[146] Arianna Favale, Maria Giovanna Dainotti, Adrià Gómez-Valent, and Marina Migliaccio. "Towards a new model-independent calibration of Gamma-Ray Bursts". In: *JHEAp* 44 (2024), pp. 323–339. DOI: 10.1016/j.jheap.2024.10.010. arXiv: 2402.13115 [astro-ph.CO].

[147] Dillon Brout et al. "The Pantheon+ Analysis: Cosmological Constraints". In: *Astrophys. J.* 938.2 (2022), p. 110. DOI: 10.3847/1538-4357/ac8e04. arXiv: 2202.04077 [astro-ph.CO].

[148] T. M. C. Abbott et al. "The Dark Energy Survey: Cosmology Results with ~1500 New High-redshift Type Ia Supernovae Using the Full 5 yr Data Set". In: *Astrophys. J. Lett.* 973.1 (2024), p. L14. DOI: 10.3847/2041-8213/ad6f9f. arXiv: 2401.02929 [astro-ph.CO].

[149] Wayne Hu and Naoshi Sugiyama. "Small scale cosmological perturbations: An Analytic approach". In: *Astrophys. J.* 471 (1996), pp. 542–570. DOI: 10.1086/177989. arXiv: astro-ph/9510117.

[150] Daniel J. Eisenstein and Wayne Hu. "Baryonic features in the matter transfer function". In: *Astrophys. J.* 496 (1998), p. 605. DOI: 10.1086/305424. arXiv: astro-ph/9709112.

[151] P. J. E. Peebles and J. T. Yu. "Primeval Adiabatic Perturbation in an Expanding Universe". In: *The Astrophysical Journal* 162 (Dec. 1970), p. 815. DOI: 10.1086/150713.

[152] Sergei Bashinsky and Uros Seljak. "Neutrino perturbations in CMB anisotropy and matter clustering". In: *Phys. Rev. D* 69 (2004), p. 083002. DOI: 10.1103/PhysRevD.69.083002. arXiv: astro-ph/0310198.

[153] Daniel J. Eisenstein et al. "Detection of the Baryon Acoustic Peak in the Large-Scale Correlation Function of SDSS Luminous Red Galaxies". In: *Astrophys. J.* 633 (2005), pp. 560–574. DOI: 10.1086/466512. arXiv: astro-ph/0501171.

[154] Bruce A. Bassett and Renee Hlozek. "Baryon Acoustic Oscillations". In: (Oct. 2009). arXiv: 0910.5224 [astro-ph.CO].

[155] Wolfgang Hillebrandt and Jens C. Niemeyer. "Type Ia supernova explosion models". In: *Ann. Rev. Astron. Astrophys.* 38 (2000), pp. 191–230. DOI: 10.1146/annurev.astro.38.1.191. arXiv: astro-ph/0006305.

[156] Julien Guy et al. "SALT2: Using distant supernovae to improve the use of Type Ia supernovae as distance indicators". In: *Astron. Astrophys.* 466 (2007), pp. 11–21. DOI: 10.1051/0004-6361:20066930. arXiv: astro-ph/0701828.

[157] Arianna Favale, Adrià Gómez-Valent, and Marina Migliaccio. "Cosmic chronometers to calibrate the ladders and measure the curvature of the Universe. A model-independent study". In: *Mon. Not. Roy. Astron. Soc.* 523.3 (2023), pp. 3406–3422. DOI: 10.1093/mnras/stad1621. arXiv: 2301.09591 [astro-ph.CO].

[158] Raul Jimenez and Abraham Loeb. "Constraining cosmological parameters based on relative galaxy ages". In: *Astrophys. J.* 573 (2002), pp. 37–42. DOI: 10.1086/340549. arXiv: astro-ph/0106145.

[159] Michele Moresco. "Measuring the expansion history of the Universe with cosmic chronometers". In: (Dec. 2024). arXiv: 2412.01994 [astro-ph.CO].

[160] Michele Moresco, Raul Jimenez, Licia Verde, Andrea Cimatti, and Lucia Pozzetti. "Setting the Stage for Cosmic Chronometers. II. Impact of Stellar Population Synthesis Models Systematics and Full Covariance Matrix". In: *Astrophys. J.* 898.1 (2020), p. 82. DOI: 10.3847/1538-4357/ab9eb0. arXiv: 2003.07362 [astro-ph.GA].

[161] M. Goliath, R. Amanullah, P. Astier, A. Goobar, and R. Pain. "Supernovae and the nature of the dark energy". In: *Astron. Astrophys.* 380 (2001), pp. 6–18. DOI: 10.1051/0004-6361:20011398. arXiv: astro-ph/0104009.

[162] Wolfram Research Inc. *Mathematica, Version 14.2*. Champaign, IL, 2025. URL: https://www.wolfram.com/mathematica.

[163] Rostislav Protassov, David A. van Dyk, Alanna Connors, Vinay L. Kashyap, and Aneta Siemiginowska. "Statistics: handle with care, detecting multiple model components with the likelihood ratio test". In: *Astrophys. J.* 571 (2002), p. 545. DOI: 10.1086/339856. arXiv: astro-ph/0201547.

[164] H. Akaike. "A new look at the statistical model identification". In: *IEEE Transactions on Automatic Control* 19.6 (1974), pp. 716–723. DOI: 10.1109/TAC.1974.1100705.

[165] Amir Aghamousa et al. "The DESI Experiment Part I: Science,Targeting, and Survey Design". In: (Oct. 2016). arXiv: 1611.00036 [astro-ph.IM].

[166] Y. Mellier et al. "Euclid. I. Overview of the Euclid mission". In: *Astron. Astrophys.* 697 (2025), A1. DOI: 10.1051/0004-6361/202450810. arXiv: 2405.13491 [astro-ph.CO].

[167] R. Laureijs et al. "Euclid Definition Study Report". In: *arXiv e-prints*, arXiv:1110.3193 (Oct. 2011), arXiv:1110.3193. DOI: 10.48550/arXiv.1110.3193. arXiv: 1110.3193 [astro-ph.CO].

[168] Željko Ivezić et al. "LSST: from Science Drivers to Reference Design and Anticipated Data Products". In: *Astrophys. J.* 873.2 (2019), p. 111. DOI: 10.3847/1538-4357/ab042c. arXiv: 0805.2366 [astro-ph].

[169] Rob Fardon, Ann E. Nelson, and Neal Weiner. "Dark energy from mass varying neutrinos". In: *JCAP* 10 (2004), p. 005. DOI: 10.1088/1475-7516/2004/10/005. arXiv: astro-ph/0309800.

[170] P. Q. Hung. "Sterile neutrino and accelerating universe". In: (Oct. 2000). arXiv: hep-ph/0010126.

[171] Hideo Kodama and Misao Sasaki. "Cosmological Perturbation Theory". In: *Progress of Theoretical Physics Supplement* 78 (Jan. 1984), pp. 1–166. ISSN: 0375-9687. DOI: 10.1143/PTPS.78.1. eprint: https://academic.oup.com/ptps/article-pdf/doi/10.1143/PTPS.78.1/5321391/78-1.pdf. URL: https://doi.org/10.1143/PTPS.78.1.

[172] Elisabetta Majerotto, Jussi Valiviita, and Roy Maartens. "Adiabatic initial conditions for perturbations in interacting dark energy models". In: *Mon. Not. Roy. Astron. Soc.* 402 (2010), pp. 2344–2354. DOI: 10.1111/j.1365-2966.2009.16140.x. arXiv: 0907.4981 [astro-ph.CO].

[173] Jussi Valiviita, Elisabetta Majerotto, and Roy Maartens. "Instability in interacting dark energy and dark matter fluids". In: *JCAP* 07 (2008), p. 020. DOI: 10.1088/1475-7516/2008/07/020. arXiv: 0804.0232 [astro-ph].

[174] Y. Akrami et al. "Planck 2018 results. X. Constraints on inflation". In: *Astron. Astrophys.* 641 (2020), A10. DOI: 10.1051/0004-6361/201833887. arXiv: 1807.06211 [astro-ph.CO].

[175] P. James Peebles. *The Large-Scale Structure of the Universe*. Princeton University Press, Nov. 1980. ISBN: 978-0-691-08240-0, 978-0-691-20983-8, 978-0-691-20671-4.

[176] Eric V. Linder. "Cosmic growth history and expansion history". In: *Phys. Rev. D* 72 (2005), p. 043529. DOI: 10.1103/PhysRevD.72.043529. arXiv: astro-ph/0507263.

[177] Benjamin Audren, Julien Lesgourgues, Karim Benabed, and Simon Prunet. "Conservative constraints on early cosmology with MONTE PYTHON". In: *Journal for Cosmology and Astroparticle Physics* 2013.2, 001 (Feb. 2013), p. 001. DOI: 10.1088/1475-7516/2013/02/001. arXiv: 1210.7183 [astro-ph.CO].

[178] Roberto Trotta. "Bayes in the sky: Bayesian inference and model selection in cosmology". In: *Contemp. Phys.* 49 (2008), pp. 71–104. DOI: 10.1080/00107510802066753. arXiv: 0803.4089 [astro-ph].

[179] Wayne Hu and Martin J. White. "CMB anisotropies: Total angular momentum method". In: *Phys. Rev. D* 56 (1997), pp. 596–615. DOI: 10.1103/PhysRevD.56.596. arXiv: astro-ph/9702170.

[180] Matthias Bartelmann and Peter Schneider. "Weak gravitational lensing". In: *Phys. Rept.* 340 (2001), pp. 291–472. DOI: 10.1016/S0370-1573(00)00082-X. arXiv: astro-ph/9912508.

[181] Marika Asgari et al. "KiDS-1000 Cosmology: Cosmic shear constraints and comparison between two point statistics". In: *Astron. Astrophys.* 645 (2021), A104. DOI: 10.1051/0004-6361/202039070. arXiv: 2007.15633 [astro-ph.CO].

[182] Marc Kamionkowski and Abraham Loeb. "Getting around cosmic variance". In: *Phys. Rev. D* 56 (1997), pp. 4511–4513. DOI: 10.1103/PhysRevD.56.4511. arXiv: astro-ph/9703118.

[183] M. B. Gavela, D. Hernandez, L. Lopez Honorez, O. Mena, and S. Rigolin. "Dark coupling". In: *JCAP* 07 (2009). [Erratum: JCAP 05, E01 (2010)], p. 034. DOI: 10.1088/1475-7516/2009/07/034. arXiv: 0901.1611 [astro-ph.CO].

[184] Maria Archidiacono and Steen Hannestad. "Updated constraints on non-standard neutrino interactions from Planck". In: *JCAP* 07 (2014), p. 046. DOI: 10.1088/1475-7516/2014/07/046. arXiv: 1311.3873 [astro-ph.CO].

[185] Daniel Aloni, Melissa Joseph, Martin Schmaltz, and Neal Weiner. "Dark Radiation from Neutrino Mixing after Big Bang Nucleosynthesis". In: *Phys. Rev. Lett.* 131.22 (2023), p. 221001. DOI: 10.1103/PhysRevLett.131.221001. arXiv: 2301.10792 [astro-ph.CO].

[186] Joan Sola Peracaula, Adria Gomez-Valent, Javier de Cruz Perez, and Cristian Moreno-Pulido. "Running Vacuum in the Universe: Phenomenological Status in Light of the Latest Observations, and Its Impact on the σ_8 and H_0 Tensions". In: *Universe* 9.6 (2023), p. 262. DOI: 10.3390/universe9060262. arXiv: 2304.11157 [astro-ph.CO].

[187] Mateus Scherer, Miguel A. Sabogal, Rafael C. Nunes, and Antonio De Felice. "Challenging the ΛCDM model: 5σ evidence for a dynamical dark energy late-time transition". In: *Phys. Rev. D* 112.4 (2025), p. 043513. DOI: 10.1103/n86r-sjgm. arXiv: 2504.20664 [astro-ph.CO].

[188] B. P. Abbott et al. "GW170817: Observation of Gravitational Waves from a Binary Neutron Star Inspiral". In: *Phys. Rev. Lett.* 119.16 (2017), p. 161101. DOI: 10.1103/PhysRevLett.119.161101. arXiv: 1710.05832 [gr-qc].

[189] David J. Thompson and Colleen A. Wilson-Hodge. "Fermi Gamma-ray Space Telescope". In: (Oct. 2022). DOI: 10.1007/978-981-16-4544-0_58-1. arXiv: 2210.12875 [astro-ph.HE].

[190] V. Savchenko et al. "INTEGRAL Detection of the First Prompt Gamma-Ray Signal Coincident with the Gravitational-wave Event GW170817". In: *Astrophys. J. Lett.* 848.2 (2017), p. L15. DOI: 10.3847/2041-8213/aa8f94. arXiv: 1710.05449 [astro-ph.HE].

[191] K. Hirata et al. "Observation of a Neutrino Burst from the Supernova SN 1987a". In: *Phys. Rev. Lett.* 58 (1987). Ed. by K. C. Wali, pp. 1490–1493. DOI: 10.1103/PhysRevLett.58.1490.

[192] R. M. Bionta et al. "Observation of a Neutrino Burst in Coincidence with Supernova SN 1987a in the Large Magellanic Cloud". In: *Phys. Rev. Lett.* 58 (1987), p. 1494. DOI: 10.1103/PhysRevLett.58.1494.

[193] E.N. Alexeyev, L.N. Alexeyeva, I.V. Krivosheina, and V.I. Volchenko. "Detection of the neutrino signal from SN 1987A in the LMC using the INR Baksan underground scintillation telescope". In: *Physics Letters B* 205.2 (1988), pp. 209–214. ISSN: 0370-2693. DOI: https://doi.org/10.1016/0370-2693(88)91651-6. URL: https://www.sciencedirect.com/science/article/pii/0370269388916516.

[194] Yoichi Aso et al. "Interferometer design of the KAGRA gravitational wave detector". In: *Phys. Rev. D* 88.4 (2013), p. 043007. DOI: 10.1103/PhysRevD.88.043007. arXiv: 1306.6747 [gr-qc].

[195] Pau Amaro-Seoane et al. "Laser Interferometer Space Antenna". In: (Feb. 2017). arXiv: 1702.00786 [astro-ph.IM].

[196] M. G. Aartsen et al. "The IceCube Neutrino Observatory: Instrumentation and Online Systems". In: *JINST* 12.03 (2017). [Erratum: JINST 19, E05001 (2024)], P03012. DOI: 10.1088/1748-0221/12/03/P03012. arXiv: 1612.05093 [astro-ph.IM].

[197] KM3NeT Collaboration. "Letter of Intent for KM3NeT 2.0". In: *J. Phys. G* 43.8 (2016), p. 084001. DOI: 10.1088/0954-3899/43/8/084001.

[198] Yury Eroshenko and Viktor Stasenko. "Gravitational Waves from the Merger of Two Primordial Black Hole Clusters". In: *Symmetry* 15.3 (2023), p. 637. DOI: 10.3390/sym15030637. arXiv: 2302.05167 [astro-ph.CO].

[199] Jorge Casalderrey-Solana, David Mateos, and Mikel Sanchez-Garitaonandia. "Mega-Hertz Gravitational Waves from Neutron Star Mergers". In: (Oct. 2022). arXiv: 2210.03171 [hep-th].

[200] Sohrab Rahvar. "Primordial black hole collision with neutron stars and astrophysical black holes and the observational signatures". In: *Int. J. Mod. Phys. D* 32.16 (2023), p. 2350103. DOI: 10.1142/S0218271823501031. arXiv: 2304.00348 [gr-qc].

[201] Jade Powell et al. "Determining the core-collapse supernova explosion mechanism with current and future gravitational-wave observatories". In: *Phys. Rev. D* 109.6 (2024), p. 063019. DOI: 10.1103/PhysRevD.109.063019. arXiv: 2311.18221 [astro-ph.HE].

[202] M. G. Aartsen et al. "Multimessenger observations of a flaring blazar coincident with high-energy neutrino IceCube-170922A". In: *Science* 361.6398 (2018), eaat1378. DOI: 10.1126/science.aat1378. arXiv: 1807.08816 [astro-ph.HE].

[203] R. Abbasi et al. "An absence of neutrinos associated with cosmic-ray acceleration in γ-ray bursts". In: *Nature* 484.7394 (Apr. 2012), pp. 351–354. DOI: 10.1038/nature11068. arXiv: 1204.4219 [astro-ph.HE].

[204] Paz Beniamini et al. "Extragalactic Magnetar Giant Flares: Population Implications, Rates, and Prospects for Gamma-Rays, Gravitational Waves, and Neutrinos". In: *Astrophys. J.* 980.2 (2025), p. 211. DOI: 10.3847/1538-4357/ada947. arXiv: 2411.16846 [astro-ph.HE].

[205] Suvi Gezari. "Tidal Disruption Events". In: *Ann. Rev. Astron. Astrophys.* 59 (2021), pp. 21–58. DOI: 10.1146/annurev-astro-111720-030029. arXiv: 2104.14580 [astro-ph.HE].

[206] M. G. Aartsen et al. "Neutrino Interferometry for High-Precision Tests of Lorentz Symmetry with IceCube". In: *Nature Phys.* 14.9 (2018), pp. 961–966. DOI: 10.1038/s41567-018-0172-2. arXiv: 1709.03434 [hep-ex].

[207] M. G. Aartsen et al. "Measurement of Atmospheric Neutrino Oscillations at 6–56 GeV with IceCube DeepCore". In: *Phys. Rev. Lett.* 120.7 (2018), p. 071801. DOI: 10.1103/PhysRevLett.120.071801. arXiv: 1707.07081 [hep-ex].

[208] M. G. Aartsen et al. "Determining neutrino oscillation parameters from atmospheric muon neutrino disappearance with three years of IceCube DeepCore data". In: *Phys. Rev. D* 91.7 (2015), p. 072004. DOI: 10.1103/PhysRevD.91.072004. arXiv: 1410.7227 [hep-ex].

[209] R. Abbasi et al. "Search for decoherence from quantum gravity with atmospheric neutrinos". In: *Nature Phys.* 20.6 (2024), pp. 913–920. DOI: 10.1038/s41567-024-02436-w. arXiv: 2308.00105 [hep-ex].

[210] Claire Guépin, Kumiko Kotera, and Foteini Oikonomou. *High-energy neutrino transients and the future of multi-messenger astronomy*. 2024. arXiv: 2207.12205 [astro-ph.HE]. URL: https://arxiv.org/abs/2207.12205.

[211] N. Fornengo, C. Giunti, C. W. Kim, and J. Song. "Gravitational effects on the neutrino oscillation". In: *Phys. Rev. D* 56 (1997), pp. 1895–1902. DOI: 10.1103/PhysRevD.56.1895. arXiv: hep-ph/9611231.

[212] Kohkichi Konno and Masumi Kasai. "General relativistic effects of gravity in quantum mechanics: A Case of ultrarelativistic, spin 1/2 particles". In: *Prog. Theor. Phys.* 100 (1998), pp. 1145–1157. DOI: 10.1143/PTP.100.1145. arXiv: gr-qc/0603035.

[213] Leo Stodolsky. "Matter and Light Wave Interferometry in Gravitational Fields". In: *Gen. Rel. Grav.* 11 (1979), pp. 391–405. DOI: 10.1007/BF00759302.

[214] Yuval Grossman and Harry J. Lipkin. "Flavor oscillations from a spatially localized source: A Simple general treatment". In: *Phys. Rev. D* 55 (1997), pp. 2760–2767. DOI: 10.1103/PhysRevD.55.2760. arXiv: hep-ph/9607201.

[215] Banibrata Mukhopadhyay. "Neutrino oscillations under gravity: Mass independent oscillation". In: (July 2003). arXiv: hep-ph/0307167.

[216] Tanmoy Bhattacharya, Salman Habib, and Emil Mottola. "Gravitationally induced neutrino oscillation phases in static space-times". In: *Phys. Rev. D* 59 (1999), p. 067301. DOI: 10.1103/PhysRevD.59.067301.

[217] Antonio Capolupo, Gaetano Lambiase, and Aniello Quaranta. "Neutrinos in curved spacetime: Particle mixing and flavor oscillations". In: *Phys. Rev. D* 101.9 (2020), p. 095022. DOI: 10.1103/PhysRevD.101.095022. arXiv: 2003.00516 [hep-th].

[218] W. G. Unruh. "Notes on black hole evaporation". In: *Phys. Rev. D* 14 (1976), p. 870. DOI: 10.1103/PhysRevD.14.870.

[219] Antonio Capolupo, Giuseppe De Maria, Simone Monda, Aniello Quaranta, and Raoul Serao. "Quantum Field Theory of Neutrino Mixing in Spacetimes with Torsion". In: *Universe* 10.4 (2024), p. 170. DOI: 10.3390/universe10040170. arXiv: 2310.09309 [hep-ph].

[220] Mikael Beuthe. "Oscillations of neutrinos and mesons in quantum field theory". In: *Phys. Rept.* 375 (2003), pp. 105–218. DOI: 10.1016/S0370-1573(02)00538-0. arXiv: hep-ph/0109119.

[221] Sean M. Carroll. *Spacetime and Geometry: An Introduction to General Relativity*. Cambridge University Press, July 2019. ISBN: 978-0-8053-8732-2, 978-1-108-48839-6, 978-1-108-77555-7. DOI: 10.1017/9781108770385.

[222] Bryce S. DeWitt. "Quantum field theory in curved spacetime". In: *Physics Reports* 19.6 (1975), pp. 295–357. ISSN: 0370-1573. DOI: https://doi.org/10.1016/0370-1573(75)90051-4. URL: https://www.sciencedirect.com/science/article/pii/0370157375900514.

[223] N. D. Birrell and P. C. W. Davies. *Quantum Fields in Curved Space*. Cambridge Monographs on Mathematical Physics. Cambridge University Press, 1982.

[224] Robert M. Wald. *Quantum Field Theory in Curved Space-Time and Black Hole Thermodynamics*. Chicago Lectures in Physics. Chicago, IL: University of Chicago Press, 1995. ISBN: 978-0-226-87027-4.

[225] Robert M. Wald. *General Relativity*. Chicago, USA: Chicago Univ. Pr., 1984. DOI: 10.7208/chicago/9780226870373.001.0001.

[226] Christian Y. Cardall and George M. Fuller. "Neutrino oscillations in curved spacetime: An Heuristic treatment". In: *Phys. Rev. D* 55 (1997), pp. 7960–7966. DOI: 10.1103/PhysRevD.55.7960. arXiv: hep-ph/9610494.

[227] Kayll Lake. "Galactic potentials". In: *Phys. Rev. Lett.* 92 (2004), p. 051101. DOI: 10.1103/PhysRevLett.92.051101. arXiv: gr-qc/0302067.

[228] C. Giunti, C. W. Kim, J. A. Lee, and U. W. Lee. "On the treatment of neutrino oscillations without resort to weak eigenstates". In: *Phys. Rev. D* 48 (1993), pp. 4310–4317. DOI: 10.1103/PhysRevD.48.4310. arXiv: hep-ph/9305276.

[229] C. Giunti, C. W. Kim, and U. W. Lee. "When do neutrinos cease to oscillate?" In: *Phys. Lett. B* 421 (1998), pp. 237–244. DOI: 10.1016/S0370-2693(98)00014-8. arXiv: hep-ph/9709494.

[230] C. J. Moore, R. H. Cole, and C. P. L. Berry. "Gravitational-wave sensitivity curves". In: *Class. Quant. Grav.* 32.1 (2015), p. 015014. DOI: 10.1088/0264-9381/32/1/015014. arXiv: 1408.0740 [gr-qc].

[231] Kathrine Mørch Groth and Markus Ahlers. "Deciphering the sources of cosmic neutrinos". In: *Phys. Rev. D* 111.10 (2025), p. 103052. DOI: 10.1103/ntm4-lgbk. arXiv: 2503.07718 [astro-ph.HE].

[232] Alex Sicilia et al. "The Black Hole Mass Function Across Cosmic Times. I. Stellar Black Holes and Light Seed Distribution". In: *Astrophys. J.* 924.2 (2022), p. 56. DOI: 10.3847/1538-4357/ac34fb. arXiv: 2110.15607 [astro-ph.GA].

[233] Angel Abusleme et al. "Calibration Strategy of the JUNO Experiment". In: *JHEP* 03 (2021), p. 004. DOI: 10.1007/JHEP03(2021)004. arXiv: 2011.06405 [physics.ins-det].

[234] J. Aasi et al. "Advanced LIGO". In: *Class. Quant. Grav.* 32 (2015), p. 074001. DOI: 10.1088/0264-9381/32/7/074001. arXiv: 1411.4547 [gr-qc].

[235] A. Sesana. "Gravitational wave emission from binary supermassive black holes". In: *Class. Quant. Grav.* 30 (2013), p. 244009. DOI: 10.1088/0264-9381/30/24/244009. arXiv: 1307.4086 [astro-ph.CO].

[236] Chang-Qing Ye, Hui-Min Fan, Alejandro Torres-Orjuela, Jian-dong Zhang, and Yi-Ming Hu. "Identification of gravitational waves from extreme-mass-ratio inspirals". In: *Phys. Rev. D* 109.12 (2024), p. 124034. DOI: 10.1103/PhysRevD.109.124034. arXiv: 2310.03520 [gr-qc].

[237] Siyuan Chen, Alberto Sesana, and Christopher J. Conselice. "Constraining astrophysical observables of Galaxy and Supermassive Black Hole Binary Mergers using Pulsar Timing Arrays". In: *Mon. Not. Roy. Astron. Soc.* 488.1 (2019), pp. 401–418. DOI: 10.1093/mnras/stz1722. arXiv: 1810.04184 [astro-ph.GA].

[238] Gabriella Agazie et al. "The NANOGrav 15 yr Data Set: Evidence for a Gravitational-wave Background". In: *Astrophys. J. Lett.* 951.1 (2023), p. L8. DOI: 10.3847/2041-8213/acdac6. arXiv: 2306.16213 [astro-ph.HE].

[239] J. Antoniadis et al. "The second data release from the European Pulsar Timing Array - III. Search for gravitational wave signals". In: *Astron. Astrophys.* 678 (2023), A50. DOI: 10.1051/0004-6361/202346844. arXiv: 2306.16214 [astro-ph.HE].

[240] Maxim Dvornikov. "Interaction of supernova neutrinos with stochastic gravitational waves". In: *Phys. Rev. D* 104.4 (2021), p. 043018. DOI: 10.1103/PhysRevD.104.043018. arXiv: 2103.15464 [hep-ph].

[241] Gaetano Lambiase, Leonardo Mastrototaro, and Luca Visinelli. "Astrophysical neutrino oscillations after pulsar timing array analyses". In: *Phys. Rev. D* 108.12 (2023), p. 123028. DOI: 10.1103/PhysRevD.108.123028. arXiv: 2306.16977 [astro-ph.HE].

[242] H. -Th. Janka. "Neutrino Emission from Supernovae". In: (Feb. 2017). DOI: 10.1007/978-3-319-21846-5_4. arXiv: 1702.08713 [astro-ph.HE].

[243] Anna M. Suliga. "Diffuse Supernova Neutrino Background". In: *Handbook of Nuclear Physics*. Ed. by Isao Tanihata, Hiroshi Toki, and Toshitaka Kajino. 2022, pp. 1–18. DOI: 10.1007/978-981-15-8818-1_129-1. arXiv: 2207.09632 [astro-ph.HE].

[244] Foteini Oikonomou. "High-energy neutrino emission from blazars". In: *PoS* ICRC2021 (2022), p. 030. DOI: 10.22323/1.395.0030. arXiv: 2201.05623 [astro-ph.HE].

[245] Markus Boettcher, Matthew Fu, Timothy Govenor, Quentin King, and Parisa Roustazadeh. "Multiwavelength and Multimessenger Observations of Blazars and Theoretical Modeling: Blazars as Astrophysical Neutrino Sources". In: *Acta Phys. Polon. Supp.* 15.3 (2022), p. 8. DOI: 10.5506/APhysPolBSupp.15.3-A8. arXiv: 2204.12242 [astro-ph.HE].

[246] Foteini Oikonomou, Kohta Murase, Paolo Padovani, Elisa Resconi, and Peter Mészáros. "High energy neutrino flux from individual blazar flares". In: *Mon. Not. Roy. Astron. Soc.* 489.3 (2019), pp. 4347–4366. DOI: 10.1093/mnras/stz2246. arXiv: 1906.05302 [astro-ph.HE].

[247] R. J. Protheroe, W. Bednarek, and Q. Luo. "Gamma-rays and neutrinos from very young supernova remnants". In: *Astropart. Phys.* 9 (1998), pp. 1–14. DOI: 10.1016/S0927-6505(98)00014-0. arXiv: astro-ph/9703045.

[248] Raj Gandhi. "Ultrahigh-energy neutrinos: A Review of theoretical and phenomenological issues". In: *Nucl. Phys. B Proc. Suppl.* 91 (2001). Ed. by J. Law, R. W. Ollerhead, and J. J. Simpson, pp. 453–461. DOI: 10.1016/S0920-5632(00)00975-0. arXiv: hep-ph/0011176.

[249] J. H. Beall and W. Bednarek. "Neutrinos from early phase, pulsar driven supernovae". In: *Astrophys. J.* 569 (2002), pp. 343–348. DOI: 10.1086/339276. arXiv: astro-ph/0108447.

[250] Dafne Guetta and Elena Amato. "Neutrino flux predictions for galactic plerions". In: *Astropart. Phys.* 19 (2003), pp. 403–407. DOI: 10.1016/S0927-6505(02)00221-9. arXiv: astro-ph/0209537.

[251] Dafne Guetta and Jonathan Granot. "Neutrinos from gamma-ray bursts in pulsar wind bubbles: ~10**16-eV". In: *Phys. Rev. Lett.* 90 (2003), p. 201103. DOI: 10.1103/PhysRevLett.90.201103. arXiv: astro-ph/0212045.

[252] Soebur Razzaque, Peter Meszaros, and Eli Waxman. "High energy neutrinos from gamma-ray bursts with precursor supernovae". In: *Phys. Rev. Lett.* 90 (2003), p. 241103. DOI: 10.1103/PhysRevLett.90.241103. arXiv: astro-ph/0212536.

[253] Charles D. Dermer and Armen Atoyan. "High energy neutrinos from gamma-ray bursts". In: *Phys. Rev. Lett.* 91 (2003), p. 071102. DOI: 10.1103/PhysRevLett.91.071102. arXiv: astro-ph/0301030.

[254] W. Bednarek. "Neutrinos from the pulsar wind nebulae". In: *Astron. Astrophys.* 407 (2003), pp. 1–6. DOI: 10.1051/0004-6361:20030929. arXiv: astro-ph/0305430.

[255] Bennett Link and Fiorella Burgio. "TeV mu neutrinos from young neutron stars". In: *Phys. Rev. Lett.* 94 (2005), p. 181101. DOI: 10.1103/PhysRevLett.94.181101. arXiv: astro-ph/0412520.

[256] Bennett Link and Fiorella Burgio. "Flux predictions of high-energy neutrinos from pulsars". In: *Mon. Not. Roy. Astron. Soc.* 371 (2006), pp. 375–379. DOI: 10.1111/j.1365-2966.2006.10665.x. arXiv: astro-ph/0604379.

[257] Ke Fang. "High-Energy Neutrino Signatures of Newborn Pulsars In the Local Universe". In: *JCAP* 06 (2015), p. 004. DOI: 10.1088/1475-7516/2015/06/004. arXiv: 1411.2174 [astro-ph.HE].

[258] P. A. Caraveo, A. De Luca, R. P. Mignani, and G. F. Bignami. "The distance to the vela pulsar gauged with hst parallax oservations". In: *Astrophys. J.* 561 (2001), p. 930. DOI: 10.1086/323377. arXiv: astro-ph/0107282.

[259] Rebecca Lin, Marten H. van Kerkwijk, Franz Kirsten, Ue-Li Pen, and Adam T. Deller. "The Radio Parallax of the Crab Pulsar: A First VLBI Measurement Calibrated with Giant Pulses". In: *Astrophys. J.* 952.2 (2023), p. 161. DOI: 10.3847/1538-4357/acdc98. arXiv: 2306.01617 [astro-ph.HE].

[260] George G. Pavlov, Divas Sanwal, and Marcus A. Teter. "Central compact objects in supernova remnants". In: *IAU Symp.* 218 (2004), p. 239. arXiv: astro-ph/0311526.

[261] Claire Guépin, Benoît Cerutti, and Kumiko Kotera. "Proton acceleration in pulsar magnetospheres". In: *Astron. Astrophys.* 635 (2020), A138. DOI: 10.1051/0004-6361/201936816. arXiv: 1910.11387 [astro-ph.HE].

[262] Aman Asthana, Alexander A. Mushtukov, Alexandra A. Dobrynina, and Igor S. Ognev. "Bright X-ray pulsars as sources of MeV neutrinos in the sky". In: *Mon. Not. Roy. Astron. Soc.* 522.3 (2023), pp. 3405–3411. DOI: 10.1093/mnras/stad1118. arXiv: 2304.04520 [astro-ph.HE].

[263] R. Abbasi et al. "Evidence for neutrino emission from the nearby active galaxy NGC 1068". In: *Science* 378.6619 (2022), pp. 538–543. DOI: 10.1126/science.abg3395. arXiv: 2211.09972 [astro-ph.HE].

[264] M. G. Aartsen et al. "Characteristics of the diffuse astrophysical electron and tau neutrino flux with six years of IceCube high energy cascade data". In: *Phys. Rev. Lett.* 125.12 (2020), p. 121104. DOI: 10.1103/PhysRevLett.125.121104. arXiv: 2001.09520 [astro-ph.HE].

[265] Toshiya Namikawa, Shohei Saga, Daisuke Yamauchi, and Atsushi Taruya. "CMB Constraints on the Stochastic Gravitational-Wave Background at Mpc scales". In: *Phys. Rev. D* 100.2 (2019), p. 021303. DOI: 10.1103/PhysRevD.100.021303. arXiv: 1904.02115 [astro-ph.CO].

[266] Joern Kersten and Alexei Yu. Smirnov. "Decoherence and oscillations of supernova neutrinos". In: *Eur. Phys. J. C* 76.6 (2016), p. 339. DOI: 10.1140/epjc/s10052-016-4187-5. arXiv: 1512.09068 [hep-ph].

[267] Bin Xu. "Neutrino Decoherence in Simple Open Quantum Systems". In: (Sept. 2020). arXiv: 2009.13471 [hep-ph].

[268] Heinz-Peter Breuer and Francesco Petruccione. *The Theory of Open Quantum Systems*. Oxford University Press, Jan. 2007. ISBN: 978-0-19-170634-9, 978-0-19-921390-0. DOI: 10.1093/acprof:oso/9780199213900.001.0001.

[269] S. W. Hawking. "Black holes in general relativity". In: *Commun. Math. Phys.* 25 (1972), pp. 152–166. DOI: 10.1007/BF01877517.

[270] Werner Israel. "Event horizons in static electrovac space-times". In: *Commun. Math. Phys.* 8 (1968), pp. 245–260. DOI: 10.1007/BF01645859.

[271] Yong Liu, Liang-zhong Hu, and Mo-Lin Ge. "The Effect of quantum mechanics violation on neutrino oscillation". In: *Phys. Rev. D* 56 (1997), pp. 6648–6652. DOI: 10.1103/PhysRevD.56.6648.

[272] Yong Liu, Jing-Ling Chen, and Mo-Lin Ge. "A Constraint on EHNS parameters from solar neutrino problem". In: *J. Phys. G* 24 (1998), pp. 2289–2296. DOI: 10.1088/0954-3899/24/12/014. arXiv: hep-ph/9711381.

[273] Chao-Hsi Chang et al. "Possible effects of quantum mechanics violation induced by certain quantum gravity on neutrino oscillations". In: *Phys. Rev. D* 60 (1999), p. 033006. DOI: 10.1103/PhysRevD.60.033006. arXiv: hep-ph/9809371.

[274] F. Benatti and R. Floreanini. "Open system approach to neutrino oscillations". In: *JHEP* 02 (2000), p. 032. DOI: 10.1088/1126-6708/2000/02/032. arXiv: hep-ph/0002221.

[275] E. Lisi, A. Marrone, and D. Montanino. "Probing possible decoherence effects in atmospheric neutrino oscillations". In: *Phys. Rev. Lett.* 85 (2000), pp. 1166–1169. DOI: 10.1103/PhysRevLett.85.1166. arXiv: hep-ph/0002053.

[276] Jonathan L. Feng. "Dark Matter Candidates from Particle Physics and Methods of Detection". In: *Ann. Rev. Astron. Astrophys.* 48 (2010), pp. 495–545. DOI: 10.1146/annurev-astro-082708-101659. arXiv: 1003.0904 [astro-ph.CO].

[277] Frank T. Avignone III, Steven R. Elliott, and Jonathan Engel. "Double Beta Decay, Majorana Neutrinos, and Neutrino Mass". In: *Rev. Mod. Phys.* 80 (2008), pp. 481–516. DOI: 10.1103/RevModPhys.80.481. arXiv: 0708.1033 [nucl-ex].

[278] Leszek Roszkowski, Enrico Maria Sessolo, and Sebastian Trojanowski. "WIMP dark matter candidates and searches—current status and future prospects". In: *Rept. Prog. Phys.* 81.6 (2018), p. 066201. DOI: 10.1088/1361-6633/aab913. arXiv: 1707.06277 [hep-ph].

[279] Nicolás Bernal, Matti Heikinheimo, Tommi Tenkanen, Kimmo Tuominen, and Ville Vaskonen. "The Dawn of FIMP Dark Matter: A Review of Models and Constraints". In: *Int. J. Mod. Phys. A* 32.27 (2017), p. 1730023. DOI: 10.1142/S0217751X1730023X. arXiv: 1706.07442 [hep-ph].

[280] G. Bélanger, A. Mjallal, and A. Pukhov. "WIMP and FIMP dark matter in the inert doublet plus singlet model". In: *Phys. Rev. D* 106 (9 Nov. 2022), p. 095019. DOI: 10.1103/PhysRevD.106.095019. URL: https://link.aps.org/doi/10.1103/PhysRevD.106.095019.

[281] Kevork N. Abazajian. "Sterile neutrinos in cosmology". In: *Phys. Rept.* 711-712 (2017), pp. 1–28. DOI: 10.1016/j.physrep.2017.10.003. arXiv: 1705.01837 [hep-ph].

[282] R. Abbasi et al. "Search for quantum gravity using astrophysical neutrino flavour with IceCube". In: *Nature Phys.* 18.11 (2022), pp. 1287–1292. DOI: 10.1038/s41567-022-01762-1. arXiv: 2111.04654 [hep-ex].

[283] Mathieu Perrin-Terrin. "Sensitivity of the KM3NeT/ORCA detector to the neutrino mass ordering and beyond". In: *PoS* ICRC2021 (2021), p. 1166. DOI: 10.22323/1.395.1166.

[284] R. Coniglione. "High-energy neutrino astronomy with KM3NeT-ARCA". In: *25th European Cosmic Ray Symposium*. Jan. 2017. arXiv: 1701.05849 [astro-ph.IM].

[285] IceCube Collaboration. *Replication Data for: Searching for Decoherence from Quantum Gravity at the IceCube South Pole Neutrino Observatory*. Version V1. 2024. DOI: 10.7910/DVN/9WGYQN. URL: https://doi.org/10.7910/DVN/9WGYQN.

[286] H. P. Breuer and F. Petruccione. *The theory of open quantum systems*. 2002.

[287] Wojciech Hubert Zurek. "Decoherence, einselection, and the quantum origins of the classical". In: *Rev. Mod. Phys.* 75 (2003), pp. 715–775. DOI: 10.1103/RevModPhys.75.715. arXiv: quant-ph/0105127.

[288] H. D. Zeh. "On the interpretation of measurement in quantum theory". In: *Found. Phys.* 1 (1970), pp. 69–76. DOI: 10.1007/BF00708656.

[289] M. C. Gonzalez-Garcia and M. Maltoni. "Status of Oscillation plus Decay of Atmospheric and Long-Baseline Neutrinos". In: *Phys. Lett. B* 663 (2008), pp. 405–409. DOI: 10.1016/j.physletb.2008.04.041. arXiv: 0802.3699 [hep-ph].

[290] Sharada Iyer Dutta, Mary Hall Reno, and Ina Sarcevic. "Tau neutrinos underground: Signals of muon-neutrino —> tau neutrino oscillations with extragalactic neutrinos". In: *Phys. Rev. D* 62 (2000), p. 123001. DOI: 10.1103/PhysRevD.62.123001. arXiv: hep-ph/0005310.

[291] John R. Ellis, J. S. Hagelin, Dimitri V. Nanopoulos, and M. Srednicki. "Search for Violations of Quantum Mechanics". In: *Nucl. Phys. B* 241 (1984). Ed. by John C. Allred, p. 381. DOI: 10.1016/0550-3213(84)90053-1.

[292] Rodolfo Gambini, Rafael Porto, and Jorge Pullin. "Fundamental decoherence from quantum gravity: A Pedagogical review". In: *Gen. Rel. Grav.* 39 (2007), pp. 1143–1156. DOI: 10.1007/s10714-007-0451-1. arXiv: gr-qc/0603090.

[293] Andrei O. Barvinsky and Alexander Yu. Kamenshchik. "Preferred Basis, Decoherence and the Quantum State of the Universe". In: *Fundam. Theor. Phys.* 204 (2022), pp. 97–120. DOI: 10.1007/978-3-030-88781-0_6. arXiv: 2006.16812 [gr-qc].

[294] A. L. G. Gomes, R. A. Gomes, and O. L. G. Peres. "Quantum decoherence and relaxation in long-baseline neutrino data". In: *JHEP* 10 (2023), p. 035. DOI: 10.1007/JHEP10(2023)035. arXiv: 2001.09250 [hep-ph].

[295] Pilar Coloma, Jacobo Lopez-Pavon, Ivan Martinez-Soler, and Hiroshi Nunokawa. "Decoherence in Neutrino Propagation Through Matter, and Bounds from IceCube/DeepCore". In: *Eur. Phys. J. C* 78.8 (2018), p. 614. DOI: 10.1140/epjc/s10052-018-6092-6. arXiv: 1803.04438 [hep-ph].

[296] Shiraz Minwalla, Mark Van Raamsdonk, and Nathan Seiberg. "Noncommutative perturbative dynamics". In: *JHEP* 02 (2000), p. 020. DOI: 10.1088/1126-6708/2000/02/020. arXiv: hep-th/9912072.

[297] Dominik Hellmann, Heinrich Päs, and Erika Rani. "Quantum gravitational decoherence in the three neutrino flavor scheme". In: *Phys. Rev. D* 106.8 (2022), p. 083013. DOI: 10.1103/PhysRevD.106.083013. arXiv: 2208.11754 [hep-ph].

[298] Ivan Esteban, M. C. Gonzalez-Garcia, Michele Maltoni, Thomas Schwetz, and Albert Zhou. "The fate of hints: updated global analysis of three-flavor neutrino oscillations". In: *JHEP* 09 (2020), p. 178. DOI: 10.1007/JHEP09(2020)178. arXiv: 2007.14792 [hep-ph].

[299] Amanda Cooper-Sarkar, Philipp Mertsch, and Subir Sarkar. "The high energy neutrino cross-section in the Standard Model and its uncertainty". In: *JHEP* 08 (2011), p. 042. DOI: 10.1007/JHEP08(2011)042. arXiv: 1106.3723 [hep-ph].

[300] John F. Beacom, Patrick Crotty, and Edward W. Kolb. "Enhanced Signal of Astrophysical Tau Neutrinos Propagating through Earth". In: *Phys. Rev. D* 66 (2002), p. 021302. DOI: 10.1103/PhysRevD.66.021302. arXiv: astro-ph/0111482.

[301] Carlos A. Argüelles, Diksha Garg, Sameer Patel, Mary Hall Reno, and Ibrahim Safa. "Tau depolarization at very high energies for neutrino telescopes". In: *Phys. Rev. D* 106.4 (2022), p. 043008. DOI: 10.1103/PhysRevD.106.043008. arXiv: 2205.05629 [hep-ph].

[302] Anatoli Fedynitch, Ralph Engel, Thomas K. Gaisser, Felix Riehn, and Todor Stanev. "Calculation of conventional and prompt lepton fluxes at very high energy". In: *EPJ Web Conf.* 99 (2015). Ed. by D. Berge, A. de Roeck, M. Mangano, and B. Pattison, p. 08001. DOI: 10.1051/epjconf/20159908001. arXiv: 1503.00544 [hep-ph].

[303] Thomas K. Gaisser. "Spectrum of cosmic-ray nucleons, kaon production, and the atmospheric muon charge ratio". In: *Astropart. Phys.* 35 (2012), pp. 801–806. DOI: 10.1016/j.astropartphys.2012.02.010. arXiv: 1111.6675 [astro-ph.HE].

[304] Felix Riehn et al. "The hadronic interaction model SIBYLL 2.3c and Feynman scaling". In: *PoS* ICRC2017 (2018), p. 301. DOI: 10.22323/1.301.0301. arXiv: 1709.07227 [hep-ph].

[305] IceCube Collaboration. *NuFlux: A library for calculating atmospheric neutrino fluxes*. Version 2.0.7. URL: %7Bhttps://doi.org/10.5281/zenodo.5874708%7D.

[306] IceCube Collaboration. "Characteristics of the diffuse astrophysical electron and tau neutrino flux with six years of IceCube high energy cascade data". In: *Phys. Rev. Lett.* 125.12 (2020), p. 121104. DOI: 10.1103/PhysRevLett.125.121104. arXiv: 2001.09520 [astro-ph.HE].

[307] M. G. Aartsen et al. "Searching for eV-scale sterile neutrinos with eight years of atmospheric neutrinos at the IceCube Neutrino Telescope". In: *Phys. Rev. D* 102.5 (2020), p. 052009. DOI: 10.1103/PhysRevD.102.052009. arXiv: 2005.12943 [hep-ex].

[308] Carlos A. Argüelles, Austin Schneider, and Tianlu Yuan. "A binned likelihood for stochastic models". In: *JHEP* 06 (2019), p. 030. DOI: 10.1007/JHEP06(2019)030. arXiv: 1901.04645 [physics.data-an].

[309] IceCube Collaboration. "Evidence for neutrino emission from the nearby active galaxy NGC 1068". In: *Science* 378.6619 (Nov. 2022), pp. 538–543. ISSN: 1095-9203. DOI: 10.1126/science.abg3395. URL: http://dx.doi.org/10.1126/science.abg3395.

[310] IceCube Collaboration. "The design and performance of IceCube DeepCore". In: *Astroparticle Physics* 35.10 (May 2012), pp. 615–624. ISSN: 0927-6505. DOI: 10.1016/j.astropartphys.2012.01.004. URL: http://dx.doi.org/10.1016/j.astropartphys.2012.01.004.

[311] Basudeb Dasgupta and Joachim Kopp. "Sterile Neutrinos". In: *Phys. Rept.* 928 (2021), pp. 1–63. DOI: 10.1016/j.physrep.2021.06.002. arXiv: 2106.05913 [hep-ph].

[312] M. A. Acero et al. "White paper on light sterile neutrino searches and related phenomenology". In: *J. Phys. G* 51.12 (2024), p. 120501. DOI: 10.1088/1361-6471/ad307f. arXiv: 2203.07323 [hep-ex].